POLITECNICO DI MILANO

School of Industrial and Information Engineering

Department of Energy

Laboratory of Catalysis and Catalytic Processes

Master of Science in Chemical Engineering

POLITECNICO DI MILANO

Kinetic Modeling of CO_2 Methanation over a Ni-Al Coprecipitated Catalyst

Supervisor :

Prof. Carlo Giorgio VISCONTI

Co-supervisor :

Alessandro PORTA, PhD

Candidates :

Gabriele RACO Matr. n. 920107

Denis VIDOTTO Matr. n. 920407

Academic Year 2019 – 2020

"Remember that all models are wrong;
the practical question is
how wrong do they have to be,
to not be useful."

(George E. P. Box, 1987)

Contents

List of Figures

List of Tables

List of Symbols and Acronyms

Acronyms

BET	Brunauer – Emmett – Teller
BJH	Barrett-Joyner-Halenda
CCS	Carbon Capture and Storage
CCU	Carbon Capture and Utilization
DOR	Degree of Reduction
EOR	Enhanced Oil Recovery
FT	Fischer-Tropsch
GHSV	Gas Hourly Space Velocity
GWP	Global Warming Potential
MASI	Most Abundant Surface Intermediate
MPE	Mean Percentage Error
NiAl1.16	Co-precipitated catalyst with Ni/Al ratio equal to 1.16
PtG	Power to Gas
PtM	Power to Methane
RDS	Rate Determining Step
RF	Radiative Forcing

RWGS	Reverse Water-Gas Shift
SNG	Synthetic Natural Gas
TPR	Temperature Programmed Reduction
VRE	Variable Renewable Energies
XRD	X-Ray Diffraction

Abstract

Power-to-Gas technology is leading the transition to a zero emissions scenario, introducing as a valid option for CO_2 utilization its hydrogenation to create methane, a very well known fuel that already has well-developed infrastructures all over the world through which it can transported and consumed. Carbon dioxide methanation turns the most deleterious greenhouse gas present in our atmosphere into a chemical commodity that we can exploit for our everyday life. Many studies have been conducted and, though the process is for the most part still at laboratory scale, some commercial-scale plants are active in the world and for a better realization of the industrial plants of tomorrow there is a strong need for detailed models describing the kinetic of the process. In this work, after an overview of the Power-to-Gas field and the analysis of reaction mechanisms and catalysts studied for the process up to now, a review of kinetic models proposed in literature is performed. The most interesting ones were then evaluated on our experimental dataset and model modifications were introduced for a best fitting. Finally, we developed on our own two kinetic models, that in their final version are able to fit the data very well in all the experimental field. All the models were divided depending on their ability to describe only CO_2 conversion or both carbon dioxide conversion and CO selectivity.

Keywords Power-to-Gas; Carbon dioxide methanation; Carbon monoxide; Kinetic study; Sabatier reaction; Reverse water gas shift reaction; Reaction mechanism; Ni/Al_2O_3;

Estratto

La tecnologia Power-to-Gas sta guidando la transizione verso uno scenario a emissioni zero, introducendo come valida opzione per l'utilizzo di CO_2 la sua idrogenazione a creare metano, un combustibile molto noto che ha già infrastrutture ben sviluppate in tutto il mondo attraverso il quale può essere trasportato e consumato. La metanazione dell'anidride carbonica trasforma il gas serra più dannoso presente nella nostra atmosfera in un prodotto chimico che possiamo sfruttare per la nostra vita quotidiana. Sono stati condotti molti studi e, sebbene il processo sia per la maggior parte ancora su scala di laboratorio, alcuni impianti su scala commerciale sono attivi nel mondo e per una migliore realizzazione degli impianti industriali di domani c'è una forte necessità di modelli dettagliati che descrivano la cinetica del processo. In questo lavoro, dopo una panoramica sul campo Power-to-Gas e l'analisi dei meccanismi di reazione e dei catalizzatori studiati per il processo fino ad ora, viene eseguita una revisione dei modelli cinetici proposti in letteratura. I più interessanti sono stati poi valutati sul nostro dataset sperimentale e sono state introdotte modifiche ai modelli per un miglior adattamento. Infine, abbiamo sviluppato in proprio due modelli cinetici, che nella loro versione finale sono in grado di predire molto bene i dati in tutto il campo sperimentale. Tutti i modelli sono stati divisi in base alla loro capacità di descrivere solo la conversione di CO_2 o sia la conversione dell'anidride carbonica che la selettività a CO.

Parole Chiave Power-to-Gas; Metanazione dell'anidride carbonica; Monossido di carbonio; Studio cinetico; Reazione di Sabatier; Reazione inversa dello spostamento del gas d'acqua; Meccanismo di reazione; Ni/Al_2O_3;

Thesis Outline

Thesis Outline

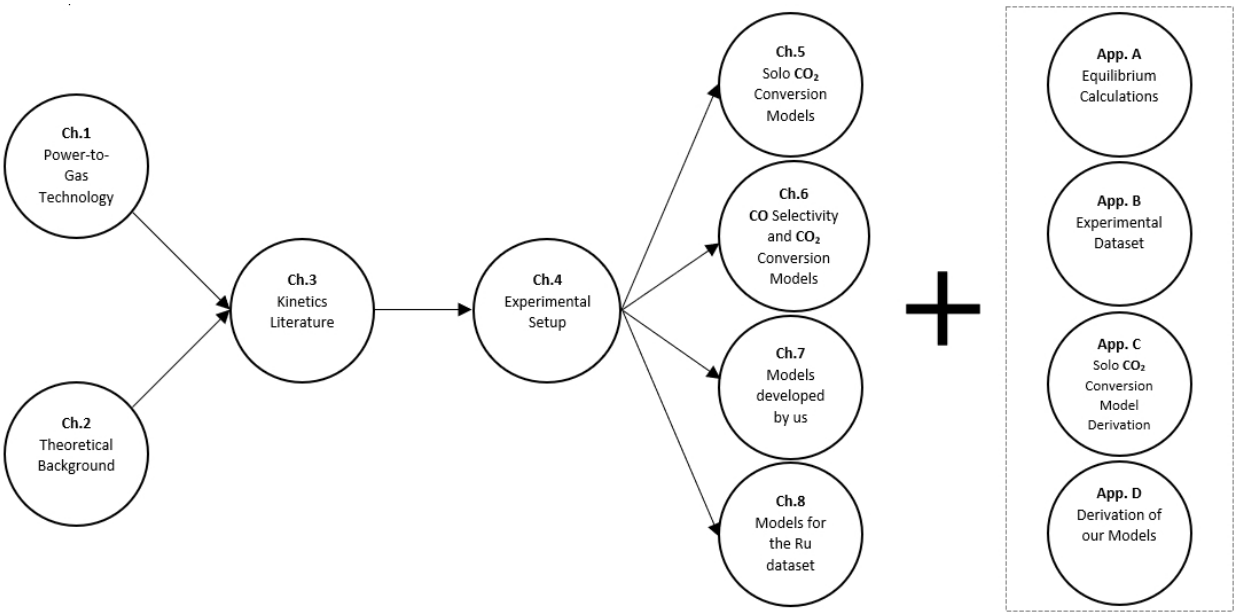

Figure 0.1: Thesis Outline.

Chapter 1 provides a general overview of the Power-to-Gas technology, CCUS processes and green hydrogen production.

Chapter 2 explores the theoretical background of the carbon dioxide methanation reaction, with an insight on catalyst adopted in the process and reaction mechanisms proposed up to now.

Chapter 3 reviews some of the kinetic models to describe the methanation process up to now, spacing from power laws to mechanistic comprehensive models.

Chapter 4 describes catalyst preparation, rig layout and how the collection of the experimental dataset was performed.

Chapter 5 reports a detailed analysis and the subsequent application of some of the models proposed in literature that can only predict CO_2 conversion.

Chapter 6 analyzes some of the comprehensive models proposed in literature, that can both predict CO_2 conversion and CO selectivity.

Chapter 7 proposes two kinetic models developed on our own, that can predict both CO_2 conversion and CO selectivity.

Chapter 8 shows the application of the models proposed in Chapter 7 on an experimental dataset collected on a Ru-based catalyst.

Lastly, four appendices are provided to specify some topics whose discussion was not strictly essential to the exposition of the work. However, they were reported in order to clarify any concern.

Appendix A includes an accurate description of the calculations required to plot the equilibrium curves.

Appendix B reports the complete dataset employed to perform the regression of the kinetic parameters in every different model.

Appendix C contains the complete derivation of the modified Koschany et al. model.

Appendix D contains the complete derivation of the Raco−Vidotto and the Vidotto−Raco models.

Chapter 1

Power-to-Gas Technology

Nowadays, climate change is a growing concern due to its drastic effects: melting glaciers, sea level rising, floods are only some of them. One of the main causes of this phenomenon is now known to be the high concentration of CO_2 in the atmosphere, a stable greenhouse gas that cannot be chemically decomposed in the stratosphere and has one of the highest radiative forcing. Radiative forcing (RF) is a parameter that quantifies the globally averaged change in the heat balance of the Earth-atmosphere system due to factors external to the climate system: its integration over certain time periods, typically 20 or 100 years, from a unit pulse emission, introduces another parameter, global warming potential (GWP), an indicator which takes in consideration the *lifetime* of a species in the atmosphere. CO_2, by definition, has a GWP equal to 1, being the gas used as reference [1]. Many policies and measures have been taken to confront this problem, such as the Paris Agreement [2] in which European governments agreed to keep the increase in global temperature strictly below 2℃ with respect to pre-industrial levels, with a particular effort to limit the increase to 1.5℃, which will likely reduce risks and impacts of climate change.

One of the primary actions to undertake is a strong reduction of CO_2 emissions: this will have deep impacts on the energy sector, which markedly relies on the combustion of fossil fuels, the main causes of carbon dioxide emissions. Thus, alternate and renewable energies need to be found and implemented from a technological point of view to match the demands coming from the energy sector. Up to now, only relying on renewable energies is

not a suitable solution. Indeed, state-of-the-art renewable energies are still unreliable, mainly because of their discontinuity and low efficiencies: renewable sources are characterized by strong availability oscillations and to ensure the stability of the electric grid, it is essential to design technologies to store the energy in excess.
Therefore, a more gradual transition from fossil fuels, on which developing countries still heavily rely, due to their low $/kWh costs, to renewable energy is necessary, with "temporary" solutions that can accompany and favor the transition.

As a matter of fact, although renewable energy is currently the fastest-growing source of energy, its share in the energy sector is expected to increase from the actual 4% to somewhere around 15% by 2040 [3], escorted by a consistent buildup of natural gas and a significant drop in the consumption of both oil and coal, the most polluting fossil fuels, respectively originating 0.85 $\frac{kg_{CO_2}}{kWh}$ and more than 1 $\frac{kg_{CO_2}}{kWh}$ in the process of electricity production.

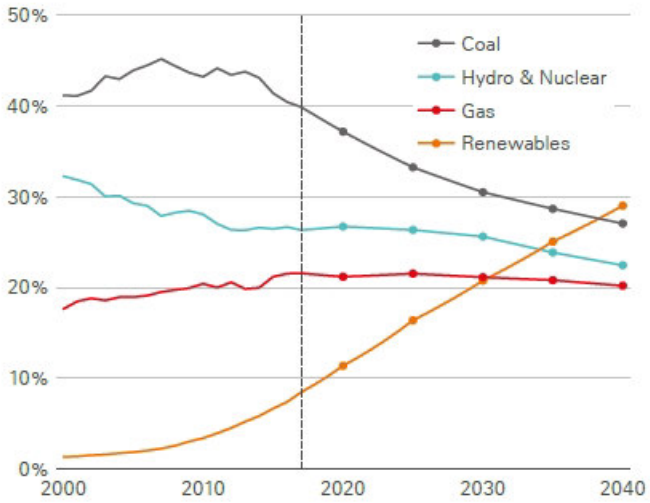

Figure 1.1: Future trends in the share of primary energies. [3]

Another target stated in the Paris Agreement is *"a balance between anthropogenic emissions by sources and removals by sinks"* [2] in the second half of this century, meaning the achievement of a net-zero emissions scenario.
To make this scenario possible, in the effort of reducing carbon dioxide emissions, in addition

to the implementing of renewable energy sources, process optimizations must be considered and realized. On the other hand, techniques to capture and further use carbon dioxide are being developed in a field called *Carbon Capture Utilization and Storage* (CCUS).
The importance of implementing CCUS is becoming more and more urgent: according to the *International Energy Agency* this decade of the 21^{st} century is going to be critical to scale up investments in developing and deploying CCUS, in a journey to the net-zero emission scenario that will likely be achieved around 2070 [4].
In this sector, we can distinguish three techniques, which are:

- Carbon Capture and Storage (CCS), which includes applications where CO_2 is captured and permanently stored;
- Carbon Capture and Utilization (CCU), which includes operations where CO_2 is used, for example in the production of methane or methanol;
- Carbon Capture, Utilization and Storage (CCUS), which puts together CCS and CCU, such as in the Enhanced Oil Recovery (EOR) process, operated by oil companies where carbon dioxide is injected inside an oil field and allows improved efficiencies in the extraction of crude oil [5];

CCUS is particularly requested in those sectors with hard-to-abate emissions, like the cement and steel production ones: retrofitting of existing plants is necessary and actions must be taken in the near future to limit more than ever carbon emissions. Furthermore, with the economic crisis caused by the Covid-19 pandemic and the consequent fall of oil prices, EOR technology will not be as a central option in CCUS as it is today.

As shown in Fig.1.2, CO_2 is captured from large point sites [6] or directly from the atmosphere, compressed and transported via pipelines, ship, rail or truck either to a site of storage, where it can be injected deep underground or into the seabed [7], or to locations where it can be further employed in the production of synthetic fuels, chemicals, building materials, or as a raw material for pharmaceutical and food industries. Among all the processes that involve CO_2 conversion, the ones that arouse the greatest interest are those that aim at the production of fuels and bulk chemicals, commercially established products such as methane,

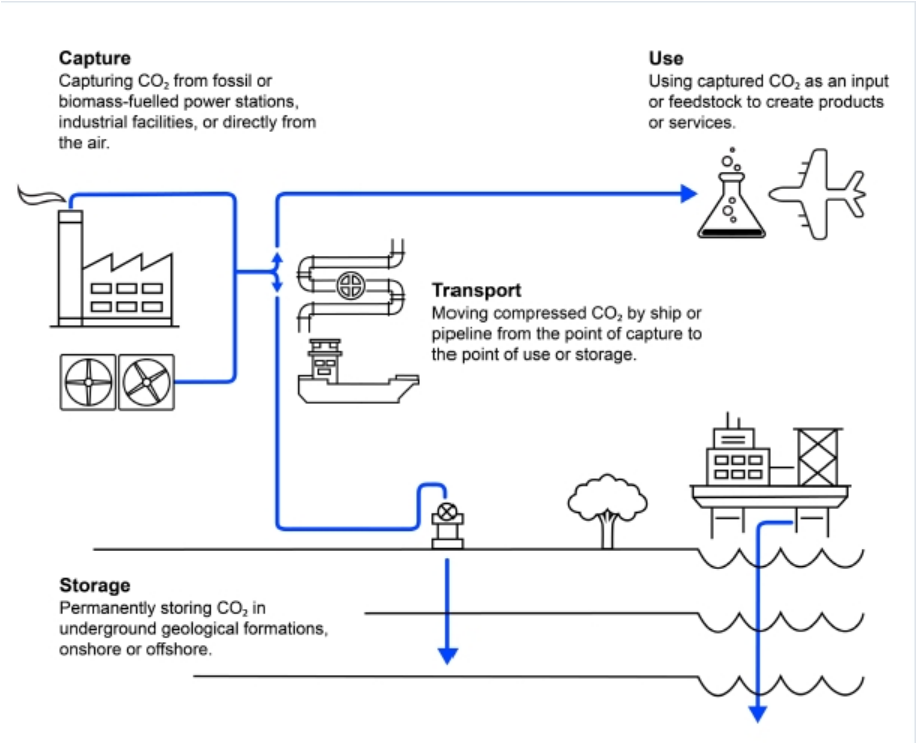

Figure 1.2: Representation of CCUS cycle. [4]

methanol and syngas, which can either be used directly as a fuel or as intermediates in the production of other fuels, such as diesel, gasoline and aviation fuels, or in the synthesis of chemicals [8]. The intrinsic chemical stability of carbon dioxide makes these processes quite challenging from a heat management and catalytic point of view, with thorough research of the best catalysts to employ in each process.

In this sense, hydrogenation and dry-reforming are the two leading paths at research scale, with the latter being a very smart way to produce syngas that can be further employed in other industrial processes. Among all the processes of hydrogenation, the most encouraging ones are those leading to methane and methanol production, due to their very high yields and their modest process conditions in which they can be realized.

In particular, carbon dioxide to CH_4 hydrogenation was first studied by Paul Sabatier in 1902 [9], who proposed the following reaction, involving the transfer of eight electrons:

$$CO_2 + 4\ H_2 \rightleftharpoons CH_4 + 2\ H_2O \quad \Delta H^0_{R,298K} = -165.0\,\frac{kJ}{mol} \tag{1.0.1}$$

Since Sabatier's work, many have tried to develop catalysts having high activity over a wide

range of different operating conditions, at the same time minimizing coke formation, keeping long-term chemical and thermal stability, in order to take the process to an industrial scale.

One problem of this use of CO_2 arises from the great consumption of hydrogen required by the process. H_2 is mainly produced by thermochemical conversion of fossil fuels into syngas and it is therefore associated with processes which have very high carbon footprints. So, to make the hydrogen production process *green* H_2 should be produced in an environmentally friendly way: the main road to match this demand is water electrolysis that, however, needs electricity to create hydrogen. If this electricity is created from renewable sources then the process becomes sustainable and *green hydrogen* is formed.
This is possible because renewable energy sources have a fluctuating and intermittent component and it may happen that energy produced from them is higher than the one requested by users and the *surplus*, if not exploited, will be wasted. Therefore, this surplus of energy can be stored through production of hydrogen by means of water electrolysis [10].

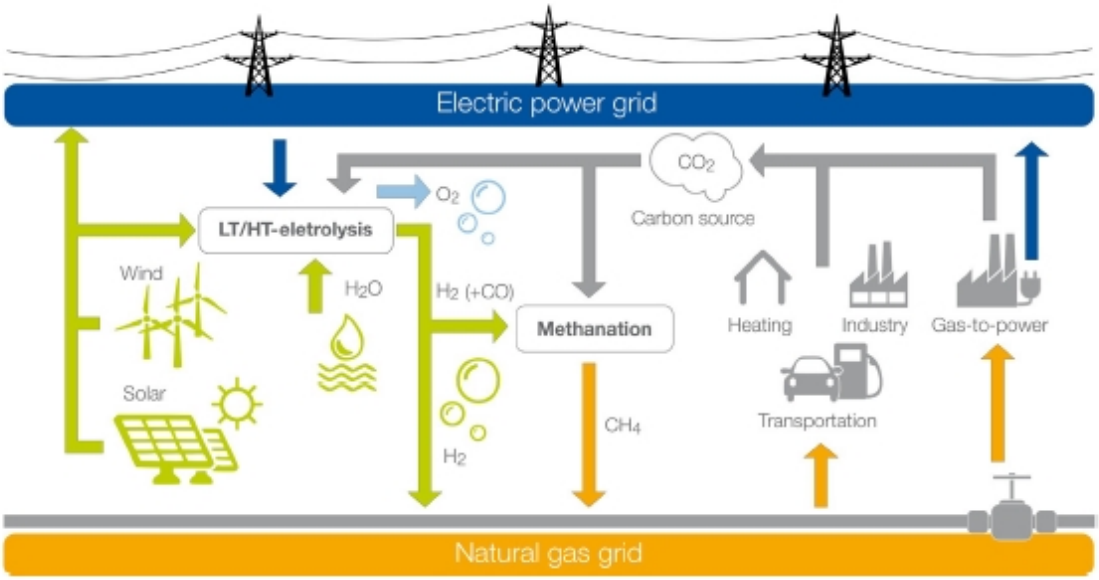

Figure 1.3: PtG network and its application. [11]

The aforementioned mechanism is part of the *Power-to-Gas* perspective, in which hydrogen created through water electrolysis is further adopted in the reaction with CO_2 to give CH_4.

The formed methane is called *Synthetic Natural Gas* when coming from this process: its production is very convenient because CH_4 is a very well known source of energy, with well-developed and already known available technologies, such as already built and efficient pipelines through which it is easily convoyed to various users (power plants, industries, users). For these reasons, Power-to-Methane is considered a pillar process in producing synthetic natural gas (SNG): the first steps of the process consist in the capture of CO_2 and in the production of green H_2.
These technologies will be described in the following pages, together with the production of green H_2, fundamental in the PtM network.

An important point to underline is that the PtG approach will be a temporary solution, very useful in a time window where renewable sources can supply the necessary energy for hydrogen production and for consequent methane formation, in a moment where CO_2 formation all over the world will still be very high [4].
As of today, there are few industrial-scale applications of PtG, such as the Audi PtG plant in Werlte (Germany), operating since 2013.
The real challenge to take this process to industrial-scale is the individuation of an active and selective catalyst, that could ensure high performances with affordable costs, the most attractive option being Ni-based catalysts, and the search of a kinetic expression that could describe the process.

1.1 CO_2 capture

In order to treat CO_2 as a reactant in the processes to convert it to methane, a certain threshold of purity is required. Hence, highly efficient and cost-effective separation methods are thoroughly studied and subsequently exploited. Carbon dioxide capture from flue gases plays a fundamental role in the CCUS network.

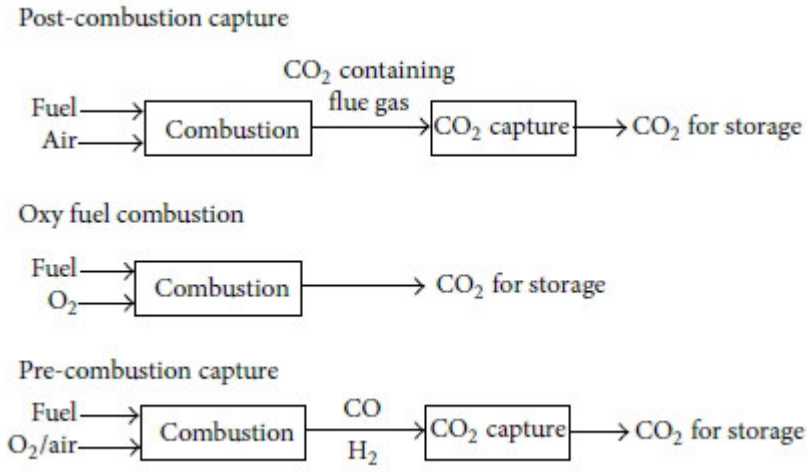

Figure 1.4: Different approaches of CO_2 capture. [12]

Three main approaches to realize the carbon capture exist:

- Pre-combustion capture;
- Oxy-fuel combustion;
- Post-combustion capture;

Pre-combustion capture is part of syngas production: when a fuel is made to react with air, oxygen or steam to obtain a CO/H_2 mixture, then carbon monoxide is made to react with steam in a Water-Gas Shift reactor, to collect CO_2 and more hydrogen. After that, carbon dioxide is removed from the stream by means of physical or chemical absorption: the stream is now a hydrogen-rich fuel which can be adopted for subsequent applications in furnaces, gas turbines and fuel cells [13], [14], [15].

In oxy-fuel combustion, pure oxygen is used instead of air, eliminating nitrogen presence and creating a flue gas mainly constituted by CO_2 and H_2O, which are separated in a step where water is condensed. This technique is not very common because it accounts for two main disadvantages: high capital cost and high electric power requirement, caused by the cryogenic section where O_2 is separated from air.

Post combustion technique is the simplest method to capture CO_2, which is removed

by the exhaust flue gases. This approach is commonly adopted in existing plants, because it presents the great advantage of easier retrofitting compared to other capture methods.

Based on the previous considerations, a good separation of carbon dioxide becomes fundamental for its further handling in the PtG network. Many different methods can be applied, the most common of which are deeply analyzed in many academic papers [4], [15], [16], [17]. These are:

- Absorption: a very common method, extensively used by oil and chemical companies, who have known this method for more than 50 years now. The process can either be physical or chemical: if the solvent reacts with CO_2 the process is known as chemical absorption, otherwise it is physical.
  Flue gases are brought into contact with the solvent stream, usually in counter-flow, and the solvent absorbs CO_2. After that, the solvent is regenerated in a stripper column where, upon heating, CO_2 is desorbed and compressed, while the regerenated solvent is recycled to the absorber.

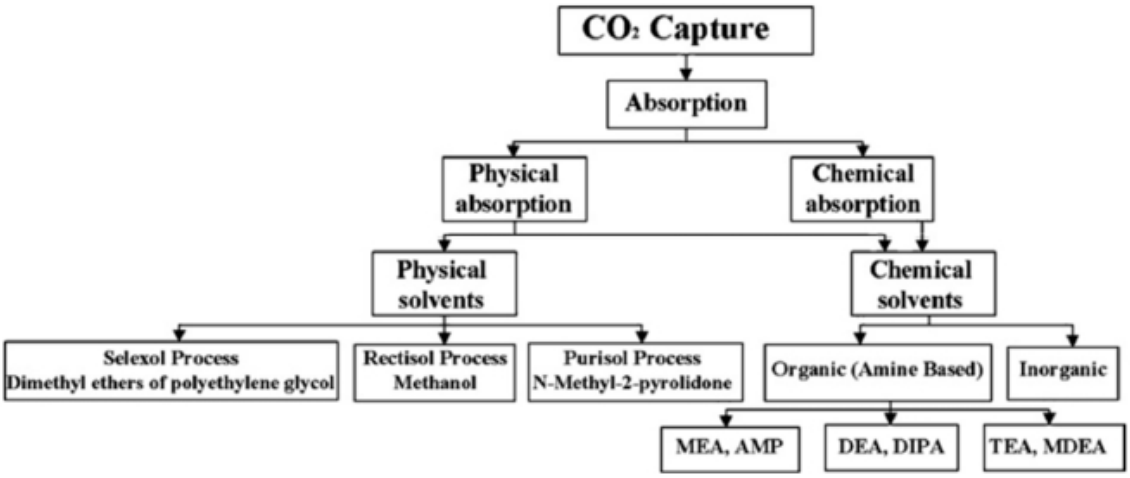

Figure 1.5: Different kinds of absorption processes. [16]

Physical absorption is preferred when the partial pressure of the acid gas in the flow to be treated is high, while chemical absorption is used when CO_2 partial pressure is low. In the former case, typical operating pressures are $6 - 10$ bar and solvents can either be Selexol®, Rectisol® or Purisol®, while in the latter case amine-based solvents like MEA

(mono-ethanolamine), DEA (di-ethanolamine) and MDEA (methil-diethanolamine) are used. Due to the formation of a chemical bond, regeneration of a solvent used in chemical absorption is much more difficult, and a reboiling is needed, while in physical absorption solvents can be regenerated through flashing.

- Adsorption: the removal of CO_2 is performed exploiting a solid surface. The formation of physical or chemical bonds takes place between the adsorbent surface and carbon dioxide till the saturation of the adsorbent. When the surface becomes saturated with the acid gas, CO_2 can be removed through different operations such as PSA (pressure swing adsorption), TSA (temperature swing adsorption), ESA (electronic swing adsorption) or VSA (vacuum swing adsorption).
  The adsorption process can be preferred due to its high adsorption capacity at ambient pressure and temperature and for its lower energy requirements compared to absorption processes. The real challenge of the process is to find suitable adsorbents which can separate CO_2 from flue gases. Up to now, natural and synthetic zeolites, activated carbons, carbon molecular sieves, hydrotalcites and metal-organic framework materials have been investigated. In this process, as in the absorption one, partial pressure of CO_2 plays a fundamental role in the efficiency of the process, particularly when activated carbons are used.

- Membranes: semi-permeable barriers that allow only one component to permeate them, exploiting the diffusion process and removing it from the flue gas. In this case, the species to be removed is carbon dioxide. Membranes can be used either as conventional membranes or as gas absorption columns, with the latter that exploit microporous solid membranes, minimizing channeling and entrainment. Many academics agree in stating that membranes are efficient only if concentration of CO_2 in the stream to purify is very high, in the order of 10%.
  Typical materials employed in this method are inorganic ceramic or organic polymeric membranes. When using this method, a trade-off between CO_2 separation efficiency and high CO_2 purity must be done.

- Cryogenic distillation: this process consists in cooling down gases to temperatures

below the sublimation temperature of CO_2 (-78.5℃), with the consequent formation of carbon dioxide crystals that can be separated from the mixture of interest. Typically, a flue gas is constituted by N_2, CO_2 and H_2O, so first water will condense and then CO_2 will solidify.
This technique is currently not considered a good alternative, due to the very high energy requirements linked to the very low temperatures to be achieved [18], [19].

- Calcium looping: this technology implies the use of two different reactors. In the first one, lime (CaO) is used as an adsorbent, capturing CO_2 by forming $CaCO_3$, easily separable from the gas mixture. Calcium carbonate is then transported to the second reactor where it is regenerated to CO_2 and CaO, in a loop that brings lime back to the first reactor. This method is still at a pre-commercial scale, and represents a valid alternative for pre-combustion capture [20], [16], [21].

1.2 Green H_2 production

Hydrogen is industrially synthesized when syngas, a mixture of CO and H_2, is produced in processes such as partial oxidation of hydrocarbons, steam reforming, auto-thermal catalytic reforming and carbon gassification, all processes with a very high carbon footprint. If this strategy is chosen to produce hydrogen, even if methane is formed through Sabatier's reaction, the overall process won't be environmentally friendly.
On the other hand, if renewable energy sources are exploited to create electricity which can be adopted in the water electrolysis process, hydrogen production becomes sustainable.
Indeed, the process of water electrolysis can generate almost pure hydrogen: based on the movement of electrons, which circulate continuously through an external circuit, a chemical reaction takes place.

$$H_2O \rightarrow H_2 + 1/2\ O_2 \qquad \Delta H_R^0 = +285.8\ \frac{kJ}{mol} \tag{1.2.1}$$

The reaction of water-splitting into its elements takes place in two steps: the semi-reaction of reduction occurs at the cathode (negatively charged) while the semi-reaction of oxidation takes place at the anode (positevly charged).

Water electrolysis occurs in electrolyzers: alkaline, proton exchange membrane and solid-oxide electrolytic cells are the ones which arise most interest in their development and application for green H_2 production.

- Alkaline water electrolyzers (AEL): in the PtG field, they are considered the most mature technology of all; AEL can work both at atmospherical and more elevated pressures, with the latter option being very convenient for direct injection of H_2 in the power grid.

  In their configuration, two electrodes are separated by a diaphragm which allows the transfer of hydroxyl ions OH^- (charge carriers of these electrolytic cells) from the cathode to the anode. The two electrodes are immersed in a liquid electrolyte solution of either KOH or NaOH.

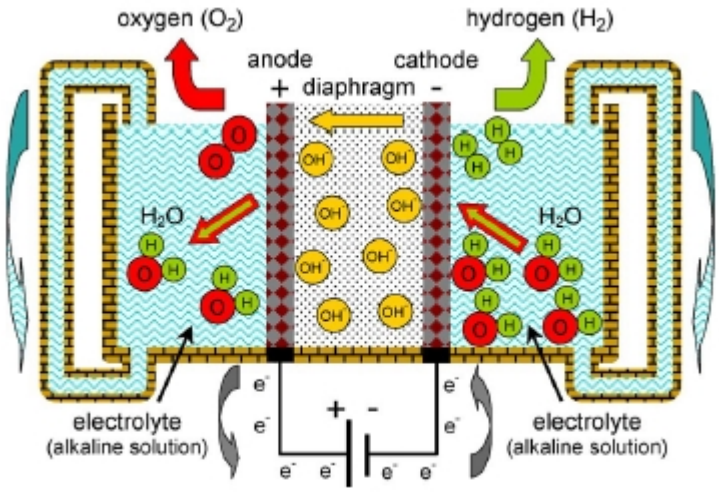

Figure 1.6: Alkaline electrolytic cell. [22]

Typical operating temperatures are between 40℃ and 90℃ [10]. Hydrogen is formed at the cathode, together with OH^- ions, which then move to the anode to form O_2, closing the electrical circuit.

$$\text{(C)} \quad 2\ H_2O_{(l)} + 2\ e^- \rightarrow H_{2(g)} + 2\ OH^-_{(aq)} \tag{1.2.2}$$

$$\text{(A)} \quad 2\ OH^-_{(aq)} \rightarrow 1/2\ O_{2(g)} + H_2O_{(g)} + 2\ e^- \tag{1.2.3}$$

Very high levels of hydrogen purity can be achieved, up to 99% [10], [23], [22].

Although already available at a commercial scale, AEL have an important issue: the liquid solution used as electrolyte is highly corrosive, causing high maintenance costs.

- Proton Exchange Membrane electrolyzers (PEM): less common then AEL, this kind of electrolyzers present shorter lifetime and higher capital costs, but they can operate with higher current densities. Moreover, they possess a higher flexibility of operation. In PEM electrolyzers, the electrolyte is a sulphonated polymeric membrane with a cross-linked structure, where the presence of functional groups of sulfonic acid ($-SO_3H$) allows the transfer of H^+, charge carriers of the process, from anode to cathode. The most common commercial membrane is Nafion by Dupont®. The electrodes are

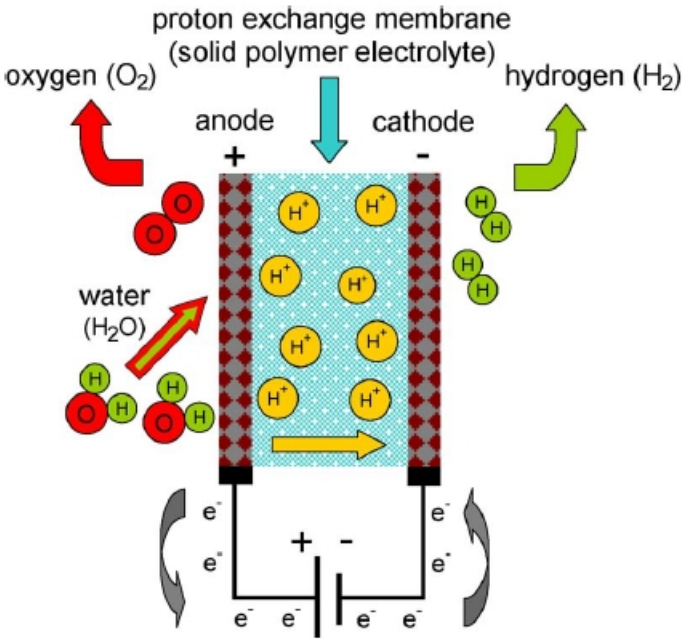

Figure 1.7: Proton Exchange Membrane electrolyzer. [22]

typically made either by platinum or iridium: the use of noble metals is one of the causes leading to significantly higher investment costs of this technology compared to AEL.

Typical operating temperatures are between 20°C and 100°C [10]. As in AEL, hydrogen is formed at the cathode and oxygen at the anode:

$$\text{(A)} \quad H_2O_{(l)} \rightarrow 1/2\ O_{2(g)} + 2\ H^+_{(aq)} + 2\ e^- \tag{1.2.4}$$

$$(C) \quad 2\,H^{+}_{(aq)} + 2\,e^{-} \rightarrow H_{2(g)} \tag{1.2.5}$$

PEM can operate under pressures up to 35 bar [22], producing high-pressure hydrogen. In addition, a very high purity of the produced H_2 can be obtained, up to 99.99%.

- Solid Oxide Electrolytic Cells (SOEC): this kind of electrolyzers is characterized by high operating temperatures, in a range between 600°C and 1000°C [10] [22] and rather than water electrolysis, steam electrolysis occurs.
  The charge carriers are O^{2-} created at the cathode, which then travel in the solid oxide matrix through the available vacancies, reaching the anode where they form O_2.

$$(C) \quad H_2O_{(g)} + 2\,e^{-} \rightarrow H_{2(g)} + O^{2-}_{(aq)} \tag{1.2.6}$$

$$(A) \quad O^{2-}_{(aq)} \rightarrow 1/2\,O_{2(g)} + 2\,e^{-} \tag{1.2.7}$$

The electrolyte, unlike those present in AEL and PEM technologies, which are liquid, is

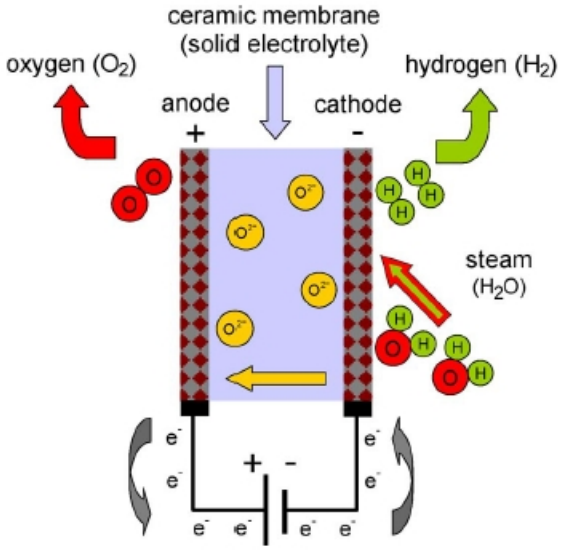

Figure 1.8: Solid Oxide Electrolytic cell. [22]

a solid matrix of Yttria-stabilized Zirconia (YSZ). The cathode is formed by a cer-met of Ni and YSZ while the anode is composed by a composite of YSZ and perovskites structures, such as $LaMnO_3$, $LaFeO_3$, $LaCoO_3$.
The particular features of the SOEC make this technique very attractive for hydrogen production, but SOEC are developed only at a lab-scale for the moment [10], due to

very challenging thermal stability of the components and sealing issues [22]. Moreover, SOEC at the present time still lack long-term stability.

Today, R&D is searching for the best technique to produce green hydrogen from water electrolysis, to insert it in the PtG network. Flexibility and durability are two of the key fundamentals required: AEL can't still work in transient, while PEM can, but have higher capital costs, less long-term durability, and more marked problem of corrosion. SOEC are still at lab-scale and still have very high investment costs.
Nevertheless, many researchers believe there will be a switch in this decade, with PEM overtaking AEL in the leadership of water electrolysis field [24].

Chapter 2

CO_2 Methanation Theoretical Background

As widely explained in Ch.1, CO_2 methanation will be a leading strategy to temporary solve the problem of carbon dioxide presence in the atmosphere, with all its consequences. In this chapter, we will explain more in detail the theoretical background of CO_2 methanation, first studied by Paul Sabatier in 1902 [25], with details on its thermodynamics, the different kinds of catalysts employed up to now, proposed reaction mechanism and the first proposals on reactors to be used.

2.1 Thermodynamics

From a thermodynamic point of view, in a system where 5 species are present (CO_2, H_2, H_2O, CH_4, CO), containing 3 elements (C,H and O), two reactions are needed to describe it. One is the Sabatier reaction, the methanation of CO_2 involving the transfer of eight electrons, with the C element passing from an oxidation number of +4 in CO_2 to a -4 in CH_4. The other one is usually considered the reverse water-gas shift, in which CO is produced together with water.

$$CO_2 + 4\ H_2 \rightleftharpoons CH_4 + 2\ H_2O \quad \Delta H^0_{R,298K} = -165.1\,\frac{kJ}{mol} \tag{2.1.1}$$

$$CO_2 + H_2 \rightleftharpoons CO + H_2O \qquad \Delta H^0_{R,298K} = +41.2\,\frac{kJ}{mol} \tag{2.1.2}$$

Where the values of $\Delta H^0_{R,298K}$ are calculated as:

$$\Delta H^0_{R,j}(298\,K) = \sum_{i=1}^{N} \nu_{i,j} \Delta h^0_{f,i}(298\,K) \tag{2.1.3}$$

The equilibrium calculations are reported in Appendix A.

The methanation reaction is highly exothermic, which makes it less favoured by a temperature increase, while reverse water-gas shift is slightly endothermic, so it is favoured by a temperature increase. This is the reason of the CO_2 conversion profile against T, shown in Fig. 2.1. At first, conversion decreases then, as RWGS becomes more and more important, conversion increases again, starting from around 550 ℃.

This trend-change is significant for the equilibrium curve calculated at 1 atm, while it becomes less and less relevant with higher pressures. This different behaviour is caused by the fact that RWGS does not involve any change of moles, while carbon dioxide methanation reaction, having a decrease in number of moles, is favoured by pressure.

The different behaviour of the two reactions is reflected also on CH_4 selectivity, which rapidly decreases at atmospheric pressure and, on the contrary, has a less steep decrement when operating at high pressure. At atmospheric pressure, the decrease is very evident for temperatures higher than 400 ℃.

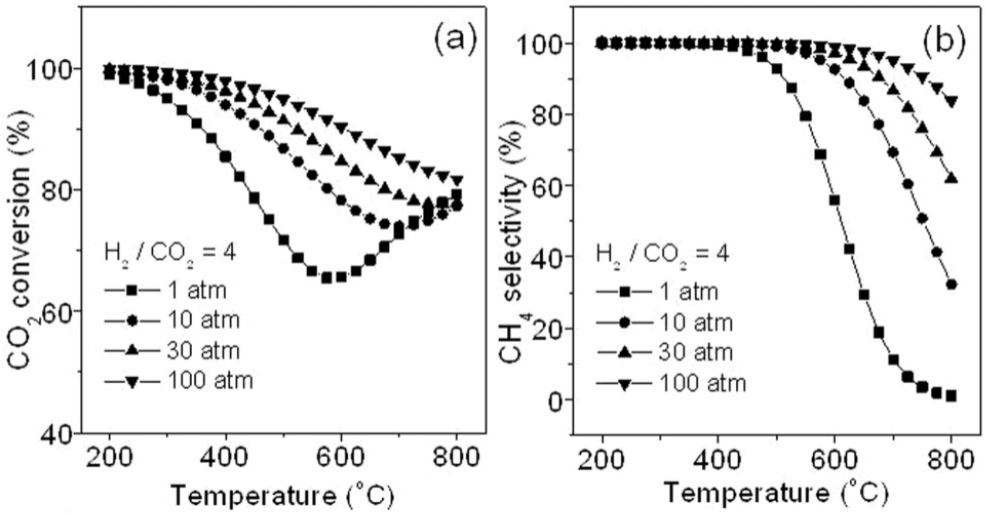

Figure 2.1: (a) Effects of pressure and temperature on CO_2 conversion. (b) CH_4 selectivity. [26]

As clearly shown by Fig. 2.1, CO_2 methanation reaction is favoured by low temperatures and high pressures.

Besides temperature and pressure, other operating conditions effects must be taken in consideration. One of these is H_2/CO_2 ratio, which has a deep influence on the process. High H_2/CO_2 ratios lead to high CO_2 conversion and CH_4 selectivity at every pressure. Nevertheless, H_2 consumption represents a significant percentage of all capital costs of the process, so values of H_2/CO_2 close to stoichiometric ones are usually preferred. When low ratios are used, conversion of CO_2 decreases at first and, when RWGS becomes prevalent, increases again.

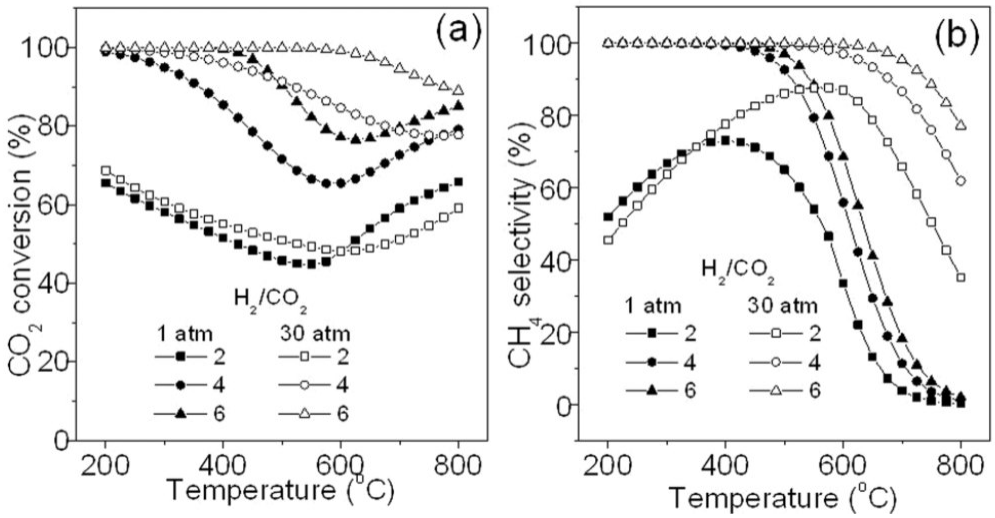

Figure 2.2: Effect of H_2/CO_2 ratio on CO_2 conversion (a) and CH_4 selectivity (b). [26]

Carbon dioxide methanation can suffer from carbon deposition. Coke is formed through four main paths: Boudouard reaction, methane cracking, CO reduction and CO_2 reduction [11] [26].

$$2\ CO_{(g)} \rightleftharpoons C_{(s)} + CO_{2(g)} \quad \Delta H^0_{R,298K} = -172.4\,\frac{kJ}{mol} \tag{2.1.4}$$

$$CH_{4(g)} \rightleftharpoons 2\ H_{2(g)} + C_{(s)} \quad \Delta H^0_{R,298K} = 74.6\,\frac{kJ}{mol} \tag{2.1.5}$$

$$CO_{(g)} + H_{2(g)} \rightleftharpoons C_{(s)} + H_2O_{(g)} \quad \Delta H^0_{R,298K} = -131.3\,\frac{kJ}{mol} \tag{2.1.6}$$

$$CO_{2(g)} + 2\ H_{2(g)} \rightleftharpoons C_{(s)} + 2\ H_2O_{(g)} \quad \Delta H^0_{R,298K} = -90.1\,\frac{kJ}{mol} \tag{2.1.7}$$

When operating at close-to-stoichiometric conditions, formation of coke is not observed: the selectivity to methane is so high that very low CO is produced and so Boudoard reaction, which is believed to be the main path to coke, is not favoured. Moreover, Sabatier's reaction

(Eq. 2.1.1) produces water, that hinders the formation of C through the reverse of reactions (2.1.6) and (2.1.7). Furthermore, methane cracking is the only endothermic reaction of the four, so it becomes relevant only at high temperatures. Therefore, in our typical operating conditions, carbon deposition is always negligible.

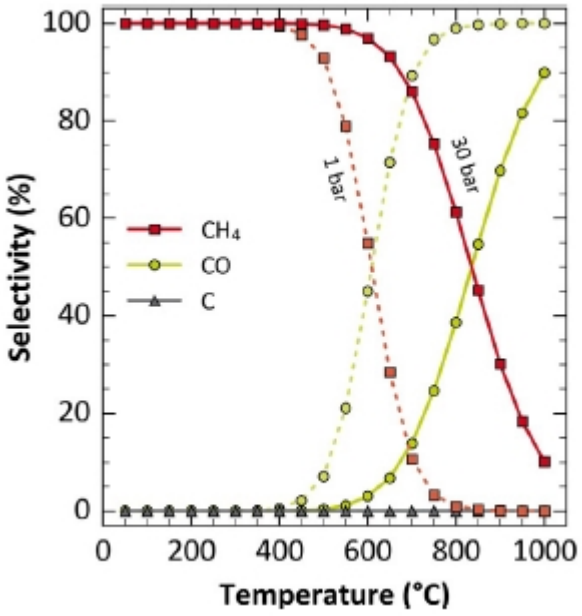

Figure 2.3: Selectivity to CH_4, CO and C for $H_2/CO_2 = 4$. [11]

In conclusion, the best operating conditions to maximize CO_2 conversion are low temperatures, high pressures and high H_2/CO_2 ratios. However, low operating temperatures imply very slow reaction rates, so a catalyst must be adopted. Moreover, even if high pressures promote the methanation reaction, a trade-off between achieved conversion and compression costs should be done. In case of over-stoichiometric H_2/CO_2 ratios, the high amount of unreacted H_2 remaining in the product stream has to be removed in a downstream separation step, more complicated and more expensive compared to the process of CO_2 removal.

2.2 Catalysts

In order to take this process to an industrial scale, both high conversions and high selectivity to methane must be achieved. Thus, for many years academics and researchers have studied different catalysts to promote CO_2 methanation, trying to achieve reasonable standards, at

the same time keeping optimal operating conditions for industries: mild temperatures and atmospheric (or close to atmospheric) pressures.
Different metals have been investigated, in particular those belonging to groups VIII-X. Among these, Ru and Ni are considered the most promising ones.

6	7	8	9	10	11
24 **Cr** Chromium	25 **Mn** Manganese	26 **Fe** Iron	27 **Co** Cobalt	28 **Ni** Nickel	29 **Cu** Copper
42 **Mo** Molybdenum	43 **Tc** Technetium	44 **Ru** Ruthenium	45 **Rh** Rhodium	46 **Pd** Palladium	47 **Ag** Silver
74 **W** Tungsten	75 **Re** Rhenium	76 **Os** Osmium	77 **Ir** Iridium	78 **Pt** Platinum	79 **Au** Gold

Figure 2.4: Extract from the periodic table. Active metals for methanation are indicated in gray. [27]

Vannice et al. [28], proposed candidate catalysts for CO methanation, sorted by activity and selectivity. The list they proposed can be further studied and analyzed in the linked field of CO_2 methanation. Hence, catalysts proposed for CO methanation and nowadays studied and exploited for CO_2 methanation are: Ru, Fe, Ni, Co, Rh, Pd, Ir.
We will now analyze more in detail the most used ones:

- Ruthenium (Ru): is the most active [27], [28], [29] metal for methanation of CO and CO_2. Many researches were conducted for metal loadings between 0.5 and 5 wt% and an optimal loading on alumina equal to 4 wt% was identified by Ashok et al. in their work [30]. In its reduced state, Ru is very active in dissociating hydrogen, which can then react with adsorbed CO_2. If Ruthenium is used in the process of carbon dioxide methanation, CO production is minimized.

- Rhodium (Rh): very active and selective in CO_2 methanation, specially at low temperatures, many studies have been conducted trying to determine the effects of Rh particle size on Sabatier's reaction, but, due to its very high cost (716.96 USD/g as of February 2021 [31]) it is not considered a valid option for industrial methanation.

- Nickel (Ni): for its convenient cost, its high activity and selectivity, is the most commonly used catalyst for commercial applications. However, Ni-based catalysts are active at higher temperatures with respect to both Ru and Rh and so higher metal loadings are required to match the performances of Ru. Typical values of Nickel loadings are higher than 20% wt, with one main drawback being the formation of large metal particles, which can lead to sintering when the catalyst operates under high temperatures. Still, the competitive price of Ni (0.019 USD/g [32]) compared to the one of Ru (10.29 USD/g [33]) makes it the preferred choice for CO_2 methanation.
- Cobalt (Co): some studies have suggested it to be the most active catalyst for methanation among the metals of Group VIII. However, Co is very well known for its use in the Fischer-Tropsch synthesis, so selectivity to methane is not high enough, due to the presence of C_2+ components.
- Iron (Fe): widely used in Fischer-Tropsch synthesis, in recent years Fe-based catalysts for CO_2 methanation are being studied: lack of research may be determined by low selectivity to CH_4, for the same reasons of Co.

Concluding, even if Ru shows the best activity in methanation, and can be loaded in very small amounts, from 0.5 to 5% wt, the competitive price of nickel makes the research on the development of a Ni-based catalyst of great interest to bring the process to an industrial level. For these reasons, in this thesis, a nickel-based catalyst will be considered in the test of different kinetics for the methanation of CO_2.

2.3 Support Materials

The support has a significant influence on the morphology of the active phase, on adsorption and on properties: dispersion of the active phase and reducibility of the precusors, due to the interactions between active phase and support, are only two of these [34], [35]. A synergistic effect is supposed to exist between the support material and the active metal employed in the catalyst [36].

Therefore, once the active metal is chosen, another important choice to make is about

the support to use in the process: metal oxides are deeply exploited for this purpose. Among different supports, Al_2O_3, SiO_2, CeO_2, ZrO_2 and TiO_2 have been studied and analyzed for the application with Nickel, and we hereby propose a quick review of them [34], [37].

Alumina is the most adopted support among all, due its high surface area, its thermal stability even at high working temperatures and very low cost.
Alumina is able to establish a strong interaction withe the supported metal particles, resulting in relatively small nickel particle diameters and poor reducibility.
Silica is another widely used oxide, showing very good performances when employed as mesostructured silica nanoparticles (MSN), due to its very high surface area and large pore volume. Aziz et al. [37] did a very extensive study on Ni/MSN and found that the activity of the reaction on this catalyst is higher compared to the one processed on γ-Al_2O_3 and that when real operating conditions are simulated, Ni/MSN performs better than Rh/MSN and Ru/MSN.
Despite this, a main drawback is present when adopting MSN as a support for Ni-based catalysts, that is its limited stability in the presence of steam. Being water one of the main products of methanation processes, these supports can be useful only if the process is carried out at very low temperatures, which makes its commercial application unfeasible [34].
Ceria has been studied as a single support, as a mixed support with zirconia and also as a promoter, with very positive effects. When adopted alone, CeO_2 promotes the reduction of carbon dioxide to CO, subsequently providing excellent activity for the following CO methanation, leading to very high selectivity towards methane [38].
Ceria supported catalysts present large particle diameters, significantly increasing with metal loading [36] and therefore suffering by sintering deactivation at high operating temperatures.
More often, ceria has been studied as a promoter on various other supports: for example, when introduced on Ni/Al_2O_3 supports, it significantly enhances CO_2 conversion [37], [34].
Mixed supports with zirconia lead to very satisfactory results: the main role of CeO_2 when adopted together with zirconia is thought to be its ability to disperse nickel [34], [39].
Zirconia, employed in its tetragonal phase, is known to enhance the activity towards CO methanation thanks to the presence of oxygen vacancies that interact with oxygen atoms,

weakening the CO bond. Although zirconia supported catalysts show some activity towards CO_2 methanation, they show better performances for the hydrogenation of CO, rather than CO_2 [40]. As for ceria, zirconia supported catalysts present large particle diameters.
In addition, titania is worth to mention: by means of a specific precipitation-deposition method, highly dispersed nickel surface nanoparticles can be obtained, resulting very active towards the hydrogenation of CO_2 [41].
Many studies also focus on aluminosilicates ordered mesoporous materials, such as MCM-41 [42] and different kinds of zeolites [43].

Among all the presented supports, for its opportunities, its low cost and its use at commercial scale, we chose $\gamma-Al_2O_3$ as a support for nickel. So, our kinetic study will be conducted on a Ni/Al_2O_3 catalyst.

2.4 Reaction mechanism

Ni catalysts supported on various oxides have been found to promote the CO_2 methanation reaction. Moreover, the activity was found to be promoted if a second metal (typically Fe or Co) or other oxides are added. As stated before, also Ru and Rh have been tested and give very good results, as they are particularly active in the hydrogenation activity. However, a clear mechanism for CO_2 methanation reaction has still not been defined, and many pathways have been proposed up to now, strongly depending on the type of metal employed in the catalyst, on the support, on the interactions between the two and on the characteristics of the catalysts such as particle sizes, morphology, and metal dispersion.
Indeed, CO_2 methanation can also be described by the linear combination of reverse water-gas shift and CO methanation:

1. $CO_2 + 4\ H_2 \rightleftharpoons CH_4 + 2\ H_2O \qquad \Delta H^0_{R,298K} = -165.1\ \frac{kJ}{mol}$
2. $CO_2 + H_2 \rightleftharpoons CO + H_2O \qquad \Delta H^0_{R,298K} = +41.2\ \frac{kJ}{mol}$
3. $CO + 3\ H_2 \rightleftharpoons CH_4 + H_2O \qquad \Delta H^0_{R,298K} = -206.3\ \frac{kJ}{mol}$

The discussion on the reaction mechanism is very vivid now that carbon dioxide methanation

is gaining interest in the scientific community. The debate aims at describing the reaction intermediates and, in particular, in determining the role that CO plays in the reaction pathway. Moreover, there are two other main issues: which are the elementary steps, specifically the RDS, and what are the active sites.

Different active metals often lead to different reaction mechanism: many schemes have been proposed, but they are deeply linked to the type of active metal, support and operating conditions, with particular regard to temperature and H_2/CO_2 ratios.

Fig. 2.5 presents a summary of the most valid mechanisms proposed up to now. Here, three

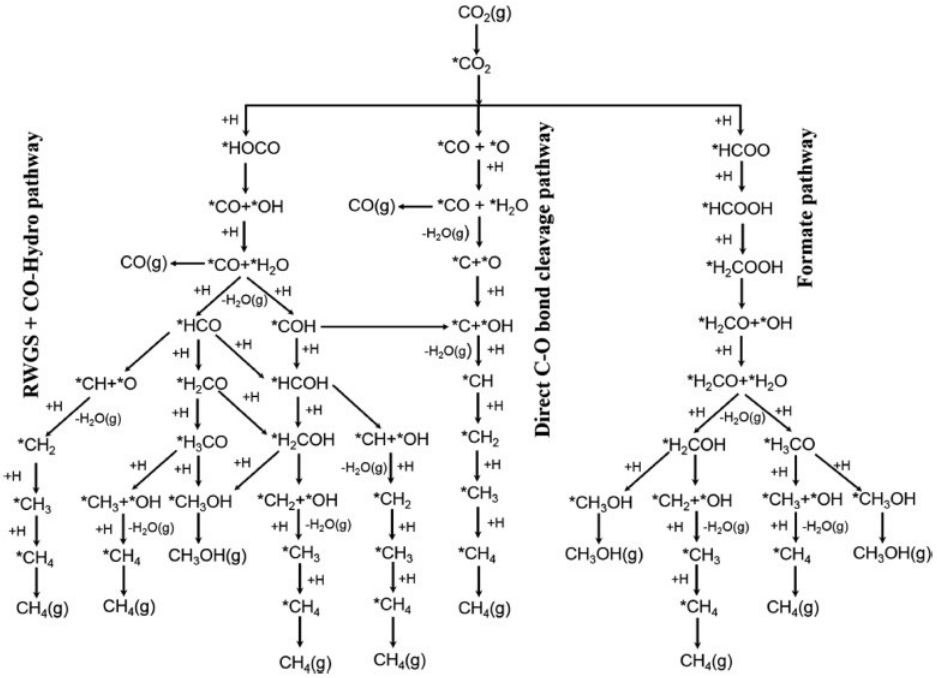

Figure 2.5: Possible reaction pathways to CO, CH_3OH and CH_4. [44]

main paths have been identified, but inside and across these main routes, other schemes can be derived, as will be explained in the following pages.

2.4.1 RWGS + CO-Hydro pathway

The first proposed mechanism hypothesizes at first CO_2^* reacting with H^* to give CO^* and OH^*; then, the adsorbed hydroxyl is further hydrogenated to give adsorbed water, so that, overall, a RWGS reaction is obtained:

$$CO_2^* + H^* \rightleftharpoons CO^* + OH^* \tag{2.4.1}$$

$$OH^* + H^* \rightleftharpoons H2O^* + l \tag{2.4.2}$$

If we sum this two steps, we obtain the RWGS reaction ($CO_2^* + 2\ H^* \rightleftharpoons CO^* + H_2O^*$). So, in this case, CO is a crucial intermediate of reaction. After its formation, carbon monoxide can be hydrogenated to either formyl (CHO^*) or carbo-hydroxyl (COH^*), both of which can either further be hydrogenated to $HCOH^*$ or directly split into CH^* or C^* respectively. If the latter option takes place, the mechanism moves to the *direct C-O bond cleavage* scheme. The C-O bond can break at any given point of the mechanism, depending on the interactions

Table 2.1: Two different pathways for the RWGS + CO-Hydro scheme.

Principal path	Alternative path
1) $H_2 + 2\ l \rightleftharpoons 2\ H^*$	
2) $CO_2 + l \rightleftharpoons CO_2^*$	
3) $CO_2^* + H^* \rightleftharpoons CO^* + OH^*$	
4) $CO^* + H^* \rightleftharpoons CHO^* + l$	
5a) $CHO^* + H^* \rightleftharpoons HCOH^* + l$	5b) $CHO^* + l \rightleftharpoons CH^* + O^*$
6a) $HCOH^* + l \rightleftharpoons CH^* + OH^*$	6b) $O^* + H^* \rightleftharpoons OH^* + l$
7) $CH^* + H^* \rightleftharpoons CH_2^* + l$	
8) $CH_2^* + H^* \rightleftharpoons CH_3^* + l$	
9) $CH_3^* + H^* \rightleftharpoons CH_4^* + l$	
10) $CH_4^* \rightleftharpoons CH_4 + l$	
11) $OH^* + H^* \rightleftharpoons H_2O^* + l$	
12) $H_2O^* \rightleftharpoons H_2O + l$	

formed between species and catalyst. As we can see from Fig. 2.5, a species CH_x must be formed at a certain point, which will subsequently be hydrogenated to give CH_4.

2.4.2 Direct C-O bond cleavage pathway

In this scheme, CO_2 dissociates directly in CO^* and O^*, without any assistance from a H^*. Then, once CO^* is formed, two routes are possible: one where carbon monoxide further splits into C^* and O^*, the other one where the C-O bond scission is H-assisted, forming a formyl species which further dissociates in CH^*. Miao et al. [45] named this two sub-paths as *CO dissociative* and *CO associative* methanation.

This mechanism of CO_2 splitting directly in CO^* and O^* was also sustained by Eckle et al. [46] in their paper where, employing in-situ IR measurements on Ru/Al_2O_3 found that formate was formed, but didn't react further, accumulating on the interface: the main intermediates are CO and CHO.

The path from CO to formyl is generally preferred with respect to the carbide one, with many academics stating that the direct C-O bond breaking is not kinetically favoured without the assistance of a H^* [45], [11].

However, evidences that suggest the direct C-O bond breaking are present [47] but many oppose to this theory, stating that, if present, C^* is formed through CO disproportion ($2\ CO^* \rightarrow C^* + CO_2^*$), mainly because of the lower activation energy of this particular reaction with respect to direct CO breaking [48] [45]. Anyway, once C^* or CH^* are formed, their subsequent hydrogenation leads to the formation of methane.

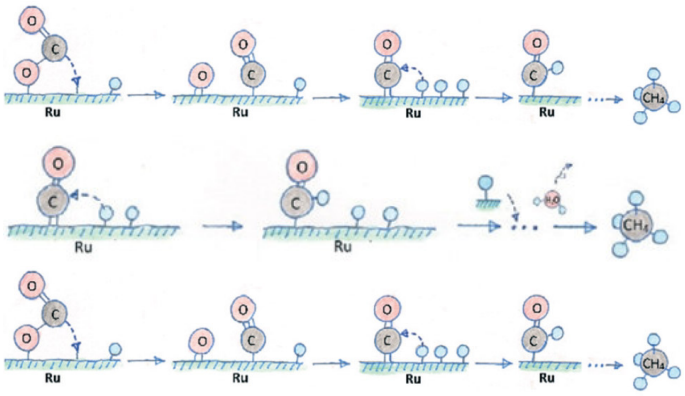

Figure 2.6: From top to bottom: direct CO_2 dissociation, H-assisted split of CO and direct split of CO on a Ru catalyst. [45]

Table 2.2: Different pathways for the direct C-O bond cleavage pathway.

Unassisted path	*H-assisted path*
1) $H_2 + 2\ l \rightleftharpoons 2\ H^*$	
2) $CO_2 + l \rightleftharpoons CO_2^*$	
3) $CO_2^* + l \rightleftharpoons CO^* + O^*$	
4a) $CO^* + l \rightleftharpoons C^* + O^*$	4b) $CO^* + H^* \rightleftharpoons HCO^* + l$
5a) $C^* + H^* \rightleftharpoons CH^* + l$	5b) $HCO^* + l \rightleftharpoons CH^* + O^*$
6) $CH^* + H^* \rightleftharpoons CH_2^* + l$	
7) $CH_2^* + H^* \rightleftharpoons CH_3^* + l$	
8) $CH_3^* + H^* \rightleftharpoons CH_4^* + l$	
9) $CH_4^* \rightleftharpoons CH_4 + l$	
10) $O^* + H^* \rightleftharpoons OH^* + l$	
11) $OH^* + H^* \rightleftharpoons H_2O^* + l$	
12) $H_2O^* \rightleftharpoons H_2O + l$	

2.4.3 Formate pathway

In their extensive job in analyzing all the proposed mechanisms up to the time, Miao et al. [45] also proposed a scheme involving the interaction of CO_2 not with the active metal, but with the support surface, naming it *associative scheme*. Many academics support this theory [11],[49], [27], as stated by Rönsch et al. [27], who affirmed that CO_2 adsorption takes place on the metal-support interface, while CO_2 dissociation takes place on the active metal surface. According to Miao et al. [45], carbon dioxide is adsorbed as a carbonate (CO_3^*) on the support of the catalyst and as CO^* on the metal active site [50].

When increasing temperature, the carbonate hydrogenates to bicarbonate (HCO_3^*) which quickly reacts to formate ($HCOO^*$). On the other hand, CO formed from CO_2 reduction remains unchanged on Ni, active metal supported ceria-zirconia present in the catalyst studied by Aldana et al. [50].

Methane is then formed from the hydrogenation of formate, identified by Westermann et al. [51] in their *operando* IR study over Ni supported on ultra-stable Y-type zeolite, as the precursor of both CH_4 and CO. Formate was identified as the main intermediate also by

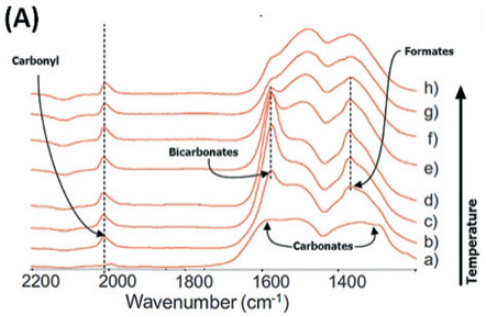

Figure 2.7: Transition from carbonate to bicarbonate when increasing T. [50]

Pan et al. [47] in their studies over Ni-ceria catalysts under methanation conditions.
As can be seen in Fig. 2.8, the support plays a vital role in defining and pursuing different methanation mechanisms. The choice of the appropriate active metal together with the most appropriate metal oxide to adopt as a support is of fundamental choice to achieve optimal conversion and selectivity to methane.

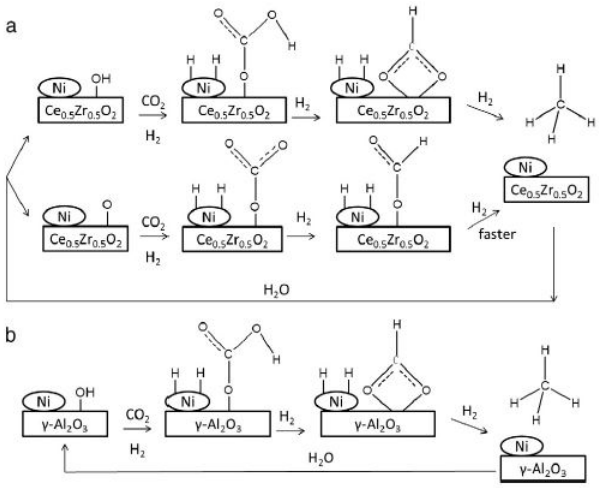

Figure 2.8: Formate pathway of CO_2 methanation on different catalysts. [52]

As previously said, the exact mechanism for methanation is still under debate and there are strong evidences for each of the proposed mechanisms in literature, but this very wide variety originates from different operating conditions and different catalytic systems. Therefore, the research about the mechanism should be carried out on the same combination of

Table 2.3: Main path to methane in the formate mechanism. The $HCOO^{**}$ species is adsorbed on two different sites.

CO_2 *associative scheme*
1) $H_2 + 2\ l \rightleftharpoons 2\ H^*$
2) $CO_2 + l \rightleftharpoons CO_2^*$
3) $CO_2^* + O^* \rightleftharpoons CO_3^* + l$
4) $CO_3^* + H^* \rightleftharpoons HCO_3^* + l$
5) $HCO_3^* + l \rightleftharpoons HCOO^* + O^*$
6) $HCOO^* + l \rightleftharpoons HCOO^{**}$
7) $HCOO^{**} + H^* \rightleftharpoons HCOOH^* + 2\ l$
8) $HCOOH^* + l \rightleftharpoons H_2CO^* + l$
9) $H_2CO^* + H^* \rightleftharpoons H_3CO^* + l$
10) $H_3CO^* + l \rightleftharpoons CH_3^* + O^*$
11) $CH_3^* + H^* \rightleftharpoons CH_4^* + l$
12) $O^* + H^* \rightleftharpoons OH^* + l$
13) $OH^* + H^* \rightleftharpoons H_2O^* + l$
14) $CH_4^* \rightleftharpoons CH_4 + l$
15) $H_2O^* \rightleftharpoons H_2O + l$

metal, support and operating conditions, specially temperature and H_2/CO_2 ratio: H_2-rich environment studies [53] have very different results from researches where the H_2/CO_2 ratio is set at stoichiometric condition for CO_2 methanation. In addition, mechanisms seem to cross each other at certain points so the boundary between different mechanisms should be defined more strictly.

In conclusion, it is very clear that, whatever the combination of metal, support and operating conditions, the selectivity to methane is driven by the competition between the C-O bond breaking and the hydrogenation of carbon species: catalysts should aim at strengthening the interaction between catalyst and adsorbed species, in this way making more favorable the C-O breaking.

2.5 Reactors

A robust and well-developed technology for the industrial production of methane from carbon dioxide is not yet available. There are many proposals and studies that are being developed, but many of the projects concerning reactors construction are still at lab-scale [54]. Today, carbon dioxide methanation process developments rely on the well-established industrial process of CO methanation [27]: many of these technologies were promoted during the oil crisis of the 70s, when synthetic natural gas production from coal was requested [55]. Nowadays, the focus on CO_2 methanation reactors is rapidly expanding in the PtG field. When studying this process progress, one should keep in mind that in order to inject methane directly into the natural gas grid some specific composition standards must be met. Although a common european standard for SNG direct injection has not been defined yet, an example of required composition for biomethane in different countries is reported in Table 2.4.

Table 2.4: Standards for biomethane injection into the natural gas grid in European countries. [56]

Country	CH_4 [%]	CO_2 [%]	H_2 [%]	CO [%]
Germany	> 98.3	< 2.5	< 0.2	–
France	> 95	< 2.5	< 6	< 2
Sweden	> 97	< 3	< 0.5	–
Netherlands	> 85	< 6	< 12	< 1
Austria	> 96	< 3	< 4	–
United Kingdom	–	< 3	< 0.1	–
Italy	–	< 3	< 0.1	–

Water must obviously be removed to meet the standards required before the injection of SNG in the grid: usually a downstream drying step is integrated [57]. Unconverted reactants (CO_2 and H_2), together with CO, must be limited too, according to national restrictions. When projecting industrial methanation reactors, one should keep in mind that hydrogen comes from a discontinuous source like renewable energy sources: the whole system must be able to respond to dynamic variations of the feed composition and flow rate. Moreover,

heat management is a crucial aspect: carbon dioxide methanation is highly exothermic ($\Delta H^0_{R,298K} = -165.1\,\frac{kJ}{mol}$), so a very detailed realization of heat management is required. Furthermore, CO_2 conversion is limited by thermodynamic equilibrium at temperatures above 300 °C [58].
Although just few examples have been taken to commercial scale, today many kinds of reactors have been investigated in order to define the best technology for an industrial application of CO_2 methanation.

Many different kinds of reactors can be exploited, but the ones that are currently believed to be the best option are fixed-bed externally cooled (multitubular) reactors [57]. This type of reactor is preferred for its large thermal control capacity: through the use of the most appropriate cooling medium, an efficient running of the process can be guaranteed. They are preferred in the industrial field with respect to the cheaper and more basic adiabatic reactors, in which a good thermal control cannot be assured.

If only one externally cooled reactor is adopted, the process can have two limitations: be limited by low per-pass conversions or having very high hotspots, around 500 °C [59], which can also lead to sintering of the catalyst.
For these reasons, typically a configuration with more than one reactor is adopted, with intermediate water removal steps, which favors the thermodynamics of the process.

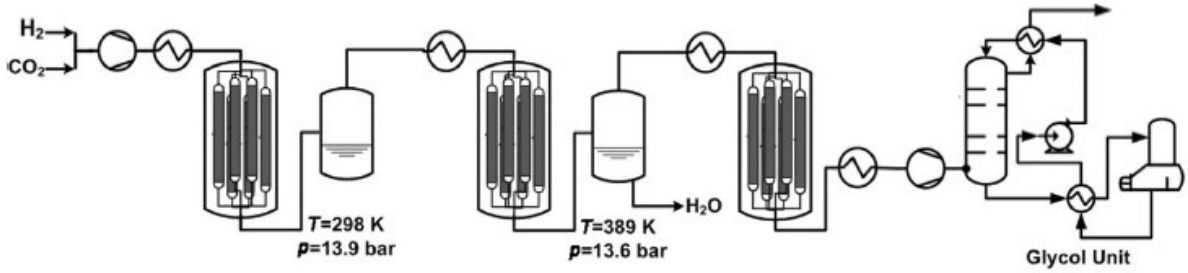

Figure 2.9: Representation of a possible configuration for the industrial process of carbon dioxide methanation. [57]

Fixed bed reactors, however, have some major drawbacks: the formation of hotspots, which

is typical if meticulous heat management is not practiced and the presence of pressure drops; in addition, the lack of flexibility of operation, is one of the other main concerns.
A solution to the problem presented by fixed-bed reactors may be the use of fluidized bed reactors, which limit the formation of hotspots, at the same time ensuring an almost isothermal process. However, fluidized bed reactors make the employed catalysts undergo strong mechanical stress: frequent replacement of the catalyst is often required, a serious problem when expensive catalysts such as those based on ruthenium are used.
In addition to these configurations, three-phase methanation in slurry bubble columns is being studied for its very good heat management, for the additional advantage of being able to substitute the catalyst during operation and for the high ability to handle the fluctuations imposed by VREs. Many drawbacks are present also in this case, the main of which is certainly reactor hydrodynamics, in particular the mass transfer limitations that can be present [10], [60].

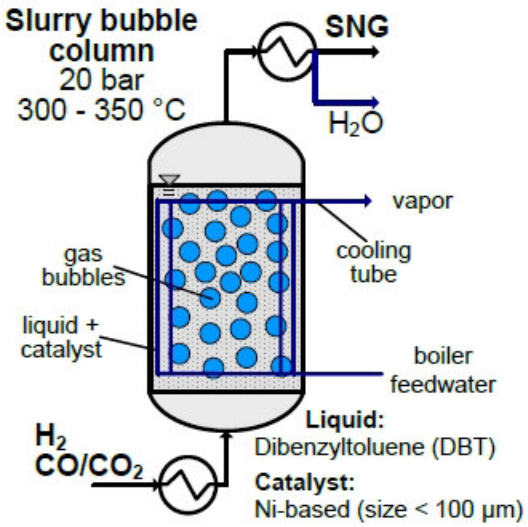

Figure 2.10: Schematic diagram of the three-phase methanation reactor. [10]

The removal of water from the process and how it affects the overall performances of methanation have been studied for a long time, and have been proven efficient to push the conversion of carbon dioxide [61], [57], [62]. For this reason, technologies in which water is subtracted inside the reactor have been proposed, such as in membrane reactors, equipped with a selective membrane that allows water to permeate towards the outside, at

the same time remaining impermeable to other compounds involved in the process, specially H_2. The technical difficulty of producing this type of reactor makes it very expensive and therefore not very attractive and scarcely practicable at the moment on an industrial scale [63].

Another kind of reactors that exploits the in-situ removal of water are the sorption-enhanced reactors. Removing water form the reaction sites, an equilibrium shift is caused, leading to the sorption enhanced methanation process [64], [65]. Zeolites, which are usually adopted as adsorber material in industrial processes, can be used as catalyst support, subtracting water from the reaction environment. However, when zeolites are adopted a regeneration step with dry gas is required.
One more possibility is the realization of structured or washcoat-type reactors, such as those proposed by Schereleth et al. [59], which combine excellent heat management, ensured by the use of a metal support, with low pressure drops.
The honeycomb reactor proposed by Schereleth et al. [59] in 2015 has a real application example in the industrial plant of Falkenhagem [66], where the reactor is constitued by a bundle of honeycomb tubes. However, washcoat reactors have the great disadvantage of tolerating only a small amount of active phase. To solve this problem, microchannel reactors have been studied and, despite providing efficient heat management, face an importante issue: when the catalyst is deactivated, the whole reactor must be replaced [67].

An industrial example of CO_2 methanation is the one of the Audi e-gas plant in Werlte, Germany.

2.6 Audi e-gas plant

Nowadays, the largest PtG plant at commercial scale is set in Werlte, Germany. It was built by Audi in 2013 and it operates with an input of around 6 kW, mainly supplied by excess wind power, but also solar and biomass energy. This energy powers the first step of the process consisting in hydrogen production by electrolysis: hydrogen is produced from water by means of a system of alkaline electrolyzers and it is stored in a tank at 10 bar before being fed to the plant. The CO_2 feed comes from a biogas plant and is obtained by purification in

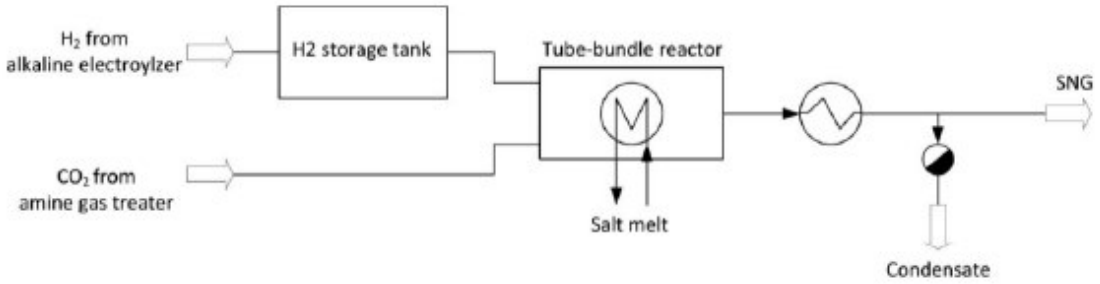

Figure 2.11: Simplified scheme of the methanation plant from Audi. [68]

an amine gas treater. Reactants are then fed to a tube-bundle reactor, filled with a Ni-based catalyst and externally cooled by molten salts [68]. Right after the methanation step, the products are cooled and water is removed by condensation. In this way, Synthesized Natural Gas (SNG) is obtained and it can be both fed to the national gas grid or used as a fuel. In the latter case, the produced fuel was called "Audi E-Gas", hence the name of the plant.

Chapter 3

Methanation Kinetics Literature Review

The SNG synthesis was first studied in 1873 when Brodie applied an electric discharge on a syngas mixture: the observed reaction rate was quite slow [69]. Indeed, the gaseous CO_2 methanation involves the movement of eight electrons and it can be considered as very slow, therefore a catalyst is needed to increase the reaction rate (as explained in Ch.2). In 1902 Sabatier et al. studied carbon dioxide methanation in presence of a heterogeneous catalyst for the first time[9]. Since then, many studies have been made to select the best catalyst and to understand the reaction mechanism, which is still under debate (Sec. 2.4).
In this chapter, we will review some of the kinetic models proposed to describe the process, which have been divided into four main categories:

- Power Law models;
- Modified Power Law models;
- mechanistic solo CO_2 methanation models;
- mechanistic comprehensive models;

3.1 Power Law models

One of the most common forms of the reaction rate dependence from species concentration is the power law model, where the rate law is the production of concentrations of reacting species, each raised to a power defined as order of reaction of the species, as defined by Fogler [70]. Hence, a typical power law expression is $r = k\, C_A^{\alpha}\, C_B^{\beta}$.

When adopting power law models, extrapolations outside the studied experimental field can not be performed. Therefore these kind of models cannot be used to predict a trend in different operating conditions with respect to the ones in which the parameters are calculated. Nevertheless, their very simple form makes these models very attractive to describe a process and for this reason they are widely exploited in CO_2 methanation literature. Indeed, Power-Laws are still used in case a ruthenium catalyst is employed in the kinetic study, due to its high methane selectivity [71] [72], while in case of nickel-based catalysis this approach has been gradually abandoned, in favor of more complex models.

In Table 3.1 an overview of Power-Law models present in the literature is reported. The activation energy of the process is in the range of $60 - 90$ [kJ/mol] and it is similar for all the tested catalysts. The reaction order of H_2 is $2 - 3$ times larger than the one of CO_2 when the process is catalyzed by noble metals, while this trend is inverted in case nickel is employed.

When the experiments were performed in integral reactors, reaction products effect on reaction rates were analyzed. The inhibition effect of methane is always negligible, and thus was not included in the rate expression by any author with the sole exception of Duyar et al. [73] among the models proposed in Table 3.1. On the contrary, water inhibition effect is much more evident, as witnessed by the proposed negative reaction orders.

Due to the similarity of all these power-law models, we decided to analyze only the Solymosi et al. models, were many different supports for the same active metals, Rhodium [74] and Ruthenium [75], were tested.

Table 3.1: Overview of Power-Law models reported in literature.

Model	Rate expression	Catalyst	Ea [kJ/mol]	Reaction orders
Garbarino et al. [71]	$r = kP_{H_2}^{n_{H_2}}$	$3\%Ru/\gamma - Al_2O_3$	60	$n_{H_2} = 0.39$
Šolc et al. [76]	$r = kP_{CO_2}^{n_{CO_2}}$	$62\%Ni/Cr_2O_3$	86	$n_{CO_2} = 0.5$
Solymosi et al. [74]	$r = kP_{CO_2}^{n_{CO_2}} P_{H_2}^{n_{H_2}}$	$5\%Rh/\gamma - Al_2O_3$ $5\%Rh/SiO_2$ $1\%Rh/TiO_2$	$68 - 81$	$n_{CO_2} = 0.26 - 0.27$ $n_{H_2} = 0.61 - 0.64$
Solymosi et al. [75]	$r = kP_{CO_2}^{n_{CO_2}} P_{H_2}^{n_{H_2}}$	$5\%Ru/\gamma - Al_2O_3$	67	$n_{CO_2} = 0.47$ $n_{H_2} = 1$
Wang et al. [72]	$r = kP_{CO_2}^{n_{CO_2}} P_{H_2}^{n_{H_2}}$	$0.5\%Ru/\gamma - Al_2O_3$ $5\%Ru/\gamma - Al_2O_3$	$57 - 80$	$n_{CO_2} = 0.1$ $n_{H_2} = 0.3 - 0.5$
Kusmierz [77]	$r = kP_{CO_2}^{n_{CO_2}} P_{H_2}^{n_{H_2}}$	$0.5\%Ru/\gamma - Al_2O_3$ $0.8\%Ru/\gamma - Al_2O_3$	60	$n_{CO_2} = 0.14 - 0.28$ $n_{H_2} = 0.46 - 0.87$
Chiang [78]	$r = kP_{CO_2}^{n_{CO_2}} P_{H_2}^{n_{H_2}}$	$58\%Ni/SiO_2$	61	$n_{CO_2} = 0.66$ $n_{H_2} = 0.21$
Marwood et al. [79]	$r = kP_{CO_2}^{n_{CO_2}} P_{H_2}^{n_{H_2}} P_{H_2O}^{n_{H_2O}}$	$2\%Ru/TiO_2$	80	$n_{CO_2} = 0.22$ $n_{H_2} = 0.57$ $n_{H_2O} = -0.28$
Takeishi et al. [80]	$r = kP_{CO_2}^{n_{CO_2}} P_{H_2}^{n_{H_2}} P_{H_2O}^{n_{H_2O}}$	Ru/SiO_2	81	$n_{CO_2} = 1$ $n_{H_2} = 2.5$ $n_{H_2O} = -2$
Duyar et al. [73]	$r = kP_{CO_2}^{n_{CO_2}} P_{H_2}^{n_{H_2}} P_{H_2O}^{n_{H_2O}} P_{CH_4}^{n_{CH_4}}$	$10\%Ru/\gamma - Al_2O_3$	66	$n_{CO_2} = 0.34$ $n_{H_2} = 0.88$ $n_{H_2O} = -0.23$ $n_{CH_4} = -0.11$

3.1.1 Solymosi et al. models

Solymosi et al. studied CO_2 methanation on both Ru-based [75] and Rh-based catalysts [74]. Different supports were adopted, such as Al_2O_3, SiO_2, TiO_2, MgO, and in both cases an IR study was performed to detect the adsorbed species.

When studying ruthenium-based catalysts, low-temperature experiments ($25 - 150$ ℃) were conducted to study the carbon dioxide adsorption. The best CO_2 adsorption performance per metal site was achieved by the Ru/TiO_2 catalyst, followed by Ru/MgO and Ru/Al_2O_3. On the contrary, CO_2 adsorption on Ru/SiO_2 was extremely poor.

Despite what was found, a kinetic study was performed only over the Al_2O_3 supported catalyst. Different operative conditions were tested, such as $T = [170 - 230]$ ℃, $P = 1\ bar$, and $H_2/CO_2 = [1 - 10]\ mol/mol$.

Methane selectivity was close to 100% every time, but small amounts of CO, C_2H_6 and CH_3OH were occasionally detected in the outlet gas. Due to the very low amount of products encountered aside from methane, by-product formation rate was neglected and only the one of methane was described, through the following expression:

$$r_{CH_4} = kP_{H_2}^{x} P_{CO_2}^{y} \tag{3.1.1}$$

Where x and y are the reaction orders of H_2 and CO_2, that in this particular case were calculated equal to 1 and 0.47 respectively.

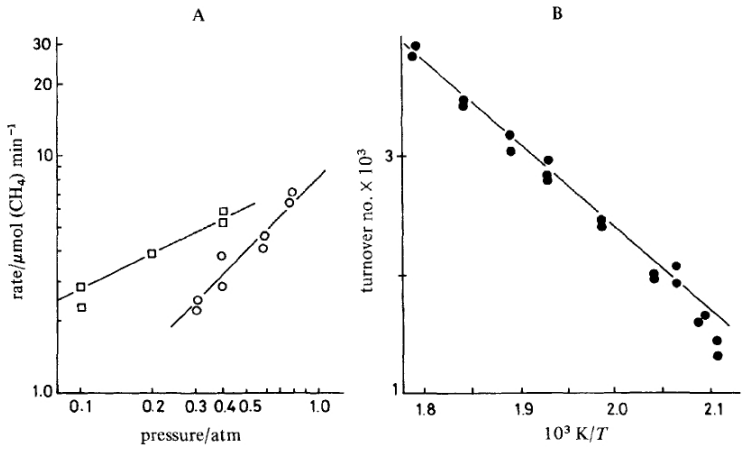

–(A) Dependence of the rate of CH_4 formation on the partial pressures of CO_2 (□) and H_2 (○). (B) Arrhenius plots for Ru/Al_2O_3.

Figure 3.1: Data fitting of Solymosi et al. model for Ru-based catalyst. [75]

Even tough the rate expression is completely empirical, the IR spectroscopy identified a formate species and CO as surface intermediates. Therefore, a reaction mechanism can be hypothesized as shown in Fig. 3.2: it suggests the H-assisted adsorption of CO_2, that leads to CO formation, and the following unassisted dissociation of carbon monoxide.

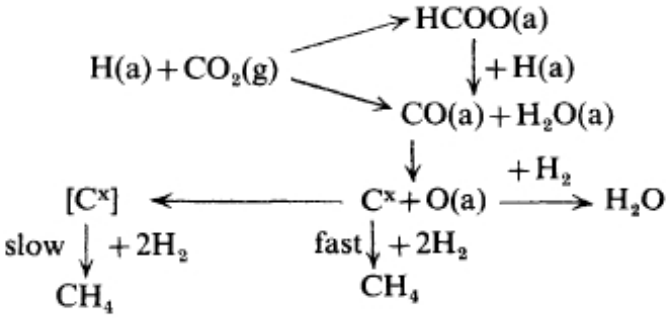

Figure 3.2: Reaction mechanism proposed by Solymosi et al. for Ru-catalyst.[75]

The same supports were studied when Rh was used and again the most active catalyst was the one supported on TiO_2 [74]. A particular mention must be done for Rh/MgO that appeared to be problematic above 290℃, where both CO_2 conversion and CH_4 selectivity suffered a marked decay. On the contrary, all the other tested catalyst showed methane selectivity close to 100%.

All the Rh-catalysts were tested at atmospheric pressure, $T = [170 - 310]$ ℃, $P_{CO_2} = [0.05 - 0.4]$ bar, and $P_{H_2} = [0.2 - 0.8]$ bar. Again only methane formation was described, through the same empirical correlation (Eq. 3.1.1). The reaction orders x and y are different for any Rh-based catalyst and depend on the operative conditions and on the nature of the support.

An IR spectroscopy was again used to study the surface intermediates and the formate group was again detected in the system (Fig. 3.3) but Solymosi et al. concluded that it was not created on the metal active site, but rather on the support, with a particular presence on the Al_2O_3 one.

From the studies performed on Rh-catalysts, a direct dissociation of carbon dioxide was suggested, leading to the formation of CO on the catalytic surface. Moreover, hydrogen was thought to be adsorbed on the same sites of CO.

After the formation of adsorbed carbon monoxide, CO is further dissociated to C and

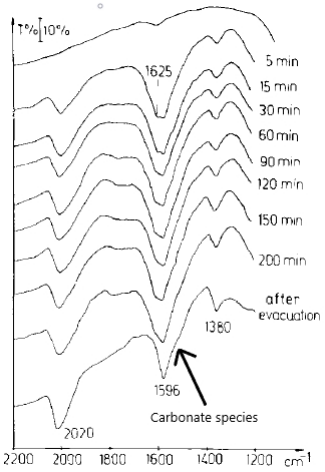

Figure 3.3: Solymosi et al. *operando* IR study on Rh-catalyst. [74]

subsequently hydrogenated to CH_4. The reaction mechanism later proposed for Rhodium catalysts is schematized in Fig. 3.4.

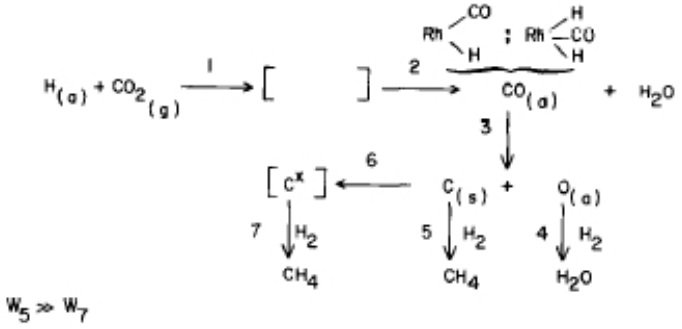

Figure 3.4: Solymosi et al. Rh-catalyst reaction mechanism. [74]

To perform these kinetic studies, Solymosi et al. exploited a differential reactor, where the conversion is limited to a small percentage, generally less than 15%, therefore only reaction rates at initial conditions could be described. Hence, these rate expressions cannot describe the system when approaching the thermodynamic equilibrium.

3.2 Modified Power Law models

In this section we will analyze power law models that either include an inhibition term, represented by a denominator, or are limited by an equilibrium term. In some cases both this modifications are included in the proposed models.

3.2.1 Dew et al. model

One of the first attempts to develop a rate expression that could describe carbon dioxide methanation was made by Dew et al. in 1955 [81]. Their study was conducted on a Ni/SiO_2 catalyst, in a temperature range between 260℃ and 400℃. The reaction rate of methane formation that best fitted their experimental data was:

$$r_{CH_4} = \frac{kP_{CO_2}^{0.5}P_{H_2}^2}{(1+K_1P_{H_2})^3} \qquad at\ 2\ atm \tag{3.2.1}$$

$$r_{CH_4} = \frac{kP_{CO_2}P_{H_2}^4}{(1+K_1P_{H_2}+K_2P_{CO_2})^5} \qquad from\ 2\ to\ 30\ atm \tag{3.2.2}$$

In the low pressure case the reaction orders were related to a dissociated carbon dioxide molecule reacting with two adsorbed molecules of hydrogen, while at higher pressures an adsorbed carbon dioxide molecule reacts with four adsorbed molecules of hydrogen.

Some CO was detected in the outlet stream, therefore Dew et al. tried to describe its formation, proposing this reaction rate:

$$r_{CO} = \frac{kP_{CO_2}^{0.5}P_{H_2}}{(1+K_1P_{H_2}+K_2P_{CO_2})^2} \tag{3.2.3}$$

These rate expressions are not based on a reaction mechanism but are of the Power-Law type, with an inhibition term constituted by the denominator and to obtain this kind of expression, Dew et al. exploited a differential reactor. Therefore, only the reaction rate at initial conditions could be described: these rate expressions cannot describe the system when approaching thermodynamic equilibrium.

3.2.2 Van Herwijnen et al. model

Another rate expression was developed 20 years later by Van Herwijnen et al. [82], based on experiments conducted at atmospheric pressure on a Ni/Al_2O_3 catalyst. In this case, Van Herwijnen et al. studied both CO and CO_2 methanation and also co-methanation of the two: for this reason, they investigated a limited temperature range while modifying both CO and CO_2 inlet partial pressure. Indeed, carbon dioxide methanation was studied at $T = [200 - 230]$ ℃ and $P_{CO_2} = [0.0022 - 0.0238]\ atm$. The measured reaction rates could

be described by the Langmuir isotherm, thus the derived rate expressions were:

$$r_{CO_{2meth}} = \frac{kP_{CO_2}}{(1 + K_{CO_2}P_{CO_2})} \tag{3.2.4}$$

$$r_{CO_{meth}} = \frac{kP_{CO}}{(1 + K_{CO}P_{CO})^2} \tag{3.2.5}$$

These rate expressions have the same issues encountered by the Dew et al. model, as they are not based on a clear reaction mechanism, so we cannot use this model outside the experimental range, and only the initial reaction rates can be described.

3.2.3 Chiang et al. model

Chiang et al. [78] performed the CO_2 methanation over a Ni/SiO_2 catalyst. The reaction was tested at $T = [275 - 320]$ °C, $P = [8 - 18]$ bar, and $H_2/CO_2 = [2 - 5]$ mol/mol. At these conditions, in most of the experiments carbon dioxide conversion was lower than 20% and CO production was negligible, hence only the methane production rate was described. At first, a simple Power-Law model that could correlate the data satisfactorily was tested. The rate expression was:

$$r_{CH_4} = kP_{H_2}^x P_{CO_2}^y \tag{3.2.6}$$

where x and y are the reaction orders of H_2 and CO_2, equal to 0.21 and 0.66 respectively. Chiang et al. also evaluated a LHHW model, just choosing a rate expression that best fitted their data, with no reaction mechanism further illustrated, falling again on a power-law model that also accounts for an inhibition term. In this case, the formation rate of methane is:

$$r_{CH_4} = \frac{kP_{H_2}P_{CO_2}}{(1 + K_{H_2}P_{H_2} + K_{CO_2}P_{CO_2})} \tag{3.2.7}$$

This rate expression exhibited better performances than the Power-Law expression, allowing to decrease the average deviation from the data from 6.93% to 4.61%. Both models proposed by Chiang et al. are empirical, therefore they can be used only in the studied experimental range. Moreover, both expressions do not take in consideration thermodynamic equilibrium: this is justified by the fact that in their work Chiang et al. worked with low conversion systems.

3.2.4 Lunde-Kester model

One of the models developed for a Ru-based catalyst is the Lunde-Kester model [83], today considered as a pillar for methanation on Ruthenium catalysts. In their work Al_2O_3 was chosen as catalyst support. Since Ruthenium is much more selective to methane than Ni, Lunde and Kester did not find necessary to describe any carbon monoxide formation; in the last few years, however, some models tried to include CO as well inside the reaction scheme [84]. The proposed rate expression is an empirical correlation:

$$r_{CH_4} = k\left(P_{CO_2}P_{H_2}^4 - \frac{P_{CH_4}P_{H_2O}^2}{K_{eq}}\right)^n \tag{3.2.8}$$

This correlation to calculate the equilibrium constant was proposed:

$$K_{eq} = exp\left[\left(\frac{1}{1.987}\right)\left(\frac{56000}{T^2} + \frac{34633}{T} - 16.4\ln T + 0.00557\cdot T\right) + 33.165\right] \tag{3.2.9}$$

Despite being an empirical law, the Lunde-Kester model has been successfully used under many different operative conditions. Every time someone decides to use this model the parameters k and n must be re-adapted, but, as long as CO is in low concentration, the data fitting is pretty good [85].

The advantage of this model is that it can describe the system also when the gas composition is close to the thermodynamic equilibrium, including the equilibrium term in parenthesis: a very big difference with all the models proposed up to now. Furthermore, only three parameters have to be estimated, hence the calculation time is reduced.

This model will be further analyzed in Sec. 5.2.

3.2.5 Farsi et al. model

More recently, in 2020, Farsi et al. [86] performed a kinetic study whose aim was to describe carbon dioxide methanation. They worked on $Ni_3Fe/\gamma - Al_2O_3$, a bimetallic catalysts, and proposed a consecutive scheme in which Sabatier's reaction is thought as a RWGS followed by a CO methanation reaction. Very short contact times were kept during all the experiments. The reactive system was tested at $T = [300 - 450]$ °C, $P = [2 - 18]$ bar, and $H_2/CO_2 = [2 - 8]$ mol/mol. Moreover, the influence of water and carbon monoxide addition in the feed was also tested.

The proposed rate expressions have this general form:

$$r_{RWGS} = \frac{k_1 P_{CO_2}^{\alpha} P_{H_2}^{\beta}}{inhibition\ term^2}\left(1 - \frac{P_{CO} P_{H_2O}}{P_{CO_2} P_{H_2} K_{eqRWGS}}\right) \tag{3.2.10}$$

$$r_{CO_{meth}} = \frac{k_2 P_{CO}^{\gamma} P_{H2}^{\varphi}}{inhibition\ term^2}\left(1 - \frac{P_{CH_4} P_{H_2O} P_{abs}^2}{P_{CO} P_{H_2}^3 K_{eqCO_{meth}}}\right) \tag{3.2.11}$$

Then, a non-linear regression was performed, through which both the reaction orders and the terms constituting the inhibition term were found, resulting in:

$$r_{RWGS} = \frac{k_1 P_{CO_2}^{0.5} P_{H_2}^{0.5}}{(1 + K_{H_2O} P_{H_2O})^2}\left(1 - \frac{P_{CO} P_{H_2O}}{P_{CO_2} P_{H_2} K_{eqRWGS}}\right) \tag{3.2.12}$$

$$r_{CO_{meth}} = \frac{k_2 P_{CO} P_{H2}^{0.5}}{(1 + K_{H_2O} P_{H_2O})^2}\left(1 - \frac{P_{CH_4} P_{H_2O} P_{abs}^2}{P_{CO} P_{H_2}^3 K_{eqCO_{meth}}}\right) \tag{3.2.13}$$

This model will be further analyzed in Sec. 6.2.

A summary of all the discussed power-law models is reported on the next page.(Table 3.2)

Table 3.2: Power-law models proposed in literature.

Model	Catalyst	Rate equations
Solymosi et al. [75] [74]	Ru/Al_2O_3 Rh/Al_2O3	$r_{CH_4} = kP_{H_2}^{x}P_{CO_2}^{y}$
Dew et al. [81]	Ni/SiO_2	$r_{CH_4} = \frac{kP_{CO_2}^{0.5}P_{H_2}^{2}}{(1+K_1P_{H_2})^3}$ *at 2 atm* $r_{CH_4} = \frac{kP_{CO_2}P_{H_2}^{4}}{(1+K_1P_{H_2}+K_2P_{CO_2})^5}$ *2 to 30 atm* $r_{CO} = \frac{kP_{CO_2}^{0.5}P_{H_2}}{(1+K_1P_{H_2}+K_2P_{CO_2})^2}$
Van Herwijnen et al. [82]	Ni/Al_2O_3	$r_{CO_{2meth}} = \frac{kP_{CO_2}}{(1+K_{CO_2}P_{CO_2})}$ $r_{CO_{meth}} = \frac{kP_{CO}}{(1+K_{CO}P_{CO})^2}$
Chiang et al. [78]	Ni/SiO_2	$r_{CH_4} = \frac{kP_{H_2}P_{CO_2}}{(1+K_{H_2}P_{H_2}+K_{CO_2}P_{CO_2})}$
Lunde-Kester [83]	Ru/Al_2O_3	$r_{CH_4} = k\left(P_{CO_2}P_{H_2}^{4} - \frac{P_{CH_4}P_{H_2O}^{2}}{K_{eq}}\right)^n$
Farsi et al. [86]	$Ni_3Fe/\gamma - Al_2O_3$	$r_{RWGS} = \frac{k_1P_{CO_2}^{0.5}P_{H_2}^{0.5}}{(1+K_{H_2O}P_{H_2O})^2}\left(1 - \frac{P_{CO}P_{H_2O}}{P_{CO_2}P_{H_2}K_{eqRWGS}}\right)$ $r_{CO_{meth}} = \frac{k_2P_{CO}P_{H2}^{0.5}}{(1+K_{H_2O}P_{H_2O})^2}\left(1 - \frac{P_{CH_4}P_{H_2O}P_{abs}^{2}}{P_{CO}P_{H_2}^{3}K_{eqCO_{meth}}}\right)$

3.3 Mechanistic solo CO_2 methanation models

In this section we will analyze kinetic models proposed in literature that clearly declare a reaction mechanism and derive a kinetic expression starting from it.
The models are all Langmuir-Hinshelwood-Hougen-Watson (LHHW) based models that only describe the direct carbon dioxide methanation through Sabatier reaction (Eq. 2.1.1).

3.3.1 Weatherbee et al. model

One of the first attempts to derive a mechanistic kinetic model was made by Weatherbee et al. in 1982 [87], who tried to exploit a LHHW model, studying CO_2 methanation over Ni/SiO_2 in a differential reactor. The reaction was tested at $T = [225 - 325]$ °C, $P = [1.4 - 1.75]$ bar, $P_{H_2} = [0.0276 - 0.138]$ bar, and $P_{CO_2} = [0.00276 - 0.0276]$ bar. CO inhibition effect was also tested by varying its partial pressure up to a maximum of 0.006 bar.
In the chosen mechanism H_2 adsorbs dissociatively, while CO_2 and CO adsorption are both unassisted and dissociative, suggesting a *direct C-O bond cleavage* scheme (Sec. 2.4.2). After that, adsorbed C and H are hydrogenated to methane and water.
Only one RDS was hypothesized by Weatherbee et al., hence only the rate formation of methane was considered. Moreover, since CO was co-fed, the RDS is the same for both CO and CO_2 methanation.
The best data fitting was obtained when the scission of CO (reaction 4) is considered the RDS of the process, with species O and CO treated as MASI. The complete rate expression derivation can be found in the Weatherbee et al. work, but it is worth mentioning that:

- The RDS (step 4) was considered as irreversible, hence the system cannot be well described at high CO_2 conversion, when approaching equilibrium;
- Not all the other steps were considered at *quasi-equilibrium*;
- The active sites occupied by CO are expressed in 2 different ways, with different results. Weatherbee et al. unilaterally chose to use one of them in the RDS rate expression, while summing them up in the free sites derivation (CO is considered a MASI).

Reaction	Equation
$H_2(g) + 2\,S \rightleftharpoons 2\,H\text{–}S$	(4-1)
$CO_2(g) + 2\,S \rightleftharpoons CO\text{–}S + O\text{–}S$	(4-2)
$CO\text{–}S \rightleftharpoons CO(g) + S$	(4-3)
$CO\text{–}S + S \rightleftharpoons C\text{–}S + O\text{–}S$	(4-4)
$C\text{–}S + H\text{–}S \rightleftharpoons CH\text{–}S + S$	(4-5)
$CH\text{–}S + H\text{–}S \rightleftharpoons CH_2\text{–}S + S$	(4-6)
$CH_2\text{–}S + H\text{–}S \rightleftharpoons CH_3\text{–}S + S$	(4-7)
$CH_3\text{–}S + H\text{–}S \rightleftharpoons CH_4\text{–}S + S$	(4-8)
$CH_4\text{–}S \rightleftharpoons CH_4(g) + S$	(4-9)
$O\text{–}S + H\text{–}S \rightleftharpoons OH\text{–}S + S$	(4-10)
$OH\text{–}S + H\text{–}S \rightleftharpoons H_2O\text{–}S + S$	(4-11)
$H_2O\text{–}S \rightleftharpoons H_2O(g) + S$	(4-12)

[a] S refers to a surface site.

Figure 3.5: Weatherbee et al. reaction mechanism. [87]

The resulting rate expression is:

$$r_{CH_4} = \frac{\left(\frac{K_1 K_2 K_{10}\, k_4\, k_{11}}{2}\right)^{0.5} L^2 P_{CO_2}^{0.5} P_{H_2}^{0.5}}{\left(1 + \left(\frac{2K_2 k_4}{K_1 K_{10}\, k_{11}}\right)^{0.5} \frac{P_{CO_2}^{0.5}}{P_{H_2}^{0.5}} + \left(\frac{K_1 K_2 K_{10}\, k_{11}}{2\, k_4}\right)^{0.5} P_{CO_2}^{0.5} P_{H_2}^{0.5} + \frac{P_{CO}}{K_3}\right)^2} \tag{3.3.1}$$

3.3.2 Ionue et al. model

In 1984 Ionue et al. [88] studied CO, CO_2 and co-methanation over a Ni catalyst, with one of their main targets being the study of the mutual interaction of carbon monoxide and carbon dioxide and their effect on the methanation reactions rates. The reaction was tested at atmospheric pressure and in a temperature range between 250 and 350 ℃. Information about space velocity, H_2/CO and H_2/CO_2 ratios are not well defined in the paper, but we can observe that a wide range of CO and CO_2 conversions were investigated. Our main

focus will be on carbon dioxide methanation.

In the experiments some CO was detected in the outlet gas, with its concentration becoming higher and higher as space velocity is increased. This is the typical behaviour of systems where consecutive reactions are present, with carbon monoxide as reaction intermediate. Despite this, in the rate expression derivation CO production rate was not described, due to the maximum selectivity towards it being about 0.5%.

The reaction mechanism involved the unassisted dissociation of both CO_2 and CO, followed by the hydrogenation of adsorbed C and O by H_2 in its gaseous form, suggesting an Eley-Rideal mechanism type. The formation of CH_2^*, CH_4 and H_2O are considered

$$CO_2 + X \overset{K_{CO_2}}{\rightleftharpoons} CO_2X$$

$$CO_2X + X \overset{K'_s}{\rightleftharpoons} COX + O^*X$$

$$COX + X \underset{k_{-s}}{\overset{k_s}{\rightleftharpoons}} CX + OX$$

$$CX + H_2 \xrightarrow{k_m} (CH_2X) \xrightarrow{\text{fast}} CH_4$$

$$OX + H_2 \xrightarrow{k_h} H_2O$$

Figure 3.6: Inoue et al. reaction mechanism, where X represents the active site. [88]

irreversible steps. The RDS is the CH_2^* formation, while the MASI are CO_2, H_2 and H_2O; the resulting rate expression is:

$$r_{CH_4} = \frac{(k_m^2 k'_h K_S K'_S K_{CO_2}/\alpha)^{1/3} P_{H_2} P_{CO_2}^{1/3}}{(1 + K_{CO_2} P_{CO_2} + K_{H_2} P_{H_2} + K_{H_2O} P_{H_2O})} \tag{3.3.2}$$

The reaction mechanism is quite strange since H_2 is not adsorbed, but is considered as a MASI, which seems a nonsense. Up to now, all the models we have studied contemplated the adsorption of H_2, none of them theorizing an Eley-Rideal mechanism type.
Once again equilibrium conditions cannot be described, since the RDS is considered irreversible.

3.3.3 Kai et al. model

In 1988 Kai et al. studied the CO_2 methanation over a $Ni/La_2O_3/Al_2O_3$ catalyst [89]. Both a differential and an integral reactor were employed, hence a wide range of CO_2 conversion was investigated. In the differential reactor the system was examined at $T = [240 - 320]$ ℃, $P = [1.4 - 11.1]$ bar, and $H_2/CO_2 = [0.6 - 30]$ mol/mol, while the integral reactor was operated at $T = [240 - 320]$ ℃, $P = 1$ bar, and $H_2/CO_2 = 4$ mol/mol.

Under all these reaction conditions, the maximum CO selectivity was below 1% and no other by-products were detected. Thus, it was sufficient to only consider a direct CO_2 methanation scheme.

The rate expression is described by means of a LHHW equation type, whose parameters are fitted through the nonlinear least squares method:

$$r_{CH_4} = \frac{kP_{H_2}^{0.5}P_{CO_2}^{0.33}}{(1 + K_{H_2}P_{H_2}^{0.5} + K_{CO_2}P_{CO_2}^{0.5} + K_{H_2O}P_{H_2O})^2} \tag{3.3.3}$$

This rate expression was justified by exploiting a reaction mechanism similar to the one proposed by Weatherbee et al. [87] and reported in Fig. 3.7.

$H_2(g) + 2S \underset{k_{-1}}{\overset{k_1}{\rightleftharpoons}} 2H-S$		(I)
$CO_2(g) + 2S \underset{k_{-2}}{\overset{k_2}{\rightleftharpoons}} CO-S + O-S$		(II)
$CO-S + S \underset{k_{-3}}{\overset{k_3}{\rightleftharpoons}} C-S + O-S$		(III)
$C-S + H-S \xrightarrow[\text{slow}]{k_4} CH-S + S$		(IV)
$CH-S + 3H-S \xrightarrow[\text{fast}]{k_5} CH_4 + 4S$		(V)
$O-S + H-S \xrightarrow{k_6} OH-S + S$		(VI)
$OH-S + H-S \xrightarrow[\text{fast}]{k_7} H_2O-S + S$		(VII)
$H_2O-S \underset{k_{-8}}{\overset{k_8}{\rightleftharpoons}} H_2O(g) + S$		(VIII)

*S is an active site.

Figure 3.7: Kai et al. reaction mechanism. [89]

The RDS was assumed to be the hydrogenation of C, while species H, CO_2, H_2O and CO were considered as MASI.
Even in this case, the equilibrium conditions are not described by the rate expression, even though high experimental CO_2 conversions were achieved.

3.3.4 Koschany et al. model

In 2016 Koschany et al. [90] studied carbon dioxide methanation as an opportunity in the PtG field. They performed their kinetic study on different coprecipitated $NiAl(O)_x$ catalysts. Two different reaction mechanism were proposed, a carbide (Sec. 2.4.2) one and a RWGS + CO-Hydro one (Sec. 2.4.1). Despite this, the carbon monoxide content in the product gas was considerably below 1000 ppm and so Koschany et al. decided to describe only the rate of methane formation. The reaction was studied at $T = [180 - 340]$ ℃, $P = [1 - 15]$ bar, and $H_2/CO_2 = [0.25 - 8]$ mol/mol. In addition to this, the effect of methane and water co-feed was studied.
The final proposed rate expression is:

$$r_{CH_4} = \frac{kP_{H_2}^{0.5}P_{CO_2}^{0.5}\left(1 - \frac{P_{CH_4}P_{H_2O}^2}{P_{CO_2}P_{H_2}^4 K_{eq}}\right)}{\left(1 + K_{OH}\frac{P_{H_2O}}{P_{H_2}^{0.5}} + K_{H_2}P_{H_2}^{0.5} + K_{mix}P_{CO_2}^{0.5}\right)^2} \tag{3.3.4}$$

Today, the study and the model proposed by Koschany et al. are considered state-of-the-art when describing direct CO_2 methanation, and are commonly exploited by research groups [34], [91].
This model will be further analyzed in Sec. 5.3.

Table 3.3: mechanistic models for solo CO_2 methanation.

Model	Catalyst	Rate equations
Weatherbee et al. [87]	Ni/SiO_2	$r_{CH_4} = \frac{\left(\frac{K_1 K_2 K_{10} k_4 k_{11}}{2}\right)^{0.5} L^2 P_{CO_2}^{0.5} P_{H_2}^{0.5}}{\left(1 + \left(\frac{2K_2 k_4}{K_1 K_{10} k_{11}}\right)^{0.5} \frac{P_{CO_2}^{0.5}}{P_{H_2}^{0.5}} + \left(\frac{K_1 K_2 K_{10} k_{11}}{2k_4}\right)^{0.5} P_{CO_2}^{0.5} P_{H_2}^{0.5} + \frac{P_{CO}}{K_3}\right)^2}$
Ionue et al. [88]	Ni	$r_{CH_4} = \frac{(k_m^2 k_h' K_S K_S' K_{CO_2}/\alpha)^{1/3} P_{H_2} P_{CO_2}^{1/3}}{(1 + K_{CO_2} P_{CO_2} + K_{H_2} P_{H_2} + K_{H_2O} P_{H_2O})}$
Kai et al. [89]	$Ni/La_2O_3/Al_2O_3$	$r_{CH_4} = \frac{k P_{H_2}^{0.5} P_{CO_2}^{0.33}}{(1 + K_{H_2} P_{H_2}^{0.5} + K_{CO_2} P_{CO_2}^{0.5} + K_{H_2O} P_{H_2O})^2}$
Koschany et al. [90]	$NiAl(O)_x$	$r_{CH_4} = \frac{k P_{H_2}^{0.5} P_{CO_2}^{0.5} \left(1 - \frac{P_{CH_4} P_{H_2O}^2}{P_{CO_2} P_{H_2}^4 K_{eq}}\right)}{\left(1 + K_{OH} \frac{P_{H_2O}}{P_{H_2}^{0.5}} + K_{H_2} P_{H_2}^{0.5} + K_{mix} P_{CO_2}^{0.5}\right)^2}$

3.4 Mechanistic comprehensive models

In this section we will describe models that illustrate a combination of the Sabatier reaction, RWGS and CO methanation, either in series, in parallel or all together in a triangular scheme. We will define these models as *comprehensive* models.

3.4.1 Xu-Froment model

In 1989 Xu and Froment studied the intrinsic kinetics of methane steam-reforming ($CH_4 + H_2O \rightleftharpoons CO + 3\ H_2$) and RWGS reaction on a $Ni/MgAl_2O_4$ catalyst [92]. As some methane was detected in the outlet gas of the RWGS reaction experiments, they decided to include CO_2 methanation in the reactive scheme, giving birth to the triangular scheme reported in Fig. 3.8.

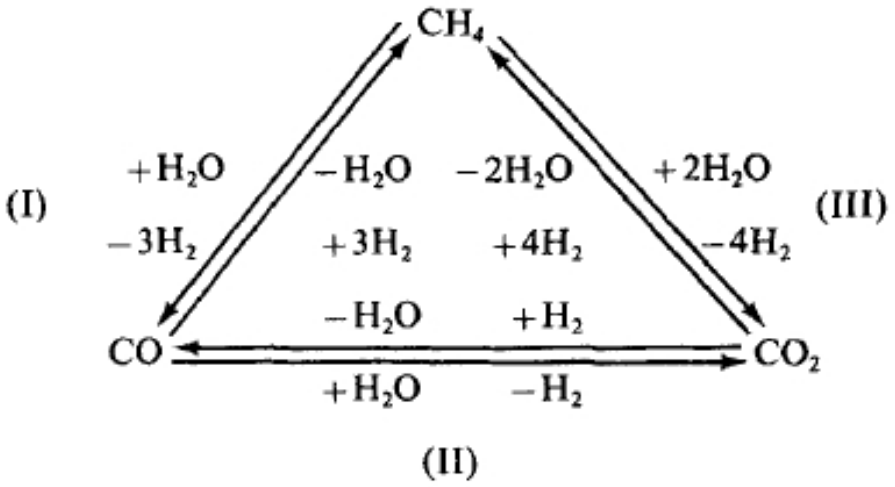

Figure 3.8: Xu-Froment reaction scheme. [92]

The experiments on the steam-reforming reaction were conducted at $T = [500 - 570]$ ℃, $P = [3 - 15]\ bar$, and $H_2O/CH_4 = [3 - 5]\ mol/mol$, while the RWGS experiments were conducted at $T = [300 - 400]$ ℃, $P = [3 - 10]\ bar$, and $H_2/CO_2 = [0.5 - 1]\ mol/mol$.
Since the considered reactions are all reversible and the catalyst adopted is similar to the ones adopted in many other studies we have seen so far, this paper is considered a milestone for CO_2 methanation, due to the deep study conducted on the reaction mechanism.
Steam reforming was considered the main reaction of the process, so it was taken as reference

in the mechanism building, with CO_2 treated as a by-product. Two parallel pathways were considered for carbon dioxide formation; the first is the direct pathway, through the reverse of the Sabatier reaction ($CH_4 + 2\ H_2O \rightleftharpoons CO_2 + 4\ H_2$), the second passes through the formation of CO, followed by a water-gas shift reaction, according to the reaction scheme showed in Fig. 3.8. The elementary steps considered by Xu and Froment are reported in Fig. 3.9.

H_2O	+ L	= O-L	+ H_2	(1)
CH_4	+ L	= CH_4-L		(2)
CH_4-L	+ L	= CH_3-L	+ H-L	(3)
CH_3-L	+ L	= CH_2-L	+ H-L	(4)
CH_2-L	+ O-L	= CH_2O-L	+ L	(21)
CH_2O-L	+ L	= CHO-L	+ H-L	(22)
CHO-L	+ L	= CO-L	+ H-L	(23) r.d.s.; r_1
CO-L	+ O-L	= CO_2-L	+ L	(8) r.d.s.; r_2
CHO-L	+ O-L	= CO_2-L	+ H-L	(25) r.d.s.; r_3
CO-L		= CO	+ L	(7)
CO_2-L		= CO_2	+ L	(10)
2H-L		= H_2-L	+ L	(1-bis)
H_2-L		= H_2	+ L	(1-bis)

Figure 3.9: Xu-Froment reaction mechanism. [92]

We can observe that 3 RDSs are considered, in agreement with the reaction scheme. The resulting rate expressions are:

$$r_{SR} = \frac{\frac{k_1}{P_{H_2}^{2.5}}\left(P_{CH_4}P_{H_2O} - \frac{P_{H_2}^3 P_{CO}}{K_1}\right)}{\left(1 + K_{CO}P_{CO} + K_{H_2}P_{H_2} + K_{CH_4}P_{CH_4} + K_{H_2O}\frac{P_{H_2O}}{P_{H_2}}\right)^2} \tag{3.4.1}$$

$$r_{WGS} = \frac{\frac{k_2}{P_{H_2}}\left(P_{CO}P_{H_2O} - \frac{P_{H_2}P_{CO_2}}{K_2}\right)}{\left(1 + K_{CO}P_{CO} + K_{H_2}P_{H_2} + K_{CH_4}P_{CH_4} + K_{H_2O}\frac{P_{H_2O}}{P_{H_2}}\right)^2} \tag{3.4.2}$$

$$r_{Rev-Sab} = \frac{\frac{k_3}{P_{H_2}^{3.5}}\left(P_{CH_4}P_{H_2O}^2 - \frac{P_{H_2}^4 P_{CO_2}}{K_3}\right)}{\left(1 + K_{CO}P_{CO} + K_{H_2}P_{H_2} + K_{CH_4}P_{CH_4} + K_{H_2O}\frac{P_{H_2O}}{P_{H_2}}\right)^2} \tag{3.4.3}$$

In general, these rate expressions can be employed for CO_2 methanation, keeping in mind that in the Xu-Froment derivation CO_2 is treated as a product: in a carbon dioxide methanation

system we eventually would find a negative reaction rate, being CO_2 a reactant; still, the model is thermodynamically consistent and based on the reaction mechanism reported in Fig. 3.9.

Unfortunately, the main purpose of this study was the steam-reforming reaction, therefore investigated temperatures and compositions were very different from those of a CO_2 methanation system. When the operating conditions change so much it is very likely that also the mechanism changes a bit and, in particular, the RDSs. For this reason, this reaction mechanism was further deepened in many other studies, taking it as a solid base, but focusing on the Sabatier reaction.

3.4.2 Champon et al. model

In 2019 Champon et al. [93] proposed a comprehensive model, very similar to the one proposed by Xu and Froment [92]. Indeed, this model is a triangular one, where both direct path (Sabatier reaction) and indirect path (RWGS + CO methanation) of carbon dioxide methanation are described.

The kinetic study was performed on a Ni/Al_2O_3 catalyst; after analyzing models proposed in literature, Champon et al. proceeded by selecting the already proposed expressions that best fitted their experimental dataset, introducing modifications when necessary.

At first, a differential reactor was exploited, to obtain a first gross estimation of the kinetic parameters, then an integral reactor study was performed, in order to describe the behaviour of the system in a wide range of CO_2 conversions.

The experiments were conducted at atmospheric pressure and in a temperature range between 350 and 450 ℃. In addition, different GHSV and the inhibiting effect of CH_4 and H_2O were tested. The following rate expressions are the final ones proposed by Champon et al. in their paper:

$$r_{CO_2meth} = \frac{k_{CO_2meth} K_{H_2} K_{CO_2} P_{H_2} P_{CO_2} \left(1 - \frac{P_{CH_4} P_{H_2O}^2}{P_{H_2}^4 P_{CO_2} K_{eq,CO_2meth}}\right)}{(1 + K_{CO_2} P_{CO_2} + K_{H_2} P_{H_2} + K_{H_2O} P_{H_2O} + K_{CO} P_{CO})^2} \tag{3.4.4}$$

$$r_{RWGS} = \frac{k_{RWGS} K_{CO_2} P_{CO_2} \left(1 - \frac{P_{CO} P_{H_2O}}{P_{H_2} P_{CO_2} K_{eq,RWGS}}\right)}{(1 + K_{CO_2} P_{CO_2} + K_{H_2} P_{H_2} + K_{H_2O} P_{H_2O} + K_{CO} P_{CO})} \tag{3.4.5}$$

$$r_{COmeth} = \frac{k_{COmeth} K_{H_2} K_{CO} P_{H_2} P_{CO} \left(1 - \frac{P_{CH_4} P_{H_2O}}{P_{H_2}^3 P_{CO} K_{eq,COmeth}}\right)}{(1 + K_{CO_2} P_{CO_2} + K_{H_2} P_{H_2} + K_{H_2O} P_{H_2O} + K_{CO} P_{CO})^2} \tag{3.4.6}$$

This model will be further analyzed in Sec. 6.1.

3.4.3 Burger et al. model

In their work over a co-precipitated $NiAl(O)_x$, Burger et al. [94] described a system in which the methanation of a common surface intermediate of both CO and CO_2 is described. Indeed, the Burger et al. work is unique in literature because of its aim to describe the hydrogenation of CO and CO_2 via a common CO^* intermediate, resulting from the associative adsorption of carbon monoxide and the dissociative adsorption of carbon dioxide. Moreover, Burger et al. concluded that both the methanation processes occur via the same RDS.
The tested operated conditions were: $T = [230 - 340]$°C and $P = [1 - 10]$ *bar*. Furthermore, inhibition effects of water and methane were tested by means of co-feeding.
In their work, the adsorption of both CO and CO_2 are not considered quasi-equilibrated, in open contrast with all previous models presented in literature, due to the intent of describing the interaction between the adsorbed carbonyl compound and the CO, CO_2 and CH_4 gaseous species.

Table 3.4: Reaction mechanism proposed by Burger et al. [94]

Burger et al. mechanism
1) $H_2 + 2\ l \rightleftharpoons 2\ H^*$
2) $CO_2 + H^* + l \rightleftharpoons CO^* + OH^*$
3) $CO + l \rightleftharpoons CO^*$
4) $CO^* + 2\ H^* \rightleftharpoons COH_2^* + 2\ l$
5) $COH_2^* + l \rightleftharpoons CH^* + OH^*$
6) $CH^* + 3\ H^* \rightleftharpoons CH_4 + 4\ l$
7) $OH^* + H^* \rightleftharpoons H_2O + 2\ l$

In this mechanism, step 2 is the H-assisted adsorption of CO_2 and RDS for the RWGS reaction, while step 3 is the RDS for CO adsorption. Therefore, two rate expressions can be

derived:

$$r_{ads,CO} - r_{des,CO} = k_{ads,CO} P_{CO} \theta_l - k_{des,CO} \theta_{CO} \tag{3.4.7}$$

$$r_{ads,CO_2} - r_{des,CO_2} = k_{ads,CO_2} P_{CO_2} \theta_H \theta_l - k_{des,CO_2} \theta_{CO} \theta_{OH} \tag{3.4.8}$$

On the other hand, the RDS for co-methanation is assumed to be the decomposition of a common COH_2^* surface intermediate, i.e. step 5. From this step, considering also the backwards reaction of steam reforming, this rate expression can be derived:

$$r_{met} - r_{SR} = k_{met} \theta_{COH_2} \theta_l - k_{SR} \theta_{CH} \theta_{OH} \tag{3.4.9}$$

Due to their very complex final expression, the reaction rates for the 3 RDSs are not reported in their final form neither here or in Table 3.5.

3.4.4 Hernandez Lalinde et al. model

In 2020 Hernandez Lalinde et al. [95] proposed a comprehensive model describing a particular system, in which CO_2 methanation and RWGS are thought as parallel reactions. This peculiar study was performed on a Ni/Al_2O_3 catalyst.

In this paper, three different reaction mechanism try to summarize all the possible schemes proposed up to the time for CO_2 methanation: as we already know, still today no consensus on a definitive reaction mechanism has been reached. These 3 mechanisms will be further explained in Sec. 6.3, where the Hernandez Lalinde et al. model is one of those deeply examined.

The experiments were conducted at $T = [320 - 420]$ °C, $H_2/CO_2 = [3 - 5]$ mol/mol, and $P = [1.2 - 7.3]$ bar. In addition, GHSV effect as well as possible inhibition of CH_4 and H_2O were studied.

All the models presented in this paper can be summarized in one generalized rate expression for methanation and RWGS, in which K_{C_x} is the adsorption constant of the intermediate carbon species:

$$r_{CH_4} = \frac{k_1 K_{C_x} P_{CO_2}^a K_{H_2}^b P_{H_2}^c P_{H_2O}^d (1 - \frac{P_{CH_4} P_{H_2O}^2}{P_{CO_2} P_{H_2}^4 K_{eqM}})}{(1 + K_{C_x} P_{CO_2}^e K_{H_2}^f P_{H_2}^g P_{H_2O}^h + \sqrt{K_{H_2} P_{H_2}} + K_{OH} \frac{P_{H_2O}}{\sqrt{P_{H_2}}})^2} \tag{3.4.10}$$

$$r_{RWGS} = \frac{k_2 P_{CO_2} K_{H_2}^{0.5} P_{H_2}^{0.5} (1 - k_\beta \frac{P_{CO} P_{H_2O}}{P_{H_2} P_{CO_2} K_{eqRWGS}})}{(1 + K_{C_x} P_{CO_2}^e K_{H_2}^f P_{H_2}^g P_{H_2O}^h + \sqrt{K_{H_2} P_{H_2}} + K_{OH} \frac{P_{H_2O}}{\sqrt{P_{H_2}}})^2} \tag{3.4.11}$$

Analyzing the three proposed mechanisms, taking into consideration all the exponents, and hypothesizing different RDSs, 20 distinct models can be found. The most promising one was model 11 (RDS: $COH^* + H^* \rightleftharpoons CH^* + OH^*$) belonging to what Hernandez Lalinde et al. call *hybrid* mechanism. So, for model 11:

$$r_{CH_4} = \frac{k_1 K_{COH} P_{CO_2}^{0.5} K_{H_2} P_{H_2} (1 - \frac{P_{CH_4} P_{H_2O}^2}{P_{CO_2} P_{H_2}^4 K_{eqM}})}{(1 + K_{COH} P_{CO_2}^{0.5} K_{H_2}^{0.5} P_{H_2}^{0.5} + \sqrt{K_{H_2} P_{H_2}} + K_{OH} \frac{P_{H_2O}}{\sqrt{P_{H_2}}})^2} \tag{3.4.12}$$

$$r_{RWGS} = \frac{k_2 P_{CO_2} K_{H_2}^{0.5} P_{H_2}^{0.5} (1 - k_\beta \frac{P_{CO} P_{H_2O}}{P_{H_2} P_{CO_2} K_{eqRWGS}})}{(1 + K_{COH} P_{CO_2}^{0.5} K_{H_2}^{0.5} P_{H_2}^{0.5} + \sqrt{K_{H_2} P_{H_2}} + K_{OH} \frac{P_{H_2O}}{\sqrt{P_{H_2}}})^2} \tag{3.4.13}$$

This model will be further analyzed in Sec. 6.3

A summary of all the mechanistic comprehensive model is reported on the next page (Table 3.5). In the next chapters, we will deeply examine some of the most promising models among all those reported in this chapter, applying them to our experimental dataset.

Table 3.5: Mechanicstic comprehensive models.

Model	Catalyst	Rate equations
Xu-Froment [92]	$Ni/MgAl_2O_4$	$r_{SR} = \frac{\frac{k_1}{P_{H_2}^{2.5}}\left(P_{CH_4}P_{H_2O} - \frac{P_{H_2}^3 P_{CO}}{K_1}\right)}{\left(1 + K_{CO}P_{CO} + K_{H_2}P_{H_2} + K_{CH_4}P_{CH_4} + K_{H_2O}\frac{P_{H_2O}}{P_{H_2}}\right)^2}$ $r_{WGS} = \frac{\frac{k_2}{P_{H_2}}\left(P_{CO}P_{H_2O} - \frac{P_{H_2}P_{CO_2}}{K_2}\right)}{\left(1 + K_{CO}P_{CO} + K_{H_2}P_{H_2} + K_{CH_4}P_{CH_4} + K_{H_2O}\frac{P_{H_2O}}{P_{H_2}}\right)^2}$ $r_{Rev-Sab} = \frac{\frac{k_3}{P_{H_2}^{3.5}}\left(P_{CH_4}P_{H_2O}^2 - \frac{P_{H_2}^4 P_{CO_2}}{K_3}\right)}{\left(1 + K_{CO}P_{CO} + K_{H_2}P_{H_2} + K_{CH_4}P_{CH_4} + K_{H_2O}\frac{P_{H_2O}}{P_{H_2}}\right)^2}$
Champon et al. [93]	Ni/Al_2O_3	$r_{CO_2meth} = \frac{k_{CO_2meth}K_{H_2}K_{CO_2}P_{H_2}P_{CO_2}\left(1 - \frac{P_{CH_4}P_{H_2O}^2}{P_{H_2}^4 P_{CO_2}K_{eq,CO_2meth}}\right)}{(1 + K_{CO_2}P_{CO_2} + K_{H_2}P_{H_2} + K_{H_2O}P_{H_2O} + K_{CO}P_{CO})^2}$ $r_{RWGS} = \frac{k_{RWGS}K_{CO_2}P_{CO_2}\left(1 - \frac{P_{CO}P_{H_2O}}{P_{H_2}P_{CO_2}K_{eq,RWGS}}\right)}{(1 + K_{CO_2}P_{CO_2} + K_{H_2}P_{H_2} + K_{H_2O}P_{H_2O} + K_{CO}P_{CO})}$ $r_{COmeth} = \frac{k_{COmeth}K_{H_2}K_{CO}P_{H_2}P_{CO}\left(1 - \frac{P_{CH_4}P_{H_2O}}{P_{H_2}^3 P_{CO}K_{eq,COmeth}}\right)}{(1 + K_{CO_2}P_{CO_2} + K_{H_2}P_{H_2} + K_{H_2O}P_{H_2O} + K_{CO}P_{CO})^2}$
Hernandez Lalinde et al. [95]	Ni/Al_2O_3	$r_{CH_4} = \frac{k_1 K_{COH} P_{CO_2}^{0.5} K_{H_2}P_{H_2}(1 - \frac{P_{CH_4}P_{H_2O}^2}{P_{CO_2}P_{H_2}^4 K_{eqM}})}{(1 + K_{COH}P_{CO_2}^{0.5}K_{H_2}^{0.5}P_{H_2}^{0.5} + \sqrt{K_{H_2}P_{H_2}} + K_{OH}\frac{P_{H_2O}}{\sqrt{P_{H_2}}})^2}$
model 11		$r_{RWGS} = \frac{k_2 P_{CO_2} K_{H_2}^{0.5} P_{H_2}^{0.5}(1 - k_\beta \frac{P_{CO}P_{H_2O}}{P_{H_2}P_{CO_2}K_{eqRWGS}})}{(1 + K_{COH}P_{CO_2}^{0.5}K_{H_2}^{0.5}P_{H_2}^{0.5} + \sqrt{K_{H_2}P_{H_2}} + K_{OH}\frac{P_{H_2O}}{\sqrt{P_{H_2}}})^2}$

Chapter 4

Experimental Setup

As mentioned in the previous chapters, due to its optimal performance/cost ratio, its high availability and the prospects surrounding its future applications in industrial scale plants, Ni was chosen as the active metal for the realization of our catalyst.
Alumina was selected as catalyst support, for its beneficial interactions with the active metal and for its very low cost, that makes Ni/Al_2O_3 the leading choice in taking the methanation process to commercial scale.
Two different methods to obtain the catalyst were adopted: *dry impregnation* and *co-precipitation*. Different loadings of Ni were tested, changing the Ni/Al ratio.

Table 4.1: Structural properties of different wt% impregnated catalysts and bare alumina.

	$\gamma - Al_2O_3$	5Ni/Al	10Ni/Al	15Ni/Al	20Ni/Al	25Ni/Al
S_{BET} [m^2/g]	186	170	156	146	129	119
$D_{p,avg}$ [nm]	10	10	10	9	9	9
V_p [cm^3/g]	0.47	0.44	0.42	0.37	0.32	0.38

Table 4.2: Structural properties of co-precipitated catalysts with different Ni/Al ratio.

	NiAl0.3	NiAl0.6	NiAl1.16	NiAl2.6	NiAl6.95
S_{BET} [m^2/g]	235	283	262	168	134
$D_{p,avg}$ [nm]	5.2	6.1	8.6	12	15
V_p [cm^3/g]	0.32	0.58	0.76	0.63	0.61

An activity test was performed over all these catalysts [96] and, despite the best performance at equal nickel loading was observed for the impregnated sample 25Ni/Al, high loaded co-precipitated catalysts allow to maximize the specific activity, since more Ni sites are available. For this reason, a co-precipitated sample, specifically NiAl1.16, was selected in order to carry out our kinetic study.

4.1 Catalyst preparation

The catalyst was prepared in cooperation with Larghi and Petulicchio [96], by co-precipitation, with a Ni/Al ratio equal to 1.16 (Nickel loading equal to 57 wt.%). The preparation procedure was the same as reported by Abellò [97] and Koschany [90].
In this particular case, an 800 mL beaker was filled with 450 mL of demineralized water and the system was kept under stirring at 30°C by the electric stove for the entire process. The salt precursor solutions of $Ni(NO_3)_2$*$6H_2O$ (by Merck ®) and $Al(NO_3)_2$*$9H_2O$ (by Sigma Aldrich ®) were added through a burette. The pH was kept constant to 9 (±0.1), by *719 S Titrino* instrument, adding the precipitating agent solution of 0.5 M NaOH (by Merck ®) and 0.5 M Na_2CO_3 (by Fischer Scientific ®). For 50 mL of salts solution, 100 – 140 mL of precipitating agent solution was added. The system was maintained under stirring at 30°C overnight, then it was filtered employing a *Millipore* pressure filter. The obtained cake was washed with demineralized water until the pH of the filtrate was two consecutive times equal to the pH of the washing water. 5 washing cycles were needed, corresponding to a total volume of washing water of about 3000 mL. The washed sample was then dried at 80°C overnight and calcined at 450°C (5°C/min) for 6 h. The whole procedure is schematised in Fig. 4.1

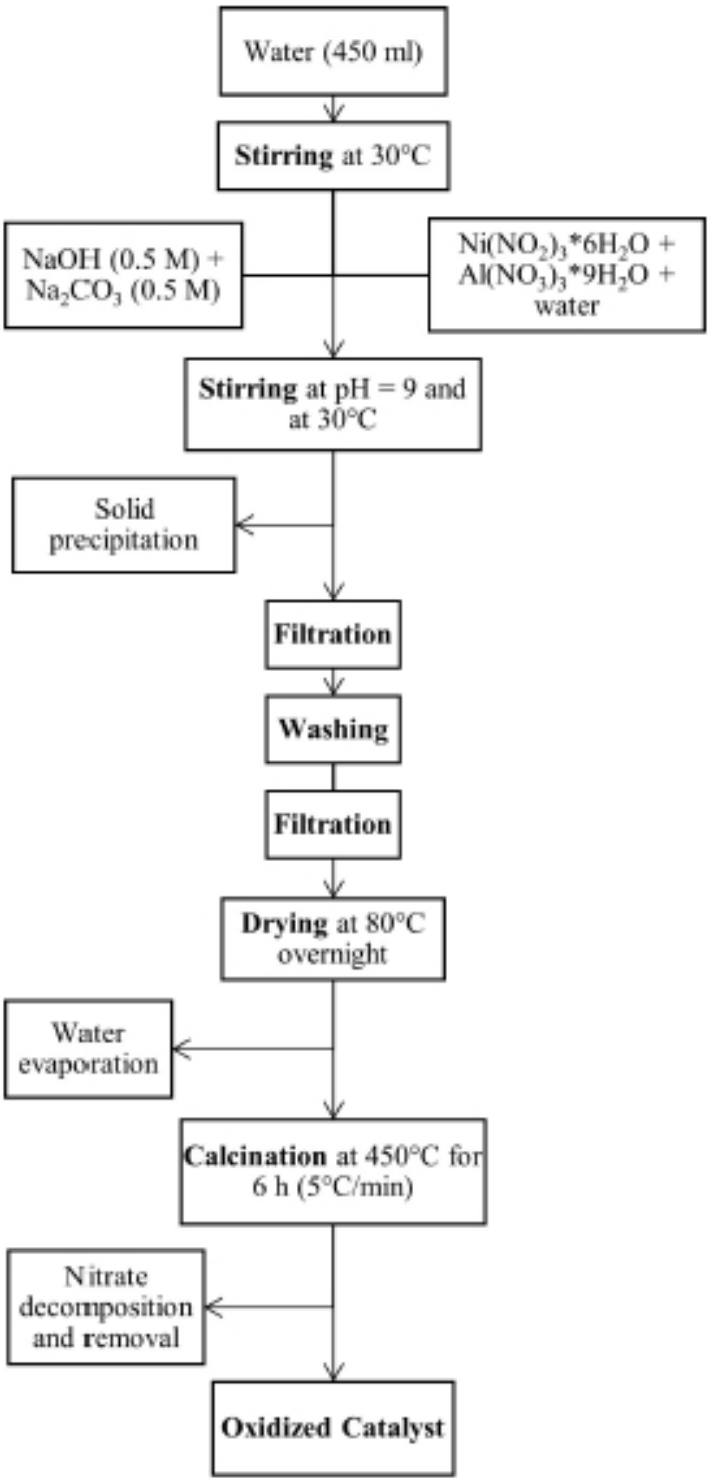

Figure 4.1: Scheme of catalyst preparation by co-precipitation method. [96]

4.2 Catalyst Characterization

The oxidized catalyst was then analyzed to determine its main characteristics, such as BET surface area, pore volume, average pore diameter, crystalline structure and reducibility. The tests performed to calculate these parameters were BET-BJH, XRD, and TPR.

4.2.1 BET-BJH

This analysis consists in the study of the adsorption and desorption of N_2 at 77.15 K (-196℃) on the catalytic surface. The BET-BJH isotherms are then employed to calculate morphological and structural properties of the catalyst, such as the superficial area and the pore volume. The instrument used for the measurements is a *Micrometrics Tristar 3000*.
In Fig. 4.2 (a) the BET curve of the catalyst is reported. The sample shows a type IV curve, typical of mesoporous materials [98], with a hysteresis of type A, corresponding to cylindrical-shaped pores.
The pore volume distribution, reported in Fig.4.2 (b), looks bimodal, with a sharp peak centered at a pore diameter of 50 nm, and a second broad peak centered at higher pore diameters. In Table 4.3 the values of BET surface area, average pore diameter and pore volume are reported.

Table 4.3: Structural properties of the NiAl1.16 catalyst. [96]

S_{BET} [m^2/g]	262
$D_{p,avg}$ [nm]	8.6
V_p [cm^3/g]	0.76

4.2.2 XRD Analysis

X-Ray Diffraction can be used on sufficiently crystalline structures that are characterized by repetitive atomic structures, which can diffract X-rays. The angle of diffraction is a characteristic of every crystallographic plane, each identified by different Miller indices, therefore, by knowing the elements present in the system, the XRD profile can be compared

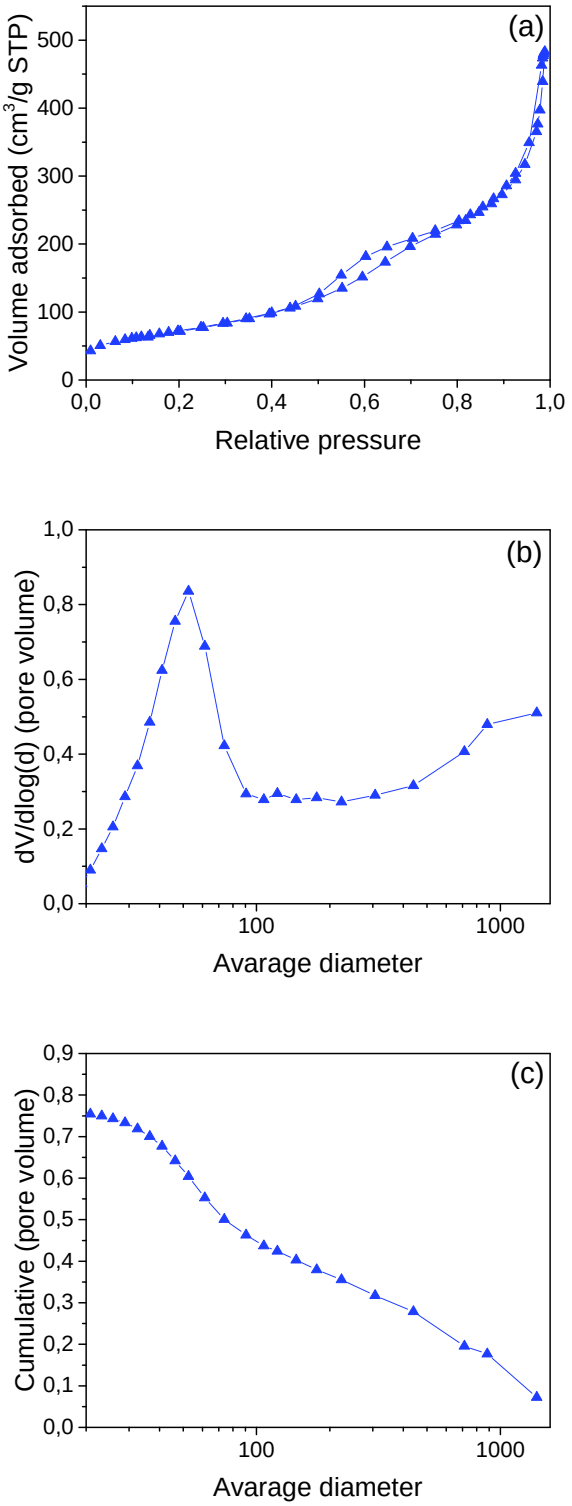

Figure 4.2: N_2 adsorption analysis results.

to some reference profile to find which crystalline chemical compounds were formed.

When X-rays impact the crystal, the incident ray is reflected by the crystallographic plane. Due to the wave nature of the X-ray and the lattice periodicity, the reflected rays create constructive interference only when Bragg's law is valid:

$$2dsin(\theta) = n\lambda \tag{4.2.1}$$

Where d is the distance between crystal planes, θ the angle of impact of the X-rays on the solid surface, n is an integer number and λ the X-rays wavelength.
The XRD analysis allows to determine the crystal structure and identify the phases when more crystals are present. The crystal dimension can also be evaluated, by using the Debye-Scherrer relation:

$$D = \frac{0.9\lambda}{Bcos(\theta)} \tag{4.2.2}$$

Where B is the half peak width.
The XRD profile of the oxidized catalyst is shown in Fig. 4.3. Two species were identified during the XRD-analysis: $NiAl_2O_4$ and NiO. Characteristics peaks of $NiAl_2O_4$ are detected at diffraction angles of 19°, 31°, 37°, 45°, 59°, and 65°. Instead, NiO is found at 37°, 47° and 63°.
Since the Ni/Al ratio was close to 1, a large amount of nickel-aluminate phase was formed in the precipitation process. γ-alumina was not detected, because the total amount of aluminium precipitates as $NiAl_2O_4$, forming a spinel structure. The excess of nickel precipitates on the surface of $NiAl_2O_4$ as NiO, strongly interacting with the support.

4.2.3 TPR Analysis

The temperature programmed reduction (TPR) is used to determine the reducibility of a solid catalyst. A gas mixture, composed by 5% H_2 in Ar, flows over the oxidized catalyst while the temperature rises from ambient temperature to 1000℃. The measurements were performed by a *TPDRO 1100*. In Fig. 4.4 the TPR curve of the calcined catalyst is reported. The reduction of NiO generally presents a single peak located at $[340-397]$ ℃ [97], and this profile witnesses that no significant amount of NiO was found. Most nickel is highly dispersed

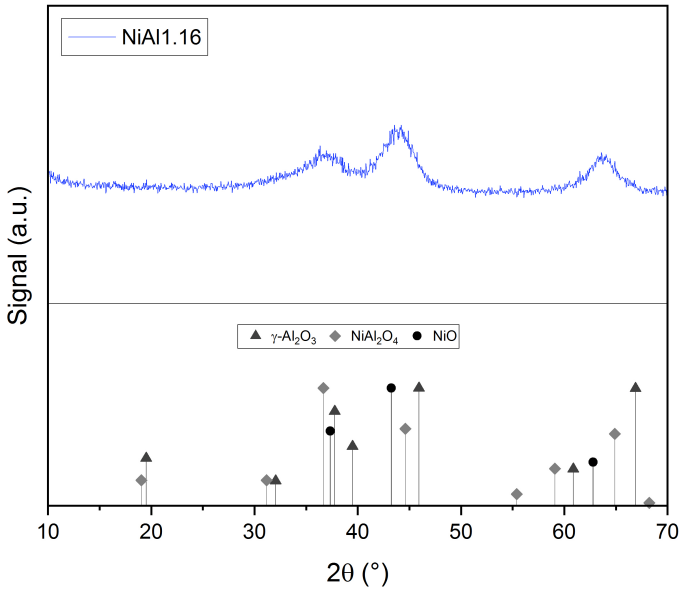

Figure 4.3: XRD profile of the calcined catalyst.

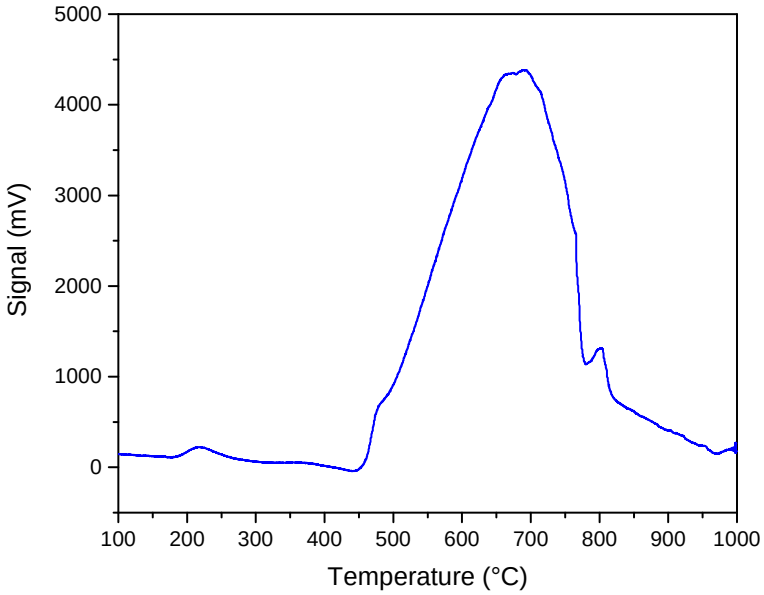

Figure 4.4: TPR profile of the calcined catalyst.

as $NiAl_2O_4$, therefore showing bad reducibility, being trapped in the spinel structure. This explains why the reduction of this catalyst starts at 450°C, and its peak is at 700°C, while the NiO is reduced below 400°C.

The experimental H_2 consumption was calculated by multiplying the area below the TPR curve per a conversion factor [96]. This value was compared with the maximum theoretical H_2 consumption, evaluated by assuming that Ni^{2+} is the only reducible species in the sample and that all nickel is calcined in that form, meaning that the reduction proceeds as:

$$Ni^{2+} + H_2 \rightarrow Ni^0 + H_2O \tag{4.2.3}$$

The ratio between the experimental and the theoretical H_2 consumption was then calculated:

$$R = \frac{mol_{H_{2,exp}}}{mol_{H_{2,th}}} = 0.851 \tag{4.2.4}$$

This incomplete reduction can be caused by nickel trapped in the spinel structure of $NiAl_2O_4$, which is unreachable for H_2. Another possibility is that some nickel was lost during the washing of the catalyst.

A second analysis was performed to determine the degree of reduction, DOR, of the activated

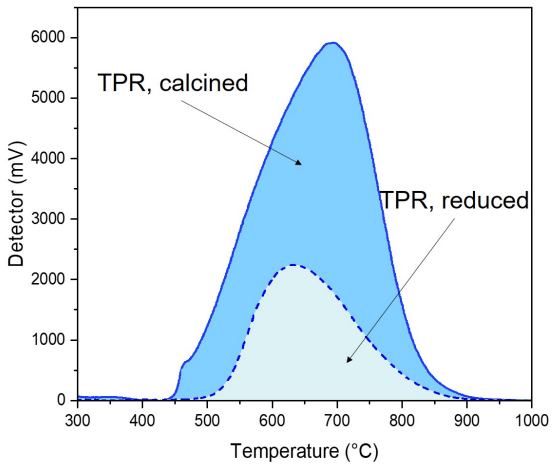

Figure 4.5: Comparison between TPR curves of the calcined and the reduced samples.

catalyst employed during the catalytic tests in Sec. 4.4.2. The catalyst activation was performed at 450°C for 3 h under a H_2 stream, as will be later explained in Sec. 4.4.1.

The activated catalyst was then analyzed and its TPR curve was compared to the calcined

sample in Fig. 4.5.
The DOR of the reduced sample is calculated as:

$$DOR(\%) = \frac{AREA_{calcined} - AREA_{reduced}}{AREA_{calcined}} \cdot 100 = 68\% \quad (4.2.5)$$

A high DOR corresponds to an increase in catalyst activity, but also implies that the temperature of reduction must be increased. High reduction temperatures can worsen the catalyst stability, leading to early catalyst deactivation. Thus, a lower degree of reduction can be acceptable if a better catalyst stability can be ensured.

4.3 Rig layout

The rig used to test the activity of the NiAl1.16 catalyst towards CO_2 methanation was designed in such a way that three different sections can be distinguished:

- Feed section
- Reaction section
- Analysis section

The rig operates at atmospheric pressure and all the line sections requiring a temperature higher than room temperature are heated up and externally insulated. All the lines are realized using INOX steel tubes (INOX ASME 316 SEAMLESS) with external diameter equal to 0.125 in.

4.3.1 Feed section

The feed section is the part of the rig where all the gas mixtures are fed and then sent to the reactor or to the analysis section. The rig consists of three different lines which allow to separately feed nitrogen, hydrogen and the reaction mixture (H_2 78.31 %, CO_2 19.69 %, Ar 2.00 %).

The line numbers have been assigned starting from the bottom line, so that this line is considered the first one, and it corresponds to nitrogen (LINE 1 – N_2). Being an inert gas, pure nitrogen is repeatedly used during the experimental tests, to cool down the reactor

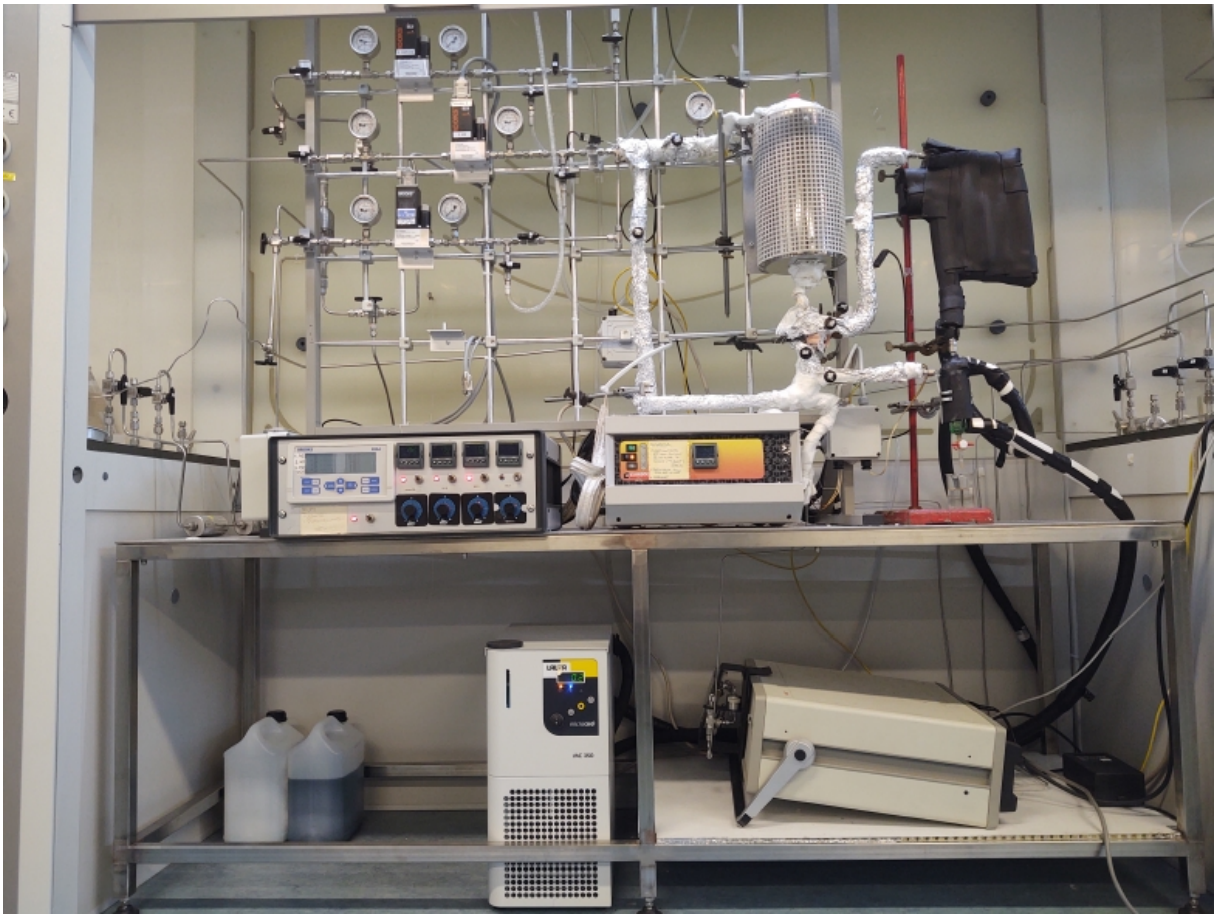

Figure 4.6: Rig picture.

or to stabilize temperature between reduction and reaction steps. Nitrogen was fed to the plant by a gas tank stocked in the designated area outside the laboratory.

During the activity tests, pure hydrogen fed by the second line (LINE 2 – H_2) is used to perform in situ reduction of the catalyst previously to the reaction. The hydrogen was provided by the department feed line at pressure below 5 bar.

The third line (LINE 3 – CO_2/H_2) is used to feed the reaction mixture containing H_2, CO_2 and Ar in the previously specified composition. The mixture was stocked in a specific gas tank in the designated area outside the laboratory.
All the gas tanks are provided with pressure reducers that allow to set the pressure value to the required level.

In its first part, each line is provided with an ON/OFF valve, a particulate filter, a pressure gauge and a mass flow controller (MFC). After the controller, another pressure gauge and a non-return valve are present and followed by a vent connection, regulated by an ON/OFF valve, and another ON/OFF valve to open or close the flow directed to the second part of the plant.

In the last part of the feed section, the gases are mixed and they can be addressed to the reaction section, or to the analysis section, thanks to the presence of a by-pass line. The path followed by the gas is regulated by means of two valves, that can block or permit the flow.

Calibration of Mass Flow Controllers

Mass Flow Controllers (MFC) are fundamental components for the plant's operation. They allow to manipulate and maintain the desired flow, fed to the reactor by setting a specific valve opening.

The calibration of a Mass Flow Controller consists in relating the percentage of opening of the valve to the correct mass flow rate. This procedure must be executed every time a new fluid is fed into the line, since parameters can be significantly different depending on the type of fluid.

The calibration method is simply based on the use of a bubble flowmeter, a calibrated tube containing soap at the bottom. This instrument is connected to the line in such a way that the gas flows from the bottom to the top of the tube. The gas flow causes the formation of a bubble that rises along the tube with a certain velocity. Given a certain opening of the valve, the time taken by the bubble to cover the tube length is measured and related to the gas volume.

The same procedure is repeated changing the valve opening until a suitable set of data is obtained. The measurements are then fit to a line and its equation finally gives the

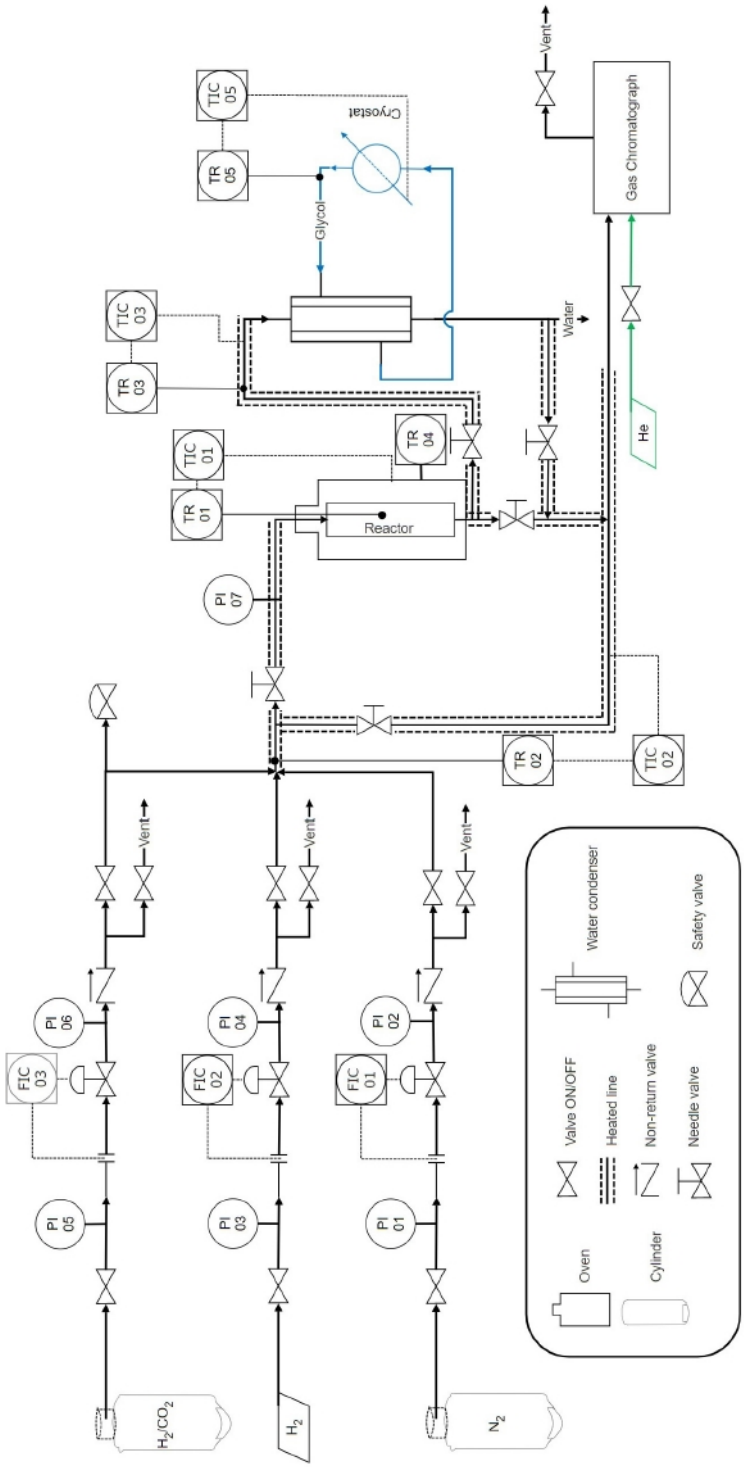

Figure 4.7: P&I diagram of the rig.

calibration parameters of the controller. The calibration lines related to the three controllers of the plants are reported in Fig. 4.8

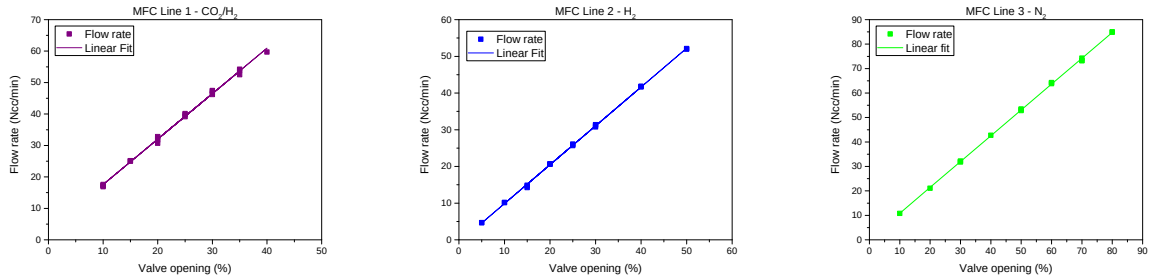

Figure 4.8: MFCs calibration.

4.3.2 Reaction Section

Once the mixture is addressed to the reactor, it enters the reaction section of the plant. The reaction section is composed by:

- Reactor
- Reactor's oven
- Cryostat

A pressure gauge is located right after the valve that allows the flow to access the reactor (V-20). Both the by-pass line and the reactor feed line are heated up by means of a heating sleeve and externally insulated. A J-type thermocouple, connected to a temperature controller, allows to set the desired value for the temperature: in this way it is possible to pre-heat the reaction mixture before entering the reactor. During the experimental tests, 110°C was set as pre-heating temperature of the lines.

The reactor outlet line is provided with an equivalent heating system. A different thermocouple, again of J-type, measures the outlet temperature of the gases and by means of a temperature controller, the temperature is set equal to 130°C.
Both inlet and outlet lines are composed by tubes with external diameter equal to 1/8 in.

The reactor outlet line is divided into two parts: one line is directly connected to the analysis section, while the other one passes through a cryostat where the mixture is cooled down in order to condense the water. The condensed water is then collected in a water trap and finally removed. The cryostat is a LAUDA – MC 350 model and works with glycol as cooling fluid at temperature set equal to 0°C.

The reactor is placed into a thermal oven and a thermocouple is installed in order to constantly measure the temperature of the catalytic bed. The control system of the oven allows to set and control the desired temperature in the reactor, modulating the provided power.

The reactor is a 230 mm long quartz tube with a 12 mm diameter. In the bottom part the reactor shows a porous septum that works as a solid basis for the packing, but at the same time allows the gas products to flow through.

The packing of the reactor is designed considering the axial thermal profile of the oven: the catalytic bed must be placed at the height level of the isothermal zone of the reactor.

Thermal profile of the reactor

The position of the isothermal zone is defined by performing a specific experimental test. In this test, a reactor completely filled with quartz grain was used. A mobile thermocouple was positioned at the bottom of the reactor and the power of the oven was set at a constant value equal to 4.51 (1/s), corresponding to a starting temperature of 300°C at the bottom of the reactor. The thermocouple was then gradually moved from the bottom to the top, in order to measure the temperature at each point of the reactor. The measurements were performed in consecutive steps with a distance of 0.5 cm. The procedure was then repeated in the backward direction to compare and validate the obtained data.
The resulting thermal profile, reported in Fig. 4.9, shows how the isothermal zone is included between 5 and 7 cm. During the activity tests, the height of the catalytic bed in the reactor is always lower than 1 cm and for this reason the obtained result has been considered suitable to the experimental purpose.

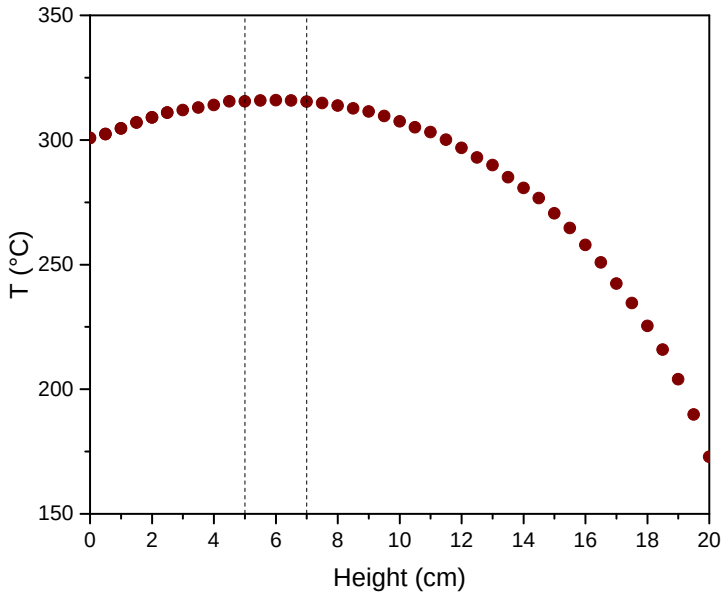

Figure 4.9: Reactor's thermal profile.

Packing of the reactor

Once the isothermal zone was defined, it was possible to design the packing of the reactor in such a way that the catalyst was located in a proper position. For this reason, during the experimental tests the following layers were disposed: the first 4.5 cm layer was constituted by inert material (quartz or glass beads), then a 1 cm layer of glass wool was inserted before the catalytic bed to separate the catalyst from the inert material. For the same purpose, another layer of glass wool was located over the catalyst, followed by a final stratum of inert material. The height of the catalytic layer was always kept below 1 cm.
The inert material has two main functions: at the bottom side it allows to raise the catalytic layer up to the isothermal zone, while at the top it makes the inlet gas flow uniform.

During the tests carried out at GHSV > 20 NL/h/g_{cat}, the catalytic layer of the reactor was filled with 37.5 mg of catalyst and 800 mg of α-alumina, used as a thermal diluent, to ensure uniform temperature along the axial coordinate of the reactor. Instead, 100 mg of catalyst and 800 mg of α-alumina were loaded when conditions in which GHSV ≤ 20 NL/h/g_{cat} were

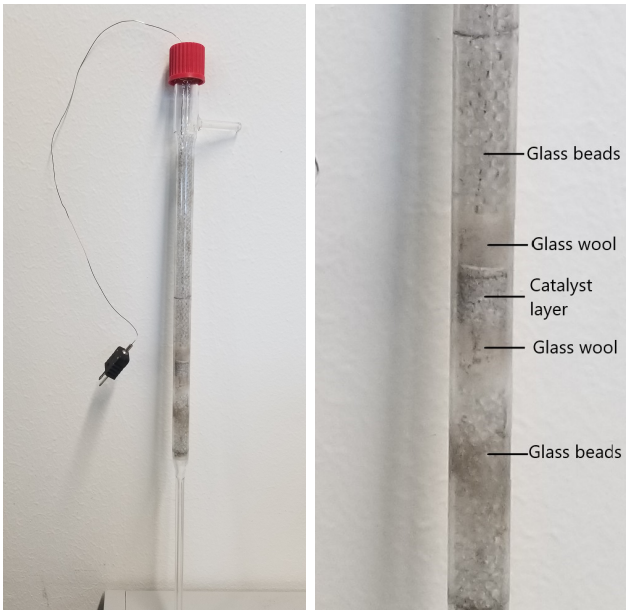

Figure 4.10: Laboratory reactor.

tested.

4.3.3 Analysis section

After the reaction section, the outlet line coming from the reactor connects with the by-pass line and they are both headed to the analysis section. The analysis is performed by means of a Agilent 3000 Micro Gas Chromatograph. Thanks to a specific valve, the instrument discontinuously takes a sample of gas mixture, and sends it to the TCD columns. The sample is analyzed in about three minutes.

A Thermal Conductivity Detector (TCD) is a device able to measure the thermal conductivity of a gas and it is commonly used in gas chromatography. It consists of an electrical conductor filament located at the end of the chromatographic column and constantly immersed in a carrier gas. When the sample is injected into the column, the gas composition changes and so does its thermal conductivity. As a consequence, the temperature of the filament changes and this implies a modification of the electrical conductivity of the material. The change of electrical conductivity is detected and measured as a voltage variation. In a gas chromatograph, each compound is separated and goes through the column at a different

time: in this way, the TCD filament analyzes one species at a time and produces a specific signal, resulting in different peaks over a baseline. The time interval at which the peak is observed allows to identify the gas species, while the peak area is representative of the compound concentration.

In the Gas Chromatograph used during the experimental tests, four columns were present, but just two of them were operating to get the analysis: column A and column C. Both of them were exerted with Helium as carrier gas.

Module A

This first column is of the molecular sieves kind and is 4 m long. It operates at 55℃ and 25 psi. Since helium is used as reference gas, all the peaks were inverted and hydrogen results in a positive peak, while all the other species are observed as a negative signal. In the module, the following species are observed, in this position order:

- Hydrogen
- Argon or Oxygen
- Nitrogen
- Carbon monoxide

Argon and oxygen cannot be separated into the column and for this reason they are observed as a single peak. However, during the activity tests, the second peak was normally attributed to Argon, included in the composition of the reaction mixture.

Module C

The other column is a PLOT-Q and operates at 50℃ and 22.7 psi. Thanks to this module it is possible to detect:

- Methane
- Carbon dioxide
- Ethane

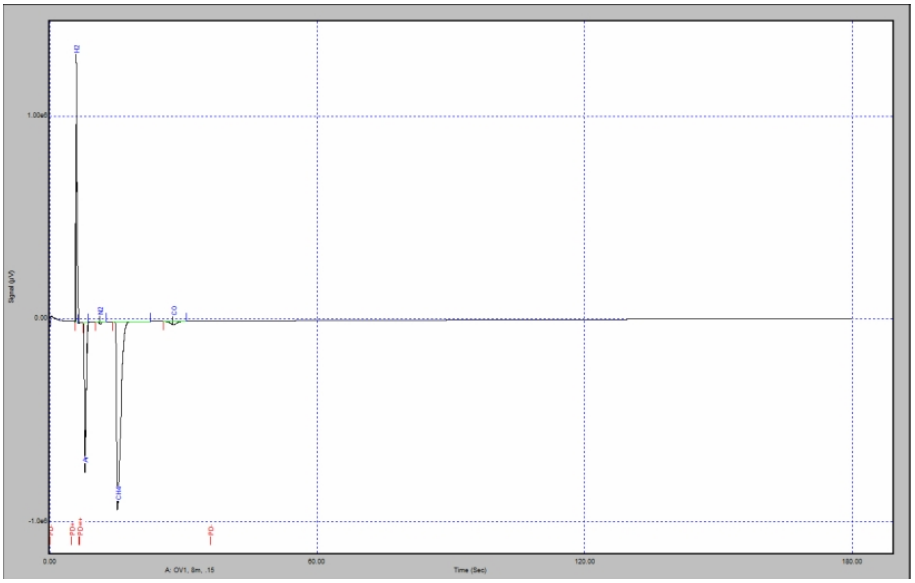

Figure 4.11: Module A - Chromatogram.

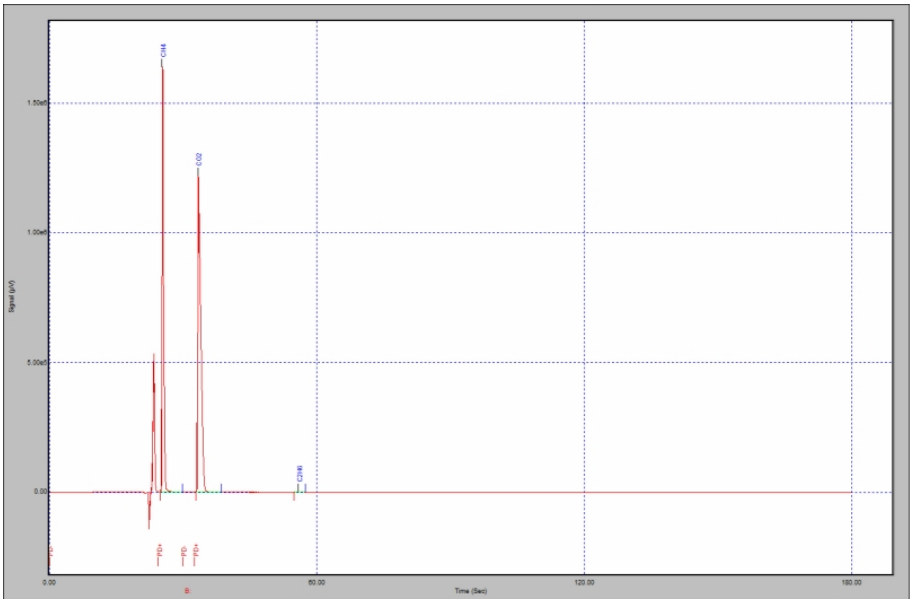

Figure 4.12: Module C - Chromatogram.

Calculation of response factors

The output signal from a chromatographic analysis is collected in a graph called chromatogram: it describes the voltage signal as a function of time and it is constituted by a series of peaks. The area of a single peak is proportional to the concentration of a specific

compound, according to the following relation:

$$\frac{A_i}{C_i} f_i = \frac{A_{ref}}{C_{ref}} \tag{4.3.1}$$

Where A_i and C_i are area and concentration of a specific component, while A_{ref} and C_{ref} respectively correspond to area and concentration of the reference component. The proportional constant f_i is called response factor of the i-component and it is experimentally derived through the calibration of the instrument.

The calibration is a procedure that allows the measured area to be related to the concentration of a certain component, and requires the utilization of a sample with known composition. This sample mixture must contain all the elements expected to be present during the catalytic tests.

A fundamental role is played by the reference component, which allows to calculate the reference factor as:

$$f_i = \frac{A_{ref}}{C_{ref}} \frac{C_i}{A_i} \tag{4.3.2}$$

In this specific case, Argon was chosen as the reference component, since it behaves like an inert in the reaction environment and it is present, with known composition, in the feed mixture.

Table 4.4: Composition of the calibration mixture, concentrations %.

Ar	N_2	CH_4	CO	CO_2	C_2H_6	H_2
3.060	3.030	19.920	0.293	12.020	0.104	61.573

It is worth to mention that two areas related to the same component are different when analyzed in two different columns. This divergence is observed due to the specific measurement distribution that characterizes each column. For this reason, to relate the measurements of the two different columns, the calibration mixture must contain an element that is detected by both column A and C, in this case methane.

During the calibration procedure, the mixture was fed to the reactor and multiple analysis

were collected at stable composition. For each analysis, the ratio $\frac{A_i}{A_{ref}}$ was calculated and an average value was defined. It was then possible to compute the response factors reported in Table 4.5.

Table 4.5: Response factors.

$f_{H_2/Ar}$	$f_{N_2/Ar}$	$f_{CH_4/Ar}$	$f_{CO/Ar}$	f_{CO_2/CH_4}	$f_{C_2H_6/CH_4}$
27.3246	1.0914	1.2870	1.1324	0.6925	0.6650

4.4 Experimental Procedure

In the following section we will analyze how the experimental dataset was collected, starting from the reduction of the catalyst and then proceeding in describing the typical procedure under which data were collected.

4.4.1 Catalyst Activation

After the calcination, the catalyst had to be reduced to be active towards CO_2 methanation. Hence, the catalyst was loaded in the reactor as reported in Sec. 4.3.2, then its reduction was performed.

The reduction was carried out under a stream of pure hydrogen at a space velocity of 18 NL/h/g_{cat}, with a specific temperature program. Starting from room temperature, the system was heated up to 450℃, with a rate of 1℃/min. After 3 h at 450℃, the temperature was reduced to 250℃ at a rate of 5℃/min.
When the temperature was stable at 250℃, the H_2 stream was substituted first with a N_2 stream to inert the bed, then the reacting mixture of H_2/CO_2 was introduced, at a space velocity of 50 NL/h/g_{cat}, to start the experimental activity.

Despite no significant catalyst deactivation was detected during the operation, the catalyst was periodically substituted to collect data at very different operative conditions. After every reactor loading, the same reduction procedure was carried out, and temperature tests

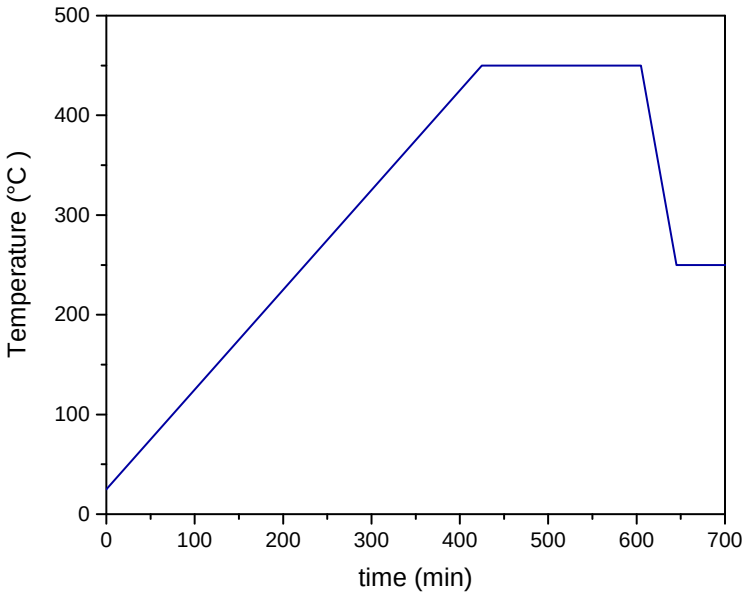

Figure 4.13: Temperature program for reduction.

were performed to verify the activity of the catalyst. (Sec. 4.4.2)

4.4.2 Catalytic Tests

The catalyst activity can now be examined. At first, the temperature effect was tested, by heating the system to 250, 270, 290, 310, 330, 350, 370, 390℃. Each temperature value was kept constant for 45 minutes to collect at least 6 stable outlet composition analyses. After every reactor loading, the same testing procedure was performed to make sure that the catalyst had always the same activity. For each reactor loading, the CO_2 conversion never differed more than 2% at every temperature tested.

Overnight no test was performed, so the reactor was taken at room temperature and under a nitrogen stream, to avoid air infiltration. In the morning, before any test, temperature was increased to 250℃ at a rate of 2℃/min. The nitrogen stream was then substituted by the H_2/CO_2 stream, at a GHSV equal to 50 $NL/h/g_{cat}$. The CO_2 conversion was measured and compared to the one found during the temperature effect testing, taken as a reference. If the difference between the measured and the reference CO_2 conversion was

more than 1% then the catalyst was conditioned, by heating up the system to 350℃, at a rate of 2℃/min. After 30 min at 350℃, the temperature was brought back to 250℃, where the CO_2 conversion was always in the acceptable range. Thus, the catalytic tests could be executed.

In all the performed tests pressure was always maintained equal to 1 atm, while the effect of temperature at different GHSV, H_2/CO_2 ratio, and inert composition were studied.

Temperature effect was studied at different GHSV values (10, 20, and 50 NL/h/g_{cat}), with steps of 20℃. In these tests, H_2/CO_2 ratio and the inert fraction were kept equal to 3.98 and 2% respectively. When space velocity was equal to 10 and 20 NL/h/g_{cat}, the reactor was loaded with 100 mg of catalyst, while at 50 NL/h/g_{cat}, 37.5 mg were loaded, as explained in Sec. 4.3.2.

GHSV effect was studied at 250 and 290℃. The H_2/CO_2 ratio and the fraction of inert were kept equal to 3.98 and 2% respectively. Space velocities studied at 250℃ were 5, 10, 15, 20, 30, 40, 50, 60, 70, and 80 NL/h/g_{cat}, while at 290℃ 5, 10, 15, 20, 30, and 50 NL/h/g_{cat} were investigated.

The inert effect was studied at 290℃ and H_2/CO_2 ratio equal to 3.98. This effect was studied at different inert co-feed: 2, 10, 15, 20, 30, 35, 40%, through the addition of N_2, while the H_2/CO_2 flow was kept constant.

The H_2/CO_2 ratio effect was studied at 250 and 290℃, at a constant space velocity of 50 NL/h/g_{cat}. H_2/CO_2 ratios equal to 1, 2, 3, 4, and 5 were studied at both P_{H_2} and P_{CO_2} constant. In order to study the low H_2/CO_2 ratio conditions, the H_2/CO_2 tank was substituted by a specific tank with H_2/CO_2 ratio equal to 1 (H_2 49%, CO_2 49.01%, Ar 1.99%). H_2/CO_2, H_2, and N_2 flows were managed to keep a constant space velocity while the H_2/CO_2 ratio changed.

Table 4.6: Experimental data collection.

Effect	Temperature [°C]	GHSV [NL/h/g_{cat}]	H_2/CO_2 [−]	Inert [%]
Temperature	250 − 390	50	3.98	2
	210 − 350	20		
	190 − 290	10		
GHSV	250	5 − 50	3.98	2
	290	5 − 80		
Inert	290	50 − 81.67	3.98	2 − 40
H_2/CO_2 $P_{CO_2\ const.}$	250	50	1 − 5	0.67 − 66.89
	290			
H_2/CO_2 $P_{H_2\ const.}$	250	50	1 − 5	1.99 − 41.2
	290			

In Table 4.6 the experimental data collection is summarized, while the complete experimental dataset used to perform the regressions in Ch. 5, 6, and 7 is reported in Appendix B.

In Fig. 4.14 and 4.15 the effect of the different parameters on CO_2 conversion and CO selectivity is shown, as observed from the experimental analysis. For sake of completeness, the calculated errors are reported for each measure. The errors were estimated on the basis of the product/converted carbon balance and on the standard deviations of the outlet flow rates:

$$\delta_c^{rel} = \left(\frac{F_{CH_4}^{out} + F_{CO}^{out} + 2F_{C_2H_6}^{out}}{F_{CO_2}^{in} - F_{CO_2}^{out}} - 1\right) + \frac{X_c}{\sigma_c} \tag{4.4.1}$$

Where δ_c^{rel} is the relative error of the calculated parameter, F_i^{out} are the outlet flow rates measured by the chromatograph, X_c is the calculated parameter, and σ_c is the standard deviation of the calculated parameter. The absolute error can be evaluated as:

$$\delta_c^{abs} = \delta_c^{rel} X_c \tag{4.4.2}$$

As a reference, the graphs also report the corresponding equilibrium curves.

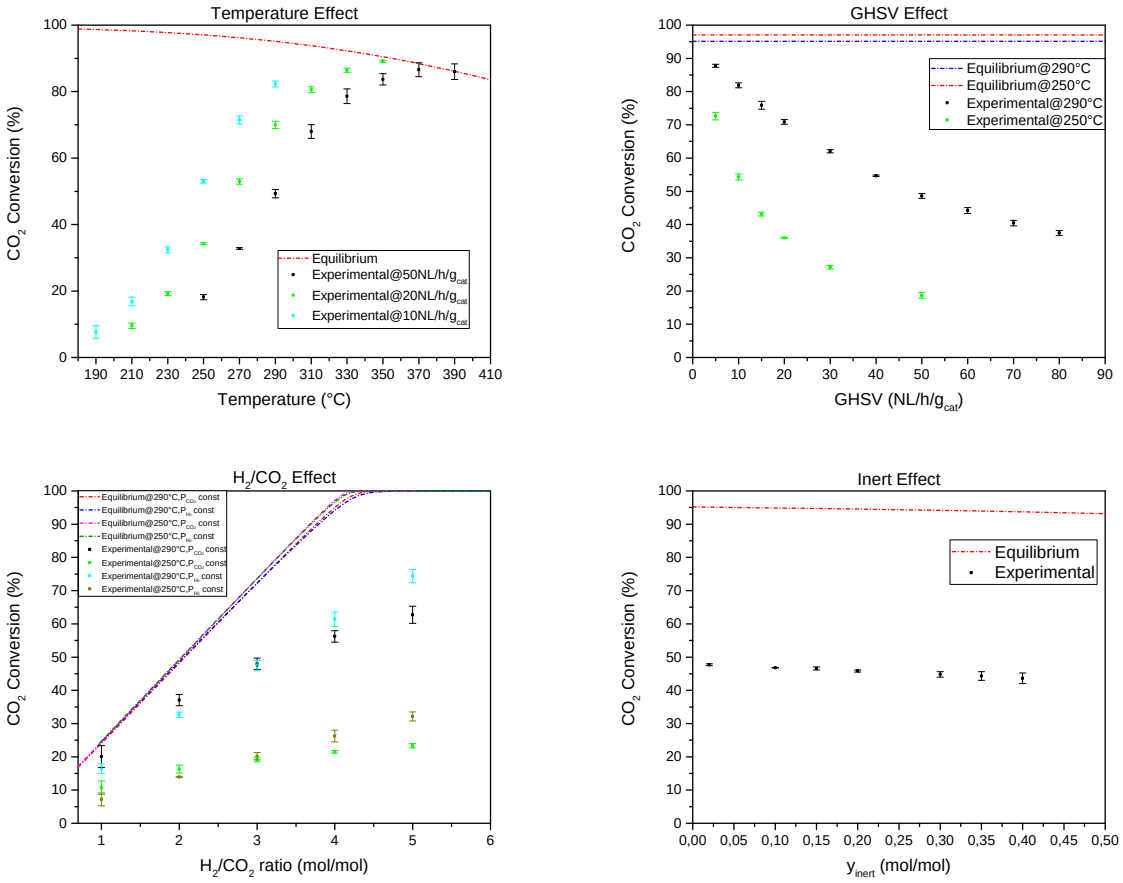

Figure 4.14: CO_2 Conversion data plots.

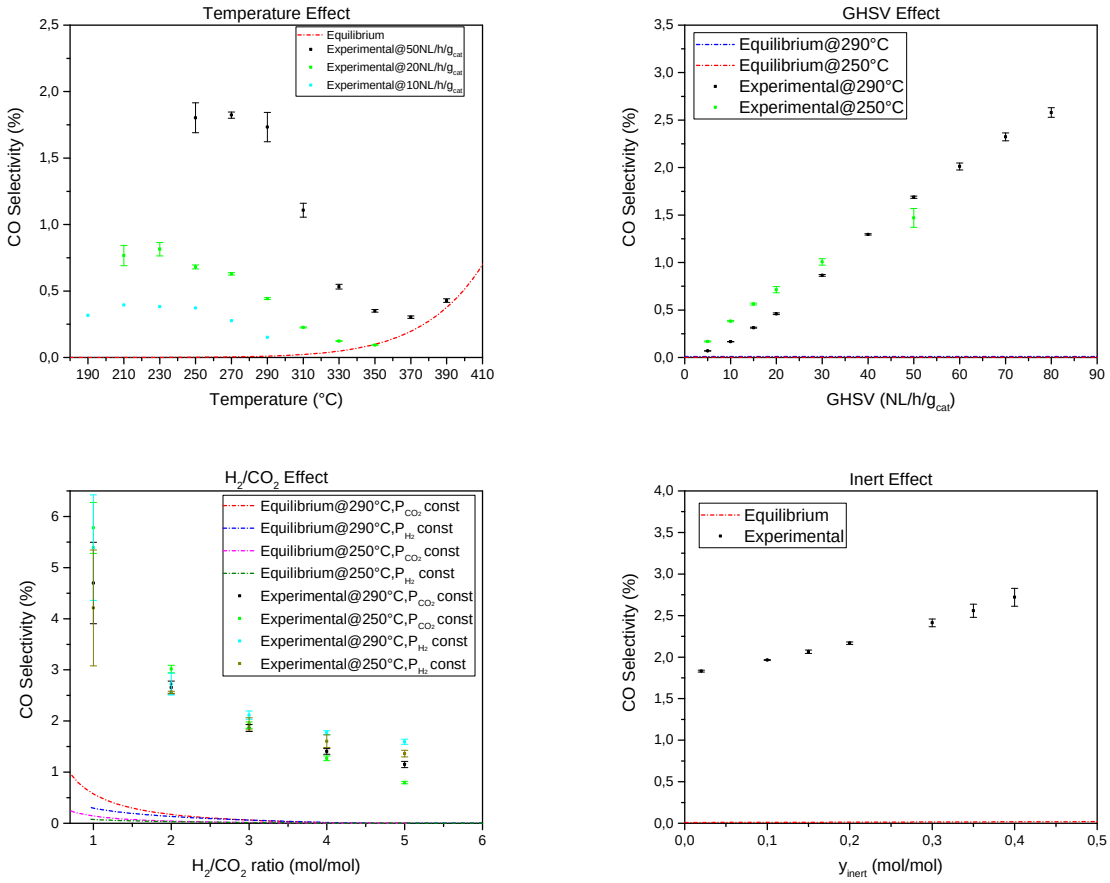

Figure 4.15: CO Selectivity data plots.

4.4.3 Assessment of Transport Limitations

In a kinetic study, it is important to work in a full chemical regime, to ensure uniform composition and temperature along the radial coordinate of the reactor. The following Mears criteria were then verified [99]:

- Interparticle mass transfer:

$$\frac{r_{CO_2}\rho_b r_p|n|}{k_c C_{CO_2}} < 0.15 \tag{4.4.3}$$

- Interparticle heat transfer:

$$\frac{|\Delta H_R| r_{CO_2}\rho_b r_p Ea}{hT^2 R_g} < 0.15 \tag{4.4.4}$$

- Intraparticle mass transfer:

$$\frac{r_{CO_2}\rho_b r_p^2|n|}{\mathcal{D}_{eff,CO_2} C_{CO_2}} < 1 \tag{4.4.5}$$

- Intraparticle heat transfer:

$$\frac{|\Delta H_R| r_{CO_2}\rho_b r_p^2 Ea}{\lambda_{eff} T^2 R_g} < 1 \tag{4.4.6}$$

The observed reaction rate r_{CO_2} was evaluated at the reactor inlet, which represents the most stringent condition, using the Koschany rate expression (Eq. 3.3.4). Only Sabatier reaction enthalpy was considered and it was assumed constant and equal to the standard enthalpy of reaction ($\Delta H_{R,298K} = -165\,kJ/mol$). The catalyst density ρ_c and the catalytic bed density ρ_b were assumed constant and equal to 1470 kg/m^3 and 860 kg/m^3 respectively. The average particle radius r_p is about 50 μm. The average pore radius of the catalyst was equal to 8.6 nm, therefore $\mathcal{D}_{CO_2}$ was in full Knudsen regime. $\mathcal{D}_{eff,CO_2}$ has been evaluated by considering a catalyst tortuosity to void fraction ratio equal to 10. The effective alumina conductivity λ_{eff} was assumed equal to 0.25 W/m/K. Fluid dynamic properties were estimated using the databases included in the Aspen HYSIS®software, and heat and mass transfer coefficients by correlation equations reported by Wakao et Kaguei in *Heat and Mass Transfer in Packed Beds* [100].

The interparticle mass and heat transfer and the intraparticle heat transfer criteria were all respected. On the contrary, the intraparticle mass transfer criterion was not fulfilled at

temperatures above 330°C. However, since most of the data were collected at 290°C, the diffusional limitations were considered ineffective in the performed regressions.

Chapter 5

CO_2 Direct Methanation Models

In this chapter we will analyze kinetic models proposed in literature, whose aim was to describe the process of carbon dioxide methanation, outlining only the direct pathway through Sabatier reaction.
In particular, we will apply these models to our experimental dataset (Appendix B.1), collected, as explained in the previous chapters, on a co-precipitated Ni/Al_2O_3 catalyst, where the Ni/Al molar ratio is equal to 1.16, corresponding to a Nickel loading of 57% wt.
The main target of our kinetic modelling work is to find a rate expression that can properly fit our data, at the same time describing and predicting all the effects linked to the main operating conditions. Our focus will be on:

- Temperature effect;
- GHSV effect;
- $\frac{H_2}{CO_2}$ effect;
- Inert effect;

A proper kinetic model is fundamental for any future development of the process: an optimal industrial reactor can be designed exploiting an appropriate kinetic expression, achieving desired performances while minimizing costs.

Despite many kinetic expressions proposed in Ch. 3 were obtained studying a differential reactor ([74], [75], [81], [82], [78]), these process conditions are very different from the ones adopted on industrial level, whose main target is to maximize SNG productivity. For this reason, our dataset will simulate as much as possible industrial conditions.

In this chapter, our focus will be on these models:

- Lunde-Kester model; (Sec. 3.2.4)
- Koschany model; (Sec. 3.3.4)
- Modified Koschany model;

Before diving into the description of each model, a detailed analysis of how the non-linear regression to find the adaptive parameters was performed is presented.

5.1 Kinetic modelling

We will define *adaptive parameters* those parameters that are found through a non-linear regression that best fit our experimental dataset. The fitting of these adaptive parameters will be performed with Microsoft Fortran®.

Having assessed that no significant transport limitations were present in the process of data collection, we can describe our laboratory reactor through a plug-flow model working in full chemical regime.
Therefore, we can define a one dimensional pseudo-homogeneous plug-flow model through the following set of reactions:

$$\frac{dF_i}{dW_{cat}} = \sum_{j=1}^{NR} \nu_{i,j} \cdot r_j \tag{5.1.1}$$

$$F_i|_{W_{cat}=0} = F_i^{IN} \tag{5.1.2}$$

where:

- F_i is the molar flow of species i;
- F_i^{IN} is the molar flow of species i in the reactor inlet;
- W_{cat} is the mass of catalyst loaded in the reactor;
- $\nu_{i,j}$ is the stoichiometric coefficient of species i in reaction j;
- r_j is the rate of reaction j;

In calculating the different rate expressions, rate constants were treated as Arrenhius type:

$$k_i(T) = k_{0,i} \cdot \exp\left(- \frac{Ea_i}{RT} \right) \tag{5.1.3}$$

where $k_{0,i}$ is the pre-exponential factor, Ea_i is the activation energy of reaction i and R is the universal gas constant, equal to 8.314 $J/(mol \cdot K)$. When performing the non-linear regression, rate constants were parameterized, to ensure code stability:

$$k_i(T) = \exp\left[k_{0,i}^* - \frac{Ea_i}{R} \cdot \left(\frac{1}{T} - \frac{1}{T_{ref}} \right) \right] \tag{5.1.4}$$

From this relation, the *actual* pre-exponential factor can be re-calculated as:

$$k_{0,i} = \frac{\exp\left(k_{0,i}^* + \dfrac{Ea_i}{RT_{ref}} \right)}{1 \times 10^6} \tag{5.1.5}$$

The division for 1×10^6 is necessary if one wants to report a value of k_0 in $mol/(s \cdot g_{cat})$: in our Fortran® code, inlet molar flow rates are in $\mu mol/(s \cdot g_{cat})$.
In each of our regressions, $T_{ref} = 563.15K = 290$℃. This choice was made based on the fact that most of the data were collected at a temperature of 290℃.

As previously said, our non-linear regression is performed with the help of Microsoft Fortran®, which works exploiting very efficient and robust algorithms. Indeed, Fortran works by minimizing an objective function, defined as:

$$F = \sum_z \frac{\sum_{i=1}^{k} (y_{i,z}^{exp} - y_{i,z}^{calc})^2}{s_z^2} \tag{5.1.6}$$

where k is the total number of experimental data, z is an index relative to the considered dependent variable (either χ_{CO_2} or σ_{CO}), s_z^2 is the variance of the considered variable, $y_{i,z}^{exp}$ are the experimental points and $y_{i,z}^{calc}$ the calculated ones.
The variance of a variable can be calculated as:

$$s_z^2 = \sum_{i=1}^{n} \frac{\sum_{j=1}^{p_i} (y_{z,ij}^{exp} - \overline{y_{z,i}^{exp}})^2}{p_i - 1} \tag{5.1.7}$$

Where p_i is the number of times a particular condition was studied, $y_{z,ij}^{exp}$ is the dependent variable z tested in an i condition j times and $\overline{y_{z,i}^{exp}}$ is the average of the considered variable in the p_i attempts.
In our work, these values were found:

$$s_{\chi_{CO_2}}^2 = 1.1929 \times 10^{-6} \tag{5.1.8}$$

$$s_{\sigma_{CO}}^2 = 1.0422 \times 10^{-4} \tag{5.1.9}$$

Together with a set of first guess values for the parameters to calculate, variances of the variables are an input to the system.

When the code calculates the best-fitting adaptive parameters, our Fortran® code prints a correlation matrix, a mean percentage error and a correlation index, through which the quality of the regression is illustrated.
In particular, when two parameters are correlated, it means that they are mathematically related to each other through some implicit functions, that is a functional relationship that does not depend on adaptive parameters.

The mean percentage error is calculated as:

$$MPE = \frac{100\%}{n} \sum_{i=1}^{n} \frac{y_{z,i}^{exp} - y_{z,i}^{calc}}{y_{z,i}^{exp}} \tag{5.1.10}$$

While the correlation index is:

$$R_z^2 = \frac{\sum_{i=1}^{k} (y_{z,i}^{exp} - \overline{y_{z,i}^{exp}})(y_{z,i}^{calc} - \overline{y_{z,i}^{calc}})}{\sqrt{\sum_{i=1}^{k} (y_{z,i}^{exp} - \overline{y_{z,i}^{exp}})^2 \sum_{i=1}^{k} (y_{z,i}^{calc} - \overline{y_{z,i}^{calc}})^2}} \tag{5.1.11}$$

When performing regressions, our input for the first guess values will be for $k^*_{0,i}$, so from values reported on papers we can calculate this parameterized pre-exponential factor as:

$$k^*_{0,i} = \ln\left(k_{0,i}\right) - \frac{Ea_i}{RT_{ref}} \tag{5.1.12}$$

In full analogy with kinetic rate constants, adsorption constants can be determined as:

$$K_i(T) = K_{0,i} \cdot \exp\left(-\frac{\Delta H_i}{RT}\right) \tag{5.1.13}$$

Where $K_{0,i}$ is the adsorption pre-exponential factor and ΔH_i is adsorption enthalpy of the different species. Again, to ensure more stability in the regression, these parameters where parameterized:

$$K_i(T) = \exp\left[K^*_{0,i} - \frac{\Delta H_i}{R} \cdot \left(\frac{1}{T} - \frac{1}{T_{ref}}\right)\right] \tag{5.1.14}$$

So:

$$K_{0,i} = \exp\left(K^*_{0,i} + \frac{\Delta H_i}{RT_{ref}}\right) \tag{5.1.15}$$

$$K^*_{0,i} = \ln\left(K_{0,i}\right) - \frac{\Delta H_i}{RT_{ref}} \tag{5.1.16}$$

Finally, in every regression the equilibrium constant for Sabatier reaction was calculated through the correlation proposed by Lunde and Kester:

$$K_{eq}(T) = exp\Big[\Big(\frac{1}{1.987}\Big)\Big(\frac{56000}{T^2} + \frac{34633}{T} - 16.4\ln T + 0.00557\cdot T\Big) + 33.165\Big] \tag{5.1.17}$$

After having found adaptive parameters for each model, a simulation of different conditions was performed with Fortran®.

A small detail should be noted: when reporting errors relative to k_0 and K_0, a propagation of errors must be done, exploiting the following relations:

$$\Delta(k_{0,i}) = k^*_{0,i}\cdot\left[\Delta(k^*_0) + \Delta(\frac{Ea}{RT_{ref}})\right] \tag{5.1.18}$$

$$\Delta(K_{0,i}) = K^*_{0,i}\cdot\left[\Delta(K^*_0) + \Delta(\frac{\Delta H_i}{RT_{ref}})\right] \tag{5.1.19}$$

We can now start describing the kinetic models that were analyzed in our work.

5.2 Lunde – Kester Model

As briefly described in Sec. 3.2.4, Lunde-Kester model is considered a milestone for Ru-based methanation, and still today is widely employed [84], [101], [102].
We decided to verify if this empirical model could work with a Ni-based experimental dataset, and if it could predict the operating conditions effect.

In their work, Lunde and Kester proposed this rate expression to describe the process:

$$r_{CH_4} = k\left(P_{CO_2}P_{H_2}^4 - \frac{P_{CH_4}P_{H_2O}^2}{K_{eq}}\right)^n \tag{5.2.1}$$

So, the parameters to be calculated are k_0^*, Ea, n.

Table 5.1: Estimated parameters for Lunde-Kester model.

Parameter	Value	U.o.M
k_0^*	$8.26 \pm 1.20 \times 10^{-3}$	-
Ea	88.55 ± 0.05	kJ/mol
n	$7.89 \times 10^{-4} \pm 1.47 \times 10^{-6}$	-

Table 5.2: Correlation matrix of the Lunde-Kester model.

	k_0^*	Ea	n
k_0^*	1.00E+00	-6.49E-02	-9.28E-01
Ea	-6.49E-02	1.00E+00	2.52E-01
n	-9.28E-01	2.52E-01	1.00E+00

We can observe that the activation energy value is quite consistent if compared to other values proposed in CO_2 methanation literature on nickel catalysts [90], [82], [87].

The value of n is very small if compared to what was found by Lunde and Kester (n=0.225) [83], but a strong correlation with the modified pre-exponential factor influences this value: a small value of n is balanced by the output value of k_0^*. Moreover the correlation is of

inverse type: the higher the k_0^*, the lower the n, and vice versa (Table 5.2).

Table 5.3: Quality of the regression for Lunde-Kester model.

Parameter	Value
MPE	10.7%
R^2	0.985

The MPE of this model is quite high for a model that describes only CO_2 conversion, but a good correlation index witnesses the good quality of the fitting.

Table 5.4: Kinetic parameters for Lunde-Kester model.

Parameter	Value	U.o.M
k_0	$6.31 \times 10^5 \pm 7.36 \times 10^3$	$mol/(s \cdot g_{cat} \cdot atm^{5n})$
Ea	88.55 ± 0.05	kJ/mol
n	$7.89 \times 10^{-4} \pm 1.47 \times 10^{-6}$	-

The parity plot (Fig. 5.1) shows how the model slightly underestimates low conversions, at the same time overestimating high conversions.
This trend is confirmed by the simulation plots (Fig. 5.2), where the model tends to reach the thermodynamic equilibrium faster than it should at high conversions (high temperatures or very low GHSV).
This behaviour of the model is revealed also examining the H_2/CO_2 ratio, where equilibrium is reached even at low CO_2 conversions. On the other hand, inert effect is well simulated, because carbon dioxide conversion is in a middle range, far from equilibrium.

This attempt to implement the Lunde-Kester model on a Ni-based catalyst shows that a more complex model must be developed to include some inhibition effects, particularly when high conversions are involved. This behaviour is justified by the fact that this is an empirical model developed on Ru-based catalysts, for which the model still performs very well.

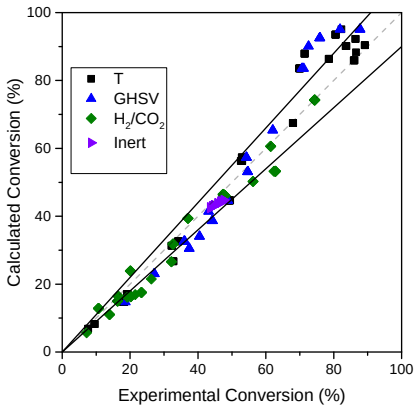

Figure 5.1: Parity plot of the Lunde-Kester model.

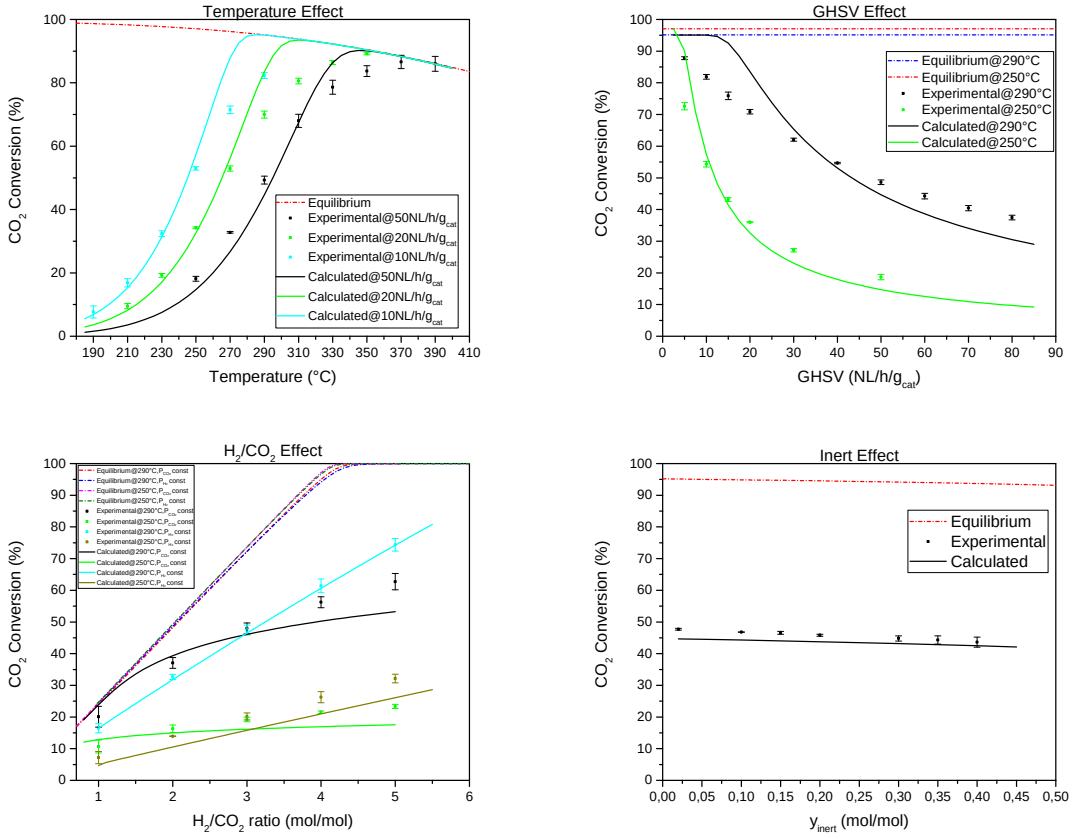

Figure 5.2: Simulation plots of the Lunde-Kester model.

5.3 Koschany et al. Model

Koschany et al. proposed a mechanistic model which can describe CO_2 methanation through Sabatier reaction. Their study was conducted on a $NiAl(O)_x$ catalyst [90], as briefly explained in Sec. 3.3.4.

In their work, Koschany et al. proposed two different mechanisms: a *direct C-O bond cleavage* (Sec. 2.4.2) one and another one, similar to a *RWGS + CO Hydro* scheme (Sec. 2.4.1). The carbide mechanism (mechanism A) is proposed in strict analogy with the one proposed by Weatherbee and Bartholomew [87] and reported in Sec. 3.3.1.

Table 5.5: Mechanisms for CO_2 methanation proposed by Koschany et al.

Mechanism A	Mechanism B
1) $CO_2 + 2\ l \rightleftharpoons CO^* + O^*$	1) $CO_2 + 2\ l \rightleftharpoons CO^* + O^*$
2) $H_2 + 2\ l \rightleftharpoons 2\ H^*$	2) $H_2 + 2\ l \rightleftharpoons 2\ H^*$
3) $CO^* + l \rightleftharpoons C^* + O^*$	3) $CO^* + H^* \rightleftharpoons CHO^* + l$
4) $C^* + H^* \rightleftharpoons CH^* + l$	4) $CHO^* + l \rightleftharpoons CH^* + O^*$
5) $O^* + H^* \rightleftharpoons OH^* + l$	5) $CH^* + 3\ H^* \rightleftharpoons CH_4^* + 3\ l$
6) $OH^* + H^* \rightleftharpoons H_2O^* + l$	6) $CH_4^* \rightleftharpoons CH_4 + l$
7) $H_2O^* \rightleftharpoons H_2O + l$	7) $O^* + H^* \rightleftharpoons OH^* + l$
8) $CH^* + 3\ H^* \rightleftharpoons CH_4^* + 3\ l$	8) $OH^* + H^* \rightleftharpoons H_2O^* + l$
9) $CH_4^* \rightleftharpoons CH_4 + l$	9) $H_2O^* \rightleftharpoons H_2O + l$

The final rate expression proposed by Koschany et al. is derived from mechanism B, assuming step 3 as RDS of the process, steps 3 and 7 as irreversible and species H, CO and OH as MASI.

The driving force term $\left(1 - \frac{P_{CH_4} P_{H_2O}^2}{P_{CO_2} P_{H_2}^4 K_{eq}}\right)$ is not present in the model derivation, but it is unilaterally reported, knowing that it should be present.

Expedients about reactions 3 and 7 being irreversible and the inclusion of an equilibrium term are not explained by the authors, neither from a theoretical nor an experimental point of view.

The proposed reaction rate is:

$$r_{CH_4} = \frac{kP_{H_2}^{0.5}P_{CO_2}^{0.5}\left(1 - \frac{P_{CH_4}P_{H_2O}^2}{P_{CO_2}P_{H_2}^4 K_{eq}}\right)}{\left(1 + K_{OH}\frac{P_{H_2O}}{P_{H_2}^{0.5}} + K_{H_2}P_{H_2}^{0.5} + K_{mix}P_{CO_2}^{0.5}\right)^2} \tag{5.3.1}$$

Adaptive parameters to be calculated for this model are:
k_0^*, Ea, $K_{0,OH}^*$, ΔH_{OH}, K_{0,H_2}^*, ΔH_{H_2}, $K_{0,mix}^*$, ΔH_{mix}.

Table 5.6: Estimated parameters of Koschany et al. model.

Parameter	Value	U.o.M
k_0^*	$9.77 \pm 4.98 \times 10^{-2}$	–
Ea	92.79 ± 1.38	kJ/mol
$K_{0,OH}^*$	$2.80 \pm 2.53 \times 10^{-2}$	–
ΔH_{OH}	6.37 ± 0.68	kJ/mol
K_{0,H_2}^*	$9.24 \times 10^{-1} \pm 3.40 \times 10^{-2}$	–
ΔH_{H_2}	-0.83 ± 0.42	kJ/mol
$K_{0,mix}^*$	$2.30 \pm 2.91 \times 10^{-2}$	–
ΔH_{mix}	2.82 ± 1.32	kJ/mol

To evaluate the quality of the regression, we here report the correlation matrix, MPE and R^2.

Table 5.7: Correlation matrix of the Koschany et al. model.

	k_0^*	Ea	$K_{0,OH}^*$	ΔH_{OH}	K_{0,H_2}^*	ΔH_{H_2}	$K_{0,mix}^*$	ΔH_{mix}
k_0^*	1.00E+00	2.35E-01	9.97E-01	2.28E-01	9.17E-01	2.05E-01	9.72E-01	1.97E-01
Ea	2.35E-01	1.00E+00	2.41E-01	9.82E-01	4.66E-02	-2.09E-01	3.21E-01	.83E-01
$K_{0,OH}^*$	9.97E-01	2.41E-01	1.00E+00	2.32E-01	9.11E-01	2.10E-01	9.67E-01	1.99E-01
ΔH_{OH}	2.28E-01	9.82E-01	2.31E-01	1.00E+00	4.53E-02	-2.03E-01	3.11E-01	9.59E-01
K_{0,H_2}^*	9.17E-01	4.66E-02	9.11E-01	4.53E-02	1.00E+00	3.16E-01	8.03E-01	5.69E-03
ΔH_{H_2}	2.05E-01	-2.09E-01	2.10E-01	-2.03E-01	3.16E-01	1.00E+00	1.18E-01	-3.67E-01
$K_{0,mix}^*$	9.72E-01	3.21E-01	9.67E-01	3.11E-01	8.03E-01	1.18E-01	1.00E+00	2.92E-01
ΔH_{mix}	1.97E-01	9.83E-01	1.99E-01	9.59E-01	5.62E-03	-3.67E-01	2.92E-01	1.00E+00

Table 5.8: Quality of the regression of the Koschany et al. model.

Parameter	Value
MPE	3.27%
R^2	0.998

The results obtained adopting the Koschany et al. model are excellent, as witnessed by both MPE and R^2 values and confirmed by the plots reported in Fig. 5.4.
Despite this, significant differences are present with the values found by Koschany et al. in their paper.

Table 5.9: Kinetic parameters of Koschany et al. model and comparison with Koschany et al. results. [90]

Parameter	Value	Koschany et al	U.o.M
k_0	$7.07 \times 10^6 \pm 2.44 \times 10^6$	$6.81 \times 10^3 \pm 1.10 \times 10^4$	$mol/(s \cdot g_{cat} \cdot atm)$
Ea	92.79 ± 1.38	77.5 ± 6.9	kJ/mol
$K_{0,OH}$	$6.41 \times 10^1 \pm 1.09 \times 10^1$	$6.41 \times 10^1 \pm 9.54 \times 10^1$	$atm^{-0.5}$
ΔH_{OH}	6.37 ± 0.68	22.4 ± 6.4	kJ/mol
K_{0,H_2}	$2.11 \pm 2.59 \times 10^{-1}$	$1.15 \times 10^{-1} \pm 2.70 \times 10^{-1}$	$atm^{-0.5}$
ΔH_{H_2}	-0.83 ± 0.42	-6.2 ± 10	kJ/mol
$K_{0,mix}$	$1.83 \times 10^1 \pm 5.67$	$1.00 \times 10^{-1} \pm 1.36 \times 10^{-1}$	$atm^{-0.5}$
ΔH_{mix}	2.82 ± 1.32	-10 ± 5.7	kJ/mol

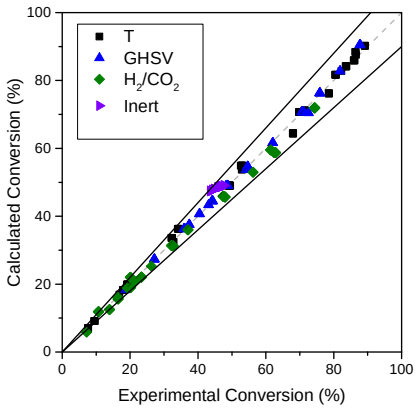

Figure 5.3: Parity plot for of Koschany et al. model.

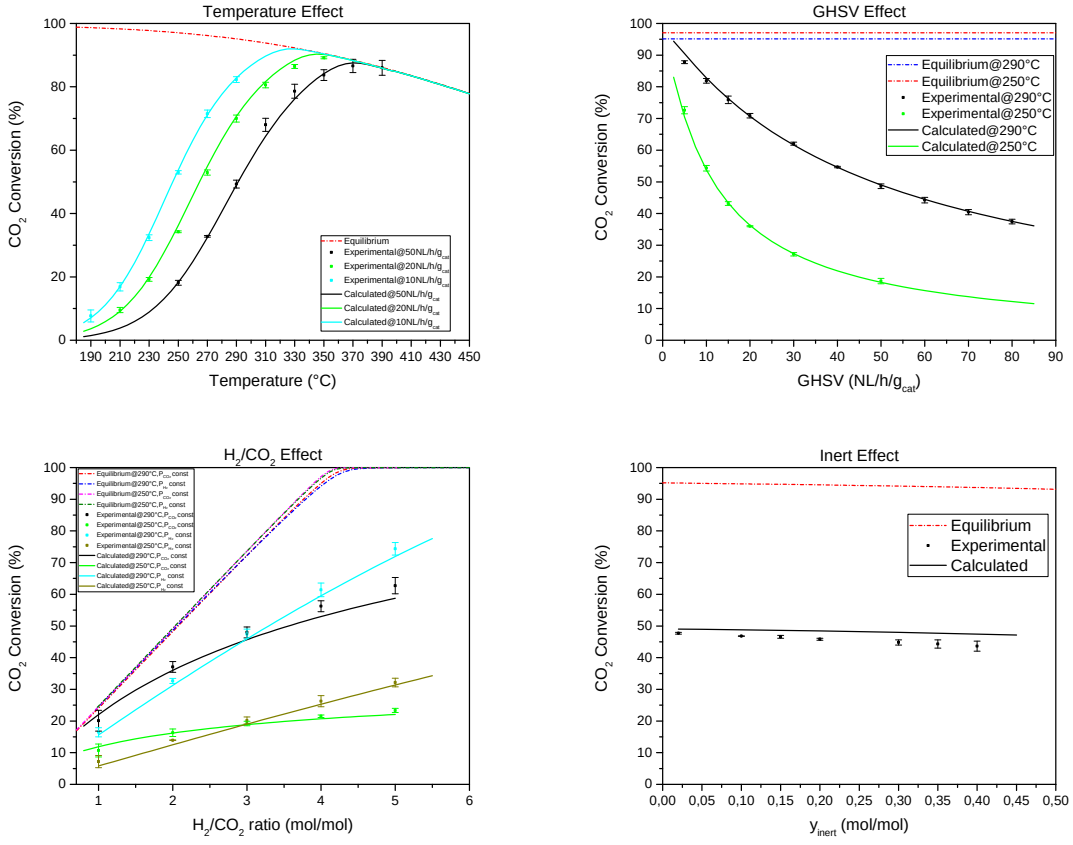

Figure 5.4: Simulation plots of the Koschany et al. model.

5.3.1 Instability Problems

Despite the excellent results obtained in our work with the Koschany model, we discovered some instability problems: when searching for the minimum in the objective function F (Eq. 5.1.6), many different minima were found, strongly depending on the first guess values chosen as input. Indeed, two sets of different first guess values were tried, leading to very different results.

Table 5.10: Kinetic parameters of *unstable* Koschany et al. model.

Parameter	Value (*unstable* model)	Value (from Sec. 5.3)	U.o.M
k_0	$1.09 \times 10^5 \pm 2.38 \times 10^4$	$7.07 \times 10^6 \pm 2.44 \times 10^6$	$mol/(s \cdot g_{cat} \cdot atm)$
Ea	78.88 ± 0.91	92.79 ± 1.38	kJ/mol
$K_{0,OH}$	6.85 ± 0.79	$6.41 \times 10^1 \pm 1.09 \times 10^1$	$atm^{-0.5}$
ΔH_{OH}	1.27 ± 0.48	6.37 ± 0.68	kJ/mol
K_{0,H_2}	$1.48 \times 10^{33} \pm 2.74 \times 10^{34}$	$2.11 \pm 2.59 \times 10^{-1}$	$atm^{-0.5}$
ΔH_{H_2}	413.72 ± 75.60	-0.83 ± 0.42	kJ/mol
$K_{0,mix}$	1.24 ± 0.18	18.30 ± 5.67	$atm^{-0.5}$
ΔH_{mix}	-8.06 ± 0.59	2.82 ± 1.32	kJ/mol

The results clearly reflect an instability of the model, as witnessed by the value of K_{0,H_2}, which represents a physical non-sense.
However, this weakness of the system is not reflected neither in the parity plot or in the values of both MPE and R^2.

Table 5.11: Quality of the regression of the unstable Koschany et al. model.

Parameter	Value
MPE	4.29%
R^2	0.985

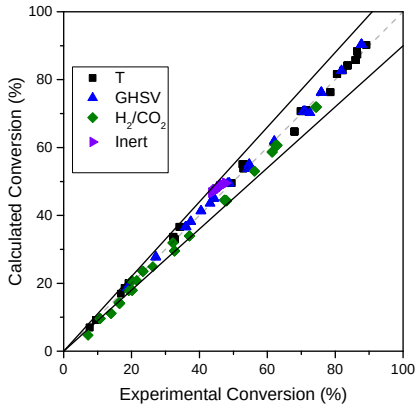

Figure 5.5: Parity plot of the *unstable* Koschany et al. model.

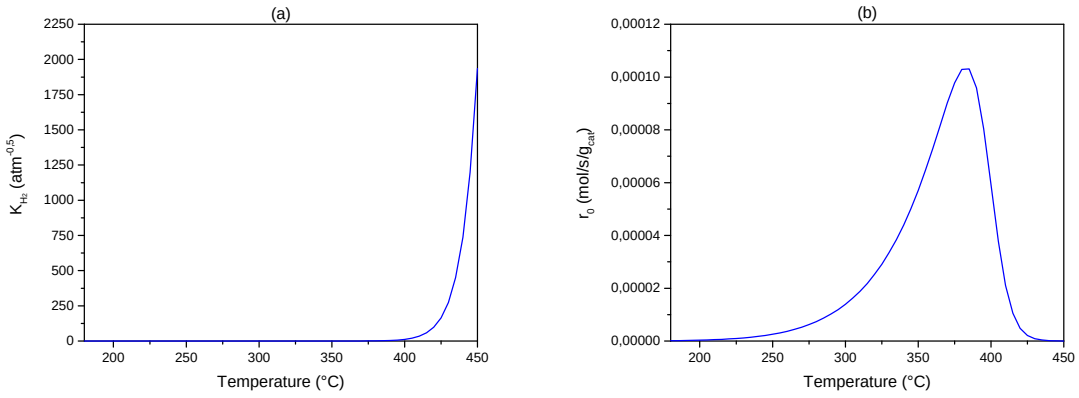

Figure 5.6: (a) *Unstable* K_{H_2} as function of temperature. (b) *Unstable* initial reaction rate r_0 as function of temperature, with y_{inert}=0.02 and H_2/CO_2=3.98.

The instability is evident for temperatures higher than 400°C, when CO_2 conversion declines abruptly. This behaviour becomes clear if the values of K_{H_2} against temperature are plotted: K_{H_2} tends to infinity and, being a term at denominator, makes the reaction rate converge to zero (Fig. 5.6).

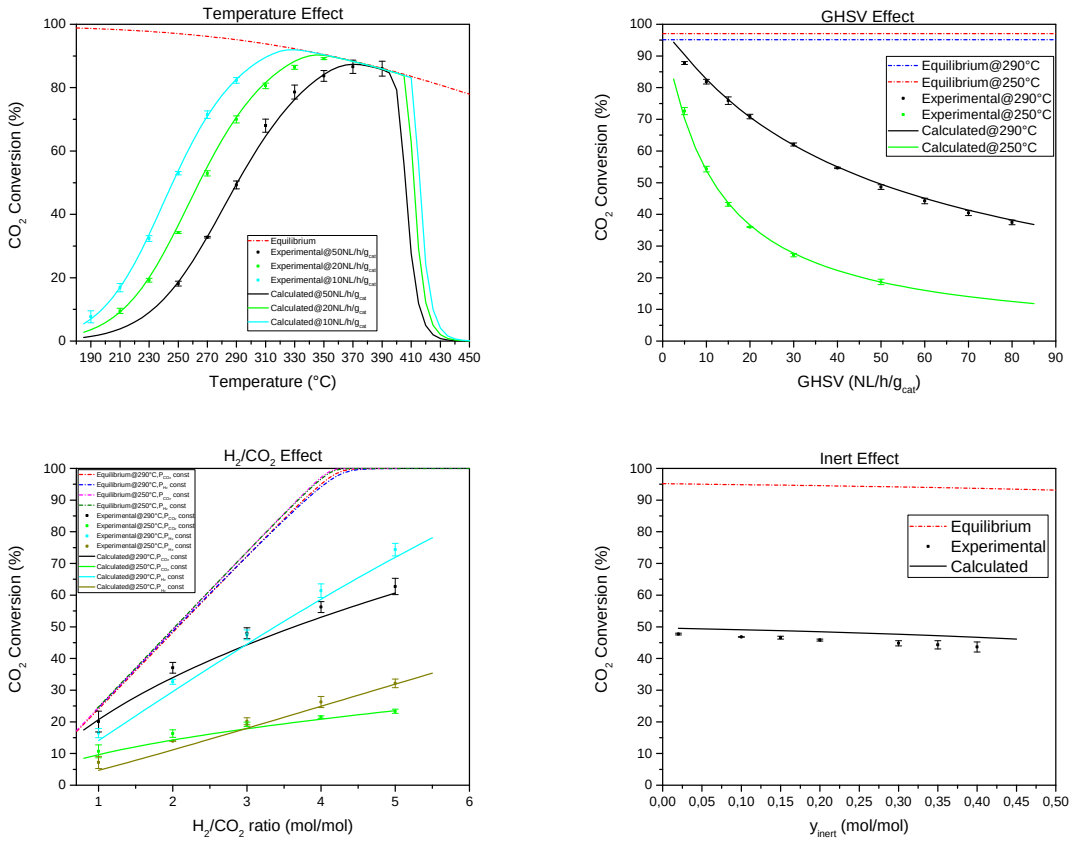

Figure 5.7: Simulation plots of the *unstable* Koschany et al. model.

5.3.2 Modified Koschany et al. Model

Analyzing in detail the model, we found many inconsistencies, as previously illustrated. For this reason, we decided to try and derive the Koschany model from mechanism B (Tab. 5.5). The detailed derivation of the model can be found in Appendix C.1.
We decided to keep all reactions as irreversible (steps 3 and 7 were considered reversible in the Koschany et al. derivation), keeping step 3 as RDS of the process and species H, CO and OH as MASI, in full analogy with the procedure followed by Koschany et al. in their work. In this case, the resulting reaction rate is:

$$r_{CH_4,mod} = \frac{k\frac{P_{CO_2}P_{H_2}^{1.5}}{P_{H_2O}}\left(1 - \frac{P_{CH_4}P_{H_2O}^2}{P_{CO_2}P_{H_2}^4 K_{eq}}\right)}{\left(1 + K_{OH}\frac{P_{H_2O}}{P_{H_2}^{0.5}} + K_{H_2}P_{H_2}^{0.5} + K_{mix}\frac{P_{CO_2}P_{H_2}}{P_{H_2O}}\right)^2} \tag{5.3.2}$$

A big difference with the expression proposed by Koschany et al. is the presence of water partial pressure at numerator. Again, the parameters to be calculated are:
k_0^*, Ea, $K_{0,OH}^*$, ΔH_{OH}, K_{0,H_2}^*, ΔH_{H_2}, $K_{0,mix}^*$, ΔH_{mix}.

Table 5.12: Estimated parameters of the modified Koschany et al. model.

Parameter	Value	U.o.M
k_0^*	$8.00 \pm 2.50 \times 10^{-2}$	–
Ea	89.83 ± 1.75	kJ/mol
$K_{0,OH}^*$	$-0.303 \pm 2.48 \times 10^{-2}$	–
ΔH_{OH}	29.56 ± 1.57	kJ/mol
K_{0,H_2}^*	$1.17 \pm 1.81 \times 10^{-2}$	–
ΔH_{H_2}	-26.69 ± 1.04	kJ/mol
$K_{0,mix}^*$	$-0.227 \pm 1.22 \times 10^{-2}$	–
ΔH_{mix}	35.08 ± 0.97	kJ/mol

An increase in MPE can be observed if we compare this model with the original Koschany one, but still the fitting is very good. Despite this, a problem is produced by the presence of

Table 5.13: Correlation matrix of the modified Koschany et al. model.

	k_0^*	Ea	$K_{0,OH}^*$	ΔH_{OH}	K_{0,H_2}^*	ΔH_{H_2}	$K_{0,mix}^*$	ΔH_{mix}
k_0^*	1.00E+00	1.74E-02	7.63E-01	-4.03E-02	9.89E-01	1.36E-01	9.92E-01	-8.09E-04
Ea	1.75E-02	1.00E+00	1.53E-01	8.65E-01	-2.92E-02	9.84E-01	5.15E-02	9.90E-01
$K_{0,OH}^*$	7.63E-01	1.53E-01	1.00E+00	-1.79E-01	6.74E-01	1.94E-01	7.99E-01	1.54E-01
ΔH_{OH}	-4.03E-02	8.65E-01	-1.79E-01	1.00E+00	-3.13E-02	8.74E-01	-3.76E-02	8.42E-01
K_{0,H_2}^*	9.89E-01	-2.92E-02	6.74E-01	-3.13E-02	1.00E+00	1.04E-01	9.64E-01	-5.58E-02
ΔH_{H_2}	1.36E-01	9.84E-01	1.94E-01	8.74E-01	1.04E-01	1.00E+00	1.57E-01	9.60E-01
$K_{0,mix}^*$	9.92E-01	5.15E-02	7.99E-01	-3.76E-02	9.64E-01	1.57E-01	1.00E+00	4.38E-02
ΔH_{mix}	-7.72E-04	9.90E-01	1.54E-01	8.42E-01	-5.58E-02	9.60E-01	4.38E-02	1.00E+00

Table 5.14: Quality of the regression of the modified Koschany et al. model.

Parameter	Value
MPE	5.64%
R^2	0.995

P_{H_2O} at numerator: if water inlet molar fraction is equal to zero, the reaction rate is not mathematically defined.

Table 5.15: Kinetic parameters of the modified Koschany et al. model.

Parameter	Value	U.o.M
k_0	$6.44 \times 10^5 \pm 2.57 \times 10^5$	$mol/(s \cdot g_{cat} \cdot atm^{1.5})$
Ea	89.83 ± 1.47	kJ/mol
$K_{0,OH}$	407 ± 205	$atm^{-0.5}$
ΔH_{OH}	29.56 ± 1.57	kJ/mol
K_{0,H_2}	$1.08 \times 10^{-2} \pm 2.59 \times 10^{-3}$	$atm^{-0.5}$
ΔH_{H_2}	-26.69 ± 1.04	kJ/mol
$K_{0,mix}$	1430 ± 301	atm^{-1}
ΔH_{mix}	35.08 ± 0.97	kJ/mol

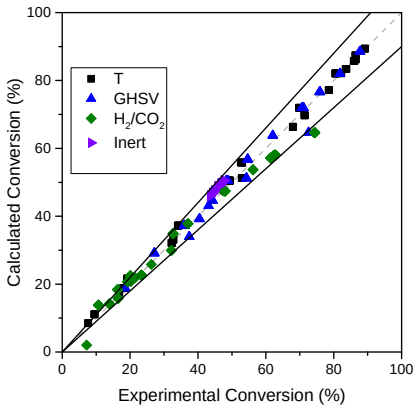

Figure 5.8: Parity plot of the modified Koschany et al. model.

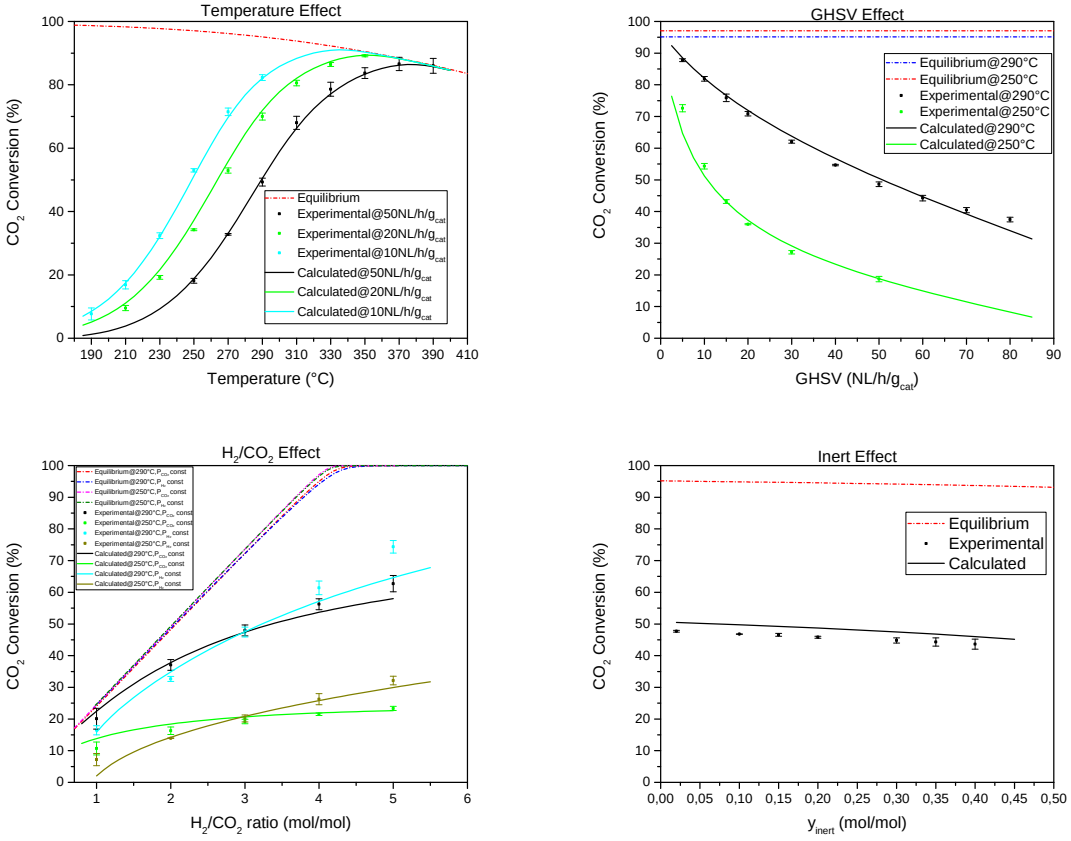

Figure 5.9: Simulation plots of the modified Koschany et al. model.

Low conversion simulations of this model have unusual results. To further clarify the trend predicted by the model, we will focus on adsorption terms present at denominator, with a particular interest on how the reaction rate changes along the reactor at different water inlet molar flow rates.

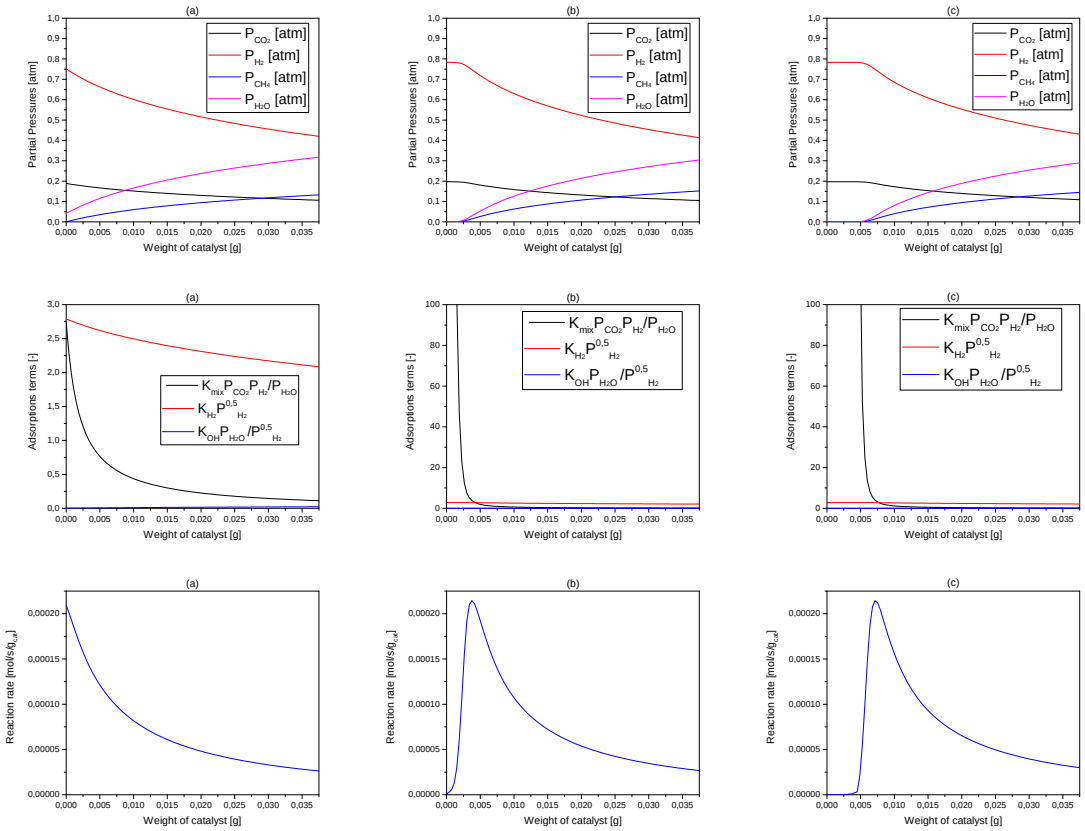

Figure 5.10: Top: Partial pressure profiles; Middle: Adsorption terms profiles; Bottom: Reaction rate profile; Inside the reactor at different inlet water flow rates, calculated at 290 °C, H_2/CO_2=3.98, GHSV=50 NL/h/gcat, and y^0_{inert}=0.02, for the modified Koschany et al. model. (a) $F^{in}_{H_2O} = 10^{-6}$ mol/s. (b) $F^{in}_{H_2O} = 10^{-9}$ mol/s. (c) $F^{in}_{H_2O} = 10^{-12}$ mol/s

.

As can be observed in the figures reported above, a strong weakness of this model is the presence of P_{H_2O} at numerator. Indeed, reaction rate should be at its maximum at the beginning of the reactor, while in this case a maximum is observed inside the reactor, as soon as a certain quantity of water is formed.

This is very evident in Fig. 5.10 (*bottom* (a)): in this case, we hypothesized a water co-feed of $1 \times 10^6\, mol/s$, corresponding to a $y^0_{H_2O} = 4.30\%$; CO_2 methanation rate is at its maximum at the beginning, decreasing along the reactor coordinate. On the contrary, if a water co-feed of $1 \times 10^{12}\, mol/s$ is considered ($y^0_{H_2O} = 4.30 \times 10^{-8} \approx 0$), the model cannot predict the correct theoretical behaviour of the reaction. Further studies must be done to understand how water affects this particular model.

We then tried to introduce some modifications, deriving what we will call *LCCP modification*.

Table 5.16: Mechanism proposed in the LCCP modification for Koschany et al. model.

LCCP Mechanism
1) $CO_2 + l \rightleftharpoons CO_2^*$
2) $H_2 + 2\, l \rightleftharpoons 2\, H^*$
3) $CO_2^* + H^* \rightleftharpoons CO^* + OH^*$
4) $CO^* + H^* \rightleftharpoons CHO^* + l$
5) $CHO^* + H^* \rightleftharpoons CH^* + OH^*$
6) $CH^* + 3\, H^* \rightleftharpoons CH_4^* + 3\, l$
7) $CH_4^* \rightleftharpoons CH_4 + l$
8) $OH^* + H^* \rightleftharpoons H_2O^* + l$
9) $H_2O^* \rightleftharpoons H_2O + l$

Modifications introduced are the H-assisted dissociation of CO_2 and the presence of H^* in step 5, which leads to the formation of OH^* rather than molecular O^*. These modifications were suggested based on previous knowledge inside the LCCP research group, which were proposed also in literature [11], [45]. When deriving a rate expression from this mechanism, a reaction rate identical to the one identified in Eq. 5.3.2 is obtained, with all the problems related to water presence. The complete derivation of this model is reported in App. C.2.

Despite some ambiguities concerning the Koschany model, this model constitutes a valid option for systems whose aim is describing the solo CO_2 methanation through the direct

path of Sabatier reaction. However, despite no consensus has been reached on reaction mechanisms, many academics agree in believing the indirect path of RWGS followed by methanation of CO to be predominant for methane formation.
For this reason, many studies are now focusing on the kinetics of carbon monoxide formation: Koschany et al. did not analyze this option, and did not include CO formation in their study, justifying this choice by saying that in their experiments CO concentration was always below 1000 ppm.

Table 5.17: Summary of results for different models for CO_2 solo methanation.

Model	Rate expression	k_0	$Ea\left[\frac{kJ}{mol}\right]$	MPE	R^2
Lunde-Kester	$r_{CH_4} = k\Big(P_{CO_2}P_{H_2}^4 - \frac{P_{CH_4}P_{H_2O}^2}{K_{eq}}\Big)^n$	$6.31 \times 10^5 \pm 7.4 \times 10^3 \left[\frac{mol}{s \cdot g_{cat} \cdot atm^{5n}}\right]$	88.55 ± 0.05	10.7%	0.985
Koschany et al.	$r_{CH_4} = \frac{kP_{H_2}^{0.5}P_{CO_2}^{0.5}\Big(1 - \frac{P_{CH_4}P_{H_2O}^2}{P_{CO_2}P_{H_2}^4 K_{eq}}\Big)}{\Big(1 + K_{OH}\frac{P_{H_2O}}{P_{H_2}^{0.5}} + K_{H_2}P_{H_2}^{0.5} + K_{mix}P_{CO_2}^{0.5}\Big)^2}$	$7.07 \times 10^6 \pm 2.91 \times 10^6 \left[\frac{mol}{s \cdot g_{cat} \cdot atm}\right]$	92.79 ± 1.38	3.27%	0.998
Modified Koschany et al.	$r_{CH_4,mod} = \frac{k\frac{P_{CO_2}P_{H_2}^{1.5}}{P_{H_2O}}\Big(1 - \frac{P_{CH_4}P_{H_2O}^2}{P_{CO_2}P_{H_2}^4 K_{eq}}\Big)}{\Big(1 + K_{OH}\frac{P_{H_2O}}{P_{H_2}^{0.5}} + K_{H_2}P_{H_2}^{0.5} + K_{mix}\frac{P_{CO_2}P_{H_2}}{P_{H_2O}}\Big)^2}$	$6.44 \times 10^5 \pm 3.16 \times 10^5 \left[\frac{mol}{s \cdot g_{cat} \cdot atm^{1.5}}\right]$	89.83 ± 1.75	5.64%	0.995

Chapter 6

Comprehensive Methanation Models

In this chapter, we will focus on models that hypothesize CO formation in their scheme, and are therefore able to describe its formation: in particular, we are interested on selectivity to CO in different operating conditions (i.e. temperature, GHSV, H_2/CO_2 and inert effect). Being σ_{CO} much lower than CO_2 conversion in the same operating condition, we decided to introduce a modification in our Fortran® code, multiplying CO selectivity per 50. In this way, CO_2 conversion and CO selectivity have almost the same weight in the regression, and adaptive parameters must fit both experimental χ_{CO_2} and σ_{CO}.
If this modification is not introduced, χ_{CO_2} has a much higher weight in the regression, therefore adaptive parameters are calculated trying to "fit more" experimental carbon dioxide conversion, almost neglecting selectivity to CO.

When analyzing these kind of models, these correlations to calculate equilibrium constants were adopted:

$$K_{eq,CO_2meth}(T) = exp\Big[\Big(\frac{1}{1.987}\Big)\Big(\frac{56000}{T^2} + \frac{34633}{T} - 16.4\ln T + 0.00557\cdot T\Big) + 33.165\Big] \quad (6.0.1)$$

$$K_{eq,RWGS}(T) = \frac{1}{10^{-2.4198+3.855\times10^{-4}\cdot T+2180.9\cdot T^{-1}}} \quad (6.0.2)$$

$$K_{eq,CO_{meth}}(T) = 10^{4.1002\times10^{-5}\cdot T^2-0.08025\cdot T+39.6039} \quad (6.0.3)$$

Eq. 6.0.1 was proposed by Lunde-Kester [83] while both Eq. 6.0.2 and Eq. 6.0.3 by Farsi et al. in their work [86].

In this chapter, we will focus on different models that tried to describe the path and conditions of CO formation; in particular, we will analyze the:

- Champon et al. model; (Sec. 3.4.2)
- Farsi et al. model; (Sec. 3.2.5)
- Hernandez Lalinde et al. model; (Sec. 3.4.4)

6.1 Champon et al. Model

The Champon et al. model [93] is a mechanistic comprehensive triangular model, strongly resembling the one proposed by Xu and Froment in 1989 [92].
By proposing a triangular scheme, Champon et al. wanted to describe both the direct path of CO_2 methanation via Sabatier reaction and the indirect path via RWGS followed by CO methanation.

Their work was developed based on experiments conducted on a Ni/Al_2O_3 catalyst: at first, a reactor operating in differential mode was exploited to identify literature models that could properly fit the experimental dataset, then an integral reactor was studied, so that further modifications could be introduced, to obtain the best possible fitting.

Champon et al. proceeded by selecting the most promising literature models for the description of each of the three reactions present in the system. Therefore, kinetic rate expressions by Xu-Froment [92] and Weatherbee-Bartholomew [87] were analyzed as a possibility to describe Sabatier reaction rate. Both this expressions were rejected by Champon et al., due to their inefficiency in fitting the experimental dataset.
Regarding the description of the Sabatier reaction rate, an usual procedure was adopted: the direct water-gas shift reaction rate proposed by Wheeler et al. [103] was adapted for CO_2 methanation, when working with the differential reactor.

$$r_{CO_{2_{meth,adapted}}} = \frac{k_{CO_{2_{meth}}} K_{H_2} K_{CO_2} P_{H_2} P_{CO_2}}{(1 + K_{CO_2} P_{CO_2} + K_{H_2} P_{H_2})^2} \tag{6.1.1}$$

The authors also decided to include a water inhibition term and to unilaterally add the equilibrium driving force term (Eq. 6.1.2), knowing it should be present if one wants to predict behaviours in near-equilibrium conditions.

A clear mechanism that can describe the phenomenology of the system is not reported by Champon et al., but in their modification of the original Wheeler model, the reaction $CO_2^* + H_2^* \rightarrow CO^* + H_2O^*$ was chosen as RDS for the CO_2 methanation reaction. The final

rate of reaction proposed by Champon et al. for direct CO_2 methanation is:

$$r_{CO_{2_{meth}}} = \frac{k_{CO_{2_{meth}}} K_{H_2} K_{CO_2} P_{H_2} P_{CO_2} \left(1 - \frac{P_{CH_4} P_{H_2O}^2}{P_{H_2}^4 P_{CO_2} K_{eq,CO_{2_{meth}}}}\right)}{(1 + K_{CO_2} P_{CO_2} + K_{H_2} P_{H_2} + K_{H_2O} P_{H_2O} + K_{CO} P_{CO})^2} \tag{6.1.2}$$

For the reverse water-gas shift reaction, Champon et al. decided to adapt a kinetic expression proposed by Spencer et al. [104] in their study on activation energies of both WGS and RWGS. Therefore, the RDS of this reaction was considered CO_2 dissociative adsorption ($CO_2 + l \rightarrow CO + O^*$) and the following relation was tested in differential conditions:

$$r_{RWGS_{diff}} = \frac{k_{RWGS} K_{CO_2} P_{CO_2}}{(1 + K_{H_2} P_{H_2} + K_{CO_2} P_{CO_2})} \tag{6.1.3}$$

Again, when the reactor was operated in integral mode, the equilibrium term was unilaterally added. Moreover, Champon et al. hypothesized a significant competition for the adsorption of all species present in the set of reactions, except for methane, and the following relation was obtained:

$$r_{RWGS} = \frac{k_{RWGS} K_{CO_2} P_{CO_2} \left(1 - \frac{P_{CO} P_{H_2O}}{P_{H_2} P_{CO_2} K_{eq,RWGS}}\right)}{(1 + K_{CO_2} P_{CO_2} + K_{H_2} P_{H_2} + K_{H_2O} P_{H_2O} + K_{CO} P_{CO})} \tag{6.1.4}$$

For carbon monoxide methanation, Champon et al. decided to adopt the correlation proposed for CO_2 methanation and study it in the case of a low conversion CO methanation reaction, with a feed of H_2/CO, further modifying it so that it can describe equilibrium conditions. The following relation was obtained:

$$r_{CO_{meth}} = \frac{k_{CO_{meth}} K_{H_2} K_{CO} P_{H_2} P_{CO} \left(1 - \frac{P_{CH_4} P_{H_2O}}{P_{H_2}^3 P_{CO} K_{eq,CO_{meth}}}\right)}{(1 + K_{CO_2} P_{CO_2} + K_{H_2} P_{H_2} + K_{H_2O} P_{H_2O} + K_{CO} P_{CO})^2} \tag{6.1.5}$$

Despite the many modifications proposed and introduced, this is the only triangular model proposed in literature for CO_2 methanation up to now, together with the Xu-Froment one [92]. Being the latter widely studied and discussed, we decided to focus on the new Champon et al. model, for its innovation potentialities. Moreover, the Xu-Froment model was focused on steam-reforming reaction, while the main target of Champon et al. was describing CO_2 methanation on a Ni/Al_2O_3 catalyst.

Many more modifications need to be introduced for this peculiar model, being very complex for a regression calculus. Indeed, adaptive parameters to be calculated are 14: k^*_{0,CO_2meth}, Ea_{CO_2meth}, $k^*_{0,RWGS}$, Ea_{RWGS}, $k^*_{0,COmeth}$, Ea_{COmeth}, K^*_{0,CO_2}, ΔH_{CO_2}, K^*_{0,H_2}, ΔH_{H_2}, K^*_{0,H_2O}, ΔH_{H_2O}, $K^*_{0,CO}$, ΔH_{CO}.

We never succeeded in calculating all the adaptive parameters. Investigating the causes, we discovered the problem was given by the two adaptive parameters of water adsorption ($K^*_{0,H_2O}, \Delta H_{H_2O}$). To try and solve this issue, we chose to isolate these two parameters, fixing all the other adaptive parameters linked to adsorption species. Still, the regression could not come to an end, as shown by the correlation matrix in Table 6.1. In our experience, we have learned that when a parameter is not correlated at all with the others, it is not included in the regression calculus.

Table 6.1: Correlation matrix of the Champon et al. model with fixed adsorption parameters, except water.

	$k^*_{0,CO_2\,meth}$	$Ea_{CO_2\,meth}$	$k^*_{0,RWGS}$	Ea_{RWGS}	$k^*_{0,CO\,meth}$	$Ea_{CO\,meth}$	K^*_{0,H_2O}	ΔH_{H_2O}
$k^*_{0,CO_2\,meth}$	1.00E+00	5.77E-02	3.61E-01	-2.92E-02	-7.61E-02	-5.54E-02	0.00E+00	0.00E+00
$Ea_{CO_2\,meth}$	5.77E-02	1.00E+00	-3.03E-02	3.88E-01	-4.72E-02	-8.33E-02	0.00E+00	0.00E+00
$k^*_{0,RWGS}$	3.61E-01	-3.03E-02	1.00E+00	3.69E-01	7.53E-01	3.71E-01	0.00E+00	0.00E+00
Ea_{RWGS}	-2.92E-02	3.88E-01	3.69E-01	1.00E+00	3.28E-01	7.86E-01	0.00E+00	0.00E+00
$k^*_{0,CO\,meth}$	-7.61E-02	-4.72E-02	7.53E-01	3.28E-01	1.00E+00	2.85E-01	0.00E+00	0.00E+00
$Ea_{CO\,meth}$	-5.54E-02	-8.33E-02	3.71E-01	7.86E-01	2.85E-01	1.00E+00	0.00E+00	0.00E+00
K^*_{0,H_2O}	0.00E+00	0.00E+00	0.00E+00	0.00E+00	0.00E+00	0.00E+00	0.00E+00	1.00E+30
ΔH_{H_2O}	0.00E+00	0.00E+00	0.00E+00	0.00E+00	0.00E+00	0.00E+00	1.00E+30	0.00E+00

To further try to solve this matter, we decided to fix the two parameters related to water adsorption and see if the code could converge to a final result and how good the possible fitting was.

6.1.1 Champon et al. Model with fixed water adsorption parameters

In this model, we decided to introduce this modification so that K^*_{0,H_2O} and ΔH_{H_2O} were left outside the regression calculus: in this way we wanted to prove if the code could converge to reasonable values. Through Eq. 5.1.16, we calculated K^*_{0,H_2O} from the value of K_{0,H_2O} reported by Champon et al.; therefore, these values were fixed: $K^*_{0,H_2O} = 2.495$, $\Delta H_{H_2O} = -14.5\, kJ/mol$. In this case the adaptive parameters to be calculated are still 12, namely $k^*_{0,CO_{2_{meth}}}$, $Ea_{CO_{2_{meth}}}$, $k^*_{0,RWGS}$, Ea_{RWGS}, $k^*_{0,CO_{meth}}$, $Ea_{CO_{meth}}$, K^*_{0,CO_2}, ΔH_{CO_2}, K^*_{0,H_2}, ΔH_{H_2}, $K^*_{0,CO}$, ΔH_{CO}.

Table 6.2: Estimated parameters of the Champon et al. model. with fixed water adsorption parameters.

Parameter	Value	U.o.M
$k^*_{0,CO_{2_{meth}}}$	$6.67 \pm 4.54 \times 10^{-3}$	–
$Ea_{CO_{2_{meth}}}$	107.09 ± 0.18	kJ/mol
$k^*_{0,RWGS}$	$1.51 \pm 7.39 \times 10^{-3}$	–
Ea_{RWGS}	88.86 ± 0.46	kJ/mol
$k^*_{0,CO_{meth}}$	$-1.64 \pm 2.06 \times 10^{-2}$	–
$Ea_{CO_{meth}}$	-86.77 ± 1.09	kJ/mol
K^*_{0,CO_2}	$4.05 \pm 1.35 \times 10^{-2}$	–
ΔH_{CO_2}	-20.67 ± 0.33	kJ/mol
K^*_{0,H_2}	$3.04 \pm 1.01 \times 10^{-2}$	–
ΔH_{H_2}	-7.90 ± 0.53	kJ/mol
$K^*_{0,CO}$	$9.86 \pm 1.21 \times 10^{-2}$	–
ΔH^*_{CO}	0.22 ± 0.10	kJ/mol

As clearly proven by the MPE values, this model works pretty well in fitting and predicting trends for carbon dioxide conversion, while it fails when trying to fit selectivity to CO. This behaviour is clearly shown in the parity plots and when plotting trends in different operating conditions (Fig. 6.1, 6.2, 6.3). This nature of the model can not be ascribed to an high correlation between parameters, as witnessed by its correlation matrix (Fig. 6.5).

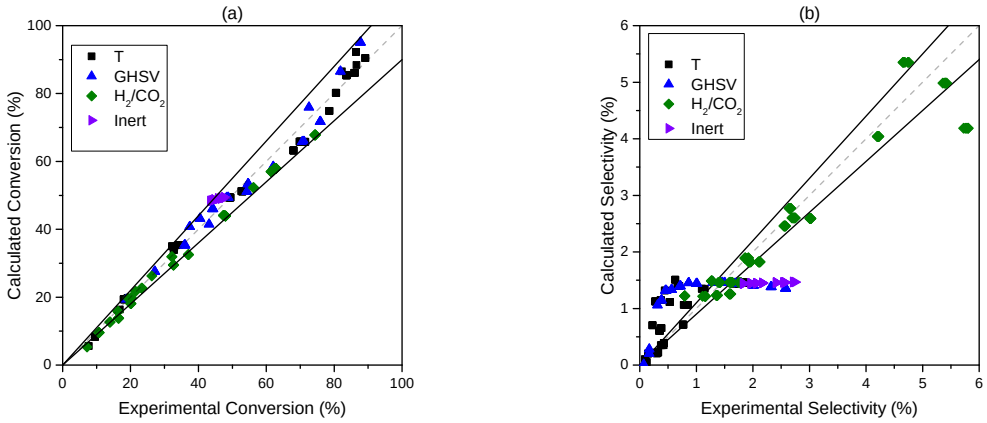

Figure 6.1: Parity plots of the Champon et al. model, with fixed water adsorption parameters. (a) CO_2 conversion. (b) CO selectivity.

Table 6.3: Quality of the regression of the Champon et al. model with fixed water adsorption parameters.

Parameter	Value
$MPE_{\chi CO_2}$	5.91%
$R^2_{\chi CO_2}$	0.993
$MPE_{\sigma_{CO}}$	52.6%
$R^2_{\sigma_{CO}}$	0.901

For sake of completeness, we report the calculated kinetic parameters, confronted with the values reported by Champon et al.: we can observe some deep differences, the most evident of which is the value of $k_{0,CO_{meth}}$. Indeed, in our calculation the value of this parameter clearly suggests a possible omission of the CO methanation reaction, being its pre-exponential factor so little if compared to those of the other two reactions and its activation energy negative, a physical non-sense.

As shown by graphs related to CO selectivity, the model does not fit at all any of the experimental data, in any operating condition, while still performs very well in predicting CO_2 conversion trends, even if some problems can be detected at high conversions, where the model runs into the

Table 6.4: Kinetic parameters of the Champon et al. model with fixed water adsorption parameters and comparison with Champon et al. results. [93]

Parameter	Value	Champon et al.	U.o.M
$k_{0,CO_{2_{meth}}}$	$6.78 \times 10^6 \pm 2.96 \times 10^5$	1.90×10^6	$mol/(s \cdot g_{cat})$
$Ea_{CO_{2_{meth}}}$	107.09 ± 0.18	110	kJ/mol
$k_{0,RWGS}$	$7.93 \times 10^2 \pm 8.33 \times 10^1$	2.97×10^4	$mol/(s \cdot g_{cat})$
Ea_{RWGS}	88.86 ± 0.46	97.1	kJ/mol
$k_{0,CO_{meth}}$	$1.69 \times 10^{-15} \pm 4.30 \times 10^{-16}$	3.72×10^4	$mol/(s \cdot g_{cat})$
$Ea_{CO_{meth}}$	-86.77 ± 1.09	97.3	kJ/mol
K_{0,CO_2}	$6.93 \times 10^{-1} \pm 5.75 \times 10^{-2}$	1.07	atm^{-1}
ΔH_{CO_2}	-20.67 ± 0.33	-9.72	kJ/mol
K_{0,H_2}	$3.88 \pm 4.82 \times 10^{-1}$	5.20×10^{-5}	atm^{-1}
ΔH_{H_2}	-7.90 ± 0.53	-52.0	kJ/mol
$K_{0,CO}$	$2.02 \times 10^4 \pm 6.86 \times 10^2$	2.39×10^{-3}	atm^{-1}
ΔH_{CO}	0.22 ± 0.10	-40.6	kJ/mol
K_{0,H_2O}	6.09×10^{-1}	6.09×10^{-1}	atm^{-1}
ΔH_{H_2O}	-14.5	-14.5	kJ/mol

equilibrium curve. This issue is evident for high temperatures or low GHSV values (Fig. 6.2).
As previously explained, a very low pre-exponential factor for CO methanation reaction can be observed, but, before proceeding in removing CO methanation reaction from the scheme, leaning towards a model similar to the Hernandez Lalinde et al. [95] one, who described a system where CO_2 methanation took place in parallel with RWGS, we decided to fix all the adsorption parameters with values equal to the ones proposed by Champon et al..
Adopting this procedure, we can investigate only *kinetic* adaptive parameters, leaving those relative to adsorption constants out of the calculus, and see if an improvement of the model takes place.

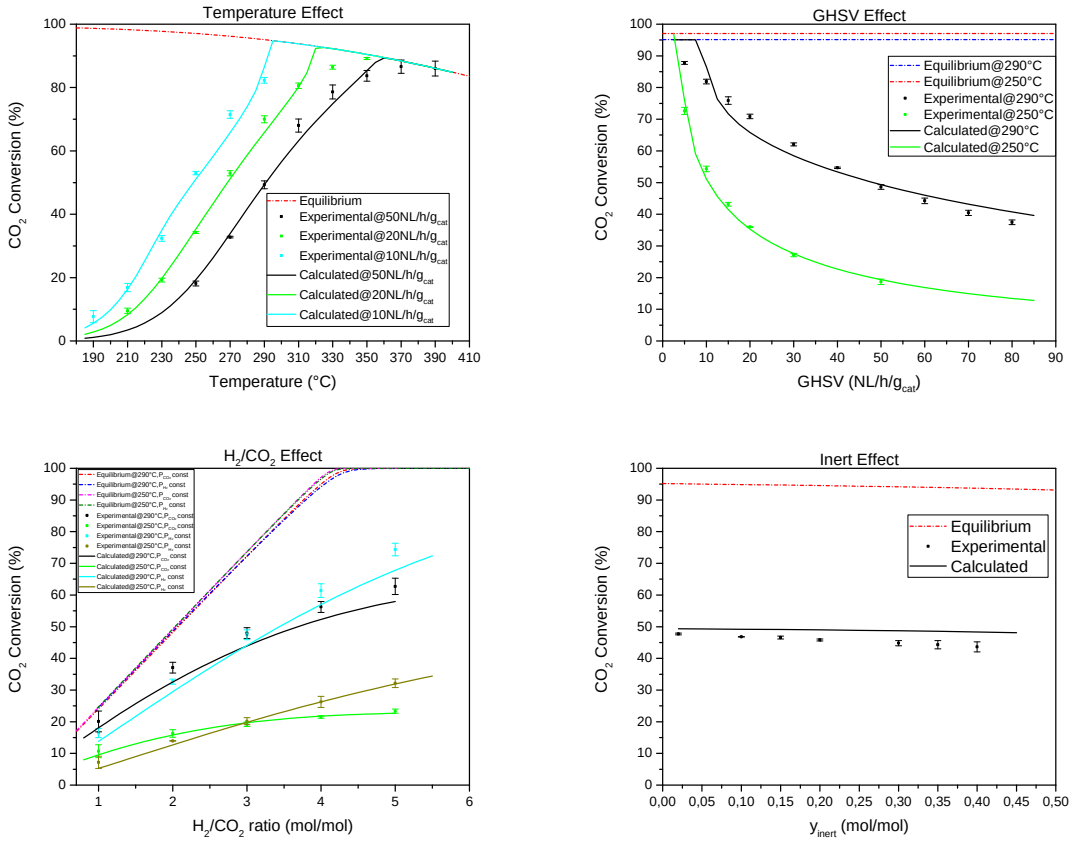

Figure 6.2: CO_2 conversion simulation plots of the Champon et al. model, with fixed water adsorption parameters.

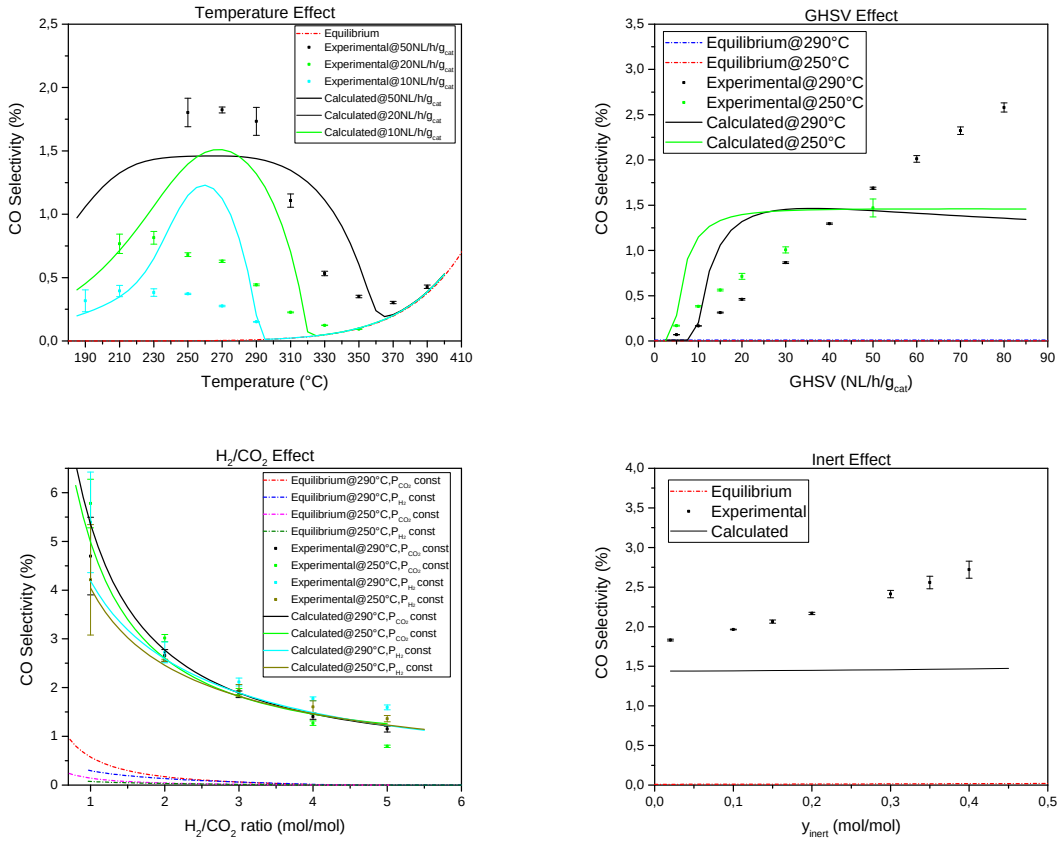

Figure 6.3: CO selectivity simulation plots of the Champon et al. model, with fixed water adsorption parameters.

Table 6.5: Correlation matrix of the Champon et al. model, with fixed water adsorption parameters.

	$k^*_{0,CO_2{}_{meth}}$	$Ea_{CO_2{}_{meth}}$	$k^*_{0,RWGS}$	Ea_{RWGS}	$k^*_{0,CO_{meth}}$	$Ea_{CO_{meth}}$	K^*_{0,CO_2}	ΔH_{CO_2}	K^*_{0,H_2}	ΔH_{H_2}	$K^*_{0,CO}$	ΔH_{CO}
$k^*_{0,CO_2{}_{meth}}$	1.00E+00	8.24E-01	8.39E-01	3.30E-01	3.43E-01	2.82E-01	-5.07E-01	-2.90E-01	-1.36E-01	5.99E-02	-5.20E-02	4.12E-02
$Ea_{CO_2{}_{meth}}$	8.24E-01	1.00E+00	6.51E-01	2.82E-01	4.52E-02	-1.35E-02	-3.29E-01	-3.54E-01	-3.54E-02	-1.53E-01	4.10E-02	-1.09E-01
$k^*_{0,RWGS}$	8.38E-01	6.51E-01	1.00E+00	5.46E-01	2.04E-01	1.55E-01	-7.17E-01	-4.67E-01	-1.39E-01	3.12E-01	-2.84E-01	-1.38E-03
Ea_{RWGS}	3.30E-01	2.82E-01	5.46E-01	1.00E+00	1.35E-03	-1.86E-01	-5.19E-01	-7.71E-01	-1.88E-01	8.55E-01	-3.51E-01	1.58E-01
$k^*_{0,CO_{meth}}$	3.43E-01	4.52E-02	2.04E-01	1.35E-03	1.00E+00	9.35E-01	-1.10E-01	2.21E-01	-1.10E-01	1.17E-01	4.39E-02	1.24E-01
$Ea_{CO_{meth}}$	2.82E-01	-1.35E-02	1.55E-01	-1.86E-01	9.35E-01	1.00E+00	-9.01E-02	4.25E-01	-1.23E-01	-9.88E-02	2.42E-02	-2.39E-02
K^*_{0,CO_2}	-5.07E-01	-3.29E-01	-7.17E-01	-5.19E-01	-1.10E-01	-9.01E-02	1.00E+00	3.83E-01	7.33E-01	-3.73E-01	8.51E-01	-7.24E-02
ΔH_{CO_2}	-2.90E-01	-3.54E-01	-4.67E-01	-7.71E-01	2.21E-01	4.25E-01	3.83E-01	1.00E+00	-3.75E-02	-6.28E-01	1.49E-01	-4.58E-02
K^*_{0,H_2}	-1.36E-01	-3.54E-02	-1.39E-01	-1.88E-01	-1.10E-01	-1.23E-01	7.33E-01	-3.75E-02	1.00E+00	-1.25E-01	9.10E-01	-1.24E-01
ΔH_{H_2}	5.99E-02	-1.53E-01	3.12E-01	8.55E-01	1.17E-01	-9.88E-02	-3.73E-01	-6.28E-01	-1.25E-01	1.00E+00	-2.99E-01	4.26E-01
$K^*_{0,CO}$	-5.20E-02	4.10E-02	-2.84E-01	-3.51E-01	4.39E-02	2.42E-02	8.51E-01	1.49E-01	9.10E-01	-2.99E-01	1.00E+00	-8.17E-02
ΔH_{CO}	4.12E-02	-1.09E-01	-1.38E-03	1.58E-01	1.24E-01	-2.39E-02	-7.24E-02	-4.58E-02	-1.24E-01	4.26E-01	-8.17E-02	1.00E+00

6.1.2 Champon et al. Model with fixed adsorption parameters

In order to focus only on adaptive parameters related to kinetic constants, as previously explained said in Sec. 6.1.1, we decided to fix all adsorption parameters, calculating $K^*_{0,i}$ through Eq.5.1.16 from the values proposed by Champon et al. in their paper. Therefore, these values were fixed:
$K^*_{0,CO_2} = 2.072$, $\Delta H_{CO_2} = -9.72\,kJ/mol$, $K^*_{0,H_2} = 0.861$, $\Delta H_{H_2} = -52\,kJ/mol$,
$K^*_{0,H_2O} = 2.495$, $\Delta H_{H_2O} = -14.5\,kJ/mol$, $K^*_{0,CO} = 2.337$, $\Delta H_{CO} = -40.6\,kJ/mol$.
Adaptive parameters to be calculated are only those related to kinetic constants:
k^*_{0,CO_2meth}, Ea_{CO_2meth}, $k^*_{0,RWGS}$, Ea_{RWGS}, $k^*_{0,COmeth}$, Ea_{COmeth}.

Table 6.6: Estimated parameteres of the Champon et al. model. with fixed adsorption parameters.

Parameter	Value	U.o.M
$k^*_{0,CO_{2_{meth}}}$	$6.07 \pm 4.30 \times 10^{-4}$	–
$Ea_{CO_{2_{meth}}}$	$85.55 \pm 4.61 \times 10^{-2}$	kJ/mol
$k^*_{0,RWGS}$	$1.46 \pm 3.04 \times 10^{-3}$	–
Ea_{RWGS}	47.53 ± 0.27	kJ/mol
$k^*_{0,CO_{meth}}$	$5.45 \pm 1.41 \times 10^{-2}$	–
$Ea_{CO_{meth}}$	-25.55 ± 0.70	kJ/mol

Table 6.7: Correlation matrix of the Champon et al. model with fixed adsorption parameters.

	$k^*_{0,CO_{2_{meth}}}$	$Ea_{CO_{2_{meth}}}$	$k^*_{0,RWGS}$	Ea_{RWGS}	$k^*_{0,CO_{meth}}$	$Ea_{CO_{meth}}$
$k^*_{0,CO_{2_{meth}}}$	1.00E+00	4.33E-01	2.49E-03	9.64E-02	-1.96E-01	-1.30E-01
$Ea_{CO_{2_{meth}}}$	4.33E-01	1.00E+00	8.52E-02	2.07E-02	2.31E-02	-9.81E-02
$k^*_{0,RWGS}$	2.49E-03	8.52E-02	1.00E+00	3.02E-01	8.15E-01	6.20E-01
Ea_{RWGS}	9.64E-02	2.07E-02	3.02E-01	1.00E+00	5.27E-02	6.09E-01
$k^*_{0,CO_{meth}}$	-1.96E-01	2.31E-02	8.15E-01	5.27E-02	1.00E+00	7.18E-01
$Ea_{CO_{meth}}$	-1.30E-01	-9.81E-02	6.20E-01	6.09E-01	7.18E-01	1.00E+00

The regression leads a great improvement of the fitting, with a significant reduction of $MPE_{\sigma_{CO}}$, at the expenses of $MPE_{\chi_{CO_2}}$, which has an important increase.
The MPE of selectivity to carbon monoxide is still very high, but trends are simulated in the right

Table 6.8: Quality of the regression of the Champon et al. model with fixed adsorption parameters.

Parameter	Value
$MPE_{\chi_{CO_2}}$	14.1%
$R^2_{\chi_{CO_2}}$	0.976
$MPE_{\sigma_{CO}}$	26.1%
$R^2_{\sigma_{CO}}$	0.972

"form". The model clearly needs further improvements to fit the selectivity to CO better.
Again, activation energy of CO methanation has a negative value, suggesting the extreme velocity of that reaction: once CO is formed, it is immediately consumed by its methanation reaction.

Table 6.9: Kinetic parameters of the Champon et al. model with fixed adsorption parameters and comparison with Champon et al. results. [93]

Parameter	Value	Champon et a.	U.o.M
$k_{0,CO_{2_{meth}}}$	$3.74 \times 10^4 \pm 3.84 \times 10^2$	1.90×10^6	$mol/(s \cdot g_{cat})$
$Ea_{CO_{2_{meth}}}$	$85.55 \pm 4.61 \times 10^{-2}$	110	kJ/mol
$k_{0,RWGS}$	$1.10 \times 10^{-1} \pm 6.73 \times 10^{-3}$	2.97×10^4	$mol/(s \cdot g_{cat})$
Ea_{RWGS}	47.53 ± 0.27	97.1	kJ/mol
$k_{0,CO_{meth}}$	$9.97 \times 10^{-7} \pm 1.63 \times 10^{-7}$	3.72×10^4	$mol/(s \cdot g_{cat})$
$Ea_{CO_{meth}}$	-25.55 ± 0.70	97.3	kJ/mol

As a step forward in our process of adaptation of the Champon et al. model, two different modifications can be introduced: the first is the removal of the Sabatier reaction from the process; the second is the removal of CO methanation reaction from reaction scheme. When giving rise to these modifications, the scheme is no more a triangular one, but reactions are described either in series or in parallel. A study on how this affects the quality of the fitting must be done.

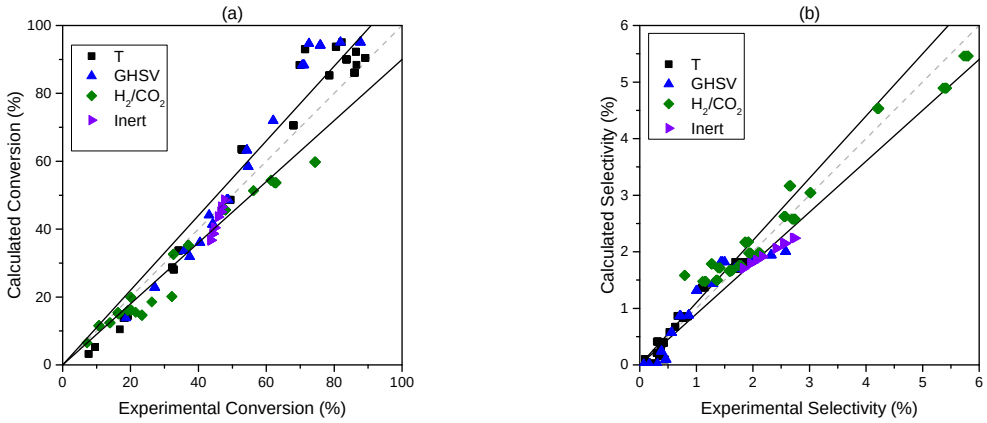

Figure 6.4: Parity plots of the Champon et al. model, with fixed adsorption parameters. (a) CO_2 conversion. (b) CO selectivity.

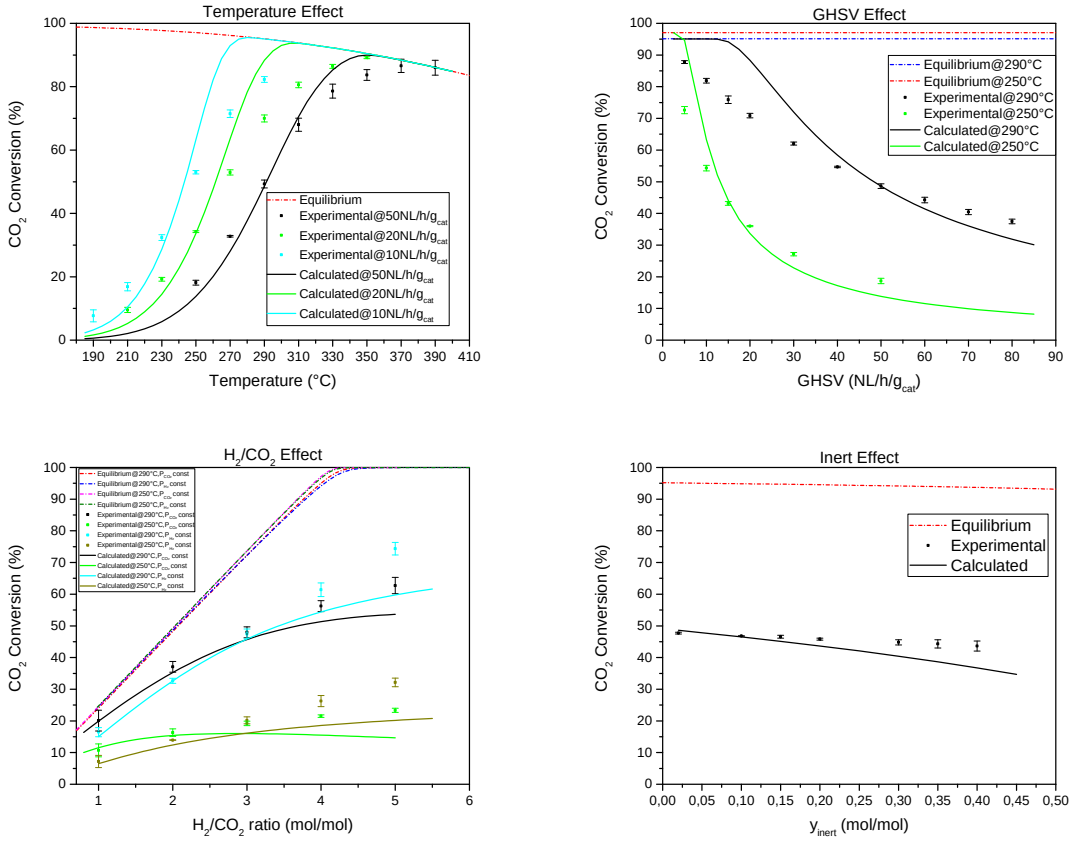

Figure 6.5: CO_2 conversion simulation plots of the Champon et al. model, with fixed adsorption parameters.

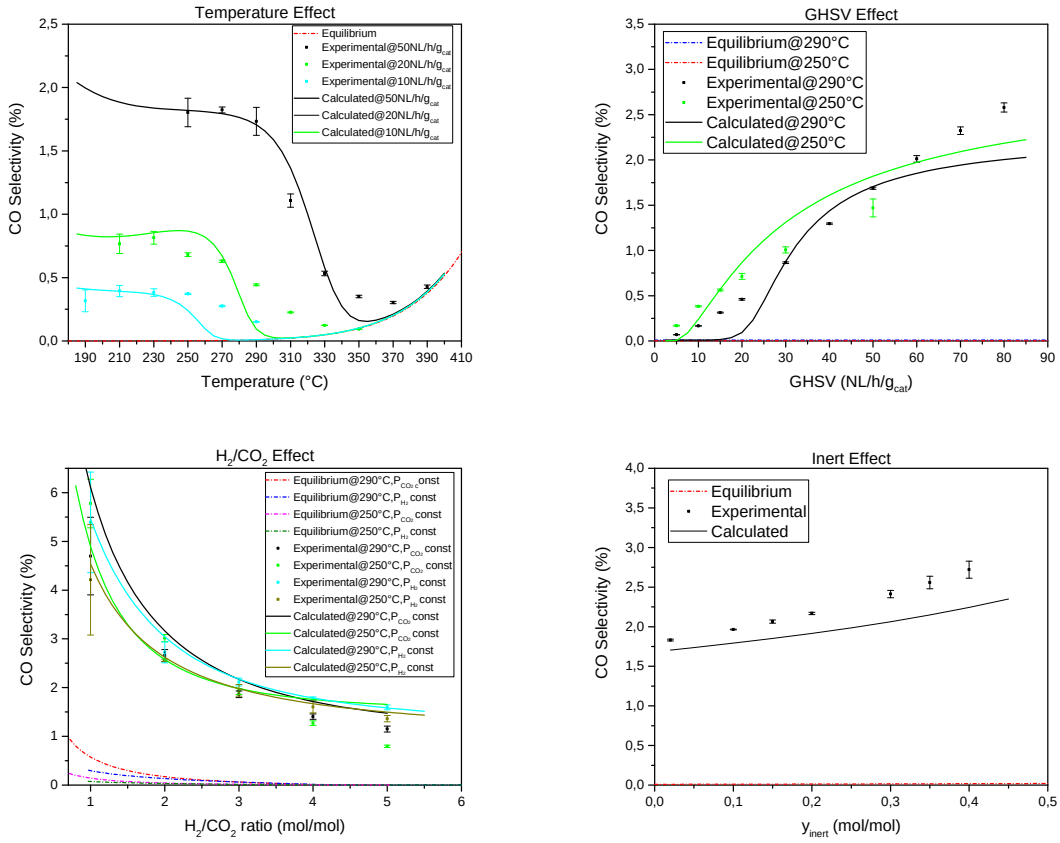

Figure 6.6: CO selectivity simulation plots of the Champon et al. model, with fixed adsorption parameters.

6.1.3 Champon et al. Model without direct CO_2 methanation

In this variation we decided to unilaterally remove Sabatier reaction from the reaction scheme, hypothesizing that carbon dioxide methanation takes place through a RWGS reaction followed by a CO methanation reaction.

So this modification of the Champon et al. model will be based on the following reaction scheme:

1. $CO_2 + H_2 \rightleftharpoons CO + H_2O \qquad \Delta H^0_{R,298K} = +41.2\,\frac{kJ}{mol}$
2. $CO + 3\,H_2 \rightleftharpoons CH_4 + H_2O \qquad \Delta H^0_{R,298K} = -206.3\,\frac{kJ}{mol}$

In this model, adaptive parameters to be calculated are: $k^*_{0,RWGS}$, Ea_{RWGS}, $k^*_{0,CO_{meth}}$, $Ea_{CO_{meth}}$, K^*_{0,CO_2}, ΔH_{CO_2}, K^*_{0,H_2}, ΔH_{H_2}, $K^*_{0,CO}$, ΔH_{CO}.

Water adsorption parameters were left outside the calculus, and were not fixed to the values calculated by Champon et al., because even by fixing them the model could not converge to a solution.

Table 6.10: Estimated parameters of the Champon et al. model. without direct CO_2 methanation and water adsorption parameters.

Parameter	Value	U.o.M
$k^*_{0,RWGS}$	$5.53 \pm 3.28 \times 10^{-3}$	–
Ea_{RWGS}	67.02 ± 0.41	kJ/mol
$k^*_{0,CO_{meth}}$	17.70 ± 0.51	–
$Ea_{CO_{meth}}$	-38.87 ± 9.68	kJ/mol
K^*_{0,CO_2}	$1.37 \pm 4.53 \times 10^{-3}$	–
ΔH_{CO_2}	32.26 ± 0.54	kJ/mol
K^*_{0,H_2}	$-0.31 \pm 8.94 \times 10^{-3}$	–
ΔH_{H_2}	5.57 ± 0.70	kJ/mol
$K^*_{0,CO}$	5.38 ± 0.51	–
ΔH^*_{CO}	38.87 ± 9.82	kJ/mol

Table 6.11: Quality of the regression of the Champon et al. model without direct CO_2 methanation and water adsorption parameters.

Parameter	Value
$MPE_{\chi_{CO_2}}$	11.1%
$R^2_{\chi_{CO_2}}$	0.981
$MPE_{\sigma_{CO}}$	23.3%
$R^2_{\sigma_{CO}}$	0.977

An additional improvement in the ability of the proposed kinetic expressions to describe the phenomenology of the system is given by the simultaneous reduction of both $MPE_{\chi_{CO_2}}$ and $MPE_{\sigma_{CO}}$. This improvement is witnessed also by the graphs, where a significant improvement of trends can be observed in the fitting of CO selectivity.

Table 6.12: Kinetic parameters of the Champon model without direct CO_2 methanation and water adsorption parameters, and comparison with Champon et al. results. [93]

Parameter	Value	Champon et al.	U.o.M
$k_{0,RWGS}$	$4.15 \times 10^2 \pm 3.78 \times 10^1$	2.97×10^4	$mol/(s \cdot g_{cat})$
Ea_{RWGS}	67.02 ± 0.41	97.1	kJ/mol
$k_{0,CO_{meth}}$	$1.21 \times 10^{-2} \pm 3.12 \times 10^{-2}$	3.72×10^4	$mol/(s \cdot g_{cat})$
$Ea_{CO_{meth}}$	-38.87 ± 9.68	97.3	kJ/mol
K_{0,CO_2}	$3.85 \times 10^3 \pm 4.93 \times 10^2$	4.64×10^2	atm^{-1}
ΔH_{CO_2}	32.26 ± 0.54	-9.72	kJ/mol
K_{0,H_2}	$2.42 \pm 3.81 \times 10^{-2}$	5.20×10^{-5}	atm^{-1}
ΔH_{H_2}	5.57 ± 0.70	-52.0	kJ/mol
$K_{0,CO}$	$1.84 \times 10^1 \pm 4.79 \times 10^1$	2.39×10^{-3}	atm^{-1}
ΔH_{CO}	38.87 ± 9.82	-40.6	kJ/mol

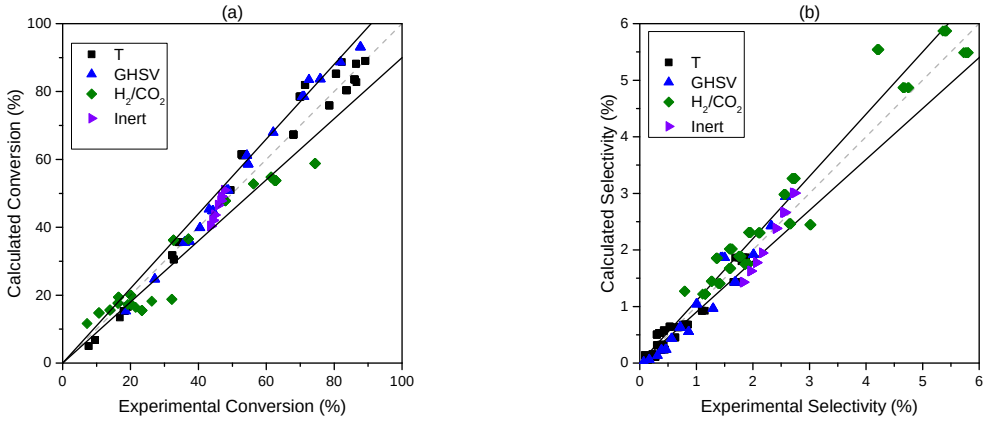

Figure 6.7: Parity plots of the Champon et al. model, without direct CO_2 methanation and water adsorption parameters. (a) CO_2 conversion. (b) CO selectivity.

In disagreement with what was suggested by the model with fixed adsorption parameters (Sec. 6.1.2), this model witnesses the relative indifference of the direct CO_2 methanation pathway through Sabatier reaction. Indeed, the direct methanation is very unlikely to take place as it is, involving the contemporary transfer of eight electrons in reducing the carbon species from carbon dioxide to methane.

In conclusion, this model performs pretty well in describing the kinetics of the system, despite a strong forcing is introduced by unilaterally removing carbon dioxide methanation reaction from the process.

To have a better understanding and a valid comparison, we decided to introduce a final modification: re-introducing carbon dioxide methanation and removing CO methanation from the mechanism. In this way, the remaining reactions, CO_2 methanation and RWGS take place in parallel, resembling what was proposed by Hernandez Lalinde et al. in their model [95].

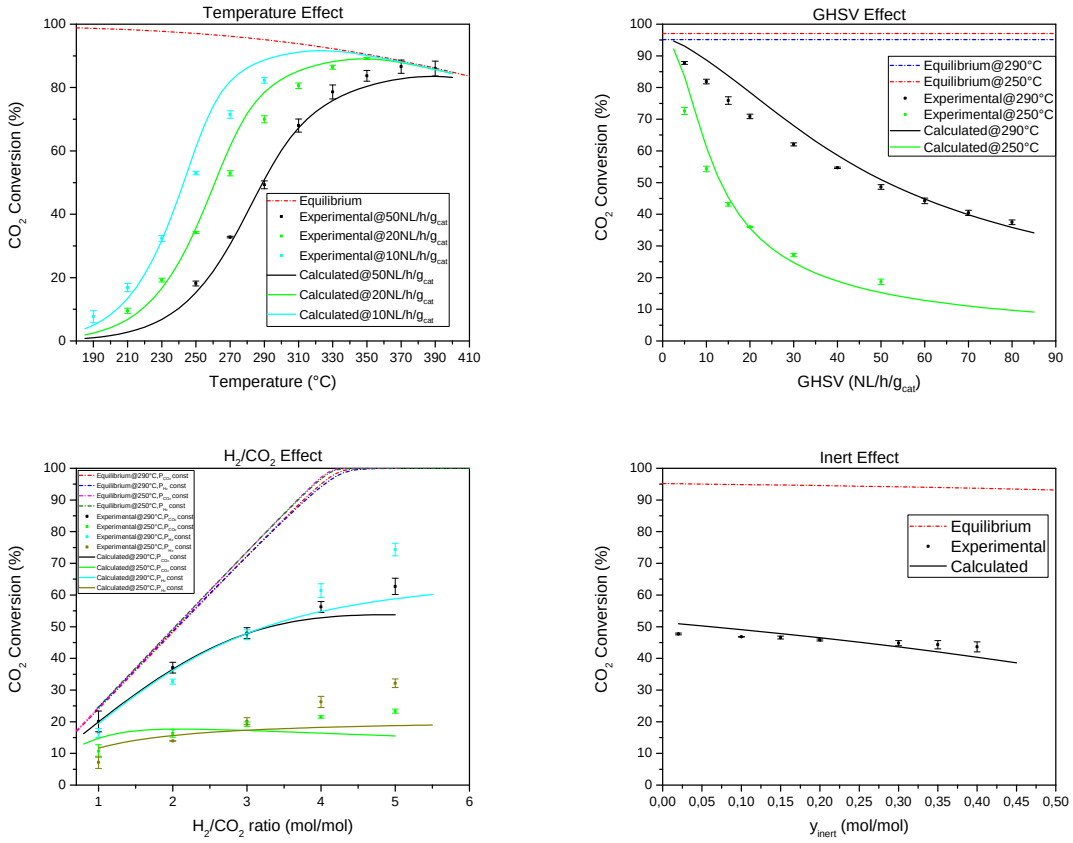

Figure 6.8: CO_2 conversion simulation plots of the Champon et al. model, without direct CO_2 methanation and water adsorption parameters.

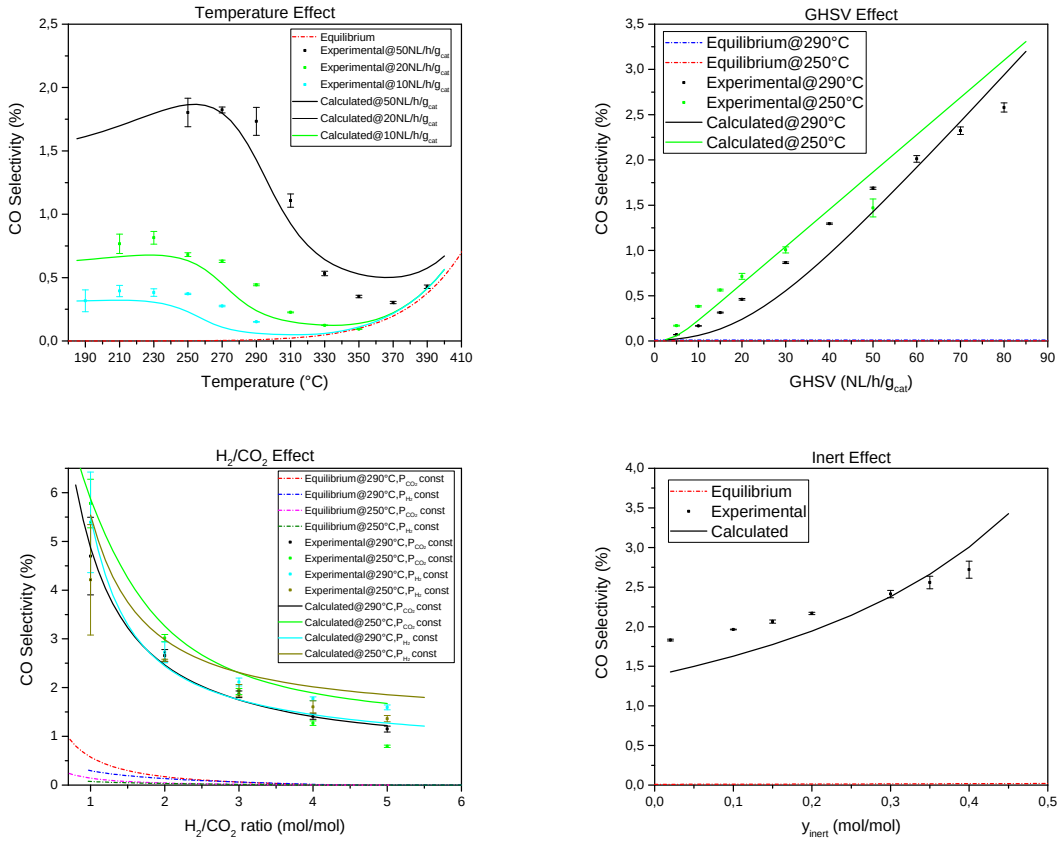

Figure 6.9: CO selectivity simulation plots of the Champon et al. model, without direct CO_2 methanation and water adsorption parameters.

Table 6.13: Correlation matrix of the Champon et al. model without direct CO_2 methanation and water adsorption parameters.

	$k^*_{0,RWGS}$	Ea_{RWGS}	$k^*_{0,CO_{meth}}$	$Ea_{CO_{meth}}$	K^*_{0,CO_2}	ΔH_{CO_2}	K^*_{0,H_2}	ΔH_{H_2}	$K^*_{0,CO}$	ΔH_{CO}
$k^*_{0,RWGS}$	1.00E+00	4.88E-01	4.59E-02	-9.76E-04	-7.44E-01	-3.92E-01	1.94E-01	1.21E-01	-5.38E-02	-2.17E-02
Ea_{RWGS}	4.88E-01	1.00E+00	1.36E-01	3.04E-01	-3.67E-01	-9.11E-01	6.16E-02	-1.40E-02	-1.40E-01	-3.32E-01
$k^*_{0,CO_{meth}}$	4.57E-02	1.37E-01	1.00E+00	-1.14E-02	-1.87E-01	-1.26E-01	-8.52E-02	1.18E-01	-1.00E+00	1.20E-03
$Ea_{CO_{meth}}$	-1.20E-03	3.03E-01	-1.44E-02	1.00E+00	1.10E-01	-2.47E-01	1.29E-01	9.37E-02	1.29E-02	-9.99E-01
K^*_{0,CO_2}	-7.44E-01	-3.67E-01	-1.87E-01	1.10E-01	1.00E+00	4.69E-01	4.65E-01	2.65E-01	1.87E-01	-1.04E-01
ΔH_{CO_2}	-3.92E-01	-9.11E-01	-1.26E-01	-2.47E-01	4.69E-01	1.00E+00	1.99E-01	3.96E-01	1.27E-01	2.59E-01
K^*_{0,H_2}	1.94E-01	6.15E-02	-8.56E-02	1.29E-01	4.65E-01	1.99E-01	1.00E+00	6.14E-01	7.50E-02	-1.52E-01
ΔH_{H_2}	1.21E-01	-1.41E-02	1.18E-01	9.39E-02	2.65E-01	3.96E-01	6.14E-01	1.00E+00	-1.24E-01	-1.31E-01
$K^*_{0,CO}$	-5.37E-02	-1.41E-01	-1.00E+00	9.84E-03	1.87E-01	1.27E-01	7.45E-02	-1.25E-01	1.00E+00	7.10E-04
ΔH_{CO}	-2.15E-02	-3.32E-01	4.19E-03	-9.99E-01	-1.05E-01	2.58E-01	-1.53E-01	-1.31E-01	-2.30E-03	1.00E+00

6.1.4 Champon et al. Model without CO methanation

As a counter-proof to the removal of the Sabatier reaction from the process, in this modification we decided to remove CO methanation, to verify that the complete model can work very well without the direct CO_2 methanation reaction, but can not operate a good fitting and predict good trends if carbon monoxide methanation is removed.
In this case, then, the system is described by two parallel reactions:

1. $CO_2 + 4\ H_2 \rightleftharpoons CH_4 + 2\ H_2O \quad \Delta H^0_{R,298K} = -165.1\ \frac{kJ}{mol}$
2. $CO_2 + H_2 \rightleftharpoons CO + H_2O \qquad \Delta H^0_{R,298K} = +41.2\ \frac{kJ}{mol}$

In full analogy with the model without Sabatier reaction, we decided to leave water adsorption parameters outside the regression calculus. So, in this case, the parameters to be calculated are:
k^*_{0,CO_2meth}, Ea_{CO_2meth}, $k^*_{0,RWGS}$, Ea_{RWGS}, K^*_{0,CO_2}, ΔH_{CO_2},
K^*_{0,H_2}, ΔH_{H_2}, K^*_{0,H_2O}, ΔH_{H_2O}, $K^*_{0,CO}$, ΔH_{CO}.

Table 6.14: Estimated parameters of the Champon et al. model. without CO methanation and water adsorption parameter.

Parameter	Value	U.o.M
$k^*_{0,CO_{2_{meth}}}$	$6.30 \pm 2.76 \times 10^{-3}$	–
$Ea_{CO_{2_{meth}}}$	93.15 ± 0.14	kJ/mol
$k^*_{0,RWGS}$	$1.31 \pm 5.16 \times 10^{-3}$	–
Ea_{RWGS}	101.39 ± 0.33	kJ/mol
K^*_{0,CO_2}	$4.21 \pm 1.86 \times 10^{-2}$	–
ΔH_{CO_2}	-12.51 ± 0.51	kJ/mol
K^*_{0,H_2}	$3.03 \pm 1.85 \times 10^{-2}$	–
ΔH_{H_2}	1.82 ± 0.34	kJ/mol
$K^*_{0,CO}$	$9.37 \pm 1.85 \times 10^{-2}$	–
ΔH^*_{CO}	-3.44 ± 0.39	kJ/mol

Table 6.15: Quality of the regression of the Champon et al. model without CO methanation and water adsorption parameters.

Parameter	Value
$MPE_{\chi CO_2}$	5.03%
$R^2_{\chi CO_2}$	0.996
$MPE_{\sigma_{CO}}$	89.4%
$R^2_{\sigma_{CO}}$	0.922

As widely expected, the model has a very considerable worsening in fitting and predicting the values of CO selectivity, proving the importance of the inclusion of carbon monoxide methanation reaction in the system. Moreover, also the trends of carbon dioxide conversion have a slight worsening, with the model that runs into equilibrium far before than where it should (Fig. 6.11, Temperature Effect).

Table 6.16: Kinetic parameters of the Champon et al. model without CO methanation and water adsorption parameters and comparison with Champon et al. results. [93]

Parameter	Value	Champon et al.	U.o.M
$k_{0,CO_{2_{meth}}}$	$2.39 \times 10^5 \pm 7.62 \times 10^3$	1.90×10^6	$mol/(s \cdot g_{cat})$
$Ea_{CO_{2_{meth}}}$	93.15 ± 0.14	110	kJ/mol
$k_{0,RWGS}$	$9.39 \times 10^3 \pm 7.02 \times 10^2$	2.97×10^4	$mol/(s \cdot g_{cat})$
Ea_{RWGS}	101.39 ± 0.33	97.1	kJ/mol
K_{0,CO_2}	$4.67 \pm 5.94 \times 10^{-1}$	1.07	atm^{-1}
ΔH_{CO_2}	-12.51 ± 0.51	-9.72	kJ/mol
K_{0,H_2}	$3.06 \times 10^1 \pm 2.78$	5.20×10^{-5}	atm^{-1}
ΔH_{H_2}	1.82 ± 0.34	-52.0	kJ/mol
$K_{0,CO}$	$5.60 \times 10^4 \pm 5.70 \times 10^2$	2.39×10^{-3}	atm^{-1}
ΔH_{CO}	-3.44 ± 0.39	-40.6	kJ/mol

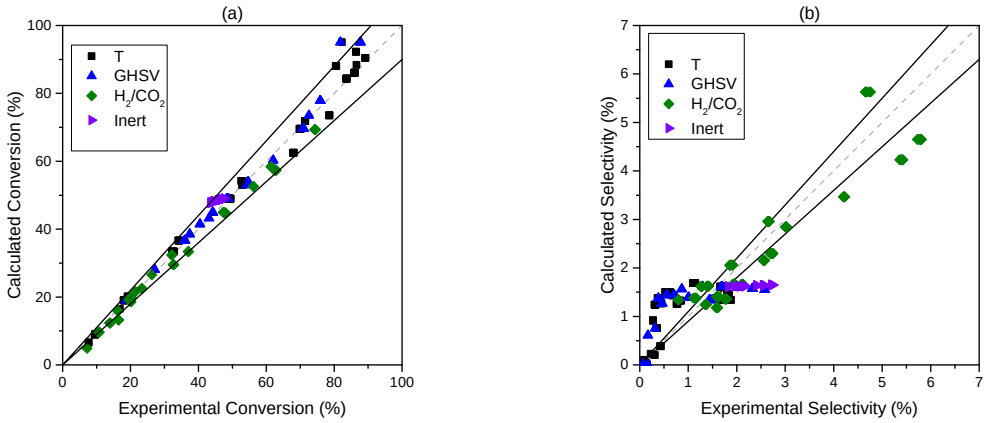

Figure 6.10: Parity plots of the Champon et al. model, without direct CO methanation and water adsorption parameters. (a) CO_2 conversion. (b) CO selectivity.

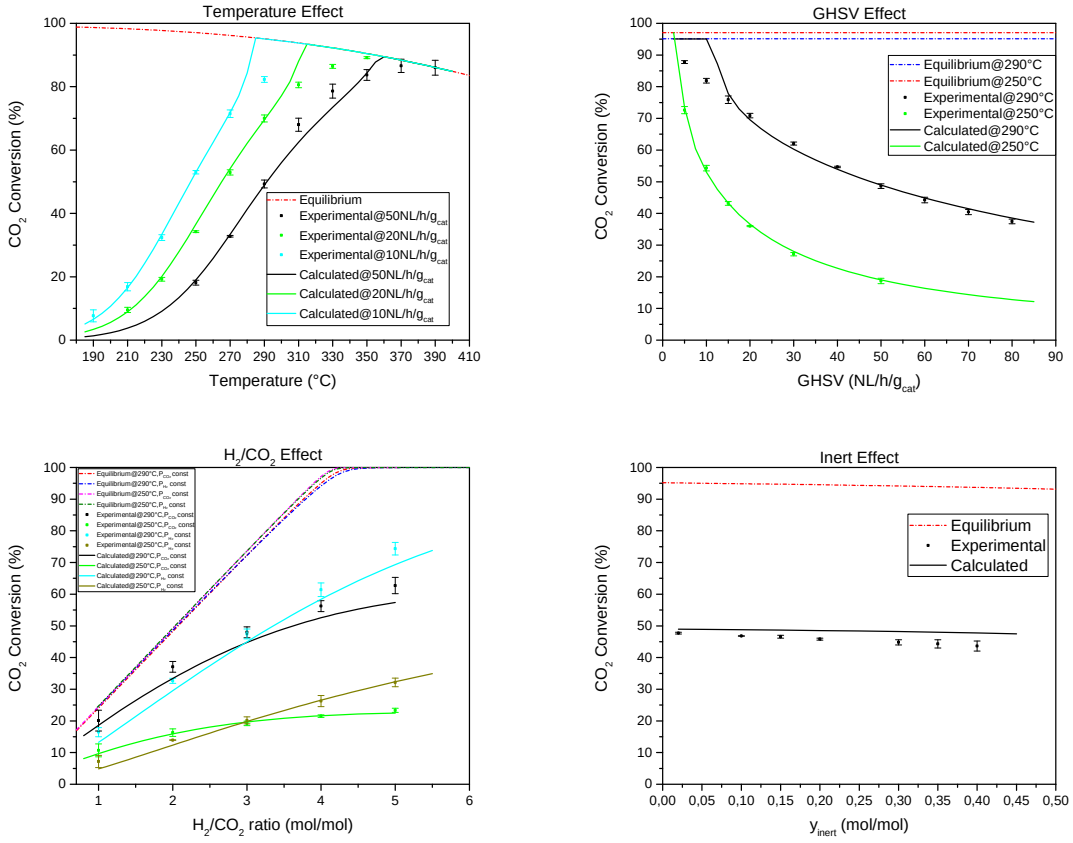

Figure 6.11: CO_2 conversion simulation plots of the Champon et al. model, without direct CO methanation and water adsorption parameters.

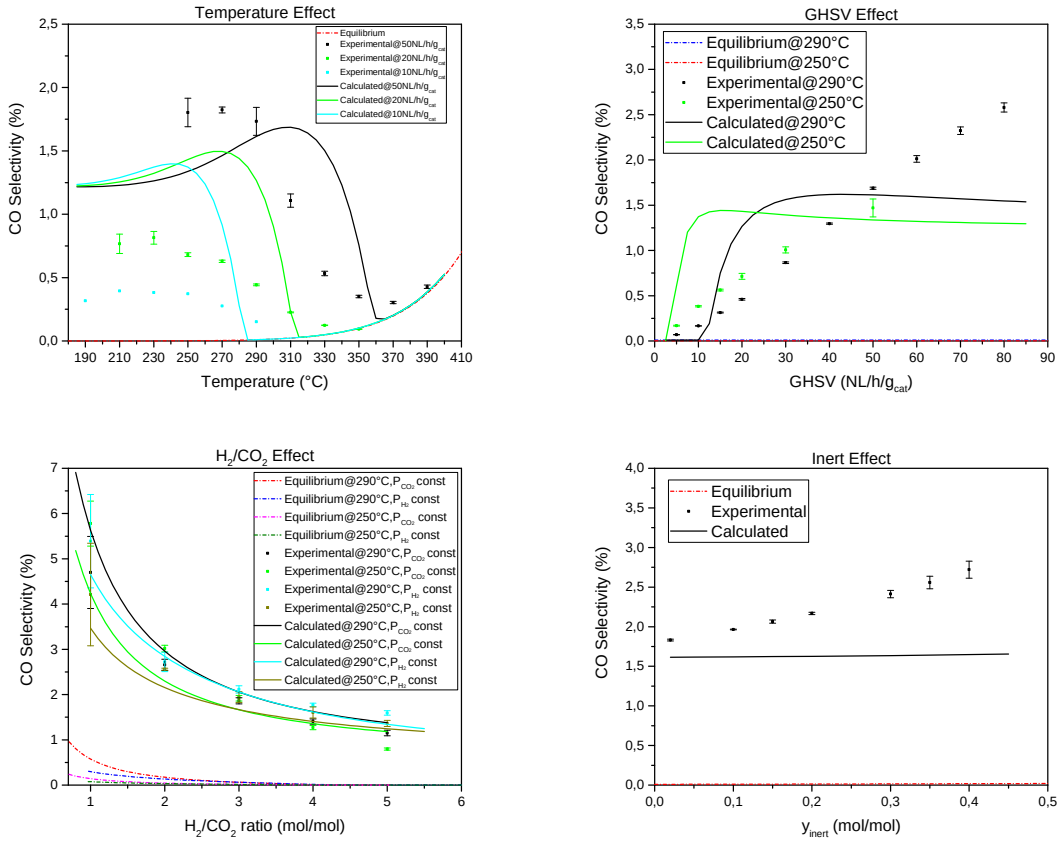

Figure 6.12: CO selectivity simulation plots of the Champon et al. model, without direct CO methanation and water adsorption parameters.

Table 6.17: Correlation matrix of the Champon et al. model without CO methanation and water adsorption parameter.

	$k^*_{0,CO_{2_{meth}}}$	$Ea_{CO_{2_{meth}}}$	$k^*_{0,RWGS}$	Ea_{RWGS}	K^*_{0,CO_2}	ΔH_{CO_2}	K^*_{0,H_2}	ΔH_{H_2}	$K^*_{0,CO}$	ΔH_{CO}
$k^*_{0,CO_{2_{meth}}}$	1.00E+00	6.39E-01	6.44E-01	2.20E-01	-5.83E-01	8.41E-02	-4.77E-01	9.16E-02	-4.34E-01	1.72E-01
$Ea_{CO_{2_{meth}}}$	6.39E-01	1.00E+00	5.31E-01	1.29E-01	-1.19E-01	1.11E-02	-6.87E-03	-4.43E-01	5.37E-03	5.06E-02
$k^*_{0,RWGS}$	6.44E-01	5.31E-01	1.00E+00	5.23E-01	-3.86E-01	-3.63E-01	-6.82E-02	-7.22E-02	-2.04E-01	-2.89E-01
Ea_{RWGS}	2.20E-01	1.29E-01	5.23E-01	1.00E+00	-2.02E-01	-7.76E-01	-2.26E-02	1.82E-01	-1.29E-01	-6.51E-01
K^*_{0,CO_2}	-5.83E-01	-1.19E-01	-3.86E-01	-2.02E-01	1.00E+00	-1.26E-01	9.32E-01	-4.31E-01	9.73E-01	-2.36E-01
ΔH_{CO_2}	8.41E-02	1.11E-02	-3.63E-01	-7.76E-01	-1.26E-01	1.00E+00	-3.13E-01	2.31E-01	-1.92E-01	9.28E-01
K^*_{0,H_2}	-4.77E-01	-6.88E-03	-6.82E-02	-2.26E-02	9.32E-01	-3.13E-01	1.00E+00	-4.65E-01	9.73E-01	-3.89E-01
ΔH_{H_2}	9.16E-02	-4.43E-01	-7.22E-02	1.82E-01	-4.31E-01	2.31E-01	-4.65E-01	1.00E+00	-4.55E-01	4.40E-01
$K^*_{0,CO}$	-4.34E-01	5.37E-03	-2.04E-01	-1.29E-01	9.73E-01	-1.92E-01	9.73E-01	-4.55E-01	1.00E+00	-2.80E-01
ΔH_{CO}	1.72E-01	5.06E-02	-2.89E-01	-6.51E-01	-2.36E-01	9.28E-01	-3.89E-01	4.40E-01	-2.80E-01	1.00E+00

6.1.5 Champon et al. Model - conclusions

This model was proposed as an innovation inside the field of carbon dioxide methanation and as an upgrade of the Xu-Froment model, due its triangular nature, resembling the one proposed by Xu-Froment [92].
The many modifications and adaptations introduced by the authors, however, make this model very weak from a theoretical point of view and many other modifications need to be introduced to make the model work properly.

In particular, the models with fixed water adsorption constant and fixed adsorption constants can not be applied as they are for an industrial application, but should rather be considered as first guess values for further studies.

Some conclusions can be formulated: when the direct path of Sabatier reaction is neglected, the model performs pretty well, confirming the significant predominance of the RWGS + CO methanation path, as further confirmed if one tries to remove CO methanation from the system. Moreover, from these simulations the RDS of all the process seems to be the RWGS reaction: negative values of activation energy for the CO methanation reaction were often found, showing that once CO is formed, the system immediately wants to transform it into CH_4.

Further studies and a final discrimination to understand the intrinsic dualism of RWGS and carbon monoxide methanation, together with the understanding of which one between RWGS and CO methanation is the RDS process should be conducted.

Table 6.18: Summary of results for different modification of Champon et al. model [93]

Champon et al.	k_0	$Ea\left[\frac{kJ}{mol}\right]$	$MPE_{\chi_{CO_2}}$	$R^2_{\chi_{CO_2}}$	$MPE_{\sigma_{CO}}$	$R^2_{\sigma_{CO}}$
Fixed water adsorption paramaters	$k_{0,CO_{2_{meth}}} = 6.78 \times 10^6 \pm 2.96 \times 10^5$ $k_{0,RWGS} = 7.93 \times 10^2 \pm 8.33 \times 10^1$ $k_{0,CO_{meth}} = 1.69 \times 10^{-15} \pm 4.30 \times 10^{-16}$	$Ea_{CO_{2_{meth}}} = 107.09 \pm 0.18$ $Ea_{RWGS} = 88.86 \pm 0.46$ $Ea_{CO_{meth}} = -86.77 \pm 1.09$	5.91%	0.993	52.6%	0.901
Fixed adsorption paramaters	$k_{0,CO_{2_{meth}}} = 3.74 \times 10^4 \pm 3.84 \times 10^2$ $k_{0,RWGS} = 1.10 \times 10^{-1} \pm 6.73 \times 10^{-3}$ $k_{0,CO_{meth}} = 9.97 \times 10^{-7} \pm 1.63 \times 10^{-7}$	$Ea_{CO_{2_{meth}}} = 85.55 \pm 4.61 \times 10^{-2}$ $Ea_{RWGS} = 47.53 \pm 0.27$ $Ea_{CO_{meth}} = -25.55 \pm 0.70$	14.1%	0.976	26.1%	0.972
Without CO_2 methanation	$k_{0,RWGS} = 4.15 \times 10^2 \pm 3.78 \times 10^1$ $k_{0,CO_{meth}} = 1.21 \times 10^{-2} \pm 3.12 \times 10^{-2}$	$Ea_{RWGS} = 67.02 \pm 0.41$ $Ea_{CO_{meth}} = -38.87 \pm 9.68$	11.1%	0.981	23.3%	0.977
Without CO methanation	$k_{0,CO_{2_{meth}}} = 2.39 \times 10^5 \pm 7.62 \times 10^3$ $k_{0,RWGS} = 9.39 \times 10^3 \pm 7.02 \times 10^2$	$Ea_{CO_{2_{meth}}} = 93.15 \pm 0.14$ $Ea_{RWGS} = 101.39 \pm 0.33$	5.03%	0.996	89.4%	0.922

6.2 Farsi et al. Model

The model proposed by Farsi et al. [86] describes the process of carbon dioxide methanation in operating conditions that try to simulate the ones useful for an industrial application, with a particular focus on the selectivity to carbon monoxide in different conditions.
Their model was developed on a bimetallic catalyst, i.e. Ni_3Fe/Al_2O_3. The system was hypothesized as the series of RWGS followed by CO methanation reaction to describe CO_2 methanation; moreover, their study was conducted on a peculiar laboratory reactor: a microstructured packed bed reactor with internal cross-flow cooling channels, which could easily manage the high exothermicity of methanation reactions.
Thus, the model Farsi et al. chose to describe the phenomenology of the system was a 1D non-isothermal plug flow: together with the use of a bimetallic catalyst, this feature makes this model the only one to have these characteristics among the ones we chose to analyze.

So, according to Farsi et al., the system is fully described through the following set of equations:

1. $CO_2 + H_2 \rightleftharpoons CO + H_2O \qquad \Delta H^0_{R,298K} = +41.2\,\frac{kJ}{mol}$
2. $CO + 3\,H_2 \rightleftharpoons CH_4 + H_2O \qquad \Delta H^0_{R,298K} = -206.3\,\frac{kJ}{mol}$

Three different literature models were analyzed by Farsi et al. before developing one on their own: the Koschany et al. model [90], deeply analyzed also in this thesis work, the Kopyschinski et al. model [105], which focuses on CO methanation but lacks the ability to describe the approach to equilibrium, and the Zhang et al. model [106], underlining the deficiencies of each of these models.

As reported in Sec. 3.2.5, Farsi et al. proposed general equations to describe the set of reactions, which are:

$$r_{RWGS} = \frac{k_1 P^{\alpha}_{CO_2} P^{\beta}_{H_2}}{inhibition\ term^2}\left(1 - \frac{P_{CO} P_{H_2O}}{P_{CO_2} P_{H_2} K_{eqRWGS}}\right) \tag{6.2.1}$$

$$r_{CO_{meth}} = \frac{k_2 P^{\gamma}_{CO} P^{\varphi}_{H2}}{inhibition\ term^2}\left(1 - \frac{P_{CH_4} P_{H_2O} P^2_{abs}}{P_{CO} P^3_{H_2} K_{eqCO_{meth}}}\right) \tag{6.2.2}$$

Then, a postulation on a LHHW-based model is proposed: Farsi et al stated that reaction orders (α, β, γ, φ) can only have the values of 0, 0.5, 1, where:

- A value of 0 implies that the species has no influence on the reaction rate;
- A value of 0.5 stands for a dissociative adsorption of the species on the catalyst surface;
- A value of 1 witnesses a direct adsorption of the species on the catalyst surface;

Different combinations of these three values for the reactant exponents were studied and, based on the method of the least squares error, the best one was chosen, leading to this rate expressions:

$$r_{RWGS} = \frac{k_1 P_{CO_2}^{0.5} P_{H_2}^{0.5}}{(1 + K_{H_2O} P_{H_2O})^2} \Big(1 - \frac{P_{CO} P_{H_2O}}{P_{CO_2} P_{H_2} K_{eqRWGS}}\Big) \tag{6.2.3}$$

$$r_{CO_{meth}} = \frac{k_2 P_{CO} P_{H2}^{0.5}}{(1 + K_{H_2O} P_{H_2O})^2} \Big(1 - \frac{P_{CH_4} P_{H_2O} P_{abs}^2}{P_{CO} P_{H_2}^3 K_{eqCO_{meth}}}\Big) \tag{6.2.4}$$

A very similar procedure was conducted to determine the inhibition effects and, in particular, if water inhibition was either given by its direct adsorption or adsorption as hydroxyl group, concluding the former gave the best fitting to their data.

Despite declaring this a kinetic study based on a LHHW model, no RDS is clearly stated and the procedure adopted to select the best numbers to fit both the reaction orders and the inhibition effects make this model much more similar to a modified power-law type than a mechanistic one.

Finally, a particular mention must be done for the unusual presence of the term P_{abs}^2 in the equilibrium term of CO methanation: if left there, the parenthesis does not converge to zero when reaction conditions approach equilibrium. For example, if $P_{abs}^2 = 36$, the term in parenthesis equals -35 when equilibrium is reached, which constitutes a chemical-nonsense. Due to these considerations, we decided to unilaterally remove P_{abs}^2 from the calculus, even though our experimental dataset was collected at atmospheric pressure, so a $P_{abs}^2 = 1$ term would not have changed the calculus.

In this case, the parameters to be calculated are:
$k^*_{0,RWGS}$, Ea_{RWGS}, $k^*_{0,CO_{meth}}$, $Ea_{CO_{meth}}$, K^*_{0,H_2O}, ΔH_{H_2O}.

Table 6.19: Estimated parameters of the Farsi et al model.

Parameter	Value	U.o.M
$k^*_{0,RWGS}$	$5.94 \pm 2.12 \times 10^{-3}$	–
Ea_{RWGS}	87.86 ± 0.18	kJ/mol
$k^*_{0,CO_{meth}}$	$10.67 \pm 2.80 \times 10^{-3}$	–
$Ea_{CO_{meth}}$	5.87 ± 0.20	kJ/mol
K^*_{0,H_2O}	$0.49 \pm 5.48 \times 10^{-3}$	–
ΔH_{H_2O}	-36.28 ± 0.44 kJ/mol	

Table 6.20: Quality of the regression of the Farsi et al. model.

Parameter	Value
$MPE_{\chi_{CO_2}}$	6.30%
$R^2_{\chi_{CO_2}}$	0.992
$MPE_{\sigma_{CO}}$	25.10%
$R^2_{\sigma_{CO}}$	0.860

As for the Champon et al. model without CO_2 methanation, this model works rather well in fitting both CO_2 conversion and CO selectivity, resembling the same discussion we did in Sec. 6.1.3: RWGS seems to be the RDS of the process, with the CO methanation reaction having a much lower activation energy reaction, again suggesting that once CO is formed, it is immediately consumed by its methanation reaction. Indeed, also the values found by Farsi et al. suggest this path to be the correct one, with a very high activation energy for RWGS: the reason for an Ea so high is the fact that their process was performed on a bimetallic catalyst were the presence of Fe influences the value of activation energy, as clearly explained by Farsi et al. [86].

Table 6.21: Kinetic parameters of the Farsi et al. model and comparison with Farsi et al. results. [86]

Parameter	Value	Farsi et al.	U.o.M
$k_{0,RWGS}$	$5.37 \times 10^4 \pm 2.12 \times 10^3$	$6.78 \times 10^{11} \pm 1.39 \times 10^{12}$	$mol/(s \cdot g_{cat} \cdot atm)$
Ea_{RWGS}	87.86 ± 0.18	166.55 ± 8.48	kJ/mol
$k_{0,CO_{meth}}$	$0.15 \pm 6.70 \times 10^{-3}$	$6.33 \times 10^3 \pm 6.73 \times 10^3$	$mol/(s \cdot g_{cat} \cdot atm^{1.5})$
$Ea_{CO_{meth}}$	5.87 ± 0.20	60.98 ± 4.59	kJ/mol
K_{0,H_2O}	$7.03 \times 10^{-4} \pm 7.03 \times 10^{-5}$	8.09 ± 9.15	atm^{-1}
ΔH_{H_2O}	-36.28 ± 0.44	11.44 ± 4.96	kJ/mol

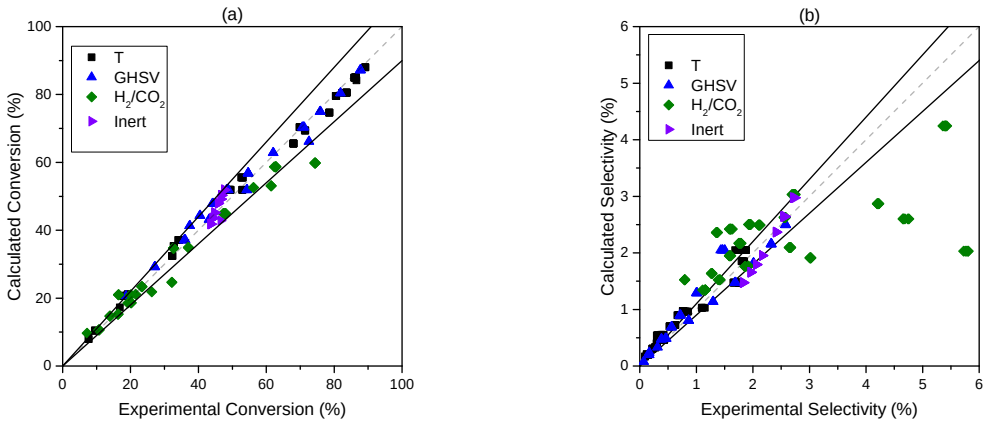

Figure 6.13: Parity plots of the Farsi et al. model. (a) CO_2 conversion. (b) CO selectivity.

This model performs relatively well, showing that the main path for methane formation is the RWGS + CO methanation one. Due to the good results obtained in the regression, no further modifications were introduced.

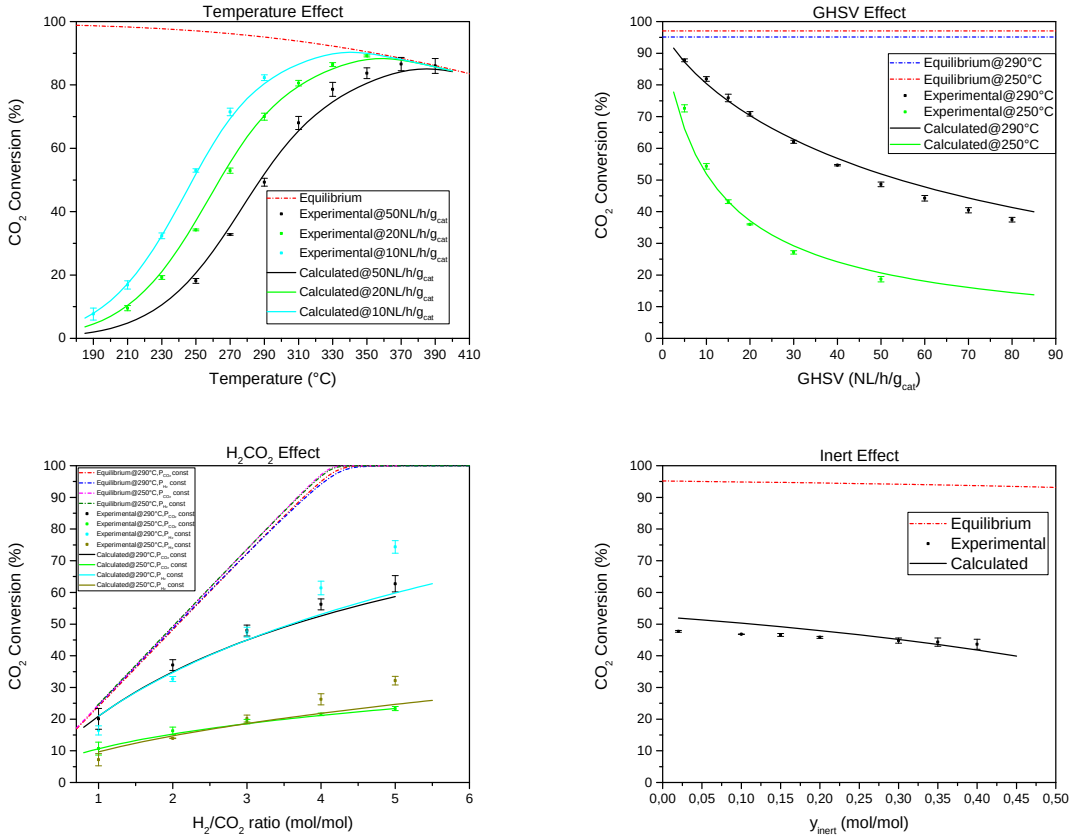

Figure 6.14: CO_2 conversion simulation plots of the Farsi et al. model.

Table 6.22: Correlation matrix of the Farsi et al. model.

	$k^*_{0,RWGS}$	Ea_{RWGS}	$k^*_{0,CO_{meth}}$	$Ea_{CO_{meth}}$	K^*_{0,H_2O}	ΔH_{H_2O}
$k^*_{0,RWGS}$	1.00E+00	6.37E-01	4.63E-01	3.95E-01	8.22E-01	5.37E-01
Ea_{RWGS}	6.37E-01	1.00E+00	4.03E-01	5.90E-01	5.67E-01	8.55E-01
$k^*_{0,CO_{meth}}$	4.63E-01	4.03E-01	1.00E+00	7.76E-01	8.04E-01	6.50E-01
$Ea_{CO_{meth}}$	3.95E-01	5.90E-01	7.76E-01	1.00E+00	6.57E-01	8.12E-01
K^*_{0,H_2O}	8.22E-01	5.67E-01	8.04E-01	6.57E-01	1.00E+00	7.03E-01
ΔH_{H_2O}	5.37E-01	8.55E-01	6.50E-01	8.12E-01	7.03E-01	1.00E+00

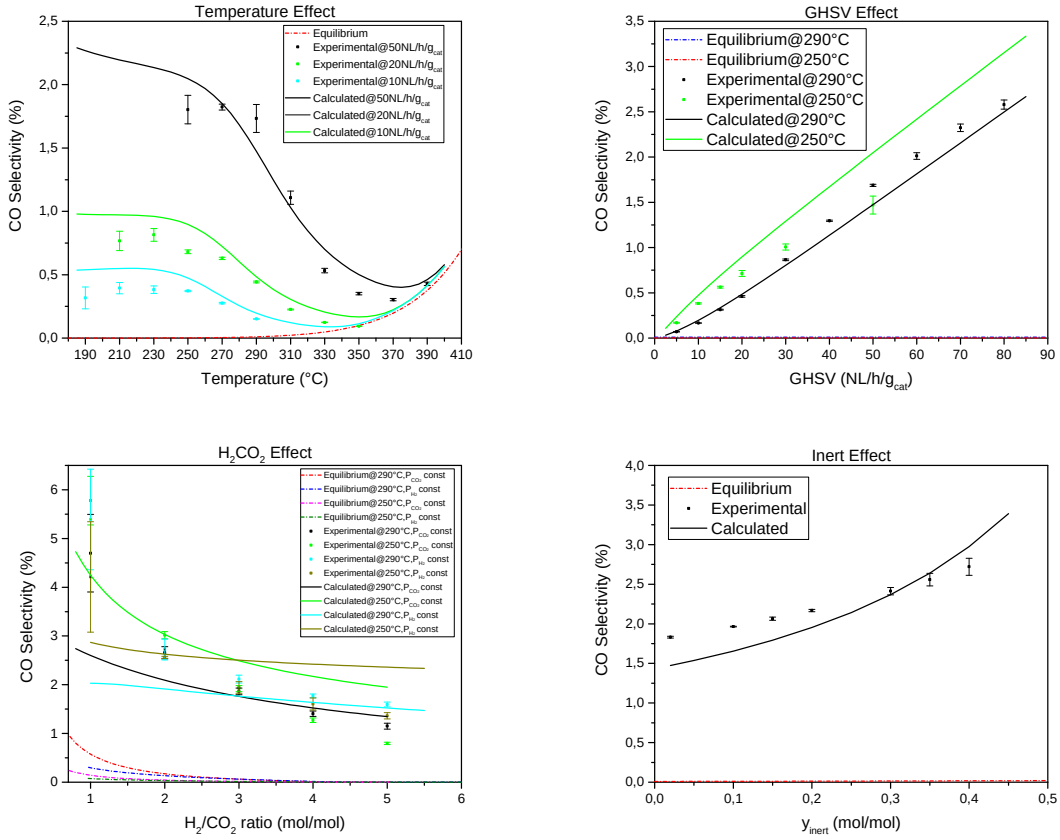

Figure 6.15: CO selectivity simulation plots of the Farsi et al. model.

6.3 Hernandez Lalinde et al. Model

Hernandez Lalinde et al. proposed a model where the process of CO_2 methanation is described through the parallel reactions of carbon dioxide methanation and RWGS. Even in this case the authors proposed to describe selectivity to carbon monoxide [95].
The study was performed on a Ni/Al_2O_3 catalyst, where a wide variety of operating conditions was deeply analyzed; in their work, Hernandez Lalinde et al. exploited spatially-resolved measurement of the gas composition in a channel reactor, so that all the evolution of the system inside the reactor could be monitored.

Hernandez Lalinde et al. proposed a summary of different possible mechanisms formulated in literature for CO2 methanation:

Table 6.23: Literature mechanisms reported by Hernandez Lalinde et al.

Mechanism A	Mechanism B	Mechanism AB
A1) $H_2 + 2\,l \rightleftharpoons 2\,H^*$	B1) $H_2 + 2\,l \rightleftharpoons 2\,H^*$	AB1) $H_2 + 2\,l \rightleftharpoons 2\,H^*$
A2) $CO_2 + l \rightleftharpoons CO_2^*$	B2) $CO_2 + l \rightleftharpoons CO_2^*$	AB2) $CO_2 + l \rightleftharpoons CO_2^*$
A3) $CO_2^* + l \rightleftharpoons CO^* + O^*$	B3) $CO_2^* + H^* \rightleftharpoons HCOO^* + l$	AB3) $CO_2^* + l \rightleftharpoons CO^* + O^*$
A4) $CO^* + l \rightleftharpoons C^* + O^*$	B4) $HCOO^* + l \rightleftharpoons CO^* + OH^*$	AB4) $CO^* + H^* \rightleftharpoons COH^* + l$
A5) $C^* + H^* \rightleftharpoons CH^* + l$	B5) $HCOO^* + H^* \rightleftharpoons COH^* + OH^*$	AB5) $CO^* + 2H^* \rightleftharpoons COH_2^* + 2l$
A6) $CH^* + H^* \rightleftharpoons CH_2^* + l$	B6) $COH^* + H^* \rightleftharpoons CH_2^* + OH^*$	AB6) $COH^* + l \rightleftharpoons CH^* + O^*$
A7) $CH_2^* + H^* \rightleftharpoons CH_3^* + l$	B7) $COH^* + l \rightleftharpoons C^* + OH^*$	AB7) $COH^* + H^* \rightleftharpoons CH^* + OH^*$
A8) $CH_3^* + H^* \rightleftharpoons CH_4^* + l$	B8) $CH^* + H^* \rightleftharpoons CH_2^* + l$	AB8) $COH_2^* + l \rightleftharpoons CH^* + OH^*$
A9) $CH_4^* \rightleftharpoons CH_4 + l$	B9) $CH_2^* + H^* \rightleftharpoons CH_3^* + l$	AB9) $CH^* + H^* \rightleftharpoons CH_2^* + l$
A10) $O^* + H^* \rightleftharpoons OH^* + l$	B10) $CH_3^* + H^* \rightleftharpoons CH_4^* + l$	AB10) $CH_2^* + H^* \rightleftharpoons CH_3^* + l$
A11) $OH^* + H^* \rightleftharpoons H_2O^* + l$	B11) $CH_4^* \rightleftharpoons CH_4 + l$	AB11) $CH_3^* + H^* \rightleftharpoons CH_4^* + l$
A12) $CO^* \rightleftharpoons CO + l$	B12) $O^* + H^* \rightleftharpoons OH^* + l$	AB12) $CH_4^* \rightleftharpoons CH_4 + l$
A13) $H_2O^* \rightleftharpoons H_2O + l$	B13) $OH^* + H^* \rightleftharpoons H_2O^* + l$	AB13) $O^* + H^* \rightleftharpoons OH^* + l$
	B14) $H_2O^* \rightleftharpoons H_2O + l$	AB14) $OH^* + H^* \rightleftharpoons H_2O^* + l$
	B15) $CO^* \rightleftharpoons CO + l$	AB15) $H_2O^* \rightleftharpoons H_2O + l$
		AB16) $CO^* \rightleftharpoons CO + l$

In these mechanisms, reactions $[A2-A7]$, $[B2-B9]$, $[AB4-AB10]$ can all be RDSs, and were indeed all proposed in literature by different authors.

Mechanism A assumes the direct dissociation of CO_2 and the further dissociation of CO to C, which is subsequently hydrogenated to methane. This mechanism is very similar to the direct C-O bond cleavage one (Sec. 2.4.2).
Mechanism B assumes the formation of formates through the interaction of CO_2 and adsorbed hydrogen, with the fundamental help from adsorbed hydrogen in lowering the dissociation energy of the second C-O bond.
Mechanism AB is an hybrid mechanism which hypothesizes the direct CO_2 dissociation and the H-assisted C-O dissociation in COH^*.

Hernandez Lalinde et al. analyzed 20 different models, depending on the chosen mechanism and the chosen RDS inside this mechanism. The model that best fitted their data was "model 11", where the proposed rate expressions are:

$$r_{CH_4} = \frac{k_1 K_{COH} P_{CO_2}^{0.5} K_{H_2} P_{H_2} \left(1 - \frac{P_{CH_4} P_{H_2O}^2}{P_{CO_2} P_{H_2}^4 K_{eqM}}\right)}{\left(1 + K_{COH} P_{CO_2}^{0.5} K_{H_2}^{0.5} P_{H_2}^{0.5} + \sqrt{K_{H_2} P_{H_2}} + K_{OH} \frac{P_{H_2O}}{\sqrt{P_{H_2}}}\right)^2} \tag{6.3.1}$$

$$r_{RWGS} = \frac{k_2 P_{CO_2} K_{H_2}^{0.5} P_{H_2}^{0.5} \left(1 - k_\beta \frac{P_{CO} P_{H_2O}}{P_{H_2} P_{CO_2} K_{eqRWGS}}\right)}{\left(1 + K_{COH} P_{CO_2}^{0.5} K_{H_2}^{0.5} P_{H_2}^{0.5} + \sqrt{K_{H_2} P_{H_2}} + K_{OH} \frac{P_{H_2O}}{\sqrt{P_{H_2}}}\right)^2} \tag{6.3.2}$$

These two rate expressions were derived hypothesizing reaction $AB7$ as RDS for the CO_2 methanation reaction ($COH^* + H^* \rightleftharpoons CH_2^* + OH^*$) and this step as RDS for RWGS: $CO_2^* + H^* \rightleftharpoons CO^* + OH^*$. Then, a hypothesis was introduced: since carbon dioxide methanation reaction and RWGS reaction take place on the same sites, inhibition effects to count for are the same for both reactions, so the same denominator must be present.

The integration of k_β in the equilibrium term of the RWGS reaction was justified by Hernandez Lalinde et al. as *"the theoretical gas phase equilibrium compared to the equilibrium on catalyst surface"* [95] but this is the only model that postulates the necessity of a particular parameter introduction inside the equilibrium term.

Therefore, we tried to perform a regression where k_β was fixed to the value proposed by the authors.

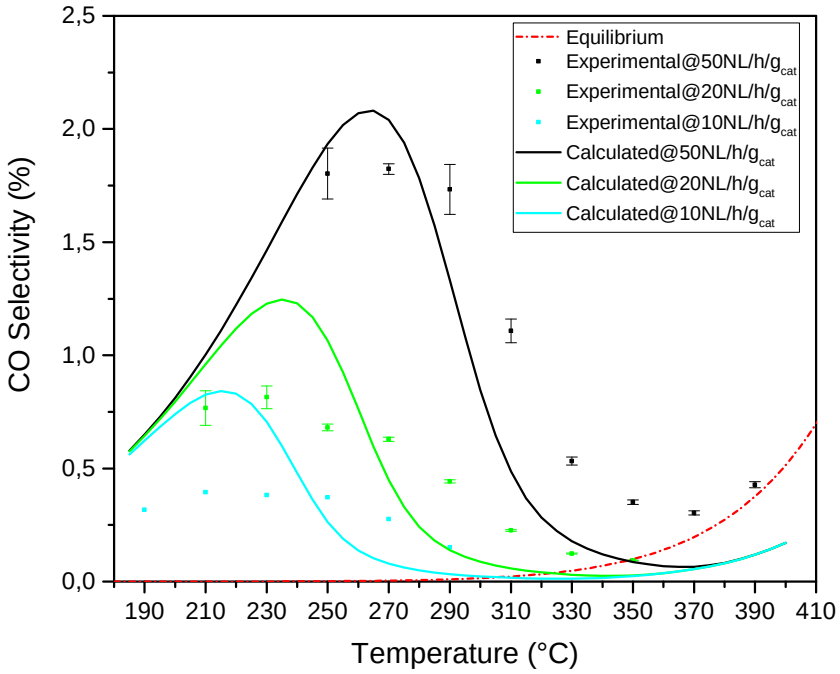

Figure 6.16: k_β influence on the CO selectivity of the Hernandez Lalinde et al. model 11.

The presence of k_β makes the trend cross the equilibrium curve, which is not possible from a physical point view. Therefore, in our complete non-linear regression we decided to neglect the presence of k_β.

The parameters to be calculated, then, are:

$k_{0,CO_{2_{meth}}}$, $Ea_{CO_{2_{meth}}}$, $k_{0,RWGS}$, Ea_{RWGS}, $K^*_{0,COH}$, ΔH_{COH}, K^*_{0,H_2}, ΔH_{H_2}, $K^*_{0,OH}$, ΔH_{OH}.

Table 6.24: Estimated parameters of the Hernandez Lalinde et al. model 11.

Parameter	Value	U.o.M
$k^*_{0,CO_{2_{meth}}}$	$6.86 \pm 3.26 \times 10^{-2}$	–
$Ea_{CO_{2_{meth}}}$	96.66 ± 0.94	kJ/mol
$k^*_{0,RWGS}$	$6.24 \pm 7.41 \times 10^{-2}$	–
Ea_{RWGS}	133.38 ± 2.50	kJ/mol
$K^*_{0,COH}$	$2.46 \pm 4.22 \times 10^{-2}$	–
ΔH_{COH}	14.74 ± 1.60	kJ/mol
K^*_{0,H_2}	$4.70 \times 10^{-2} \pm 1.01 \times 10^{-1}$	–
ΔH_{H_2}	-65.60 ± 2.87	kJ/mol
$K^*_{0,OH}$	$2.19 \pm 1.74 \times 10^{-2}$	–
ΔH_{OH}	-29.17 ± 1.21	kJ/mol

Table 6.25: Quality of the regression of the Hernandez Lalinde et al. model 11.

Parameter	Value
$MPE_{\chi_{CO_2}}$	3.63%
$R^2_{\chi_{CO_2}}$	0.998
$MPE_{\sigma_{CO}}$	81.0%
$R^2_{\sigma_{CO}}$	0.925

The model performs very well in fitting and predicting the conversion but, on the contrary, is very bad in fitting the selectivity to CO. In our opinion, this is caused by the fact that carbon monoxide is only formed and never consumed in this scheme.

Table 6.26: Kinetic parameters of the Hernandez Lalinde et al. model 11 and comparison with Hernandez Lalinde et al. results. [95]

Parameter	Value	Hernandez Lalinde et al.	U.o.M
$k_{0,CO_{2_{meth}}}$	$8.80 \times 10^5 \pm 2.05 \times 10^5$	$4.93 \times 10^9 \pm 4.60 \times 10^9$	$mol/(s \cdot g_{cat})$
$Ea_{CO_{2_{meth}}}$	96.66 ± 0.94	79.7 ± 4.7	kJ/mol
$k_{0,RWGS}$	$1.21 \times 10^9 \pm 7.36 \times 10^8$	$7.33 \times 10^{18} \pm 1.08 \times 10^{19}$	$mol/(s \cdot g_{cat} \cdot atm)$
Ea_{RWGS}	133.38 ± 2.50	194.7 ± 7	kJ/mol
$K_{0,COH}$	$2.72 \times 10^2 \pm 1.04 \times 10^2$	$3.95 \times 10^5 \pm 6.47 \times 10^5$	$atm^{-0.5}$
ΔH_{COH}	14.74 ± 1.60	60.5 ± 7.9	kJ/mol
K_{0,H_2}	$8.97 \times 10^{-7} \pm 6.15 \times 10^{-7}$	$2.07 \times 10^{-2} \pm 1.12 \times 10^{-2}$	atm^{-1}
ΔH_{H_2}	-65.60 ± 2.87	-12.5 ± 2	kJ/mol
$K_{0,OH}$	$1.76 \times 10^{-2} \pm 4.86 \times 10^{-3}$	$5.30 \times 10^5 \pm 5.58 \times 10^5$	$atm^{-0.5}$
ΔH_{OH}	-29.17 ± 1.21	64.4 ± 4.9	kJ/mol

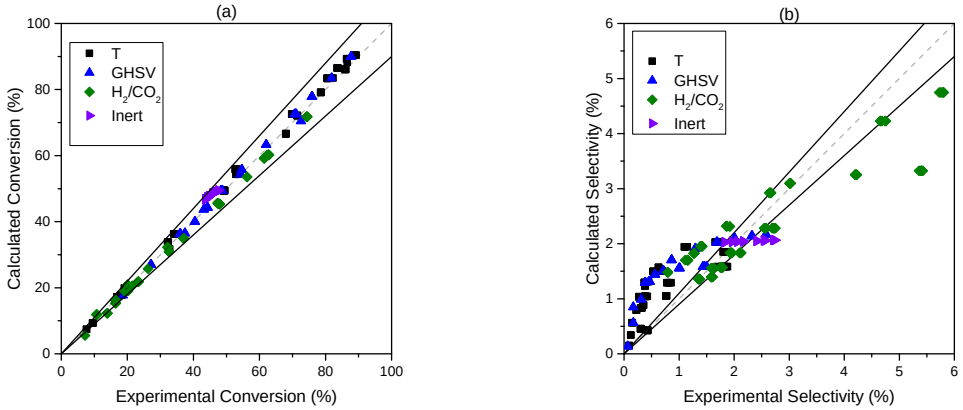

Figure 6.17: Parity plots of the Hernandez Lalinde et al. model 11. (a) CO_2 conversion. (b) CO selectivity.

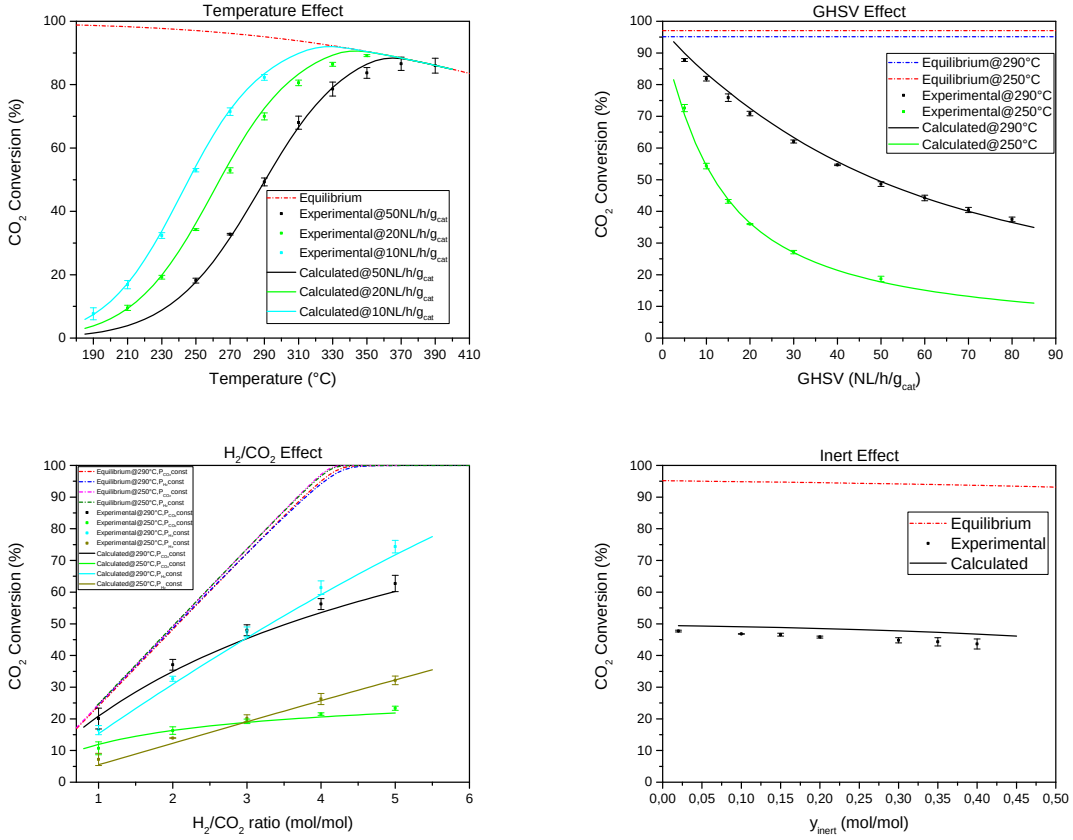

Figure 6.18: CO_2 conversion simulation plots of the Hernandez Lalinde et al. model 11.

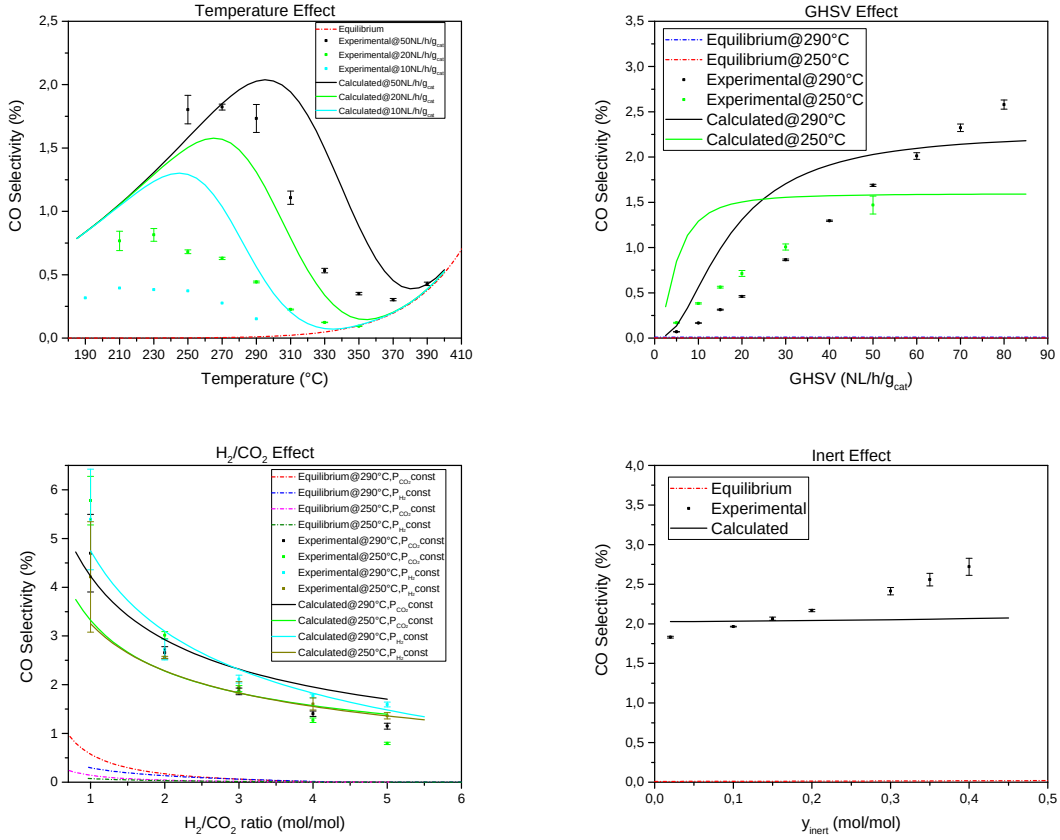

Figure 6.19: CO selectivity simulation plots of the Hernandez Lalinde et al. model 11.

Table 6.27: Correlation matrix of the Hernandez Lalinde et al. model 11.

	$k^*_{0,CO_{2_{met}}}$	$Ea_{CO_{2_{met}}}$	$k^*_{0,RWGS}$	Ea_{RWGS}	$K^*_{0,COH}$	ΔH_{COH}	K^*_{0,H_2}	ΔH_{H_2}	$K^*_{0,OH}$	ΔH_{OH}
$k^*_{0,CO_{2_{met}}}$	1.00E+00	6.17E-01	9.96E-01	5.13E-01	9.89E-01	4.38E-01	-9.91E-01	-2.45E-01	-7.70E-01	2.21E-01
$Ea_{CO_{2_{met}}}$	6.17E-01	1.00E+00	6.30E-01	9.76E-01	6.37E-01	9.42E-01	-6.04E-01	-7.80E-01	-4.33E-01	4.12E-02
$k^*_{0,RWGS}$	9.96E-01	6.31E-01	1.00E+00	5.36E-01	9.98E-01	4.65E-01	-9.79E-01	-2.51E-01	-7.25E-01	2.41E-01
Ea_{RWGS}	5.13E-01	9.76E-01	5.36E-01	1.00E+00	5.49E-01	9.90E-01	-4.88E-01	-7.18E-01	-2.89E-01	1.55E-01
$K^*_{0,COH}$	9.89E-01	6.37E-01	9.98E-01	5.49E-01	1.00E+00	4.83E-01	-9.66E-01	-2.54E-01	-6.88E-01	2.55E-01
ΔH_{COH}	4.38E-01	9.42E-01	4.65E-01	9.90E-01	4.83E-01	1.00E+00	-4.07E-01	-6.67E-01	-1.95E-01	2.20E-01
K^*_{0,H_2}	-9.91E-01	-6.04E-01	-9.79E-01	-4.88E-01	-9.66E-01	-4.07E-01	1.00E+00	2.70E-01	8.47E-01	-1.55E-01
ΔH_{H_2}	-2.45E-01	-7.80E-01	-2.51E-01	-7.18E-01	-2.54E-01	-6.67E-01	2.70E-01	1.00E+00	3.08E-01	5.70E-01
$K^*_{0,OH}$	-7.70E-01	-4.33E-01	-7.25E-01	-2.89E-01	-6.88E-01	-1.95E-01	8.47E-01	3.08E-01	1.00E+00	1.34E-01
ΔH_{OH}	2.21E-01	4.12E-02	2.41E-01	1.55E-01	2.55E-01	2.20E-01	-1.55E-01	5.70E-01	1.34E-01	1.00E+00

Table 6.28: Summary of results for different models presented in this chapter.

Model	Rate expression	k_0	$Ea\left[\frac{kJ}{mol}\right]$	$MPE_{\chi_{CO_2}}$	$R^2_{\chi_{CO_2}}$	$MPE_{\sigma_{CO}}$	$R^2_{\sigma_{CO}}$
Champon no $CO_{2_{meth}}$	$r_{RWGS} = \frac{k_{RWGS} K_{CO_2} P_{CO_2}\left(1 - \frac{P_{CO} P_{H_2O}}{P_{H_2} P_{CO_2} K_{eq,RWGS}}\right)}{(1 + K_{CO_2} P_{CO_2} + K_{H_2} P_{H_2} + K_{CO} P_{CO})}$	$4.15 \times 10^2 \left[\frac{mol}{s \cdot g_{cat}.}\right]$	67.02	11.1%	0.981	23.3%	0.977
	$r_{CO_{meth}} = \frac{k_{CO_{meth}} K_{H_2} K_{CO} P_{H_2} P_{CO}\left(1 - \frac{P_{CH_4} P_{H_2O}}{P^3_{H_2} P_{CO} K_{eq,CO_{meth}}}\right)}{(1 + K_{CO_2} P_{CO_2} + K_{H_2} P_{H_2} + K_{CO} P_{CO})^2}$	$1.21 \times 10^{-2} \left[\frac{mol}{s \cdot g_{cat}.}\right]$	-38.87				
Champon no CO_{meth}	$r_{CO_{2_{meth}}} = \frac{k_{CO_{2_{meth}}} K_{H_2} K_{CO_2} P_{H_2} P_{CO_2}\left(1 - \frac{P_{CH_4} P^2_{H_2O}}{P^4_{H_2} P_{CO_2} K_{eq,Sab}}\right)}{(1 + K_{CO_2} P_{CO_2} + K_{H_2} P_{H_2} + K_{CO} P_{CO})^2}$	$2.39 \times 10^5 \left[\frac{mol}{s \cdot g_{cat}.}\right]$	93.15	5.03%	0.996	89.4%	0.922
	$r_{RWGS} = \frac{k_{RWGS} K_{CO_2} P_{CO_2}\left(1 - \frac{P_{CO} P_{H_2O}}{P_{H_2} P_{CO_2} K_{eq,RWGS}}\right)}{(1 + K_{CO_2} P_{CO_2} + K_{H_2} P_{H_2} + K_{CO} P_{CO})}$	$9.39 \times 10^3 \left[\frac{mol}{s \cdot g_{cat}.}\right]$	101.39				
Farsi	$r_{RWGS} = \frac{k_1 P^{0.5}_{CO_2} P^{0.5}_{H_2}}{(1 + K_{H_2O} P_{H_2O})^2}\left(1 - \frac{P_{CO} P_{H_2O}}{P_{H_2} P_{CO_2} K^{eq}_{RWGS}}\right)$	$5.37 \times 10^4 \left[\frac{mol}{s \cdot g_{cat} \cdot atm}\right]$	87.86	6.30%	0.992	25.1%	0.860
	$r_{CO_{meth}} = \frac{k_2 P_{CO} P^{0.5}_{H_2}}{(1 + K_{H_2O} P_{H_2O})^2}\left(1 - \frac{P_{CH_4} P_{H_2O}}{P_{CO} P^3_{H_2} K_{eq,CO_{meth}}}\right)$	$0.150 \left[\frac{mol}{s \cdot g_{cat} \cdot atm^{1.5}}\right]$	5.87				
Hernandez	$r_{CO_{2_{meth}}} = \frac{k_1 K_{COH} P^{0.5}_{CO_2} K_{H_2} P_{H_2}\left(1 - \frac{P_{CH_4} P^2_{H_2O}}{P_{CO_2} P^4_{H_2} K_{eqM}}\right)}{\left(1 + K_{COH} P^{0.5}_{CO_2} K^{0.5}_{H_2} P^{0.5}_{H_2} + \sqrt{K_{H_2} P_{H_2}} + K_{OH} \frac{P_{H_2O}}{\sqrt{P_{H_2}}}\right)^2}$	$8.80 \times 10^5 \left[\frac{mol}{s \cdot g_{cat}}\right]$	96.66	3.63%	0.998	81.0%	0.925
	$r_{RWGS} = \frac{k_2 P_{CO_2} K^{0.5}_{H_2} P^{0.5}_{H_2}\left(1 - k_\beta \frac{P_{CO} P_{H_2O}}{P_{H_2} P_{CO_2} K_{eqRWGS}}\right)}{\left(1 + K_{COH} P^{0.5}_{CO_2} K^{0.5}_{H_2} P^{0.5}_{H_2} + \sqrt{K_{H_2} P_{H_2}} + K_{OH} \frac{P_{H_2O}}{\sqrt{P_{H_2}}}\right)^2}$	$1.21 \times 10^9 \left[\frac{mol}{s \cdot g_{cat} \cdot atm}\right]$	133.38				

Chapter 7

Internally Developed Models

In our analysis of the Hernandez Lalinde et al. model, we decided to try and derive the rate expressions proposed in that model. We discovered that Hernandez Lalinde et al. adopted many expedients to derive their model, and we were never able to reach the same expressions proposed by them. On the other hand, in our derivation, we discovered two completely new models, that describe the process of CO_2 methanation through the RWGS followed by CO methanation, in a mechanism strongly resembling the RWGS + CO-Hydro pathway (Sec. 2.4.1). The two models differ only in the presence of adsorbed O hypothesize by one and neglected by the other.

In this chapter, we will focus on the derivation and application of these two models, which we named Raco − Vidotto and Vidotto − Raco.

7.1 Raco − Vidotto model

Mechanism AB proposed by Hernandez Lalinde et al. [95] and reported in Table 6.23 was modified by removing steps 5, 6, and 8. The RDS proposed by Hernandez Lalinde et al. for the RWGS reaction was removed from the mechanism, being it equal to the sum between the CO_2 dissociation step (step 3) and the OH formation step (step 10). The elementary steps used in the Raco − Vidotto model to describe the process, and from which reaction rates were derived, are reported in Table 7.1.

Table 7.1: Mechanism proposed to derive the Raco – Vidotto model.

Raco – Vidotto Mechanism
1) $H_2 + 2\ l \rightleftharpoons 2\ H^*$
2) $CO_2 + l \rightleftharpoons CO_2^*$
3) $CO_2^* + l \rightleftharpoons CO^* + O^*$
4) $CO^* + H^* \rightleftharpoons COH^* + l$
5) $COH^* + H^* \rightleftharpoons CH^* + OH^*$
6) $CH^* + H^* \rightleftharpoons CH_2^* + l$
7) $CH_2^* + H^* \rightleftharpoons CH_3^* + l$
8) $CH_3^* + H^* \rightleftharpoons CH_4^* + l$
9) $CH_4^* \rightleftharpoons CH_4 + l$
10) $O^* + H^* \rightleftharpoons OH^* + l$
11) $OH^* + H^* \rightleftharpoons H_2O^* + l$
12) $H_2O^* \rightleftharpoons H_2O + l$
13) $CO^* \rightleftharpoons CO + l$

We chose as RDS of the RWGS reaction step 3 and, in accordance with *model 11* of the Hernandez Lalinde et al. model (Sec. 6.3), we considered step 5 as the RDS of the CO methanation reaction. Moreover, species H, OH, and COH were chosen as MASI, to reflect the inhibition effects of hydrogen, water, and carbonaceous species.

A LHHW-based approach was used to determine the rate expressions, which are:

$$r_{RWGS} = \frac{k_{RWGS} P_{CO_2} \left(1 - \dfrac{P_{CO} P_{H_2O}}{P_{H_2} P_{CO_2} K_{eqRWGS}}\right)}{\left(1 + \sqrt{K_{H_2} P_{H_2}} + K_{OH} \dfrac{P_{H_2O}}{\sqrt{P_{H_2}}} + K_{COH} \sqrt{P_{H_2}} P_{CO}\right)^2} \tag{7.1.1}$$

$$r_{CO_{meth}} = \frac{k_{CO_{meth}} P_{CO} P_{H_2} \left(1 - \dfrac{P_{CH_4} P_{H_2O}}{P_{CO} P_{H_2}^3 K_{eqCO_{meth}}}\right)}{\left(1 + \sqrt{K_{H_2} P_{H_2}} + K_{OH} \dfrac{P_{H_2O}}{\sqrt{P_{H_2}}} + K_{COH} \sqrt{P_{H_2}} P_{CO}\right)^2} \tag{7.1.2}$$

The complete derivation of this model is reported in Appendix D.1.

Table 7.2: Estimated parameters of the Raco – Vidotto model.

Parameter	Value	U.o.M
$k^*_{0,RWGS}$	$9.07 \pm 1.41 \times 10^{-2}$	–
Ea_{RWGS}	90.96 ± 1.09	kJ/mol
$k^*_{0,CO_{meth}}$	$13.57 \pm 1.40 \times 10^{-2}$	–
$Ea_{CO_{meth}}$	-10.28 ± 0.11	kJ/mol
$K^*_{0,COH}$	$6.57 \pm 7.31 \times 10^{-3}$	–
ΔH_{COH}	-61.09 ± 0.78	kJ/mol
K^*_{0,H_2}	$1.23 \pm 2.29 \times 10^{-2}$	–
ΔH_{H_2}	-13.61 ± 1.55	kJ/mol
$K^*_{0,OH}$	$1.21 \pm 9.74 \times 10^{-3}$	–
ΔH_{OH}	-45.09 ± 0.72	kJ/mol

In this case, the parameters to be calculated are:
$k^*_{0,RWGS}$, Ea_{RWGS}, $k^*_{0,CO_{meth}}$, $Ea_{CO_{meth}}$, $K^*_{0,COH}$, ΔH_{COH}, K^*_{0,H_2}, ΔH_{H_2}, $K^*_{0,OH}$, ΔH_{OH}.

This model showed very good stability, therefore we tried to use very different first guess values in different cases, to verify if the code converged to the same values in every case. The calculus always converged to values similar to those reported in Table 7.2, witnessing that an absolute minimum of the objective function F (Eq. 5.1.6) was found.

The activation energies of the two reactions are typical of a system where reactions are in series, in which the reaction intermediate is rapidly consumed. Indeed, the experimental σ_{CO} is always around 2%, while CH_4 is the main product, at the studied operative conditions. The rate of formation of CH_4 is mainly controlled by the RWGS reaction and, as soon as CO is formed, it is rapidly consumed. Thus, Ea_{RWGS} is similar to $Ea_{CO_{2_{meth}}}$ values we found studying the solo CO_2 methanation models (Table 5.17), while the energy barrier that CO methanation reaction has to overcome is much lower, in this case slightly negative.
Although activation energies should assume positive values, small negative values should not be rejected at first glance, considering that $Ea_{CO_{meth}}$ is the apparent activation energy of

the CO methanation reaction ($Ea_{CO_{meth}} = Ea_{step\,5} + \Delta H_{step\,4} + \Delta H_{CO} + \Delta H_{H_2}$), as proven in the model derivation reported in Appendix D.1.

Table 7.3: Quality of the regression of the Raco – Vidotto model.

Parameter	Value
$MPE_{\chi_{CO_2}}$	5.41%
$R^2_{\chi_{CO_2}}$	0.995
$MPE_{\sigma_{CO}}$	16.5%
$R^2_{\sigma_{CO}}$	0.975

So far, this is the best model in fitting CO selectivity (as witnessed by the value of $MPE_{\sigma_{CO}}$) and still performs very well in the fitting of CO_2 conversion, even though $MPE_{\chi_{CO_2}}$ value is not the best among the models analyzed up to now, the best being the Koschany et al. model (Sec. 5.3).

Table 7.4: Kinetic parameters of the Raco – Vidotto model.

Parameter	Value	U.o.M
$k_{0,RWGS}$	$2.38 \times 10^6 \pm 5.90 \times 10^5$	$mol/(s \cdot g_{cat} \cdot atm)$
Ea_{RWGS}	90.96 ± 1.09	kJ/mol
$k_{0,CO_{meth}}$	$8.71 \times 10^{-2} \pm 2.08 \times 10^{-2}$	$mol/(s \cdot g_{cat} \cdot atm^2)$
$Ea_{CO_{meth}}$	-10.28 ± 0.105	kJ/mol
$K_{0,COH}$	$1.54 \times 10^{-3} \pm 2.68 \times 10^{-4}$	$atm^{-1.5}$
ΔH_{COH}	-61.09 ± 0.78	kJ/mol
K_{0,H_2}	$1.88 \times 10^{-1} \pm 6.64 \times 10^{-2}$	atm^{-1}
ΔH_{H_2}	-13.61 ± 1.55	kJ/mol
$K_{0,OH}$	$2.20 \times 10^{-4} \pm 3.57 \times 10^{-5}$	$atm^{-0.5}$
ΔH_{OH}	-45.09 ± 0.72	kJ/mol

From Fig. 7.3 we can see that the model underestimates the temperature effect at lower temperatures, while the H_2/CO_2 ratio is problematic at low values, but still all the trends are well represented.

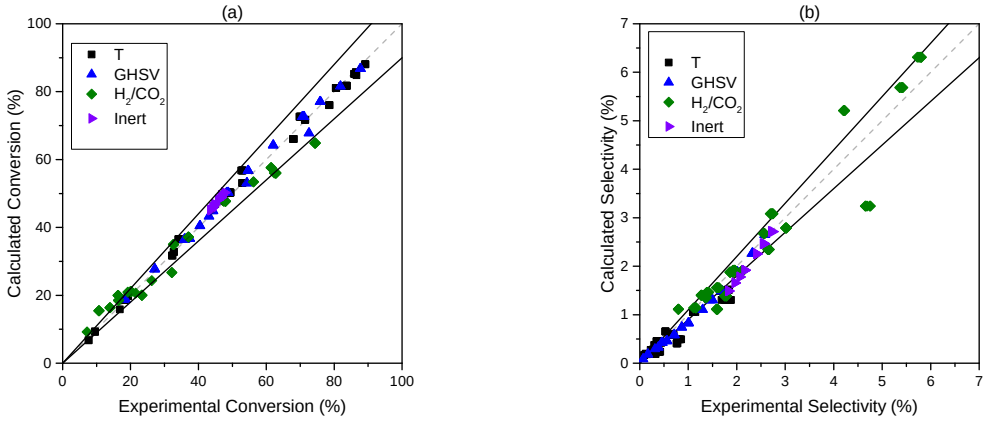

Figure 7.1: Parity plots of the Raco – Vidotto model. (a) CO_2 conversion. (b) CO selectivity.

It is worth remembering that reaction mechanisms can change when different reaction conditions are adopted, as already explained in Sec. 2.4, hence it is possible that some modifications to this model should be done when studying low H_2/CO_2 ratios.

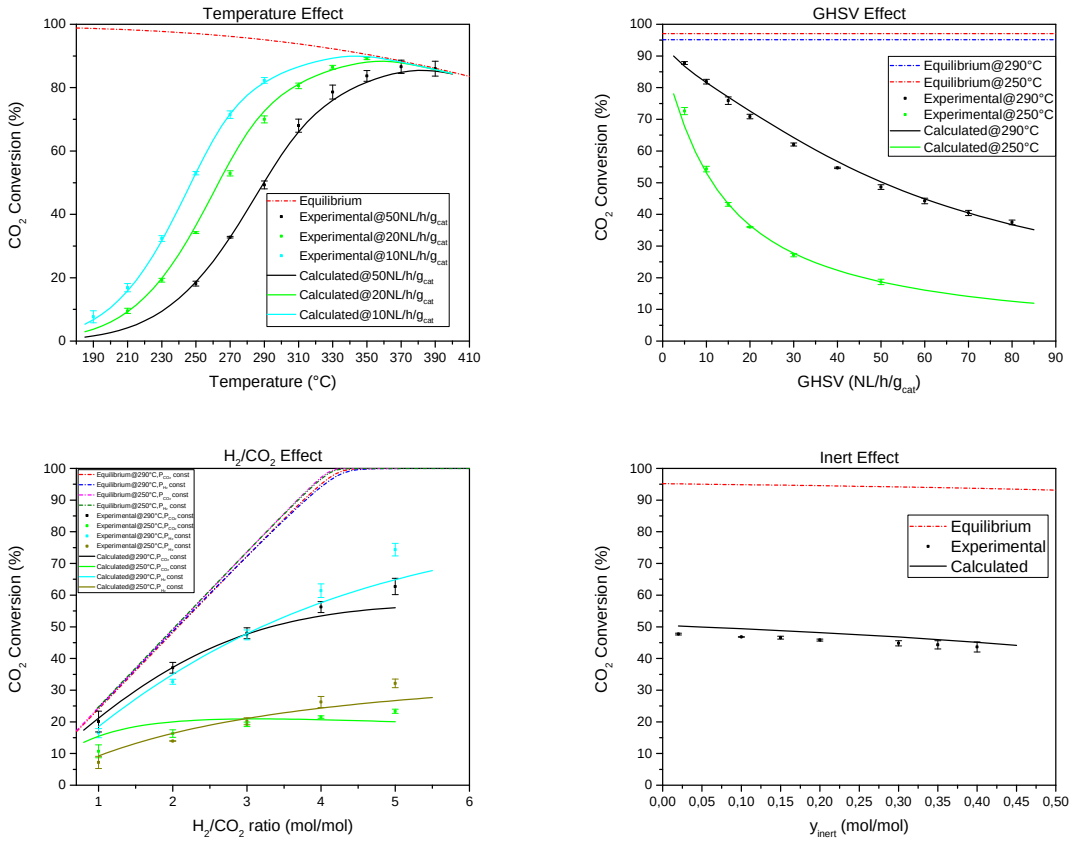

Figure 7.2: CO_2 conversion simulation plots of the Raco – Vidotto model.

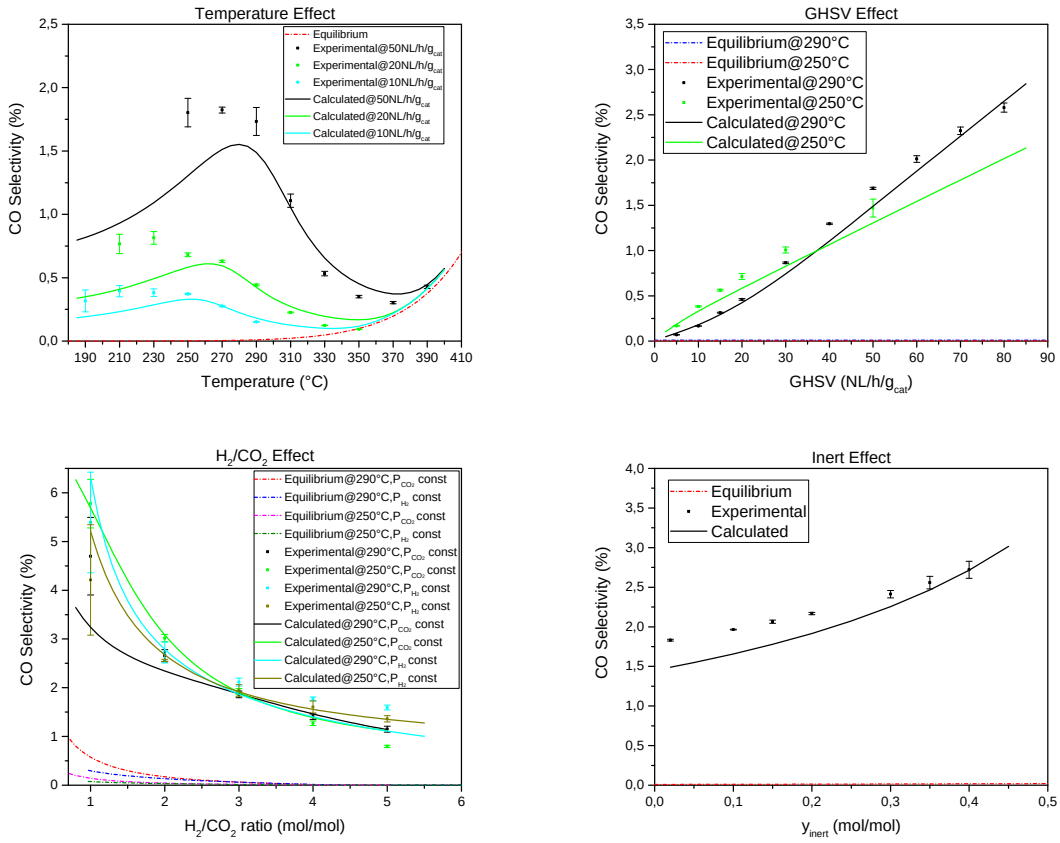

Figure 7.3: CO selectivity simulation plots of the Raco – Vidotto model.

Table 7.5: Correlation matrix of the Raco – Vidotto model.

	$k^*_{0,RWGS}$	Ea_{RWGS}	$k^*_{0,CO_{meth}}$	$Ea_{CO_{meth}}$	$K^*_{0,COH}$	ΔH_{COH}	K^*_{0,H_2}	ΔH_{H_2}	$K^*_{0,OH}$	ΔH_{OH}
$k^*_{0,RWGS}$	1.00E+00	3.38E-01	9.75E-01	3.05E-01	8.97E-01	1.36E-01	9.82E-01	3.89E-01	9.09E-01	3.67E-01
Ea_{RWGS}	3.38E-01	1.00E+00	2.96E-01	9.73E-01	2.22E-01	8.33E-01	3.23E-01	9.73E-01	3.43E-01	8.77E-01
$k^*_{0,CO_{meth}}$	9.75E-01	2.96E-01	1.00E+00	2.98E-01	9.60E-01	1.42E-01	9.60E-01	3.44E-01	9.37E-01	3.83E-01
$Ea_{CO_{meth}}$	3.05E-01	9.73E-01	2.98E-01	1.00E+00	2.48E-01	9.11E-01	2.91E-01	9.33E-01	3.59E-01	9.00E-01
$K^*_{0,COH}$	8.97E-01	2.22E-01	9.60E-01	2.48E-01	1.00E+00	1.24E-01	8.64E-01	2.53E-01	8.88E-01	3.45E-01
ΔH_{COH}	1.36E-01	8.33E-01	1.42E-01	9.11E-01	1.24E-01	1.00E+00	1.22E-01	7.48E-01	2.10E-01	7.50E-01
K^*_{0,H_2}	9.82E-01	3.23E-01	9.60E-01	2.91E-01	8.64E-01	1.22E-01	1.00E+00	3.96E-01	8.56E-01	3.27E-01
ΔH_{H_2}	3.89E-01	9.73E-01	3.44E-01	9.33E-01	2.53E-01	7.48E-01	3.96E-01	1.00E+00	3.56E-01	8.02E-01
$K^*_{0,OH}$	9.09E-01	3.43E-01	9.37E-01	3.59E-01	8.88E-01	2.10E-01	8.56E-01	3.56E-01	1.00E+00	4.95E-01
ΔH_{OH}	3.68E-01	8.77E-01	3.83E-01	9.00E-01	3.45E-01	7.50E-01	3.27E-01	8.02E-01	4.95E-01	1.00E+00

7.2 Vidotto – Raco model

In the second model we derived, steps 3 and 10 of the Raco – Vidotto model were summed, so that the O^* species never appears in the mechanism, neither in one of the steps or in the derivation of the rate expressions. The reaction mechanism is clearly suggesting a RWGS + CO-Hydro pathway (Sec. 2.4.1).

Table 7.6: Mechanism proposed to derive the Vidotto – Raco model.

Vidotto – Raco Mechanism
1) $H_2 + 2\ l \rightleftharpoons 2\ H^*$
2) $CO_2 + l \rightleftharpoons CO_2^*$
3) $CO_2^* + H^* \rightleftharpoons CO^* + OH^*$
4) $CO^* + H^* \rightleftharpoons COH^* + l$
5) $COH^* + H^* \rightleftharpoons CH^* + OH^*$
6) $CH^* + H^* \rightleftharpoons CH_2^* + l$
7) $CH_2^* + H^* \rightleftharpoons CH_3^* + l$
8) $CH_3^* + H^* \rightleftharpoons CH_4^* + l$
9) $CH_4^* \rightleftharpoons CH_4 + l$
10) $OH^* + H^* \rightleftharpoons H_2O^* + l$
11) $H_2O^* \rightleftharpoons H_2O + l$
12) $CO^* \rightleftharpoons CO + l$

In this model, the RDS of the RWGS reaction is the H-assisted CO_2 dissociation (step 3), while the RDS of the CO methanation is again the H-assisted carbo-hydroxyl consumption (step 5). H, OH, and COH are again considered as MASI. The following rate expressions can be derived:

$$r_{RWGS} = \frac{k_{RWGS} P_{CO_2} \sqrt{P_{H_2}} \left(1 - \dfrac{P_{CO} P_{H_2O}}{P_{H_2} P_{CO_2} K_{eqRWGS}}\right)}{\left(1 + \sqrt{K_{H_2} P_{H_2}} + K_{OH} \dfrac{P_{H_2O}}{\sqrt{P_{H_2}}} + K_{COH} \sqrt{P_{H_2}} P_{CO}\right)^2} \tag{7.2.1}$$

$$r_{CO_{meth}} = \frac{k_{CO_{meth}} P_{CO} P_{H_2} \left(1 - \frac{P_{CH_4} P_{H_2O}}{P_{CO} P_{H_2}^3 K_{eqCO_{meth}}}\right)}{\left(1 + \sqrt{K_{H_2} P_{H_2}} + K_{OH} \frac{P_{H_2O}}{\sqrt{P_{H_2}}} + K_{COH} \sqrt{P_{H_2}} P_{CO}\right)^2} \tag{7.2.2}$$

The complete derivation of this model is reported in Appendix D.2.

Adaptive parameters to be calculated are:
$k^*_{0,RWGS}$, Ea_{RWGS}, $k^*_{0,CO_{meth}}$, $Ea_{CO_{meth}}$, $K^*_{0,COH}$, ΔH_{COH}, K^*_{0,H_2}, ΔH_{H_2}, $K^*_{0,OH}$, ΔH_{OH}.

Table 7.7: Estimated parameters of the Vidotto – Raco model.

Parameter	Value	U.o.M
$k^*_{0,RWGS}$	$9.66 \pm 1.38 \times 10^{-2}$	–
$Ea_{CO_{RWGS}}$	106.15 ± 0.26	kJ/mol
$k^*_{0,CO_{meth}}$	$1.37 \times 10^{1} \pm 1.40 \times 10^{-2}$	–
$Ea_{CO_{meth}}$	4.40 ± 0.37	kJ/mol
$K^*_{0,COH}$	$6.71 \pm 7.41 \times 10^{-3}$	–
ΔH_{COH}	-53.43 ± 0.50	kJ/mol
K^*_{0,H_2}	$1.43 \pm 2.23 \times 10^{-2}$	–
ΔH_{H_2}	$-0.18 \pm 3.12 \times 10^{-2}$	kJ/mol
$K^*_{0,OH}$	$1.31 \pm 9.22 \times 10^{-3}$	–
ΔH_{OH}	-39.59 ± 0.44	kJ/mol

A strong similarity with the previous model can be observed both in the regression and the simulations, but a significant improvement in both $MPE_{\chi_{CO_2}}$ and $MPE_{\sigma_{CO}}$ can be observed.

The same considerations that were made about activation energies of the two reactions and the global reaction scheme of the Raco – Vidotto model can be adopted for this model. However, in this case a positive activation energy for CO methanation can be observed, which is physically consistent, despite being very low, together with an increase in the value of $k_{0,CO_{meth}}$.

Table 7.8: Quality of the regression of the Vidotto – Raco model.

Parameter	Value
$MPE_{\chi_{CO_2}}$	4.71%
$R^2_{\chi_{CO_2}}$	0.995
$MPE_{\sigma_{CO}}$	12.5%
$R^2_{\sigma_{CO}}$	0.976

Table 7.9: Kinetic parameters of the Vidotto – Raco model.

Parameter	Value	U.o.M
$k_{0,RWGS}$	$1.10 \times 10^8 \pm 7.62 \times 10^6$	$mol/(s \cdot g_{cat} \cdot atm^{1.5})$
$Ea_{CO_{RWGS}}$	106.15 ± 0.26	kJ/mol
$k_{0,CO_{meth}}$	2.34 ± 0.22	$mol/(s \cdot g_{cat} \cdot atm^2)$
$Ea_{CO_{meth}}$	4.40 ± 0.37	kJ/mol
$K_{0,COH}$	$9.15 \times 10^{-3} \pm 1.04 \times 10^{-3}$	$atm^{-1.5}$
ΔH_{COH}	-53.43 ± 0.50	kJ/mol
K_{0,H_2}	4.00 ± 0.12	atm^{-1}
ΔH_{H_2}	$-0.18 \pm 3.12 \times 10^{-2}$	kJ/mol
$K_{0,OH}$	$7.91 \times 10^{-4} \pm 8.08 \times 10^{-5}$	$atm^{-0.5}$
ΔH_{OH}	-39.59 ± 0.44	kJ/mol

The Vidotto-Raco model has the lowest value of $MPE_{\sigma_{CO}}$ and, despite its $MPE_{\chi_{CO_2}}$ is not the best encountered in our analysis of all the kinetic models, this model offers the best compromise between the fitting of CO_2 conversion and selectivity to CO.

Therefore, this model results the best one in describing the process of carbon dioxide methanation, exploiting a RWGS followed by CO methanation reaction, when also the selectivity to CO is a parameter of interest.

Further studies on the proposed Raco – Vidotto and Vidotto – Raco models should be conducted, focusing in particular on the difference between these two models, i.e. the presence (or absence) of the adsorbed oxygen species in the reaction mechanism.

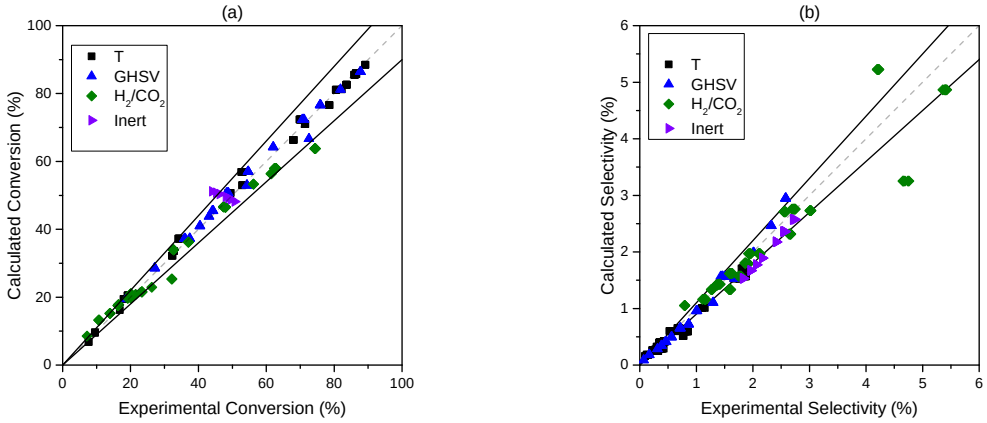

Figure 7.4: Parity plots of the Vidotto – Raco model. (a) CO_2 conversion. (b) CO selectivity.

We have verified, by deriving these two models, that the implementation of a model based on a consistent LHHW approach where no expedients are introduced leads to a better description of the system. These two models represent only our proposal for a reaction mechanism, but yet support the belief that the RWGS + CO-Hydro mechanism is the best pathway to describe the process.

As previously said, more studies on these models should be performed, with a particular emphasis on the species interacting on the catalyst surface.

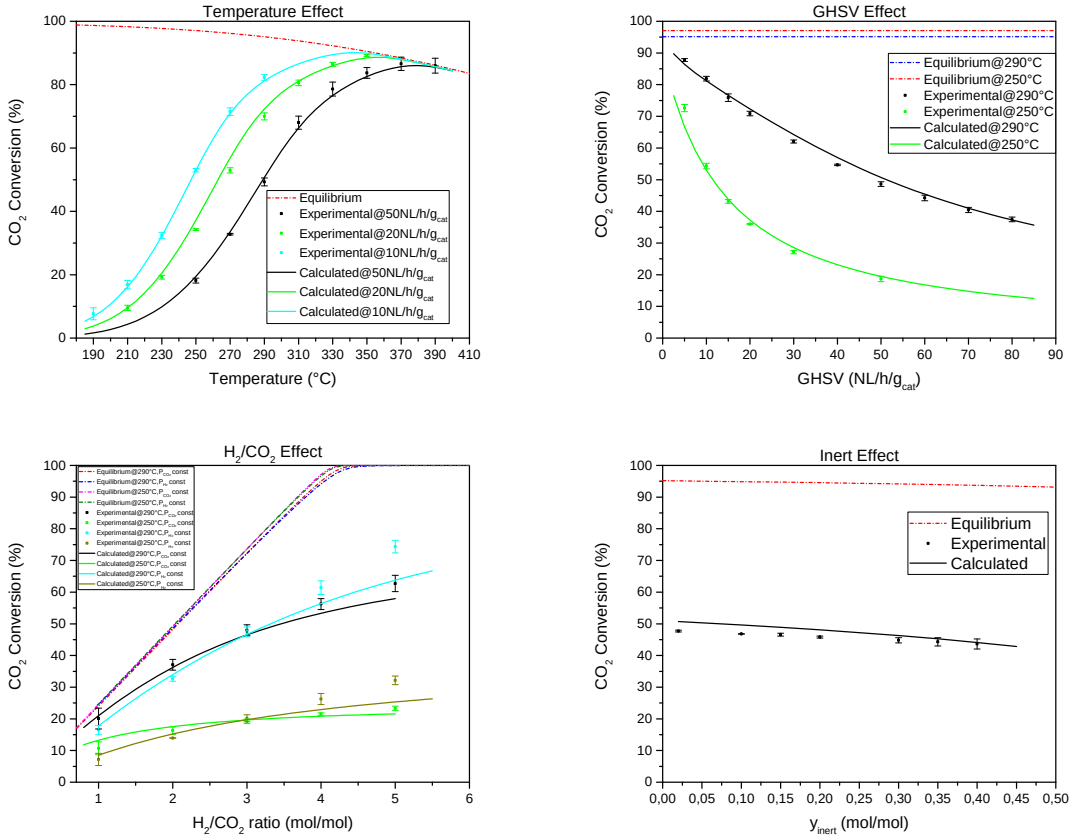

Figure 7.5: CO_2 conversion simulation plots of the Vidotto – Raco model.

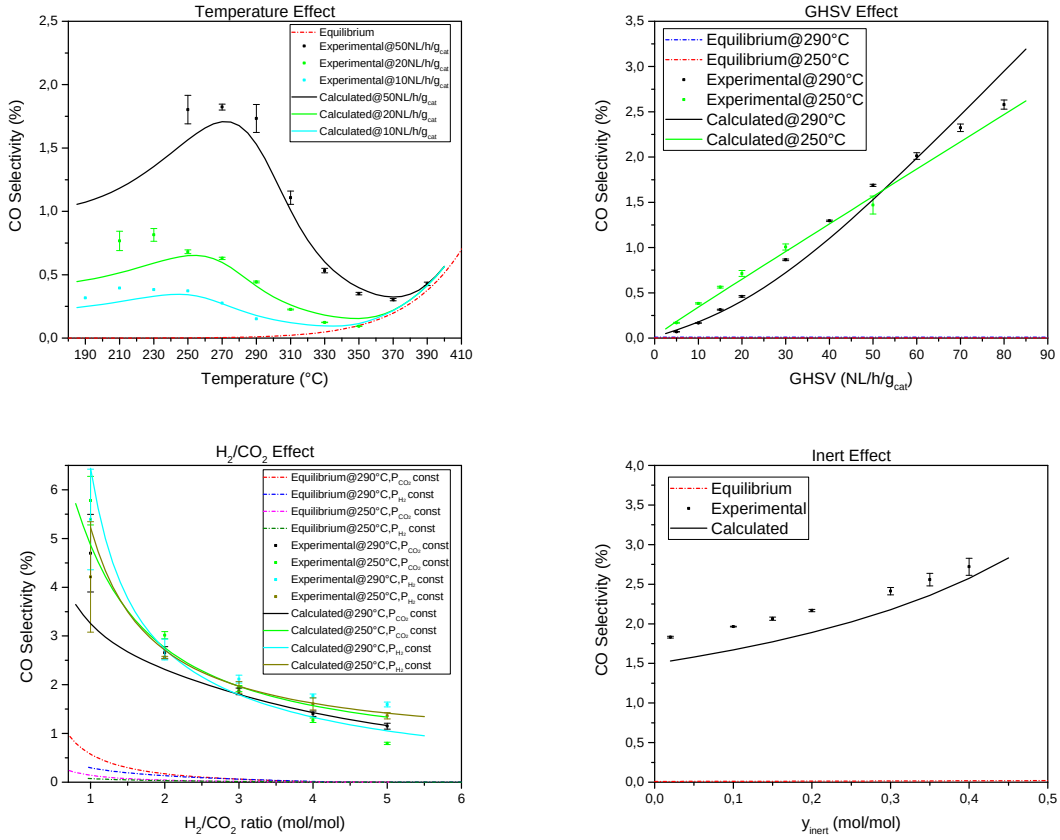

Figure 7.6: CO selectivity simulation plots of the Vidotto – Raco model.

Table 7.10: Correlation matrix of the Vidotto – Raco model.

	$k^*_{0,RWGS}$	$Ea_{CO_{RWGS}}$	$k^*_{0,CO_{met}}$	$Ea_{CO_{met}}$	$K^*_{0,COH}$	ΔH_{COH}	K^*_{0,H_2}	ΔH_{H_2}	$K^*_{0,OH}$	ΔH_{OH}
$k^*_{0,RWGS}$	1.00E+00	5.39E-02	9.76E-01	8.72E-02	8.89E-01	6.36E-02	9.75E-01	-1.35E-01	9.13E-01	1.47E-01
$Ea_{CO_{RWGS}}$	5.39E-02	1.00E+00	5.37E-02	7.90E-01	1.23E-01	6.80E-01	-5.23E-02	-5.62E-02	1.37E-01	7.32E-01
$k^*_{0,CO_{met}}$	9.76E-01	5.38E-02	1.00E+00	1.84E-01	9.56E-01	1.30E-01	9.54E-01	-1.60E-01	9.35E-01	2.15E-01
$Ea_{CO_{met}}$	8.71E-02	7.90E-01	1.84E-01	1.00E+00	3.00E-01	8.93E-01	2.42E-02	-7.93E-02	2.33E-01	7.28E-01
$K^*_{0,COH}$	8.89E-01	1.23E-01	9.56E-01	3.01E-01	1.00E+00	2.12E-01	8.40E-01	-1.56E-01	8.87E-01	2.92E-01
ΔH_{COH}	6.35E-02	6.80E-01	1.30E-01	8.93E-01	2.12E-01	1.00E+00	4.12E-02	-2.02E-01	1.27E-01	4.06E-01
K^*_{0,H_2}	9.75E-01	-5.23E-02	9.54E-01	2.42E-02	8.40E-01	4.12E-02	1.00E+00	-1.40E-01	8.45E-01	5.96E-02
ΔH_{H_2}	-1.35E-01	-5.62E-02	-1.60E-01	-7.93E-02	-1.56E-01	-2.02E-01	-1.40E-01	1.00E+00	-1.80E-01	1.16E-01
$K^*_{0,OH}$	9.13E-01	1.37E-01	9.35E-01	2.33E-01	8.87E-01	1.27E-01	8.45E-01	-1.80E-01	1.00E+00	3.32E-01
ΔH_{OH}	1.47E-01	7.32E-01	2.15E-01	7.28E-01	2.92E-01	4.06E-01	5.96E-02	1.16E-01	3.32E-01	1.00E+00

Table 7.11: Summary of results for the models proposed by us, compared with the most accurate model proposed in Ch. 6.

Model	Rate expression	k_0	$Ea\left[\frac{kJ}{mol}\right]$	$MPE_{\chi_{CO_2}}$	$R^2_{\chi_{CO_2}}$	$MPE_{\sigma_{CO}}$	$R^2_{\sigma_{CO}}$
R – V	$r_{RWGS} = \frac{k_{RWGS}P_{CO_2}\left(1-\frac{P_{CO}P_{H_2O}}{P_{H_2}P_{CO_2}K^{eq}_{RWGS}}\right)}{\left(1+\sqrt{K_{H_2}P_{H_2}}+K_{OH}\frac{P_{H_2O}}{\sqrt{P_{H_2}}}+K_{COH}\sqrt{P_{H_2}}P_{CO}\right)^2}$	$2.38\times10^6\pm5.9\times10^5\left[\frac{mol}{s\cdot g_{cat}\cdot atm}\right]$	90.96 ± 1.1	5.41%	0.995	16.5%	0.975
	$r_{CO_{meth}} = \frac{k_{CO_{meth}}P_{CO}P_{H_2}\left(1-\frac{P_{CH_4}P_{H_2O}}{P_{CO}P^3_{H_2}K_{eq,CO_{meth}}}\right)}{\left(1+\sqrt{K_{H_2}P_{H_2}}+K_{OH}\frac{P_{H_2O}}{\sqrt{P_{H_2}}}+K_{COH}\sqrt{P_{H_2}}P_{CO}\right)^2}$	$8.71\times10^{-2}\pm2.1\times10^{-2}\left[\frac{mol}{s\cdot g_{cat}\cdot atm^2}\right]$	-10.28 ± 0.11				
V – R	$r_{RWGS} = \frac{k_{RWGS}P_{CO_2}\sqrt{P_{H_2}}\left(1-\frac{P_{CO}P_{H_2O}}{P_{H_2}P_{CO_2}K^{eq}_{RWGS}}\right)}{\left(1+\sqrt{K_{H_2}P_{H_2}}+K_{OH}\frac{P_{H_2O}}{\sqrt{P_{H_2}}}+K_{COH}\sqrt{P_{H_2}}P_{CO}\right)^2}$	$1.10\times10^8\pm7.6\times10^6\left[\frac{mol}{s\cdot g_{cat}\cdot atm^{1.5}}\right]$	106.15 ± 0.26	4.71%	0.995	12.5%	0.976
	$r_{CO_{meth}} = \frac{k_{CO_{meth}}P_{CO}P_{H_2}\left(1-\frac{P_{CH_4}P_{H_2O}}{P_{CO}P^3_{H_2}K_{eq,CO_{meth}}}\right)}{\left(1+\sqrt{K_{H_2}P_{H_2}}+K_{OH}\frac{P_{H_2O}}{\sqrt{P_{H_2}}}+K_{COH}\sqrt{P_{H_2}}P_{CO}\right)^2}$	$2.34\pm0.22\left[\frac{mol}{s\cdot g_{cat}\cdot atm^2}\right]$	4.40 ± 0.37				
Farsi	$r_{RWGS} = \frac{k_1P^{0.5}_{CO_2}P^{0.5}_{H_2}}{(1+K_{H_2O}P_{H_2O})^2}\left(1-\frac{P_{CO}P_{H_2O}}{P_{H_2}P_{CO_2}K^{eq}_{RWGS}}\right)$	$5.37\times10^4\pm2.12\times10^3\left[\frac{mol}{s\cdot g_{cat}\cdot atm}\right]$	87.86 ± 0.18	6.30%	0.992	25.1%	0.860
	$r_{CO_{meth}} = \frac{k_2P_{CO}P^{0.5}_{H_2}}{(1+K_{H_2O}P_{H_2O})^2}\left(1-\frac{P_{CH_4}P_{H_2O}}{P_{CO}P^3_{H_2}K_{eq,CO_{meth}}}\right)$	$0.150\pm6.70\times10^{-3}\left[\frac{mol}{s\cdot g_{cat}\cdot atm^{1.5}}\right]$	5.87 ± 0.20				

Chapter 8

Model Applications on Ruthenium Input

It is reasonable to think that a mechanism that performs well on a Ni-based catalyst can be effective also with a different catalyst. For this reason, in this chapter we will apply the same mechanisms we hypothesized in the Raco − Vidotto and Vidotto − Raco models (Ch. 7) on a Ru-based dataset, collected on a 0.5% wt. Ru/Al_2O_3 in a previous work by Sangalli [84]. The complete ruthenium dataset is reported in Appendix B.2.

Working with this dataset, these operating conditions effects were studied:

- Temperature effect;
- Pressure effect;
- GHSV effect;
- $\frac{H_2}{CO_2}$ effect;
- Inert effect;
- H_2O effect.

In this case, most of the data were collected at 310°C, therefore a $T_{ref} = 583.15\,K = 310$°C was chosen as reference temperature in the non-linear regressions for the Ru-based dataset.

8.1 Raco – Vidotto Model

At first, we performed the regression on the Raco – Vidotto model, whose rate expressions are the same proposed in Sec. 7.1 (Eq. 7.1.1 and 7.1.2). The adaptive parameters, again, are: $k^*_{0,RWGS}$, Ea_{RWGS}, $k^*_{0,CO_{meth}}$, $Ea_{CO_{meth}}$, $K^*_{0,COH}$, ΔH_{COH}, K^*_{0,H_2}, ΔH_{H_2}, $K^*_{0,OH}$, ΔH_{OH}.

Table 8.1: Estimated parameters of the Raco – Vidotto model for the ruthenium input.

Parameter	Value	U.o.M
$k^*_{0,RWGS}$	$5.09 \pm 5.47 \times 10^{-2}$	–
Ea_{RWGS}	71.29 ± 17.09	kJ/mol
$k^*_{0,CO_{meth}}$	$1.05 \pm 5.17 \times 10^{-2}$	–
$Ea_{CO_{meth}}$	-4.15 ± 16.08	kJ/mol
$K^*_{0,COH}$	$6.65 \pm 6.36 \times 10^{-2}$	–
ΔH_{COH}	-75.47 ± 17.27	kJ/mol
K^*_{0,H_2}	$-2.23 \times 10^{1} \pm 5.71 \times 10^{1}$	–
ΔH_{H_2}	-9.19 ± 83.93	kJ/mol
$K^*_{0,OH}$	$3.93 \times 10^{-1} \pm 1.03 \times 10^{-1}$	–
ΔH_{OH}	-8.53 ± 29.54	kJ/mol

From Table 8.2 that the quality of the regression on this Ru-based dataset is even better than the one performed on the Nickel dataset 7.3. The parity plots, in Fig. 8.1, confirm the high quality of the model, showing that only few points are outside the 10% limit for the CO_2 conversion. A good fitting can be observed also for CO selectivity.

Table 8.2: Quality of the regression of the Raco – Vidotto model for the ruthenium input.

Parameter	Value
$MPE_{\chi_{CO_2}}$	3.51%
$R^2_{\chi_{CO_2}}$	0.991
$MPE_{\sigma_{CO}}$	11.1%
$R^2_{\sigma_{CO}}$	0.980

Table 8.3: Kinetic parameters of the Raco – Vidotto model for the ruthenium input.

Parameter	Value	U.o.M
$k_{0,RWGS}$	$6.68 \times 10^2 \pm 2.39 \times 10^3$	$mol/(s \cdot g_{cat} \cdot atm)$
Ea_{RWGS}	71.29 ± 17.09	kJ/mol
$k_{0,CO_{meth}}$	$1.52 \times 10^{-2} \pm 5.11 \times 10^{-2}$	$mol/(s \cdot g_{cat} \cdot atm^2)$
$Ea_{CO_{meth}}$	-4.15 ± 16.08	kJ/mol
$K_{0,COH}$	$7.73 \times 10^{-5} \pm 2.80 \times 10^{-4}$	$atm^{-1.5}$
ΔH_{COH}	-75.47 ± 17.27	kJ/mol
K_{0,H_2}	$2.99 \times 10^{-11} \pm 2.22 \times 10^{-9}$	atm^{-1}
ΔH_{H_2}	-9.19 ± 83.93	kJ/mol
$K_{0,OH}$	$1.09 \times 10^{-1} \pm 6.76 \times 10^{-1}$	$atm^{-0.5}$
ΔH_{OH}	-8.53 ± 29.54	kJ/mol

Activation energies for the RWGS and CO methanation reactions are comparable to those found on the nickel dataset, but in this case $k_{0,RWGS}$ has a lower value, suggesting a lower catalyst activity. Indeed, the CO selectivities of the two datasets are comparable, while higher temperature and lower GHSV are needed on the Ru-based catalyst to obtain the same CO_2 conversion obtained on the Ni-based catalyst, since Ruthenium loading was very low. Moreover, K_{0,H_2} is very low if compared to the other adsorption terms, and ΔH_{H_2} is not low enough to compensate the value of K_{0,H_2} in calculating K_{H_2}. Thus, in further developments of this model on Ruthenium catalysts, the hydrogen adsorption term can be left outside the calculus (or even neglected) to make the model more efficient.

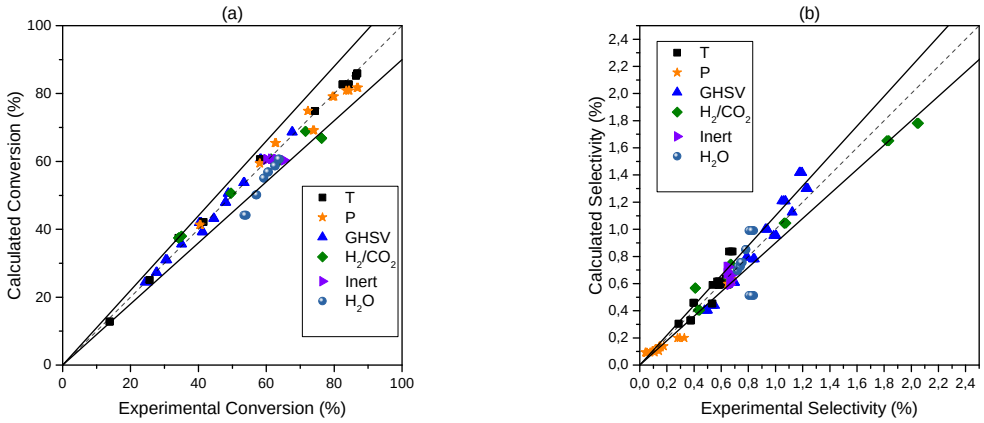

Figure 8.1: Parity plots of the Raco – Vidotto model for the ruthenium input. (a) CO_2 conversion. (b) CO selectivity.

From the simulation plots in Fig. 8.2 and 8.3, we can see that all the set of data is well approximated. The only unusual behavior is represented by the increase of CO selectivity at low pressure: the model strongly overestimates the experimental values. This trend is confirmed in the inert effect plot, in which the model overestimates the selectivity at high inert concentration, hence at low reactants partial pressures.

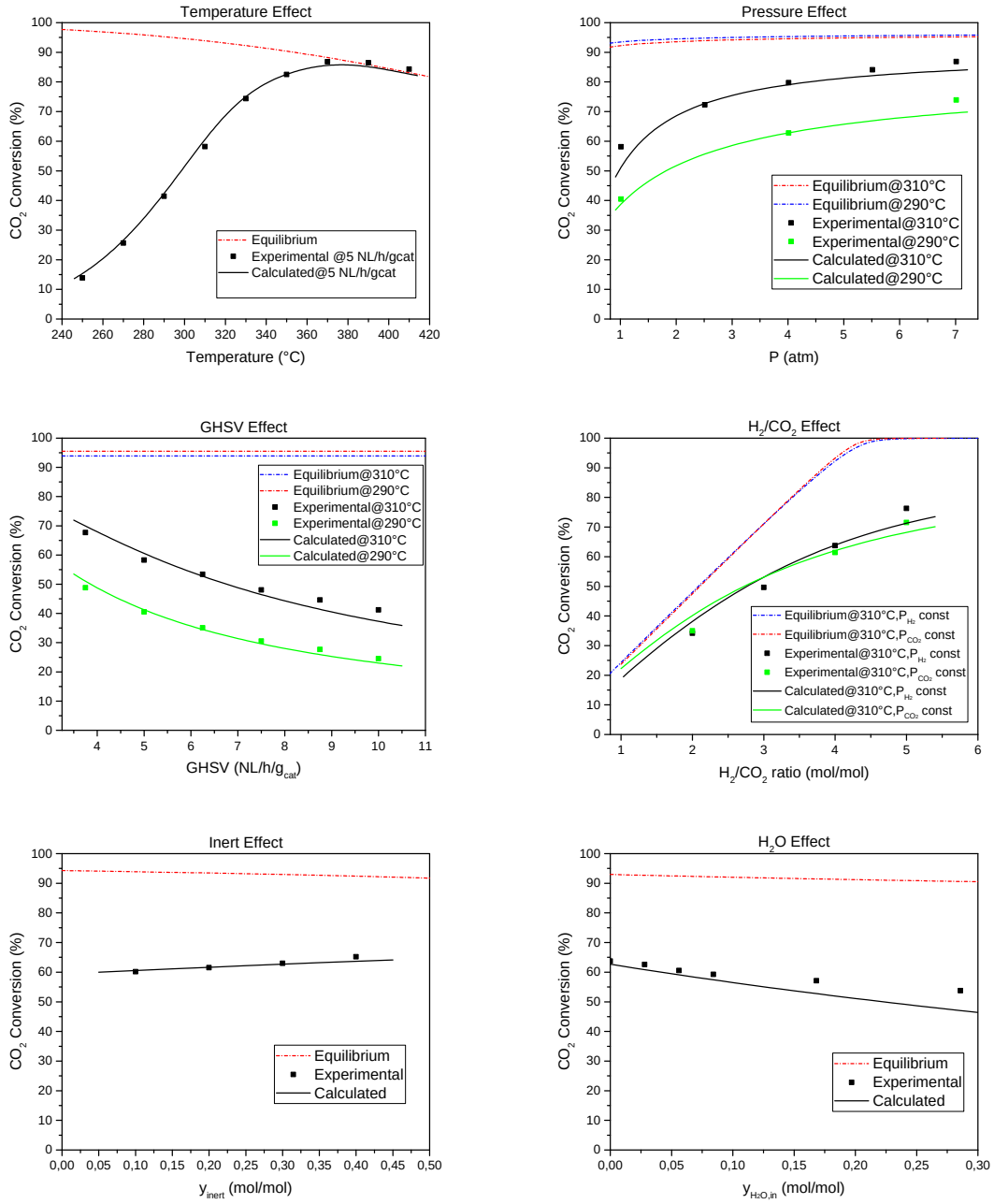

Figure 8.2: CO_2 conversion simulation plots of the Raco – Vidotto model for the ruthenium input.

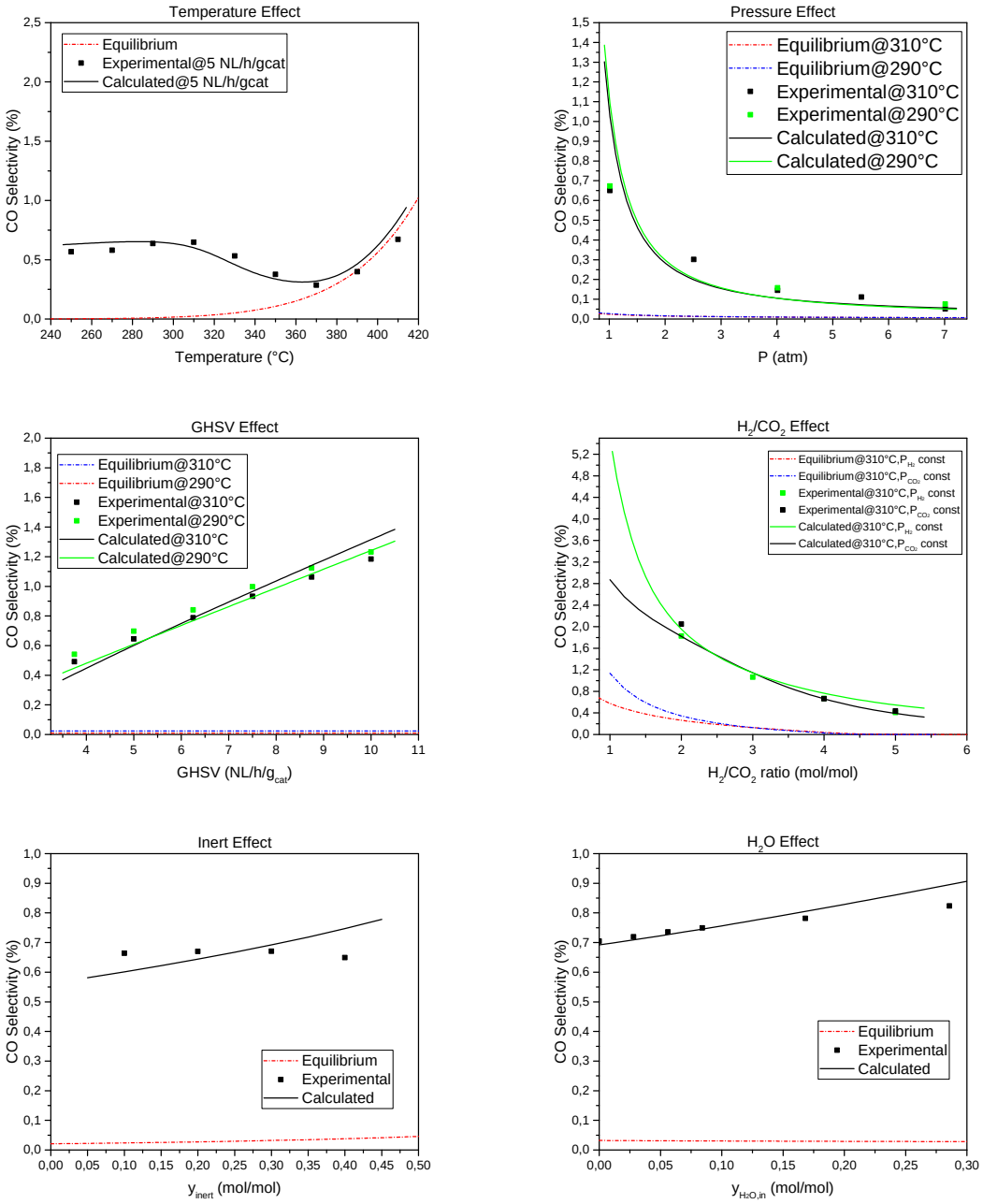

Figure 8.3: CO selectivity simulation plots of the Raco – Vidotto model for the ruthenium input.

Table 8.4: Correlation matrix of the Raco – Vidotto model for the ruthenium input.

	$k^*_{0,RWGS}$	Ea_{RWGS}	$k^*_{0,CO_{meth}}$	$Ea_{CO_{meth}}$	$K^*_{0,COH}$	ΔH_{COH}	K^*_{0,H_2}	ΔH_{H_2}	$K^*_{0,OH}$	ΔH_{OH}
$k^*_{0,RWGS}$	1.00E+00	2.03E-01	8.73E-01	1.73E-01	7.15E-01	1.52E-01	-7.44E-02	-1.24E-01	6.33E-01	2.19E-01
Ea_{RWGS}	2.03E-01	1.00E+00	1.53E-01	9.58E-01	6.13E-02	8.76E-01	-9.14E-02	-5.10E-01	2.90E-01	8.51E-01
$k^*_{0,CO_{meth}}$	8.73E-01	1.54E-01	1.00E+00	1.97E-01	9.18E-01	1.95E-01	3.93E-02	-1.94E-01	5.60E-01	2.39E-01
$Ea_{CO_{meth}}$	1.73E-01	9.58E-01	1.96E-01	1.00E+00	1.18E-01	9.64E-01	-5.55E-02	-5.42E-01	2.94E-01	8.37E-01
$K^*_{0,COH}$	7.15E-01	6.14E-02	9.18E-01	1.18E-01	1.00E+00	1.51E-01	3.64E-02	-1.20E-01	2.16E-01	1.77E-01
ΔH_{COH}	1.52E-01	8.76E-01	1.94E-01	9.64E-01	1.51E-01	1.00E+00	-1.03E-01	-4.47E-01	2.40E-01	7.12E-01
K^*_{0,H_2}	-7.44E-02	-9.14E-02	3.93E-02	-5.55E-02	3.64E-02	-1.03E-01	1.00E+00	-3.12E-01	-1.87E-03	3.51E-02
ΔH_{H_2}	-1.24E-01	-5.10E-01	-1.94E-01	-5.42E-01	-1.20E-01	-4.47E-01	-3.12E-01	1.00E+00	-2.37E-01	-6.65E-01
$K^*_{0,OH}$	6.33E-01	2.90E-01	5.60E-01	2.94E-01	2.16E-01	2.40E-01	-1.88E-03	-2.37E-01	1.00E+00	2.39E-01
ΔH_{OH}	2.19E-01	8.51E-01	2.39E-01	8.37E-01	1.77E-01	7.12E-01	3.51E-02	-6.65E-01	2.39E-01	1.00E+00

8.2 Vidotto – Raco Model

The Vidotto – Raco model was also implemented on the Ruthenium dataset, by applying the equation proposed in Sec. 7.2 to describe the process (Eq. 7.2.1 and 7.2.2).
Adaptive parameters to be calculated are:
$k^*_{0,RWGS}$, Ea_{RWGS}, $k^*_{0,CO_{meth}}$, $Ea_{CO_{meth}}$, $K^*_{0,COH}$, ΔH_{COH}, K^*_{0,H_2}, ΔH_{H_2}, $K^*_{0,OH}$, ΔH_{OH}.

Table 8.5: Estimated parameters of the Vidotto – Raco model for the ruthenium input.

Parameter	Value	U.o.M
$k^*_{0,RWGS}$	$5.43 \pm 5.23 \times 10^{-2}$	–
Ea_{RWGS}	112.74 ± 9.29	kJ/mol
$k^*_{0,CO_{meth}}$	$1.04 \pm 4.68 \times 10^{-2}$	–
$Ea_{CO_{meth}}$	14.40 ± 6.92	kJ/mol
$K^*_{0,COH}$	$6.42 \pm 6.31 \times 10^{-2}$	–
ΔH_{COH}	-48.00 ± 11.71	kJ/mol
K^*_{0,H_2}	-27.45 ± 53.79	–
ΔH_{H_2}	$-46.51 \pm 4.33 \times 10^2$	kJ/mol
$K^*_{0,OH}$	0.21 ± 0.11	–
ΔH_{OH}	-9.30 ± 15.56	kJ/mol

Also in this case the model performs very well, even if it is slightly worse than the Raco – Vidotto model on Ru-based catalyst, if one confronts the value of $MPE_{\chi_{CO_2}}$ and $MPE_{\sigma_{CO}}$.

Table 8.6: Quality of the regression of the Vidotto – Raco model for the ruthenium input.

Parameter	Value
$MPE_{\chi_{CO_2}}$	3.63%
$R^2_{\chi_{CO_2}}$	0.986
$MPE_{\sigma_{CO}}$	11.9%
$R^2_{\sigma_{CO}}$	0.970

Table 8.7: Kinetic parameters of the Vidotto – Raco model for the ruthenium input.

Parameter	Value	U.o.M
$k_{0,RWGS}$	$6.55 \times 10^6 \pm 1.29 \times 10^7$	$mol/(s \cdot g_{cat} \cdot atm^{1.5})$
Ea_{RWGS}	112.74 ± 9.29	kJ/mol
$k_{0,CO_{meth}}$	0.69 ± 1.01	$mol/(s \cdot g_{cat} \cdot atm^2)$
$Ea_{CO_{meth}}$	14.40 ± 6.92	kJ/mol
$K_{0,COH}$	$2.17 \times 10^{-2} \pm 5.37 \times 10^{-2}$	$atm^{-1.5}$
ΔH_{COH}	-48.00 ± 11.71	kJ/mol
K_{0,H_2}	$5.82 \times 10^{-17} \pm 8.33 \times 10^{-15}$	atm^{-1}
ΔH_{H_2}	$-46.51 \pm 4.33 \times 10^2$	kJ/mol
$K_{0,OH}$	0.11 ± 0.37	$atm^{-0.5}$
ΔH_{OH}	-9.30 ± 15.56	kJ/mol

A strong difference with the previous model is represented by the value of Ea_{RWGS}, much higher. Again, K_{0,H_2} is very low, and should be neglected to optimize the code in further studies on this model.

As for the Ni-based dataset, the Raco – Vidotto and Vidotto – Raco models show very similar behavior, and again the activation energy for the CO methanation reaction is negative in the Raco – Vidotto, positive and very low in the Vidotto – Raco model.
The Vidotto – Raco model considered in this section shows a good fitting of the experimental data and, despite higher values of $MPE_{\chi_{CO_2}}$ and $MPE_{\sigma_{CO}}$, does not overestimate selectivity to CO at low pressures, showing a better fitting than the previous model.

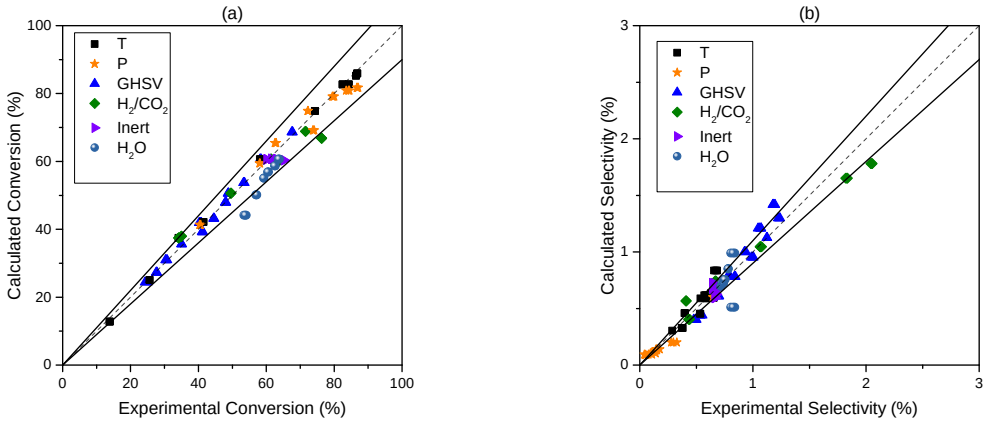

Figure 8.4: Parity plots of the Vidotto – Raco model for the ruthenium input. (a) CO_2 conversion. (b) CO selectivity.

In conclusion, both the models studied in this chapter show very good performances in fitting the Ru-based dataset. Moreover, a comparison between what was found with these two models and the results reported by Sangalli [84] on the same dataset can be found in Table 8.9. Both the Raco – Vidotto and the Vidotto – Raco models perform better than the Sangalli model, specially in the fitting of CO selectivity, having much lower $MPE_{\sigma_{CO}}$.

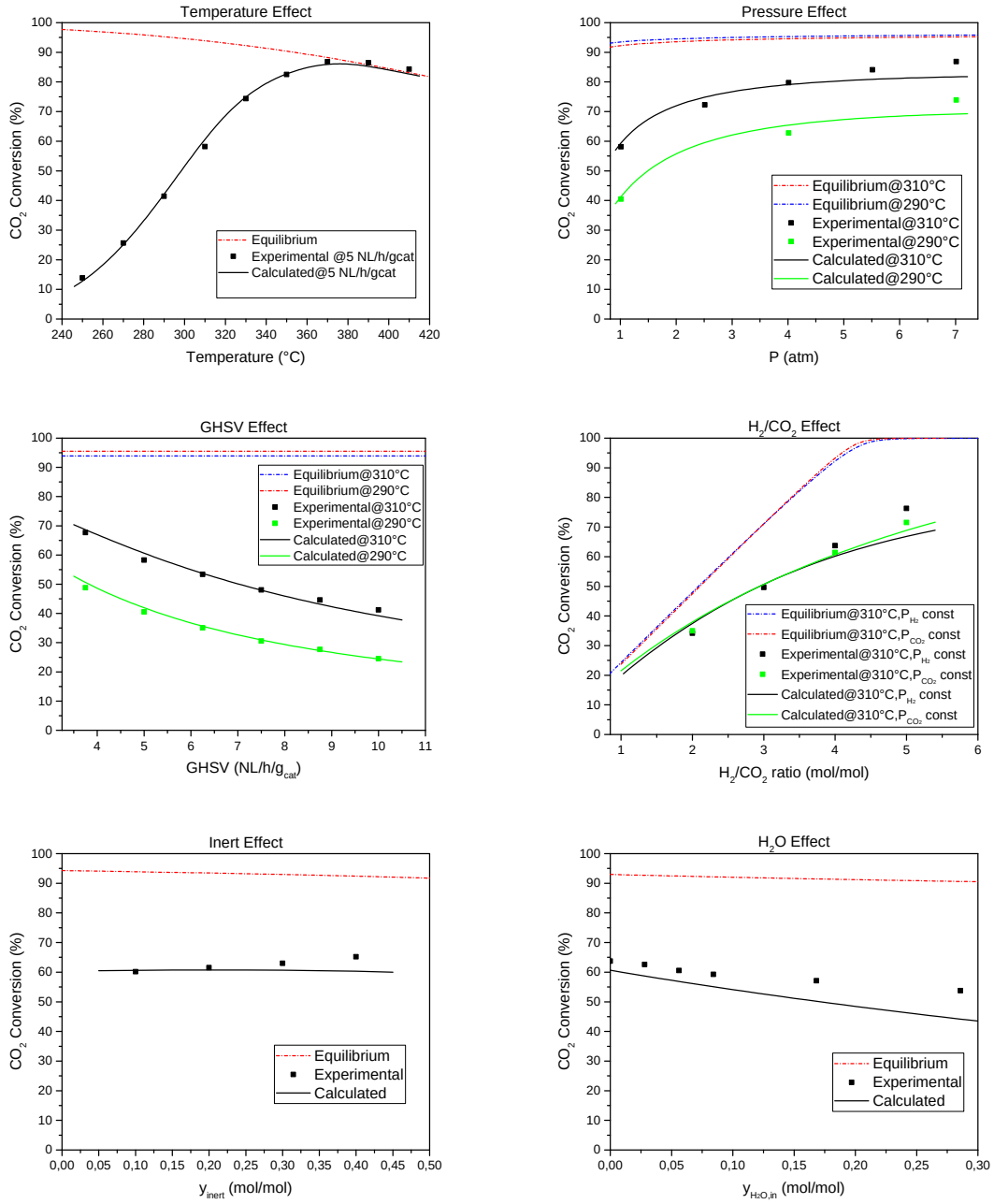

Figure 8.5: CO_2 conversion simulation plots of the Vidotto – Raco model for the ruthenium input.

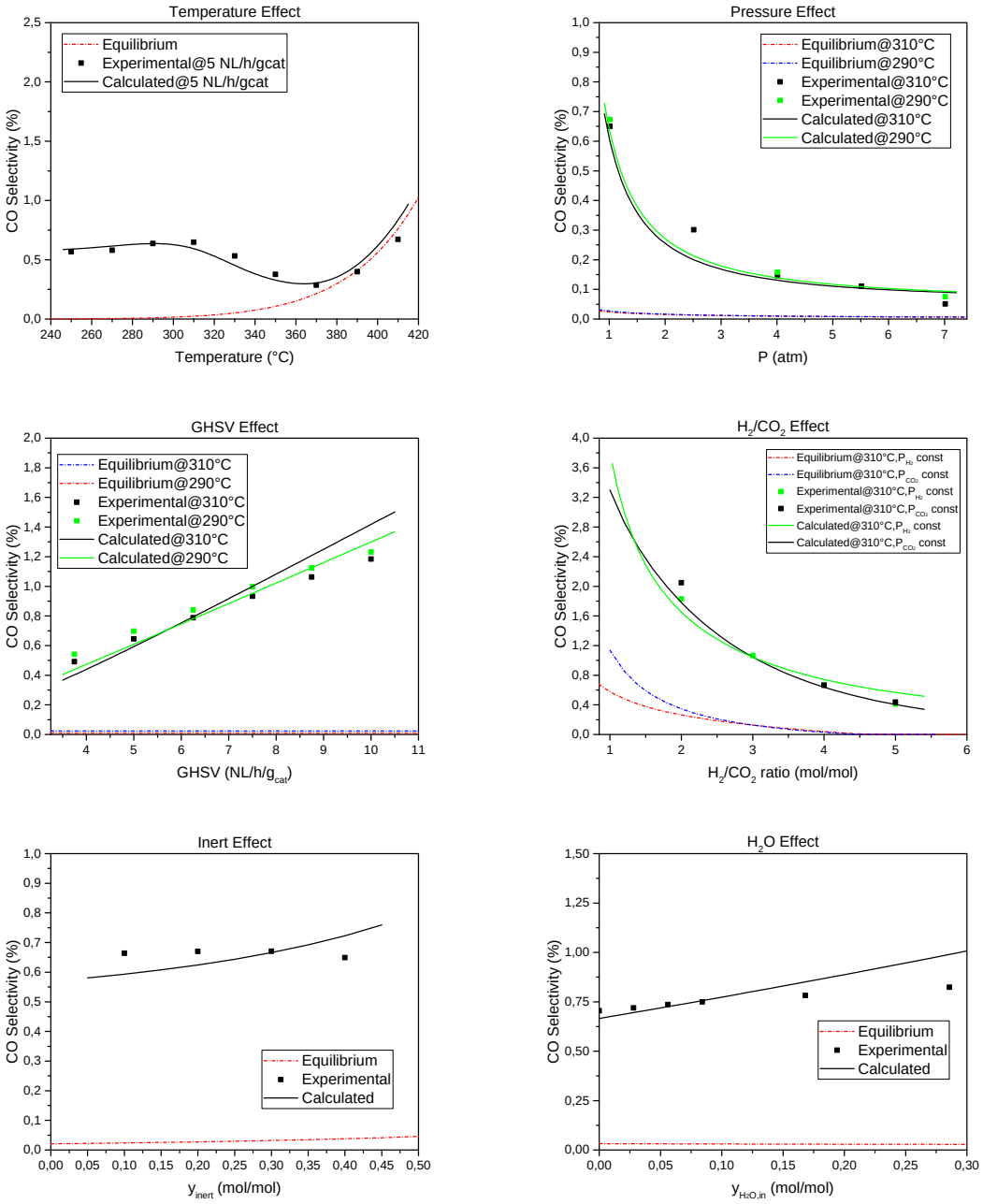

Figure 8.6: CO selectivity simulation plots of the Vidotto – Raco model for the ruthenium input.

Table 8.8: Correlation matrix of the Vidotto – Raco model for the ruthenium input.

	$k^*_{0,RWGS}$	Ea_{RWGS}	$k^*_{0,CO_{meth}}$	$Ea_{CO_{meth}}$	$K^*_{0,COH}$	ΔH_{COH}	K^*_{0,H_2}	ΔH_{H_2}	$K^*_{0,OH}$	ΔH_{OH}
$k^*_{0,RWGS}$	1.00E+00	4.94E-01	8.30E-01	4.80E-01	5.89E-01	3.37E-01	-2.40E-01	-4.71E-03	6.48E-01	1.70E-01
Ea_{RWGS}	4.94E-01	1.00E+00	3.67E-01	7.92E-01	2.64E-01	5.37E-01	-1.54E-01	-1.36E-01	2.88E-01	2.76E-01
$k^*_{0,CO_{meth}}$	8.30E-01	3.67E-01	1.00E+00	5.50E-01	8.72E-01	4.46E-01	-2.14E-01	1.13E-02	5.85E-01	1.63E-01
$Ea_{CO_{meth}}$	4.80E-01	7.92E-01	5.50E-01	1.00E+00	4.83E-01	8.67E-01	-1.92E-01	-1.18E-01	3.38E-01	1.54E-01
$K^*_{0,COH}$	5.89E-01	2.64E-01	8.72E-01	4.83E-01	1.00E+00	4.83E-01	-1.16E-01	1.09E-02	1.57E-01	1.25E-01
ΔH_{COH}	3.37E-01	5.37E-01	4.46E-01	8.67E-01	4.83E-01	1.00E+00	-6.38E-02	-9.00E-02	1.84E-01	-2.21E-01
K^*_{0,H_2}	-2.40E-01	-1.54E-01	-2.14E-01	-1.92E-01	-1.16E-01	-6.38E-02	1.00E+00	-2.09E-01	-1.62E-01	-2.28E-01
ΔH_{H_2}	-4.71E-03	-1.36E-01	1.13E-02	-1.18E-01	1.09E-02	-9.00E-02	-2.09E-01	1.00E+00	3.60E-02	1.32E-01
$K^*_{0,OH}$	6.48E-01	2.88E-01	5.85E-01	3.38E-01	1.57E-01	1.84E-01	-1.62E-01	3.60E-02	1.00E+00	5.91E-02
ΔH_{OH}	1.70E-01	2.76E-01	1.63E-01	1.54E-01	1.25E-01	-2.21E-01	-2.28E-01	1.32E-01	5.91E-02	1.00E+00

Table 8.9: Summary of results for the models proposed by us on the ruthenium dataset, compared with Sangalli's best results. [84]

Model	Rate expression	k_0	$Ea\left[\frac{kJ}{mol}\right]$	$MPE_{\chi_{CO_2}}$	$R^2_{\chi_{CO_2}}$	$MPE_{\sigma_{CO}}$	$R^2_{\sigma_{CO}}$
R – V	$r_{RWGS} = \frac{k_{RWGS} P_{CO_2}\left(1 - \frac{P_{CO}P_{H_2O}}{P_{H_2}P_{CO_2}K^{eq}_{RWGS}}\right)}{\left(1 + \sqrt{K_{H_2}P_{H_2}} + K_{OH}\frac{P_{H_2O}}{\sqrt{P_{H_2}}} + K_{COH}\sqrt{P_{H_2}}P_{CO}\right)^2}$	$668 \pm 2391\left[\frac{mol}{s \cdot g_{cat} \cdot atm}\right]$	71.29 ± 17.1	3.51%	0.991	11.1%	0.980
	$r_{CO_{met}} = \frac{k_{CO_{met}} P_{CO} P_{H_2}\left(1 - \frac{P_{CH_4}P_{H_2O}}{P_{CO}P_{H_2}3K^{eq}_{CO_{met}}}\right)}{\left(1 + \sqrt{K_{H_2}P_{H_2}} + K_{OH}\frac{P_{H_2O}}{\sqrt{P_{H_2}}} + K_{COH}\sqrt{P_{H_2}}P_{CO}\right)^2}$	$1.52 \times 10^{-2} \pm 5.1 \times 10^{-2}\left[\frac{mol}{s \cdot g_{cat} \cdot atm^2}\right]$	-4.15 ± 16.1				
V – R	$r_{RWGS} = \frac{k_{RWGS} P_{CO_2}\sqrt{P_{H_2}}\left(1 - \frac{P_{CO}P_{H_2O}}{P_{H_2}P_{CO_2}K^{eq}_{RWGS}}\right)}{\left(1 + \sqrt{K_{H_2}P_{H_2}} + K_{OH}\frac{P_{H_2O}}{\sqrt{P_{H_2}}} + K_{COH}\sqrt{P_{H_2}}P_{CO}\right)^2}$	$6.65 \times 10^6 \pm 1.3 \times 10^7\left[\frac{mol}{s \cdot g_{cat} \cdot atm^{1.5}}\right]$	112.74 ± 9.3	3.63%	0.986	11.9%	0.970
	$r_{CO_{met}} = \frac{k_{CO_{met}} P_{CO} P_{H_2}\left(1 - \frac{P_{CH_4}P_{H_2O}}{P_{CO}P^3_{H_2}K^{eq}_{CO_{met}}}\right)}{\left(1 + \sqrt{K_{H_2}P_{H_2}} + K_{OH}\frac{P_{H_2O}}{\sqrt{P_{H_2}}} + K_{COH}\sqrt{P_{H_2}}P_{CO}\right)^2}$	$0.686 \pm 1.0\left[\frac{mol}{s \cdot g_{cat} \cdot atm^2}\right]$	14.40 ± 6.9				
Sangalli	$r_{WGS} = \frac{k_{WGS}\frac{P_{CO}P_{H_2O}}{P_{H_2}}\left(1 - \frac{P_{CO_2}P_{H_2}}{P_{CO}P_{H_2O}K^{eq}_{WGS}}\right)}{\left(1 + K_{CO}P_{CO} + K_{H_2O}\frac{P_{H_2O}}{P_{H_2}}\right)^2}$	$1.61 \times 10^5\left[\frac{mol}{s \cdot g_{cat} \cdot atm}\right]$	81.4	3.77%	0.995	30.9%	0.999
	$r_{SR} = \frac{k_{SR}\frac{P_{CH_4}P_{H_2O}}{P^{2.5}_{H_2}}\left(1 - \frac{P_{CH_4}P_{H_2O}}{P_{CO}P^3_{H_2}K^{eq}_{SR}}\right)}{\left(1 + K_{CO}P_{CO} + K_{H_2O}\frac{P_{H_2O}}{P_{H_2}}\right)^2}$	$3.88 \times 10^{16}\left[\frac{mol}{s \cdot g_{cat} \cdot atm^{-0.5}}\right]$	277				

Concluding Remarks

Power-to-Gas technology will play a key role in this decade due to its potentiality in tackling climate change. In particular, Power-to-Methane has the great opportunity of removing CO_2 at the same time creating a widely known source of energy such as methane.
Combining CO_2 utilization and energy storage, carbon dioxide methanation will have a crucial role in the transition from fossil fuels to renewable energy. Nowadays, this process has been deeply studied at laboratory scale in order to take it to industrial level.

The reduction of the carbon species from CO_2 to CH_4 must be promoted by a catalyst and Nickel is now regarded as the best metal to adopt in the process, constituting the best trade-off between catalytic activity and costs.

Therefore, in this work Ni was chosen as the active metal and a co-precipitated Ni-Al catalyst with molar ratio equal to 1.16 (57% wt.) was selected as the best one on which a detailed kinetic study could be performed.

Although a clear reaction mechanism is yet to be found, many academics agree in considering the reaction to take place in two following steps: a reverse water-gas shift reaction followed by the methanation of CO. Despite this, many research groups tried to describe the process through the direct pathway of Sabatier reaction.

For these reasons, our work focuses on both models that describe the system via direct pathway and those that describe it through an indirect pathway. Therefore, carbon dioxide conversion (χ_{CO_2}) and selectivity to CO (σ_{CO}) were chosen as key parameters of this study.

Many models proposed in literature were briefly analyzed and the most promising ones were applied on our experimental dataset. As expected, power laws are not suitable to take the process to an industrial scale, due to inefficiencies related to the impossibility of extrapolating outside the experimental field of study.
To demonstrate this, we chose the Lunde-Kester model, a simple model currently considered a milestone in the field, and applied it on our experimental dataset. As expected, this did not perform well: the model is a modified power law, and was developed from studies conducted on Ru.

The best model to describe the process through the direct pathway of Sabatier reaction is the LHHW-based Koschany et al. model, which can well predict all the operating conditions effect, despite some instabilities underlined in our work, deriving from many expedients introduced by the authors.

On the other hand, to describe both χ_{CO_2} and σ_{CO} the most appropriate model is the Vidotto − Raco, derived by the authors of this work, which must be further studied to identify the surface species involved in the reaction, with a particular focus on the presence or absence of adsorbed oxygen. We have demonstrated that this model performs very well also with a Ru-based dataset (as does the Raco-Vidotto, the other model developed by the authors of this work), suggesting that the same reaction mechanism can be applied for Ni-based and Ru-based catalysts.
Both this models describe the process through the consecutive scheme of RWGS reaction followed by CO methanation reaction, with a number of adaptive parameters to found (10) that is in line with many models proposed in literature.

Triangular models such as the Champon et al. model were also tested on our experimental dataset, but failed to fit and predict both carbon dioxide conversion and carbon monoxide selectivity; in the case of the recent Champon et al. model, its best performance was obtained when Sabatier reaction was removed from the scheme, again simulating a

RWGS reaction followed by carbon monoxide methanation reaction.

In conclusion, we can state that the best way to describe the phenomenology of the system is obtained when a reaction mechanism very similar to the RWGS+CO-Hydro proposed in literature and described in this work is applied: with the identification of a proper RDS, the process is well described through a consecutive scheme of reverse water-gas shift and carbon monoxide methanation.

All the other mechanisms, even tough very valid, fail to describe the trend of selectivity to CO, fundamental for an industrial application of the process, which aims at maximizing CH_4 production in different operating conditions.

Appendix A

Thermodynamic Equilibrium Calculation

A perfect gas mixture is considered in the calculation of the equilibrium curves. CO_2, H_2, and Ar are fed in the reactor. The reaction product, detected by the gas chromatograph, are CH_4, H_2O, CO, and C_2H_6, together with unconverted CO_2, H_2 and Ar.
The *species vector* for this system is:

$$S = \begin{bmatrix} CO_2 & H_2 & Ar & CH_4 & H_2O & CO & C_2H_6 \end{bmatrix}^T \tag{A.0.1}$$

The *atoms vector* is:

$$E = \begin{bmatrix} C & H & Ar & O \end{bmatrix} \tag{A.0.2}$$

The *atoms-species matrix* is:

$$A = \begin{bmatrix} 1 & 0 & 0 & 1 & 0 & 1 & 2 \\ 0 & 2 & 0 & 4 & 2 & 0 & 6 \\ 0 & 0 & 1 & 0 & 0 & 0 & 0 \\ 2 & 0 & 0 & 0 & 1 & 1 & 0 \end{bmatrix} \tag{A.0.3}$$

The rank of matrix A is equal to 4.
The number of reaction equations that are necessary to solve the system can be calculated through the formula:

$$NR = N - NA \tag{A.0.4}$$

Where NR is the number of reaction equation, N is the number of species present in the system, and NA is the rank of the matrix A. Hence:

$$NR = 7 - 4 = 3 \tag{A.0.5}$$

The 3 reactions that can be written are:

$$CO_2 + 4\ H_2 \rightleftharpoons CH_4 + 2\ H_2O \quad \textit{(Sabatier)} \tag{A.0.6}$$

$$CO_2 + H_2 \rightleftharpoons CO + H_2O \quad \textit{(RWGS)} \tag{A.0.7}$$

$$2\ CO + 5\ H_2 \rightleftharpoons C2H6 + 2\ H_2O \quad \textit{(Fischer-Tropsch)} \tag{A.0.8}$$

The equilibrium composition is calculated adopting the extent of reaction method. The equilibrium constant of reaction j, as function of the reaction temperature, is:

$$K_{eq_j}(T) = exp\left(-\frac{\Delta G^0_{R_j}(T, P_{ref})}{RT}\right) \tag{A.0.9}$$

Where R is the gas constant $\left(8.314\frac{J}{molK}\right)$, T is the reaction temperature, P_{ref} is the reference pressure (1 [bar]), $\Delta G^0_{R_j}(T, P_{ref})$ is the Gibbs free energy, calculated at the reaction temperature and pressure of reference, as follows:

$$\frac{\Delta G^0_{R_j}(T)}{RT} = \sum_{i=1}^{N} \nu_{i,j} \frac{\Delta g^0_{f_j}(T, P_{ref})}{RT} \tag{A.0.10}$$

Where $\nu_{i,j}$ is the stoichiometric coefficient of the component i in reaction j, and $\Delta g^0_{f_j}(T, P_{ref})$ is the Gibbs free energy of formation of the species i, evaluated at the reaction temperature and reference pressure. Usually, the values of $\Delta g^0_{f_j}$ are tabulated at standard conditions *(298 [K]; 1 [bar])*, therefore $\Delta g^0_{f_j}(T, P_{ref})$ must be calculated through the Van't Hoff equation [107]:

$$\frac{\Delta g^0_{f_j}(T, P_{ref})}{RT} = \frac{\Delta g^0_{f_j}(T_{ref}, P_{ref})}{RT_{ref}} + \int_{T_{ref}}^{T} \frac{\Delta h^0_{f_j}(T')}{RT'^2} dT' \tag{A.0.11}$$

Where $\Delta h^0_{f_j}(T')$ is the enthalpy of formation of the species i at T', evaluated with the formula:

$$\Delta h^0_{f_j}(T') = \Delta h^0_{f_j}(T_{ref}) + \int_{T_{ref}}^{T'} c_{P,i} dT \tag{A.0.12}$$

$c_{P,i}$ is the heat capacity of the species i, which is generally expressed as:

$$\frac{c_{P,i}}{R} = A_i + B_i T + C_i T^2 + D_i^3 + E_i T^4 \tag{A.0.13}$$

The equilibrium composition is then calculated:

$$K_{eq_j}(T) = \prod_{i=1}^{N} a_i^{\nu_{i,j}} \tag{A.0.14}$$

Where a_i is the the activity of the species i, calculated as follows:

$$a_i = \frac{\hat{f}_i(T, P, \boldsymbol{y})}{f_i(T, P_{ref})} = \frac{P x_i}{1\ [bar]} \tag{A.0.15}$$

$\hat{f}_i(T, P, \boldsymbol{y})$ is the fugacity of the species i at temperature, pressure, and composition of the system, which for an ideal gas is equal to the partial pressure of the gas. The partial pressure of the species i is equal to the pressure of the system times the molar fraction of the species i. $f_i(T, P_{ref})$ is the reference fugacity, equal to 1[bar]. The molar fractions can be calculated introducing the extent of reaction λ_j:

$$y_i = \frac{F_{out,i}}{F_{out}} = \frac{F_{in,i} + \sum_{j=1}^{NR} \nu_{i,j}\lambda_j}{\sum_{i=1}^{N}\left(F_{in,i} + \sum_{j=1}^{NR} \nu_{i,j}\lambda_j\right)} \tag{A.0.16}$$

Where $F_{out,i}$ is the outlet molar flow rate of the species i, F_{out} is the total outlet flow rate, $F_{in,i}$ is the inlet molar flow rate of the species i.

For simplicity, fictitious flow rates are used, since for the equilibrium calculation the molar flow rates are not of interest. As a base of calculus F_{in}=1[mol/s] is generally set, where F_{in} is the total inlet flow rate. The inlet molar flow rates are then calculated:

$$F_{in,i} = F_{in} y_i \tag{A.0.17}$$

The three equations to find the extent of reaction of A.0.6, A.0.7, and A.0.8 can now be written:

$$exp\left(-\frac{\Delta G^0_{R,Sab}(T, P_{ref})}{RT}\right) = \frac{1}{P^2}\frac{y_{CH_4} y^2_{H_2O}}{y_{CO_2} y^4_{H_2}} \tag{A.0.18}$$

$$exp\left(-\frac{\Delta G^0_{R,RWGS}(T, P_{ref})}{RT}\right) = \frac{y_{CO} y_{H_2O}}{y_{CO_2} y_{H_2}} \tag{A.0.19}$$

$$exp\left(-\frac{\Delta G^0_{R,FT}(T, P_{ref})}{RT}\right) = \frac{1}{P^4}\frac{y_{C_2H_6} y^2_{H_2O}}{y^2_{CO} y^5_{H_2}} \tag{A.0.20}$$

By root finding, λ_{Sab}, λ_{RWGS}, and λ_{FT} can be evaluated as function of temperature, pressure and inlet composition. The equilibrium composition can be then calculated, as well as CO_2 conversion A.0.21, CO selectivity A.0.22, and C_2H_6 selectivity A.0.23.

$$\chi_{CO_2} = \frac{F_{in,CO_2} - F_{out,CO_2}}{F_{in,CO_2}} \tag{A.0.21}$$

$$\sigma_{CO} = \frac{F_{out,CO}}{F_{in,CO_2} - F_{out,CO_2}} \tag{A.0.22}$$

$$\sigma_{C_2H_6} = \frac{F_{out,C_2H_6}}{F_{in,CO_2} - F_{out,CO_2}} \tag{A.0.23}$$

The inlet conditions are the same as the experimental dataset on the Nickel catalyst, listed in Appendix B. The numerical values, of the thermodynamic parameters, used in the calculation are in Table A.1. In Fig. A.1, A.2, A.3, and A.4 are shown the equilibrium curves of interest for this study.

Table A.1: Thermodynamic properties of the compounds, listed on [108].

Species	$\Delta h^0_{f,i}(298K)$ $[j/mol]$	$\Delta g^0_{f,i}(298K)$ $[j/mol]$	A $[-]$	$B*10^3$ $[K^{-1}]$	$C*10^5$ $[K^{-2}]$	$D*10^8$ $[K^{-3}]$	$E*10^{11}$ $[K^{-4}]$
CO_2	-393510	-394380	3.259	1.356	1.502	-2.374	1.056
H_2	0	0	2.883	3.681	-0.772	0.692	-0.213
Ar	0	0	2.5	0	0	0	0
CH_4	-74520	-50450	4.568	-8.975	3.631	-3.407	1.091
H_2O	-241810	-228420	4.395	-4.186	1.405	-1.564	0.632
CO	-110530	-137160	3.912	-3.913	1.182	-1.302	0.515
C_2H_6	-83820	-31860	4.178	-4.427	5.66	-6.651	2.487

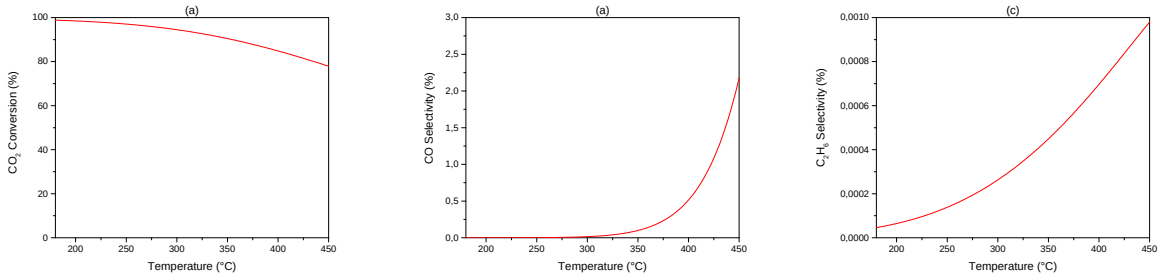

Figure A.1: Equilibrium curves, temperature effect. (a) CO_2 conversion; (b) CO selectivity; (c) C_2H_6 selectivity.

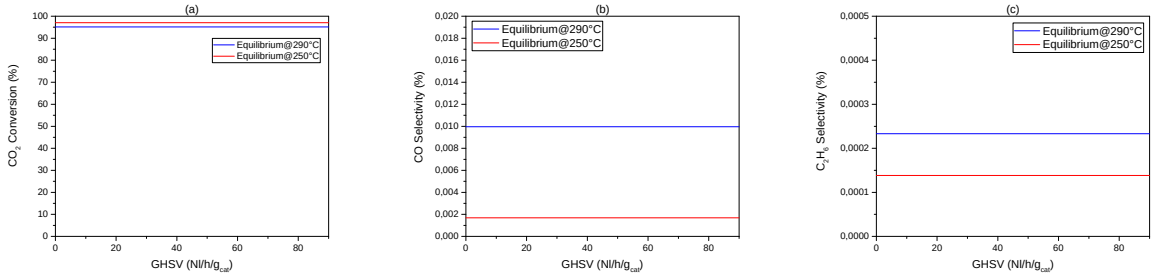

Figure A.2: Equilibrium curves, space velocity effect. (a) CO_2 conversion; (b) CO selectivity; (c) C_2H_6 selectivity.

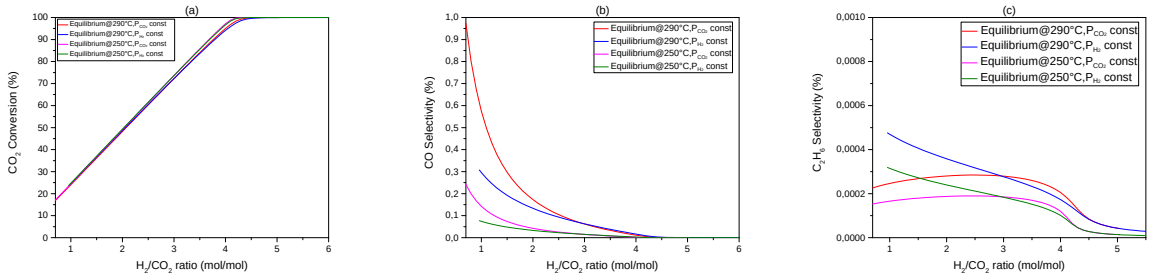

Figure A.3: Equilibrium curves, H_2/CO_2 ratio effect. (a) CO_2 conversion; (b) CO selectivity; (c) C_2H_6 selectivity.

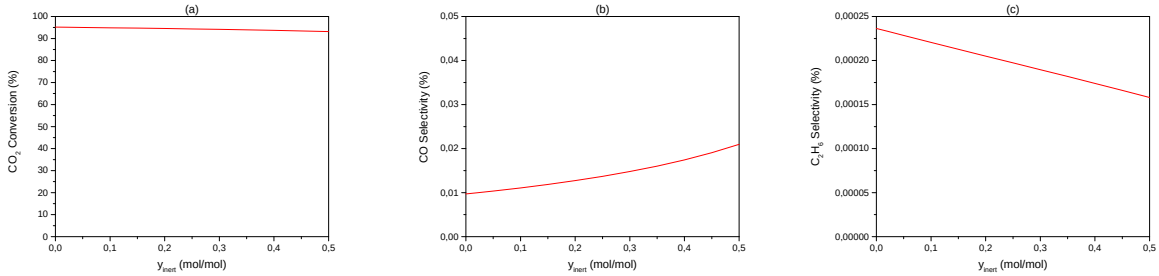

Figure A.4: Equilibrium curves, inert effect. (a) CO_2 conversion; (b) CO selectivity; (c) C_2H_6 selectivity.

Appendix B

Experimental Dataset

Here the experimental dataset employed in the regressions are reported.

B.1 Nickel Dataset

Table B.1: Experimental dataset, obtained from the Ni-based catalyst, collected at atmospheric pressure.

N°	T [°C]	H_2/CO_2	GHSV $[Ncc/h/g_{cat}]$	Inert [%]	CO_2 Conversion [%]	CO Selectivity [%]
			Temperature Effect			
1	350	3.98	50000	2	83.54693	0.350093
2	350	3.98	50000	2	83.61575	0.349652
3	350	3.98	50000	2	83.63806	0.347924
4	350	3.98	50000	2	83.66906	0.347667
5	350	3.98	50000	2	83.67115	0.353359
6	350	3.98	50000	2	83.68203	0.351439
7	350	3.98	50000	2	83.69255	0.35179
8	330	3.98	50000	2	78.54205	0.534004
9	330	3.98	50000	2	78.68756	0.526129
10	330	3.98	50000	2	78.61908	0.530507
11	330	3.98	50000	2	78.60681	0.533682
12	330	3.98	50000	2	78.60165	0.534769
13	330	3.98	50000	2	78.57797	0.534975
14	310	3.98	50000	2	68.06092	1.098731
15	310	3.98	50000	2	68.01177	1.150468
16	310	3.98	50000	2	67.97259	1.102878
17	310	3.98	50000	2	68.00408	1.096532
18	310	3.98	50000	2	67.98852	1.096957

Continues on next page...

N°	T [°C]	H_2/CO_2	GHSV $[Ncc/h/g_{cat}]$	Inert [%]	CO_2 Conversion [%]	CO Selectivity [%]
19	310	3.98	50000	2	68.01886	1.098032
20	290	3.98	50000	2	48.77026	1.759892
21	290	3.98	50000	2	49.08048	1.762821
22	290	3.98	50000	2	49.11189	1.760166
23	290	3.98	50000	2	49.24559	1.762885
24	290	3.98	50000	2	49.25174	1.754669
25	290	3.98	50000	2	49.26531	1.763689
26	290	3.98	50000	2	49.32115	1.763163
27	270	3.98	50000	2	32.76023	1.845788
28	270	3.98	50000	2	32.73761	1.801127
29	270	3.98	50000	2	32.7275	1.821791
30	270	3.98	50000	2	32.83436	1.824324
31	270	3.98	50000	2	32.85055	1.820098
32	270	3.98	50000	2	32.83051	1.826159
33	250	3.98	50000	2	18.1694	1.744739
34	250	3.98	50000	2	18.35523	1.773771
35	250	3.98	50000	2	18.26106	1.784761
36	250	3.98	50000	2	18.28228	1.776773
37	250	3.98	50000	2	18.0297	1.881496
38	250	3.98	50000	2	18.06189	1.833017
39	250	3.98	50000	2	18.02372	1.687089
40	250	3.98	50000	2	18.11451	1.828259
41	250	3.98	50000	2	18.02101	1.872208
42	250	3.98	50000	2	18.12852	1.849593
43	290	3.98	50000	2	49.35825	1.761314
44	290	3.98	50000	2	49.36436	1.759449
45	290	3.98	50000	2	49.40493	1.755804
46	290	3.98	50000	2	49.46383	1.656026
47	290	3.98	50000	2	49.47376	1.66267
48	290	3.98	50000	2	49.50868	1.660611
49	290	3.98	50000	2	49.52488	1.675932
50	350	3.98	50000	2	83.69703	0.353911
51	350	3.98	50000	2	83.71063	0.352676
52	350	3.98	50000	2	83.7148	0.346673
53	350	3.98	50000	2	83.71685	0.349967
54	350	3.98	50000	2	83.72134	0.350929
55	350	3.98	50000	2	83.73473	0.351074
56	350	3.98	50000	2	83.74471	0.354145
57	370	3.98	50000	2	86.6125	0.303574
58	370	3.98	50000	2	86.59681	0.304497
59	370	3.98	50000	2	86.59416	0.302906
60	370	3.98	50000	2	86.59518	0.30258

Continues on next page...

N°	T [°C]	H_2/CO_2	GHSV $[Ncc/h/g_{cat}]$	Inert [%]	CO_2 Conversion [%]	CO Selectivity [%]
61	370	3.98	50000	2	86.57552	0.299786
62	370	3.98	50000	2	86.58016	0.307119
63	390	3.98	50000	2	86.06935	0.42503
64	390	3.98	50000	2	86.11517	0.42651
65	390	3.98	50000	2	85.98291	0.43232
66	390	3.98	50000	2	86.09481	0.427312
67	390	3.98	50000	2	85.8903	0.426603
68	390	3.98	50000	2	85.91367	0.430002
69	350	3.98	20000	2	89.25665	0.09223
70	350	3.98	20000	2	89.20833	0.091916
71	350	3.98	20000	2	89.15716	0.092676
72	350	3.98	20000	2	89.13747	0.094711
73	350	3.98	20000	2	89.12513	0.09545
74	350	3.98	20000	2	89.13642	0.094807
75	330	3.98	20000	2	86.41487	0.122325
76	330	3.98	20000	2	86.47275	0.123467
77	330	3.98	20000	2	86.45676	0.12393
78	330	3.98	20000	2	86.46934	0.123687
79	330	3.98	20000	2	86.39656	0.124286
80	330	3.98	20000	2	86.39301	0.125086
81	310	3.98	20000	2	80.49503	0.22609
82	310	3.98	20000	2	80.53258	0.227222
83	310	3.98	20000	2	80.59008	0.225221
84	310	3.98	20000	2	80.58444	0.226263
85	310	3.98	20000	2	80.62546	0.224634
86	310	3.98	20000	2	80.61211	0.224946
87	290	3.98	20000	2	69.865	0.446551
88	290	3.98	20000	2	69.79634	0.442581
89	290	3.98	20000	2	69.94352	0.442238
90	290	3.98	20000	2	70.0009	0.442938
91	290	3.98	20000	2	70.12029	0.440692
92	290	3.98	20000	2	70.14844	0.441427
93	270	3.98	20000	2	52.7907	0.631902
94	270	3.98	20000	2	52.63794	0.632388
95	270	3.98	20000	2	53.02245	0.628066
96	270	3.98	20000	2	53.06735	0.62978
97	270	3.98	20000	2	53.09006	0.627672
98	270	3.98	20000	2	53.04019	0.625222
99	250	3.98	20000	2	34.04634	0.683429
100	250	3.98	20000	2	34.25528	0.677794
101	250	3.98	20000	2	34.26853	0.666019
102	250	3.98	20000	2	34.32505	0.665577

Continues on next page...

N°	T [°C]	H_2/CO_2	GHSV $[Ncc/h/g_{cat}]$	Inert [%]	CO_2 Conversion [%]	CO Selectivity [%]
103	250	3.98	20000	2	34.28731	0.69133
104	250	3.98	20000	2	34.2998	0.702647
105	230	3.98	20000	2	19.11868	0.814552
106	230	3.98	20000	2	19.16045	0.810731
107	230	3.98	20000	2	19.25246	0.839919
108	230	3.98	20000	2	19.28847	0.778241
109	230	3.98	20000	2	19.30308	0.856791
110	230	3.98	20000	2	19.23141	0.785858
111	210	3.98	20000	2	9.528032	0.767407
112	210	3.98	20000	2	9.5444	0.778988
113	210	3.98	20000	2	9.508056	0.765583
114	210	3.98	20000	2	9.50199	0.76054
115	210	3.98	20000	2	9.55417	0.763641
116	210	3.98	20000	2	9.536589	0.766209
117	290	3.98	10000	2	82.29131	0.149982
118	290	3.98	10000	2	82.27959	0.151286
119	290	3.98	10000	2	82.29848	0.151365
120	290	3.98	10000	2	82.28135	0.151132
121	290	3.98	10000	2	82.30312	0.151311
122	290	3.98	10000	2	82.31064	0.149687
123	270	3.98	10000	2	71.44699	0.275452
124	270	3.98	10000	2	71.37376	0.277533
125	270	3.98	10000	2	71.4758	0.275258
126	270	3.98	10000	2	71.53502	0.27453
127	270	3.98	10000	2	71.54445	0.277593
128	270	3.98	10000	2	71.53	0.272917
129	250	3.98	10000	2	52.90728	0.372335
130	250	3.98	10000	2	52.96211	0.373803
131	250	3.98	10000	2	52.99317	0.370729
132	250	3.98	10000	2	53.03378	0.371564
133	250	3.98	10000	2	53.04257	0.372451
134	250	3.98	10000	2	53.02019	0.369478
135	230	3.98	10000	2	32.25919	0.381346
136	230	3.98	10000	2	32.20185	0.382681
137	230	3.98	10000	2	32.40738	0.381102
138	230	3.98	10000	2	32.40099	0.381205
139	230	3.98	10000	2	32.41209	0.384579
140	230	3.98	10000	2	32.41371	0.378655
141	210	3.98	10000	2	16.88257	0.423762
142	210	3.98	10000	2	16.84058	0.395491
143	210	3.98	10000	2	16.85499	0.403078
144	210	3.98	10000	2	16.86703	0.391272

Continues on next page...

N°	T [°C]	H_2/CO_2	GHSV $[Ncc/h/g_{cat}]$	Inert [%]	CO_2 Conversion [%]	CO Selectivity [%]
145	210	3.98	10000	2	16.86403	0.3745
146	210	3.98	10000	2	16.86618	0.378101
147	190	3.98	10000	2	7.64689	0.317956
148	190	3.98	10000	2	7.659813	0.32909
149	190	3.98	10000	2	7.657977	0.321915
150	190	3.98	10000	2	7.693651	0.318948
151	190	3.98	10000	2	7.673423	0.310299
152	190	3.98	10000	2	7.682289	0.303286
			GHSV effect			
153	290	3.98	50000	2	48.25849	1.698088
154	290	3.98	50000	2	48.61792	1.689865
155	290	3.98	50000	2	48.80254	1.685285
156	290	3.98	50000	2	48.83508	1.67896
157	290	3.98	40000	2	54.70104	1.299631
158	290	3.98	40000	2	54.68703	1.294187
159	290	3.98	40000	2	54.62085	1.295793
160	290	3.98	40000	2	54.68223	1.29666
161	290	3.98	40000	2	54.63655	1.296952
162	290	3.98	40000	2	54.67695	1.294873
163	290	3.98	60000	2	44.10978	2.012198
164	290	3.98	60000	2	44.18864	2.014046
165	290	3.98	60000	2	44.19848	2.009192
166	290	3.98	60000	2	44.23962	2.014649
167	290	3.98	60000	2	44.32373	2.007394
168	290	3.98	60000	2	44.36156	2.011321
169	290	3.98	30000	2	62.01931	0.866012
170	290	3.98	30000	2	62.07776	0.863618
171	290	3.98	30000	2	62.06715	0.86481
172	290	3.98	30000	2	62.07801	0.862502
173	290	3.98	30000	2	62.00407	0.86713
174	290	3.98	20000	2	70.5835	0.470903
175	290	3.98	20000	2	70.82713	0.460739
176	290	3.98	20000	2	70.92212	0.455401
177	290	3.98	20000	2	71.17915	0.45327
178	290	3.98	70000	2	40.4124	2.321111
179	290	3.98	70000	2	40.38765	2.330842
180	290	3.98	70000	2	40.48321	2.320381
181	290	3.98	70000	2	40.45243	2.32816
182	290	3.98	70000	2	40.51551	2.319098
183	290	3.98	80000	2	37.4709	2.573981
184	290	3.98	80000	2	37.43214	2.583081
185	290	3.98	80000	2	37.41394	2.580031

Continues on next page...

N°	T [°C]	H_2/CO_2	GHSV $[Ncc/h/g_{cat}]$	Inert [%]	CO_2 Conversion [%]	CO Selectivity [%]
186	290	3.98	80000	2	37.45007	2.578465
187	290	3.98	80000	2	37.47656	2.578504
188	290	3.98	80000	2	37.47637	2.585141
189	290	3.98	15000	2	75.89068	0.31277
190	290	3.98	15000	2	75.97664	0.313099
191	290	3.98	15000	2	75.86689	0.313958
192	290	3.98	15000	2	75.88332	0.31314
193	290	3.98	15000	2	75.86247	0.313955
194	290	3.98	15000	2	75.87274	0.314784
195	290	3.98	10000	2	81.83041	0.168178
196	290	3.98	10000	2	81.89092	0.166548
197	290	3.98	10000	2	81.90266	0.166178
198	290	3.98	10000	2	81.88637	0.166033
199	290	3.98	10000	2	81.89732	0.16754
200	290	3.98	10000	2	81.88814	0.166628
201	290	3.98	5000	2	87.68776	0.071873
202	290	3.98	5000	2	87.77278	0.070073
203	290	3.98	5000	2	87.80066	0.069247
204	290	3.98	5000	2	87.70458	0.068416
205	290	3.98	5000	2	87.85144	0.069051
206	290	3.98	5000	2	87.85181	0.068247
207	250	3.98	50000	2	18.68119	1.461653
208	250	3.98	50000	2	18.68853	1.466543
209	250	3.98	50000	2	18.66608	1.454448
210	250	3.98	50000	2	18.67798	1.428432
211	250	3.98	50000	2	18.68338	1.500895
212	250	3.98	50000	2	18.67016	1.505753
213	250	3.98	30000	2	27.20314	0.996939
214	250	3.98	30000	2	27.2156	0.999859
215	250	3.98	30000	2	27.12031	1.00308
216	250	3.98	30000	2	27.13797	1.011025
217	250	3.98	30000	2	27.13038	1.012238
218	250	3.98	30000	2	27.12544	1.014938
219	250	3.98	20000	2	36.18183	0.706893
220	250	3.98	20000	2	36.04262	0.708376
221	250	3.98	20000	2	35.93267	0.710902
222	250	3.98	20000	2	35.973	0.7149
223	250	3.98	20000	2	35.93097	0.719512
224	250	3.98	20000	2	35.90512	0.722707
225	250	3.98	15000	2	43.1743	0.560194
226	250	3.98	15000	2	43.17712	0.561422
227	250	3.98	15000	2	43.17818	0.564305

Continues on next page...

N°	T [°C]	H_2/CO_2	GHSV $[Ncc/h/g_{cat}]$	Inert [%]	CO_2 Conversion [%]	CO Selectivity [%]
228	250	3.98	15000	2	43.18096	0.55649
229	250	3.98	15000	2	43.11093	0.56446
230	250	3.98	15000	2	43.13338	0.567176
231	250	3.98	10000	2	54.35483	0.38329
232	250	3.98	10000	2	54.28095	0.382679
233	250	3.98	10000	2	54.32445	0.382333
234	250	3.98	10000	2	54.31821	0.380131
235	250	3.98	10000	2	54.28573	0.383811
236	250	3.98	10000	2	54.25413	0.386112
237	250	3.98	5000	2	72.61175	0.169245
238	250	3.98	5000	2	72.63412	0.169788
239	250	3.98	5000	2	72.62769	0.169177
240	250	3.98	5000	2	72.63378	0.168554
241	250	3.98	5000	2	72.59503	0.168941
242	250	3.98	5000	2	72.58	0.167031
H_2/CO_2 Ratio Effect (P_{CO_2} const.)						
243	290	4	50000	17.23	56.23831	1.38399
244	290	4	50000	17.23	56.22994	1.386453
245	290	4	50000	17.23	56.22275	1.413248
246	290	4	50000	17.23	56.22496	1.413207
247	290	4	50000	17.23	56.21301	1.422446
248	290	4	50000	17.23	56.22308	1.408466
249	290	3	50000	33.78	47.98754	1.856813
250	290	3	50000	33.78	47.94811	1.866596
251	290	3	50000	33.78	47.98626	1.86069
252	290	3	50000	33.78	47.95578	1.865596
253	290	3	50000	33.78	47.95071	1.862892
254	290	3	50000	33.78	47.96086	1.86636
255	290	2	50000	50.34	37.05962	2.640015
256	290	2	50000	50.34	37.04773	2.644186
257	290	2	50000	50.34	36.99866	2.662708
258	290	2	50000	50.34	37.08276	2.668333
259	290	2	50000	50.34	37.08273	2.657617
260	290	2	50000	50.34	37.08407	2.668297
261	290	1	50000	66.89	20.13392	4.659083
262	290	1	50000	66.89	20.13825	4.650342
263	290	1	50000	66.89	20.10728	4.686839
264	290	1	50000	66.89	20.03755	4.740324
265	290	1	50000	66.89	20.03835	4.75594
266	290	5	50000	0.67	62.78704	1.16066
267	290	5	50000	0.67	62.84749	1.154452
268	290	5	50000	0.67	62.34628	1.158851

Continues on next page...

N°	T [°C]	H_2/CO_2	GHSV $[Ncc/h/g_{cat}]$	Inert [%]	CO_2 Conversion [%]	CO Selectivity [%]
269	290	5	50000	0.67	62.81909	1.160512
270	290	5	50000	0.67	62.78605	1.155511
271	290	5	50000	0.67	62.80937	1.110051
272	250	4	50000	17.23	21.50846	1.789327
273	250	4	50000	17.23	21.48108	1.783841
274	250	4	50000	17.23	21.48068	1.757185
275	250	4	50000	17.23	21.50994	1.747588
276	250	4	50000	17.23	21.48254	1.790376
277	250	4	50000	17.23	21.50329	1.763337
278	250	3	50000	33.78	19.18485	2.120139
279	250	3	50000	33.78	19.21043	2.130451
280	250	3	50000	33.78	19.21312	2.105935
281	250	3	50000	33.78	19.18059	2.098368
282	250	3	50000	33.78	19.18674	2.117029
283	250	3	50000	33.78	19.20125	2.108984
284	250	2	50000	50.34	16.32215	2.688564
285	250	2	50000	50.34	16.33635	2.749854
286	250	2	50000	50.34	16.32658	2.717136
287	250	2	50000	50.34	16.32098	2.731277
288	250	2	50000	50.34	16.30817	2.73574
289	250	2	50000	50.34	16.28738	2.706934
290	250	1	50000	66.89	10.73416	5.358072
291	250	1	50000	66.89	10.68611	5.358113
292	250	1	50000	66.89	10.68712	5.427449
293	250	1	50000	66.89	10.71891	5.410455
294	250	1	50000	66.89	10.66382	5.403134
295	250	1	50000	66.89	10.67599	5.388301
296	250	5	50000	0.67	23.34752	1.609633
297	250	5	50000	0.67	23.34087	1.582227
298	250	5	50000	0.67	23.33682	1.60106
299	250	5	50000	0.67	23.35686	1.593889
300	250	5	50000	0.67	23.34276	1.582279
301	250	5	50000	0.67	23.33497	1.59225
H_2/CO_2 Ratio Effect (P_{H_2} const.)						
302	290	4	50000	38.75	61.392	1.278846
303	290	4	50000	38.75	61.41194	1.268464
304	290	4	50000	38.75	61.37867	1.271675
305	290	4	50000	38.75	61.43412	1.272388
306	290	4	50000	38.75	61.41872	1.268898
307	290	4	50000	38.75	61.39696	1.263511
308	290	3	50000	34.67	47.43129	1.921902
309	290	3	50000	34.67	47.38792	1.92092

Continues on next page...

N°	T [°C]	H_2/CO_2	GHSV $[Ncc/h/g_{cat}]$	Inert [%]	CO_2 Conversion [%]	CO Selectivity [%]
310	290	3	50000	34.67	47.45965	1.922461
311	290	3	50000	34.67	47.43146	1.921768
312	290	3	50000	34.67	47.49235	1.918099
313	290	3	50000	34.67	47.45604	1.918451
314	290	2	50000	26.5	32.67194	3.006488
315	290	2	50000	26.5	32.63962	3.014527
316	290	2	50000	26.5	32.6867	3.020066
317	290	2	50000	26.5	32.64821	3.024052
318	290	2	50000	26.5	32.67199	3.011395
319	290	2	50000	26.5	32.62549	3.026216
320	290	1	50000	1.99	16.52045	5.724367
321	290	1	50000	1.99	16.4636	5.75467
322	290	1	50000	1.99	16.44127	5.780464
323	290	1	50000	1.99	16.40217	5.803909
324	290	1	50000	1.99	16.40794	5.80144
325	290	1	50000	1.99	16.40706	5.806698
326	290	5	50000	41.2	74.34643	0.795173
327	290	5	50000	41.2	74.30587	0.797153
328	290	5	50000	41.2	74.47511	0.797952
329	290	5	50000	41.2	74.39378	0.798781
300	290	5	50000	41.2	74.40029	0.79212
301	290	5	50000	41.2	74.29723	0.796069
332	250	4	50000	38.75	26.26394	1.616502
333	250	4	50000	38.75	26.25905	1.597729
334	250	4	50000	38.75	26.25539	1.605648
335	250	4	50000	38.75	26.25206	1.596275
336	250	4	50000	38.75	26.26484	1.581509
337	250	4	50000	38.75	26.25573	1.635877
338	250	3	50000	34.67	20.17343	1.922242
339	250	3	50000	34.67	20.15689	1.939233
340	250	3	50000	34.67	20.18056	1.94193
341	250	3	50000	34.67	20.16936	1.95682
342	250	3	50000	34.67	20.17105	1.962142
343	250	3	50000	34.67	20.15049	1.943347
344	250	2	50000	26.5	13.92987	2.55647
345	250	2	50000	26.5	13.92382	2.575697
346	250	2	50000	26.5	13.95156	2.572767
347	250	2	50000	26.5	13.94001	2.55911
348	250	2	50000	26.5	13.94403	2.546283
349	250	2	50000	26.5	13.94151	2.564071
350	250	1	50000	1.99	7.191799	4.197871
351	250	1	50000	1.99	7.195508	4.200198

Continues on next page...

N°	T [°C]	H_2/CO_2	GHSV $[Ncc/h/g_{cat}]$	Inert [%]	CO_2 Conversion [%]	CO Selectivity [%]
352	250	1	50000	1.99	7.198951	4.209319
353	250	1	50000	1.99	7.193271	4.214713
354	250	1	50000	1.99	7.189711	4.224655
355	250	1	50000	1.99	7.193308	4.227743
356	250	5	50000	41.2	32.14659	1.375783
357	250	5	50000	41.2	32.14815	1.354544
358	250	5	50000	41.2	32.13511	1.351278
359	250	5	50000	41.2	32.16899	1.365936
360	250	5	50000	41.2	32.14939	1.357557
361	250	5	50000	41.2	32.19209	1.369606
			Inert Effect			
362	290	3.98	50000	2	47.57576	1.838366
363	290	3.98	50000	2	47.67496	1.834091
364	290	3.98	50000	2	47.78311	1.824912
365	290	3.98	50000	2	47.77936	1.823122
366	290	3.98	50000	2	47.74776	1.834799
367	290	3.98	50000	2	47.71758	1.833134
368	290	3.98	54440	10	46.84554	1.960248
369	290	3.98	54440	10	46.75029	1.962529
370	290	3.98	54440	10	46.79255	1.964746
371	290	3.98	54440	10	46.76435	1.964894
372	290	3.98	54440	10	46.77953	1.962109
373	290	3.98	54440	10	46.83421	1.970144
374	290	3.98	61250	20	45.83025	2.167407
375	290	3.98	61250	20	45.78469	2.169641
376	290	3.98	61250	20	45.82689	2.166457
377	290	3.98	61250	20	45.84821	2.169358
378	290	3.98	61250	20	45.84321	2.170413
379	290	3.98	61250	20	45.88415	2.167617
380	290	3.98	70000	30	44.82902	2.406941
381	290	3.98	70000	30	44.80821	2.416367
382	290	3.98	70000	30	44.7949	2.413157
383	290	3.98	70000	30	44.7928	2.411404
384	290	3.98	70000	30	44.7995	2.408691
385	290	3.98	70000	30	44.79088	2.417118
386	290	3.98	81670	40	43.69192	2.713124
387	290	3.98	81670	40	43.59979	2.748109
388	290	3.98	81670	40	43.55366	2.721697
389	290	3.98	81670	40	43.63676	2.714742
390	290	3.98	81670	40	43.67945	2.708898
391	290	3.98	81670	40	43.62685	2.714993
392	290	3.98	75380	35	44.37447	2.55827

Continues on next page...

N°	T [°C]	H_2/CO_2	GHSV $[Ncc/h/g_{cat}]$	Inert [%]	CO_2 Conversion [%]	CO Selectivity [%]
393	290	3.98	75380	35	44.26235	2.564906
394	290	3.98	75380	35	44.19098	2.56695
395	290	3.98	75380	35	44.26002	2.570388
396	290	3.98	75380	35	44.31121	2.546069
397	290	3.98	75380	35	44.36877	2.53807
398	290	3.98	57650	15	46.66336	2.060694
399	290	3.98	57650	15	46.59902	2.066694
400	290	3.98	57650	15	46.63356	2.067056
401	290	3.98	57650	15	46.54991	2.062542
402	290	3.98	57650	15	46.57659	2.063518
403	290	3.98	57650	15	46.55475	2.062634

B.2 Ruthenium Dataset

Table B.2: Experimental dataset, obtained from the Ru-based catalyst. [84]

N°	P [barg]	T [°C]	H_2/CO_2	GHSV $[Ncc/h/g_{cat}]$	y^0_{inert}	$y^0_{H_2O}$	CO_2 Conversion	CO Selectivity
GHSV Effect								
1	0	310	4	3750	0.1	0	0.6776	0.0047635
2	0	310	4	3750	0.1	0	0.6776	0.0049389
3	0	310	4	3750	0.1	0	0.6770	0.0050035
4	0	310	4	3750	0.1	0	0.6753	0.0049234
5	0	310	4	5000	0.1	0	0.5851	0.0064732
6	0	310	4	5000	0.1	0	0.5817	0.0064548
7	0	310	4	5000	0.1	0	0.5822	0.0064503
8	0	310	4	5000	0.1	0	0.5824	0.0064498
9	0	310	4	6250	0.1	0	0.5335	0.00785
10	0	310	4	6250	0.1	0	0.5332	0.0078625
11	0	310	4	6250	0.1	0	0.5330	0.0078727
12	0	310	4	6250	0.1	0	0.5357	0.0079327
13	0	310	4	7500	0.1	0	0.4801	0.0093959
14	0	310	4	7500	0.1	0	0.4796	0.009382
15	0	310	4	7500	0.1	0	0.4801	0.0092949
16	0	310	4	7500	0.1	0	0.4818	0.009252
17	0	310	4	8750	0.1	0	0.4450	0.0104612
18	0	310	4	8750	0.1	0	0.4452	0.0107138
19	0	310	4	8750	0.1	0	0.4464	0.010603
20	0	310	4	8750	0.1	0	0.4468	0.0107349
21	0	310	4	10000	0.1	0	0.4109	0.0119583
22	0	310	4	10000	0.1	0	0.4128	0.0117808
23	0	310	4	10000	0.1	0	0.4116	0.0118587
24	0	310	4	10000	0.1	0	0.4139	0.0117617
25	0	290	4	3750	0.0121	0	0.4887	0.0053788
26	0	290	4	3750	0.0121	0	0.4881	0.0053091
27	0	290	4	3750	0.0121	0	0.4872	0.0055293
28	0	290	4	5000	0.0121	0	0.4085	0.007008
29	0	290	4	5000	0.0121	0	0.4026	0.0069389
30	0	290	4	5000	0.0121	0	0.4053	0.0069829
31	0	290	4	6250	0.0121	0	0.3509	0.008
32	0	290	4	6250	0.0121	0	0.3501	0.008
33	0	290	4	6250	0.0121	0	0.3510	0.008
34	0	290	4	7500	0.0121	0	0.3076	0.010
35	0	290	4	7500	0.0121	0	0.3034	0.010
36	0	290	4	7500	0.0121	0	0.3046	0.010
37	0	290	4	8750	0.0121	0	0.2755	0.011
38	0	290	4	8750	0.0121	0	0.2767	0.011
39	0	290	4	8750	0.0121	0	0.2777	0.011
40	0	290	4	10000	0.0121	0	0.2500	0.012
41	0	290	4	10000	0.0121	0	0.2428	0.012
42	0	290	4	10000	0.0121	0	0.2428	0.012
Temperature Effect								
43	0	250	4	5000	0.1	0	0.1384	0.005866
44	0	250	4	5000	0.1	0	0.1379	0.005804
45	0	250	4	5000	0.1	0	0.1396	0.005365
46	0	270	4	5000	0.1	0	0.2569	0.005818
47	0	270	4	5000	0.1	0	0.2569	0.005698
48	0	270	4	5000	0.1	0	0.2559	0.005873
49	0	290	4	5000	0.1	0	0.4152	0.0063544
50	0	290	4	5000	0.1	0	0.4140	0.0063381
51	0	290	4	5000	0.1	0	0.4146	0.0063442
52	0	290	4	5000	0.1	0	0.4142	0.0064356

Continues on next page...

N°	P [barg]	T [°C]	H_2/CO_2	GHSV [$Ncc/h/g_{cat}$]	y^0_{inert}	$y^0_{H_2O}$	CO_2 Conversion[-]	CO Selectivity[-]
53	0	310	4	5000	0.1	0	0.5822	0.0064503
54	0	310	4	5000	0.1	0	0.5812	0.0065227
55	0	310	4	5000	0.1	0	0.5824	0.0064498
56	0	330	4	5000	0.1	0	0.7432	0.0053588
57	0	330	4	5000	0.1	0	0.7439	0.0053057
58	0	330	4	5000	0.1	0	0.7443	0.0053057
59	0	350	4	5000	0.1	0	0.8245	0.0037652
60	0	350	4	5000	0.1	0	0.8250	0.0037267
61	0	350	4	5000	0.1	0	0.8257	0.003798
62	0	370	4	5000	0.1	0	0.8676	0.0028619
63	0	370	4	5000	0.1	0	0.8687	0.0028669
64	0	370	4	5000	0.1	0	0.8683	0.0028662
65	0	390	4	5000	0.1	0	0.8641	0.0040079
66	0	390	4	5000	0.1	0	0.8648	0.0039531
67	0	390	4	5000	0.1	0	0.8645	0.0039882
68	0	410	4	5000	0.1	0	0.8433	0.0068497
69	0	410	4	5000	0.1	0	0.8425	0.0065778
70	0	410	4	5000	0.1	0	0.8434	0.0067338
				H_2/CO_2 Ratio Effect				
71	0	310	2	5000	0.3145	0	0.3421	0.0182967
72	0	310	2	5000	0.3145	0	0.3422	0.0181969
73	0	310	2	5000	0.3145	0	0.3419	0.0183498
74	0	310	3	5000	0.3906	0	0.4956	0.0107638
75	0	310	3	5000	0.3906	0	0.4966	0.0106624
76	0	310	3	5000	0.3906	0	0.4966	0.0106322
77	0	310	3	5000	0.3906	0	0.4960	0.010679
78	0	310	4	5000	0.4287	0	0.6369	0.0066723
79	0	310	4	5000	0.4287	0	0.6376	0.0067206
80	0	310	5	5000	0.4516	0	0.7630	0.0040859
81	0	310	5	5000	0.4516	0	0.7637	0.0040727
82	0	310	5	5000	0.4516	0	0.7626	0.0041015
83	0	310	2	5000	0.5431	0	0.3495	0.0204279
84	0	310	2	5000	0.5431	0	0.3499	0.0204924
85	0	310	2	5000	0.5431	0	0.3504	0.0205351
86	0	310	4	5000	0.2385	0	0.6135	0.0065376
87	0	310	4	5000	0.2385	0	0.6134	0.0066893
88	0	310	4	5000	0.2385	0	0.6144	0.0066928
89	0	310	5	5000	0.0862	0	0.7151	0.0044165
90	0	310	5	5000	0.0862	0	0.7159	0.0043057
91	0	310	5	5000	0.0862	0	0.7157	0.0043693
				Inert Effect				
92	0	310	4	5000	0.1	0	0.6008	0.0066634
93	0	310	4	5000	0.1	0	0.6023	0.0066208
94	0	310	4	5000	0.1	0	0.6018	0.0066321
95	0	310	4	5000	0.2	0	0.6147	0.0067021
96	0	310	4	5000	0.2	0	0.6162	0.0066351
97	0	310	4	5000	0.2	0	0.6147	0.0067668
98	0	310	4	5000	0.3	0	0.6296	0.0066078
99	0	310	4	5000	0.3	0	0.6289	0.0068305
100	0	310	4	5000	0.3	0	0.6317	0.0066842
101	0	310	4	5000	0.4	0	0.6529	0.0064046
102	0	310	4	5000	0.4	0	0.6520	0.0065487
103	0	310	4	5000	0.4	0	0.6518	0.0065156
				Reference Condition				
104	0	310	4	5000	0.1	0	0.5935	0.0063803
105	0	310	4	5000	0.1	0	0.5934	0.0064441
106	0	310	4	5000	0.1	0	0.5936	0.0064703
107	0	310	4	5000	0.1	0	0.5944	0.0064272

Continues on next page...

N°	P [barg]	T [°C]	H_2/CO_2	GHSV $[Ncc/h/g_{cat}]$	y^0_{inert}	$y^0_{H_2O}$	CO_2 Conversion[-]	CO Selectivity[-]
108	0	310	4	5000	0.1	0	0.5976	0.0065712
109	0	310	4	5000	0.1	0	0.5986	0.0064266
110	0	310	4	5000	0.1	0	0.6004	0.0064578
111	0	310	4	5000	0.1	0	0.6022	0.0065452
112	0	310	4	5000	0.1	0	0.6015	0.0065399
113	0	310	4	5000	0.1	0	0.6008	0.0066634
114	0	310	4	5000	0.1	0	0.6018	0.0066321
115	0	310	4	5000	0.1	0	0.5935	0.0063803
116	0	310	4	5000	0.1	0	0.5934	0.0064441
117	0	310	4	5000	0.1	0	0.5936	0.0064703
118	0	310	4	5000	0.1	0	0.5944	0.0064272
119	0	310	4	5000	0.1	0	0.5976	0.0065712
120	0	310	4	5000	0.1	0	0.5986	0.0064266
121	0	310	4	5000	0.1	0	0.6004	0.0064578
122	0	310	4	5000	0.1	0	0.6022	0.0065452
123	0	310	4	5000	0.1	0	0.6015	0.0065399
124	0	310	4	5000	0.1	0	0.6008	0.0066634
125	0	310	4	5000	0.1	0	0.6018	0.0066321
				Water Effect				
126	0	310	4	5000	0.3000	0.0000	0.6387	0.0070669
127	0	310	4	5000	0.3000	0.0000	0.6358	0.0070342
128	0	310	4	5000	0.3000	0.0000	0.6373	0.0070
129	0	310	4	5000	0.2719	0.0281	0.6259	0.0072
130	0	310	4	5000	0.2719	0.0281	0.6265	0.0072
131	0	310	4	5000	0.2719	0.0281	0.6250	0.0072
132	0	310	4	5000	0.2439	0.0561	0.6067	0.0073
133	0	310	4	5000	0.2439	0.0561	0.6042	0.0074
134	0	310	4	5000	0.2439	0.0561	0.6049	0.0074
135	0	310	4	5000	0.2158	0.0842	0.5929	0.0075585
136	0	310	4	5000	0.2158	0.0842	0.5929	0.0074
137	0	310	4	5000	0.2158	0.0842	0.5924	0.007502
138	0	310	4	5000	0.1317	0.1683	0.5693	0.0078
139	0	310	4	5000	0.1317	0.1683	0.5709	0.0078273
140	0	310	4	5000	0.1317	0.1683	0.5721	0.0078102
141	0	310	4	5000	0.0142	0.2858	0.5409	0.0080437
142	0	310	4	5000	0.0142	0.2858	0.5345	0.0083962
143	0	310	4	5000	0.0142	0.2858	0.5383	0.0082546
				Pressure Effect				
144	0	310	3.9	5000	0.02	0	0.5800	0.0064643
145	0	310	3.9	5000	0.02	0	0.5816	0.0065197
146	0	310	3.9	5000	0.02	0	0.5820	0.007
147	1.5	310	3.9	5000	0.02	0	0.7231	0.003
148	1.5	310	3.9	5000	0.02	0	0.7222	0.003
149	1.5	310	3.9	5000	0.02	0	0.7226	0.003
150	3	310	3.9	5000	0.02	0	0.7948	0.0014
151	3	310	3.9	5000	0.02	0	0.8002	0.0015
152	3	310	3.9	5000	0.02	0	0.7968	0.0014
153	4.5	310	3.9	5000	0.02	0	0.8450	0.0009264
154	4.5	310	3.9	5000	0.02	0	0.8353	0.0009926
155	4.5	310	3.9	5000	0.02	0	0.8422	0.0014
156	6	310	3.9	5000	0.02	0	0.8674	0.000
157	6	310	3.9	5000	0.02	0	0.8707	0.001
158	6	310	3.9	5000	0.02	0	0.8672	0.001
159	0	290	3.9	5000	0.02	0	0.4070	0.007
160	0	290	3.9	5000	0.02	0	0.4041	0.007
161	0	290	3.9	5000	0.02	0	0.4035	0.007
162	3	290	3.9	5000	0.02	0	0.6291	0.0017671
163	3	290	3.9	5000	0.02	0	0.6255	0.0015

Continues on next page...

N°	P [barg]	T [°C]	H_2/CO_2	GHSV $[Ncc/h/g_{cat}]$	y^0_{inert}	$y^0_{H_2O}$	CO_2 Conversion[-]	CO Selectivity[-]
164	3	290	3.9	5000	0.02	0	0.6281	0.001449
165	6	290	3.9	5000	0.02	0	0.7416	0.0004
166	6	290	3.9	5000	0.02	0	0.7372	0.0008
167	6	290	3.9	5000	0.02	0	0.7380	0.0011

Appendix C

Modified Koschany et al. models derivation

C.1 Koschany et al. Model without irreversible steps

C.1.1 Elementary Steps

The elementary reactions are the same described by Koschany et al. [90], the RDS is again the step 3, but now all the reactions are reversible:

1. $CO_2 + 2\ l \rightleftharpoons CO^* + O^*$
2. $H_2 + 2\ l \rightleftharpoons 2\ H^*$
3. $CO^* + H^* \rightleftharpoons CHO^* + l$
4. $CHO^* + l \rightleftharpoons CH^* + O^*$
5. $CH^* + 3\ H^* \rightleftharpoons CH_4^* + 3\ l$
6. $CH_4^* \rightleftharpoons CH_4 + l$
7. $O^* + H^* \rightleftharpoons OH^* + l$
8. $OH^* + H^* \rightleftharpoons H_2O^* + l$
9. $H_2O^* \rightleftharpoons H_2O + l$

The RDS is step 3, as it was for the original model.

C.1.2 Derivation

First of all, we introduce some definitions:
$\frac{\overrightarrow{k}_1}{\overleftarrow{k}_1} = K_{CO_2}; \quad \frac{\overrightarrow{k}_2}{\overleftarrow{k}_2} = K_{H_2}; \quad \frac{\overleftarrow{k}_6}{\overrightarrow{k}_6} = K_{CH_4}; \quad \frac{\overleftarrow{k}_9}{\overrightarrow{k}_9} = K_{H_2O}; \quad \frac{\overrightarrow{k}_3}{\overleftarrow{k}_3} = K_3;$
$\frac{\overrightarrow{k}_4}{\overleftarrow{k}_4} = K_4; \quad \frac{\overrightarrow{k}_5}{\overleftarrow{k}_5} = K_5; \quad \frac{\overrightarrow{k}_7}{\overleftarrow{k}_7} = K_7; \quad \frac{\overrightarrow{k}_8}{\overleftarrow{k}_8} = K_8;$

So, from r_2:
$$\overrightarrow{k}_2 P_{H_2}\theta_l^2 - \overleftarrow{k}_2\theta_H^2 = 0 \Rightarrow \theta_H = \sqrt{\frac{\overrightarrow{k}_2 P_{H_2}}{\overleftarrow{k}_2}}\theta_l \Rightarrow \theta_H = \sqrt{K_{H_2}P_{H_2}}\theta_l$$

From r_6:
$$\overrightarrow{k}_6\theta_{CH_4} - \overleftarrow{k}_6 P_{CH_4}\theta_l = 0 \Rightarrow \theta_{CH_4} = \frac{\overleftarrow{k}_6}{\overrightarrow{k}_6}P_{CH_4}\theta_l \Rightarrow \theta_{CH_4} = K_{CH_4}P_{CH_4}\theta_l$$

From r_9:
$$\overrightarrow{k}_9\theta_{H_2O} - \overleftarrow{k}_9 P_{H_2O}\theta_l = 0 \Rightarrow \theta_{H_2O} = \frac{\overleftarrow{k}_9}{\overrightarrow{k}_9}P_{H_2O}\theta_l \Rightarrow \theta_{H_2O} = K_{H_2O}P_{H_2O}\theta_l$$

From r_8:
$$\overrightarrow{k}_8\theta_{OH}\theta_H - \overleftarrow{k}_8\theta_{H_2O}\theta_l = 0 \Rightarrow \theta_{OH} = \frac{\overleftarrow{k}_8\theta_{H_2O}}{\overrightarrow{k}_8\theta_H}\theta_l \Rightarrow \theta_{OH} = \frac{K_{H_2O}P_{H_2O}}{K_8\sqrt{K_{H_2}P_{H_2}}}\theta_l$$

From r_7:
$$\overrightarrow{k}_7\theta_O\theta_H - \overleftarrow{k}_7\theta_{OH}\theta_l = 0 \Rightarrow \theta_O = \frac{\overleftarrow{k}_7\theta_{OH}}{\overrightarrow{k}_7\theta_H}\theta_l \Rightarrow \theta_O = \frac{K_{H_2O}P_{H_2O}}{K_7K_8K_{H_2}P_{H_2}}\theta_l$$

From r_1:
$$\overrightarrow{k}_1 P_{CO_2}\theta_l - \overleftarrow{k}_1\theta_{CO}\theta_O = 0 \Rightarrow \theta_{CO} = \frac{\overrightarrow{k}_1 P_{CO_2}}{\overleftarrow{k}_1\theta_O}\theta_l^2 \Rightarrow \theta_{CO} = \frac{K_7K_8K_{CO_2}K_{H_2}P_{CO_2}P_{H_2}}{K_{H_2O}P_{H_2O}}\theta_l$$

From r_5:
$$\overrightarrow{k}_5\theta_{CH}\theta_H^3 - \overleftarrow{k}_5\theta_{CH_4}\theta_l^3 = 0 \Rightarrow \theta_{CH} = \frac{\overleftarrow{k}_5\theta_{CH_4}}{\overrightarrow{k}_5\theta_H^3}\theta_l^3 \Rightarrow \theta_{CH} = \frac{K_{CH_4}P_{CH_4}}{K_5\sqrt{(K_{H_2O}P_{H_2O})^3}}\theta_l$$

From r_4:
$$\overrightarrow{k}_4\theta_{CHO}\theta_l - \overleftarrow{k}_4\theta_{CH}\theta_O = 0 \Rightarrow \theta_{CHO} = \frac{\overleftarrow{k}_4\theta_{CH}\theta_O}{\overrightarrow{k}_4\theta_l} \Rightarrow \theta_{CHO} = \frac{K_{CH_4}K_{H_2O}P_{CH_4}P_{H_2O}}{K_4K_5K_7K_8\sqrt{(K_{H_2O}P_{H_2O})^5}}\theta_l$$

Active site balance

Now we can exploit the active sites balance to find θ_l, defining as MASI the species CO, H, OH

$$\theta_{CO} + \theta_H + \theta_{OH} + \theta_l = 1$$

$$\frac{K_7 K_8 K_{CO_2} K_{H_2} P_{CO_2} P_{H_2}}{K_{H_2O} P_{H_2O}} \theta_l + \sqrt{K_{H_2} P_{H_2}} \theta_l + \frac{K_{H_2O} P_{H_2O}}{K_8 \sqrt{K_{H_2} P_{H_2}}} \theta_l + \theta_l = 1$$

$$\theta_l = \frac{1}{\left(1 + \frac{K_7 K_8 K_{CO_2} K_{H_2} P_{CO_2} P_{H_2}}{K_{H_2O} P_{H_2O}} + \sqrt{K_{H_2} P_{H_2}} + \frac{K_{H_2O} P_{H_2O}}{K_8 \sqrt{K_{H_2} P_{H_2}}}\right)}$$

RDS

Now we can write the rate expression for the RDS. So:

$$r_3 = r_{CH_4} = \overrightarrow{k}_3 \theta_{CO} \theta_H - \overleftarrow{k_3} \theta_{CHO} \theta_l =$$

$$= \overrightarrow{k}_3 \frac{K_7 K_8 K_{CO_2} K_{H_2} P_{CO_2} P_{H_2}}{K_{H_2O} P_{H_2O}} \sqrt{K_{H_2} P_{H_2}} \theta_l^2 - \overleftarrow{k_3} \frac{K_{CH_4} K_{H_2O} P_{CH_4} P_{H_2O}}{K_4 K_5 K_7 K_8 \sqrt{(K_{H_2O} P_{H_2O})^5}} \theta_l^2 =$$

$$= \frac{\overrightarrow{k}_3 \frac{K_7 K_8 K_{CO_2} K_{H_2}^{1.5} P_{CO_2} P_{H_2}^{1.5}}{K_{H_2O} P_{H_2O}} \left(1 - \frac{K_{CH_4} K_{H_2O}^2}{K_3 K_4 K_5 K_7^2 K_8^2 K_{H_2}^4 K_{CO_2}} \frac{P_{CH_4} P_{H_2O}^2}{P_{CO_2} P_{H_2}^4}\right)}{\left(1 + \frac{K_7 K_8 K_{CO_2} K_{H_2} P_{CO_2} P_{H_2}}{K_{H_2O} P_{H_2O}} + \sqrt{K_{H_2} P_{H_2}} + \frac{K_{H_2O} P_{H_2O}}{K_8 \sqrt{K_{H_2} P_{H_2}}}\right)^2}$$

C.1.3 Rate Expression

Finally, we can see that:

$$K_{H_2} = \frac{\theta_H^2}{P_{H_2} \theta_l^2}; \quad K_{CO_2} = \frac{\theta_{CO} \theta_O}{P_{CO_2} \theta_l}; \quad K_{CH_4} = \frac{\theta_{CH_4}}{P_{CH_4} \theta_l}; \quad K_{H_2O} = \frac{\theta_{H_2O}}{P_{H_2O} \theta_l}; \quad K_3 = \frac{\theta_{CO} \theta_H}{\theta_{CHO} \theta_l};$$
$$K_4 = \frac{\theta_{CO} \theta_H}{\theta_{CHO} \theta_l}; \quad K_5 = \frac{\theta_{CH_4} \theta_l^3}{\theta_{CH} \theta_H^3}; \quad K_7 = \frac{\theta_{OH} \theta_l}{\theta_O \theta_H}; \quad K_8 = \frac{\theta_{H_2O} \theta_l}{\theta_{OH} \theta_H};$$

Therefore:

$$\frac{K_{CH_4}K_{H_2O}^2}{K_3K_4K_5K_7^2K_8^2K_{H_2}^4K_{CO_2}} = \frac{P_{H_2}^4P_{CO_2}}{P_{CH_4}P_{H_2O}^2} = \frac{1}{K_{eq}}$$

We can also define:

- $k = \overrightarrow{k}_3 \frac{K_7K_8K_{CO_2}K_{H_2}^{1.5}}{K_{H_2O}}$
- $K_{H_2} = \sqrt{K_{H_2}}$
- $K_{mix} = \frac{K_7K_8K_{CO_2}K_{H_2}}{K_{H_2O}}$
- $K_{OH} = \frac{K_{H_2O}}{K_8\sqrt{K_{H_2}}}$

The resulting reaction rate is:

$$r_{CH_4} = \frac{k\frac{P_{CO_2}P_{H_2}^{1.5}}{P_{H_2O}}\left(1 - \frac{P_{CH_4}P_{H_2O}^2}{P_{CO_2}P_{H_2}^4K_{eq}}\right)}{\left(1 + K_{H_2}P_{H_2}^{0.5} + K_{mix}\frac{P_{CO_2}P_{H_2}}{P_{H_2O}} + K_{OH}\frac{P_{H_2O}}{P_{H_2}^{0.5}}\right)^2}$$

C.2 Koschany model - LCCP modification

The elementary reactions are similar to those proposed by Koschany et al. [90]. The RDS is again the step of CHO formation, but the CO_2 dissociation and CH formation from CHO are H-assisted, therefore "O" is never formed in the process. The resulting elementary steps are:

1. $CO_2 + l \rightleftharpoons CO_2^*$
2. $H_2 + 2\ l \rightleftharpoons 2\ H^*$
3. $CO_2^* + H^* \rightleftharpoons CO^* + OH^*$
4. $CO^* + H^* \rightleftharpoons CHO^* + l$
5. $CHO^* + H^* \rightleftharpoons CH^* + OH^*$
6. $CH^* + 3\ H^* \rightleftharpoons CH_4^* + 3\ l$
7. $CH_4^* \rightleftharpoons CH_4 + l$
8. $OH^* + H^* \rightleftharpoons H_2O^* + l$
9. $H_2O^* \rightleftharpoons H_2O + l$

C.2.1 Derivation

First of all, we introduce some definitions:
$\frac{\overrightarrow{k}_1}{\overleftarrow{k}_1} = K_{CO_2}$; $\frac{\overrightarrow{k}_2}{\overleftarrow{k}_2} = K_{H_2}$; $\frac{\overleftarrow{k}_7}{\overrightarrow{k}_7} = K_{CH_4}$; $\frac{\overleftarrow{k}_9}{\overrightarrow{k}_9} = K_{H_2O}$; $\frac{\overrightarrow{k}_3}{\overleftarrow{k}_3} = K_3$;
$\frac{\overrightarrow{k}_4}{\overleftarrow{k}_4} = K_4$; $\frac{\overrightarrow{k}_5}{\overleftarrow{k}_5} = K_5$; $\frac{\overrightarrow{k}_6}{\overleftarrow{k}_6} = K_6$; $\frac{\overrightarrow{k}_8}{\overleftarrow{k}_8} = K_8$;

So, from r_1:
$$\overrightarrow{k}_1 P_{CO_2}\theta_l - \overleftarrow{k}_1\theta_{CO_2} = 0 \Rightarrow \theta_{CO_2} = \frac{\overrightarrow{k}_1 P_{CO_2}}{\overleftarrow{k}_1}\theta_l \Rightarrow \theta_{CO_2} = K_{CO_2}P_{CO_2}\theta_l$$

From r_2:
$$\overrightarrow{k}_2 P_{H_2}\theta_l^2 - \overleftarrow{k}_2\theta_H^2 = 0 \Rightarrow \theta_H = \sqrt{\frac{\overrightarrow{k}_2 P_{H_2}}{\overleftarrow{k}_2}}\theta_l \Rightarrow \theta_H = \sqrt{K_{H_2}P_{H_2}}\theta_l$$

From r_7:

$$\overrightarrow{k}_7\theta_{CH_4} - \overleftarrow{k}_7 P_{CH_4}\theta_l = 0 \Rightarrow \theta_{CH_4} = \frac{\overleftarrow{k}_7}{\overrightarrow{k}_7} P_{CH_4}\theta_l \Rightarrow \theta_{CH_4} = K_{CH_4}P_{CH_4}\theta_l$$

From r_9:

$$\overrightarrow{k}_9\theta_{H_2O} - \overleftarrow{k}_9 P_{H_2O}\theta_l = 0 \Rightarrow \theta_{H_2O} = \frac{\overleftarrow{k}_9}{\overrightarrow{k}_9} P_{H_2O}\theta_l \Rightarrow \theta_{H_2O} = K_{H_2O}P_{H_2O}\theta_l$$

From r_8:

$$\overrightarrow{k}_8\theta_{OH}\theta_H - \overleftarrow{k}_8\theta_{H_2O}\theta_l = 0 \Rightarrow \theta_{OH} = \frac{\overleftarrow{k}_8\theta_{H_2O}}{\overrightarrow{k}_8\theta_H}\theta_l \Rightarrow \theta_{OH} = \frac{K_{H_2O}P_{H_2O}}{K_8\sqrt{K_{H_2}P_{H_2}}}\theta_l$$

From r_6:

$$\overrightarrow{k}_6\theta_{CH}\theta_H^3 - \overleftarrow{k}_6\theta_{CH_4}\theta_l^3 = 0 \Rightarrow \theta_{CH} = \frac{\overleftarrow{k}_6\theta_{CH_4}}{\overrightarrow{k}_6\theta_H^3}\theta_l^3 \Rightarrow \theta_{CH} = \frac{K_{CH_4}P_{CH_4}}{K_6\sqrt{(K_{H_2O}P_{H_2O})^3}}\theta_l$$

From r_5:

$$\overrightarrow{k}_5\theta_{CHO}\theta_H - \overleftarrow{k}_5\theta_{CH}\theta_{OH} = 0 \Rightarrow \theta_{CHO} = \frac{\overleftarrow{k}_5\theta_{CH}\theta_{OH}}{\overrightarrow{k}_5\theta_H} \Rightarrow \theta_{CHO} = \frac{K_{CH_4}K_{H_2O}P_{CH_4}P_{H_2O}}{K_5K_6K_8\sqrt{(K_{H_2O}P_{H_2O})^5}}\theta_l$$

From r_3:

$$\overrightarrow{k}_3\theta_{CO_2}\theta_H - \overleftarrow{k}_3\theta_{CO}\theta_{OH} = 0 \Rightarrow \theta_{CO} = \frac{\overrightarrow{k}_3\theta_{CO_2}\theta_H}{\overleftarrow{k}_3\theta_{OH}} \Rightarrow \theta_{CO} = \frac{K_3K_8K_{CO_2}K_{H_2}P_{CO_2}P_{H_2}}{K_{H_2O}P_{H_2O}}\theta_l$$

Active site balance

Now we can exploit the active sites balance to find θ_l, defining as MASI the species CO, H, OH

$$\theta_{CO} + \theta_H + \theta_{OH} + \theta_l = 1$$

$$\frac{K_3K_8K_{CO_2}K_{H_2}P_{CO_2}P_{H_2}}{K_{H_2O}P_{H_2O}}\theta_l + \sqrt{K_{H_2}P_{H_2}}\theta_l + \frac{K_{H_2O}P_{H_2O}}{K_8\sqrt{K_{H_2}P_{H_2}}}\theta_l + \theta_l = 1$$

$$\theta_l = \frac{1}{\left(1 + \frac{K_3K_8K_{CO_2}K_{H_2}P_{CO_2}P_{H_2}}{K_{H_2O}P_{H_2O}} + \sqrt{K_{H_2}P_{H_2}} + \frac{K_{H_2O}P_{H_2O}}{K_8\sqrt{K_{H_2}P_{H_2}}\theta_l}\right)}$$

RDS

Now we can write the rate expression for the RDS. So:

$$r_4 = r_{CH_4} = \overrightarrow{k}_4 \theta_{CO}\theta_H - \overleftarrow{k_4}\theta_{CHO}\theta_l =$$

$$= \overrightarrow{k}_4 \frac{K_3K_8K_{CO_2}K_{H_2}P_{CO_2}P_{H_2}}{K_{H_2O}P_{H_2O}}\sqrt{K_{H_2}P_{H_2}}\theta_l^2 - \overleftarrow{k_4}\frac{K_{CH_4}K_{H_2O}P_{CH_4}P_{H_2O}}{K_5K_6K_8\sqrt{(K_{H_2O}P_{H_2O})^5}}\theta_l^2 =$$

$$= \frac{\overrightarrow{k}_4 \frac{K_3K_8K_{CO_2}K_{H_2}^{1.5}P_{CO_2}P_{H_2}^{1.5}}{K_{H_2O}P_{H_2O}}\left(1 - \frac{K_{CH_4}K_{H_2O}^2}{K_3K_4K_5K_6K_8^2K_{H_2}^4K_{CO_2}}\frac{P_{CH_4}P_{H_2O}^2}{P_{CO_2}P_{H_2}^4}\right)}{\left(1 + \frac{K_3K_8K_{CO_2}K_{H_2}P_{CO_2}P_{H_2}}{K_{H_2O}P_{H_2O}} + \sqrt{K_{H_2}P_{H_2}} + \frac{K_{H_2O}P_{H_2O}}{K_8\sqrt{K_{H_2}P_{H_2}}}\right)^2}$$

C.2.2 Rate Expression

Finally, we can see that:

$$K_{H_2} = \frac{\theta_H^2}{P_{H_2}\theta_l^2}; \quad K_{CO_2} = \frac{\theta_{CO_2}}{P_{CO_2}\theta_l}; \quad K_{CH_4} = \frac{\theta_{CH_4}}{P_{CH_4}\theta_l}; \quad K_{H_2O} = \frac{\theta_{H_2O}}{P_{H_2O}\theta_l}; \quad K_3 = \frac{\theta_{CO}\theta_{OH}}{\theta_{CO_2}\theta_H};$$
$$K_4 = \frac{\theta_{CO}\theta_H}{\theta_{CHO}\theta_l}; \quad K_5 = \frac{\theta_{CH}\theta_{OH}}{\theta_{CHO}\theta_H}; \quad K_6 = \frac{\theta_{CH_4}\theta_l^3}{\theta_{CH}\theta_H^3}; \quad K_8 = \frac{\theta_{H_2O}\theta_l}{\theta_{OH}\theta_H};$$

Therefore:

$$\frac{K_{CH_4}K_{H_2O}^2}{K_3K_4K_5K_6K_8^2K_{H_2}^4K_{CO_2}} = \frac{P_{H_2}^4P_{CO_2}}{P_{CH_4}P_{H_2O}^2} = \frac{1}{K_{eq}}$$

We can also define:

- $k = \overrightarrow{k}_4 \frac{K_3K_8K_{CO_2}\sqrt{(K_{H_2})^3}}{K_{H_2O}}$
- $K_{H_2} = \sqrt{K_{H_2}}$
- $K_{mix} = \frac{K_3K_8K_{CO_2}K_{H_2}}{K_{H_2O}}$
- $K_{OH} = \frac{K_{H_2O}}{K_8\sqrt{K_{H_2}}}$

The resulting reaction rate is:

$$r_{CH_4} = \frac{k\frac{P_{CO_2}P_{H_2}^{1.5}}{P_{H_2O}}\left(1 - \frac{P_{CH_4}P_{H_2O}^2}{P_{CO_2}P_{H_2}^4 K_{eq}}\right)}{\left(1 + K_{H_2}P_{H_2}^{0.5} + K_{mix}\frac{P_{CO_2}P_{H_2}}{P_{H_2O}} + K_{OH}\frac{P_{H_2O}}{P_{H_2}^{0.5}}\right)^2}$$

Appendix D

Internally developed models derivation

D.1 Raco − Vidotto Model

D.1.1 Elementary Steps

The elementary steps, that we decided to consider, are:

1. $H_2 + 2\ l \rightleftharpoons 2\ H^*$
2. $CO_2 + l \rightleftharpoons CO_2^*$
3. $CO_2^* + l \rightleftharpoons CO^* + O^*$
4. $CO^* + H^* \rightleftharpoons COH^* + l$
5. $COH^* + H^* \rightleftharpoons CH^* + OH^*$
6. $CH^* + H^* \rightleftharpoons CH_2^* + l$
7. $CH_2^* + H^* \rightleftharpoons CH_3^* + l$
8. $CH_3^* + H^* \rightleftharpoons CH_4^* + l$
9. $CH_4^* \rightleftharpoons CH_4 + l$
10. $O^* + H^* \rightleftharpoons OH^* + l$
11. $OH^* + H^* \rightleftharpoons H_2O^* + l$

12. $H_2O^* \rightleftharpoons H_2O + l$

13. $CO^* \rightleftharpoons CO + l$

The elementary step 5 is the RDS for CO-methanation, while we decided to consider the step 3 as RDS for the RWGS.

D.1.2 Derivation

Now we can proceed with the derivation of the final rate expression, considering that all the steps aside from the RDSs are at quasi-equilibrium.
First of all, we introduce some definitions:

$$\frac{\overrightarrow{k}_1}{\overleftarrow{k}_1} = K_{H_2}; \quad \frac{\overrightarrow{k}_2}{\overleftarrow{k}_2} = K_{CO_2}; \quad \frac{\overleftarrow{k}_9}{\overrightarrow{k}_9} = K_{CH_4}; \quad \frac{\overleftarrow{k}_{12}}{\overrightarrow{k}_{12}} = K_{H_2O};$$
$$\frac{\overleftarrow{k}_{13}}{\overrightarrow{k}_{13}} = K_{CO}; \quad \frac{\overrightarrow{k}_3}{\overleftarrow{k}_3} = K_3; \quad \frac{\overrightarrow{k}_4}{\overleftarrow{k}_4} = K_4; \quad \frac{\overrightarrow{k}_5}{\overleftarrow{k}_5} = K_5; \quad \frac{\overrightarrow{k}_6}{\overleftarrow{k}_6} = K_6;$$
$$\frac{\overrightarrow{k}_7}{\overleftarrow{k}_7} = K_7; \quad \frac{\overrightarrow{k}_8}{\overleftarrow{k}_8} = K_8; \quad \frac{\overrightarrow{k}_{10}}{\overleftarrow{k}_{10}} = K_{10}; \quad \frac{\overrightarrow{k}_{11}}{\overleftarrow{k}_{11}} = K_{11};$$

So, from r_1:
$$\overrightarrow{k}_1 P_{H_2} \theta_l^2 - \overleftarrow{k}_1 \theta_H^2 = 0 \Rightarrow \theta_H = \sqrt{\frac{\overrightarrow{k}_1 P_{H_2}}{\overleftarrow{k}_1}}\theta_l \Rightarrow \theta_H = \sqrt{K_{H_2} P_{H_2}}\theta_l$$

From r_2:
$$\overrightarrow{k}_2 P_{CO_2} \theta_l - \overleftarrow{k}_2 \theta_{CO_2} = 0 \Rightarrow \theta_{CO_2} = \frac{\overrightarrow{k}_2}{\overleftarrow{k}_2} P_{CO_2}\theta_l \Rightarrow \theta_{CO_2} = K_{CO_2} P_{CO_2}\theta_l$$

From r_9:
$$\overrightarrow{k}_9 \theta_{CH_4} - \overleftarrow{k}_9 P_{CH_4}\theta_l = 0 \Rightarrow \theta_{CH_4} = \frac{\overleftarrow{k}_9}{\overrightarrow{k}_9} P_{CH_4}\theta_l \Rightarrow \theta_{CH_4} = K_{CH_4} P_{CH_4}\theta_l$$

From r_{12}:
$$\overrightarrow{k}_{12} \theta_{H_2O} - \overleftarrow{k}_{12} P_{H_2O}\theta_l = 0 \Rightarrow \theta_{H_2O} = \frac{\overleftarrow{k}_{12}}{\overrightarrow{k}_{12}} P_{H_2O}\theta_l \Rightarrow \theta_{H_2O} = K_{H_2O} P_{H_2O}\theta_l$$

From r_{13}:

$$\overrightarrow{k}_{13}\theta_{CO} - \overleftarrow{k}_{13}P_{CO}\theta_l = 0 \Rightarrow \theta_{CO} = \frac{\overleftarrow{k}_{13}}{\overrightarrow{k}_{13}}P_{CO}\theta_l \Rightarrow \theta_{CO} = K_{CO}P_{CO}\theta_l$$

From r_4:

$$\overrightarrow{k}_{4}\theta_{CO}\theta_H - \overleftarrow{k}_{4}\theta_{COH}\theta_l = 0 \Rightarrow \theta_{COH} = \frac{\overrightarrow{k}_{4}}{\overleftarrow{k}_{4}}\frac{\theta_{CO}\theta_H}{\theta_l} \Rightarrow \theta_{COH} = K_4 K_{CO} P_{CO}\sqrt{K_{H_2}P_{H_2}}\theta_l$$

From r_8:

$$\overrightarrow{k}_{8}\theta_{CH_3}\theta_H - \overleftarrow{k}_{8}\theta_{CH_4}\theta_l = 0 \Rightarrow \theta_{CH_3} = \frac{\overleftarrow{k}_{8}}{\overrightarrow{k}_{8}}\frac{\theta_{CH_4}}{\theta_H}\theta_l \Rightarrow \theta_{CH_3} = \frac{K_{CH_4}P_{CH_4}}{K_8\sqrt{K_{H_2}P_{H_2}}}\theta_l$$

From r_7:

$$\overrightarrow{k}_{7}\theta_{CH_2}\theta_H - \overleftarrow{k}_{7}\theta_{CH_3}\theta_l = 0 \Rightarrow \theta_{CH_2} = \frac{\overleftarrow{k}_{7}}{\overrightarrow{k}_{7}}\frac{\theta_{CH_3}}{\theta_H}\theta_l \Rightarrow \theta_{CH_2} = \frac{K_{CH_4}P_{CH_4}}{K_7K_8K_{H_2}P_{H_2}}\theta_l$$

From r_6:

$$\overrightarrow{k}_{6}\theta_{CH}\theta_H - \overleftarrow{k}_{6}\theta_{CH_2}\theta_l = 0 \Rightarrow \theta_{CH} = \frac{\overleftarrow{k}_{6}}{\overrightarrow{k}_{6}}\frac{\theta_{CH_2}}{\theta_H}\theta_l \Rightarrow \theta_{CH} = \frac{K_{CH_4}P_{CH_4}}{K_6K_7K_8\sqrt{(K_{H_2}P_{H_2})^3}}\theta_l$$

From r_{11}:

$$\overrightarrow{k}_{11}\theta_{OH}\theta_H - \overleftarrow{k}_{11}\theta_{H_2O}\theta_l = 0 \Rightarrow \theta_{OH} = \frac{\overleftarrow{k}_{11}}{\overrightarrow{k}_{11}}\frac{\theta_{H_2O}}{\theta_H}\theta_l \Rightarrow \theta_{OH} = \frac{K_{H_2O}P_{H_2O}}{K_{11}\sqrt{K_{H_2}P_{H_2}}}\theta_l$$

From r_{10}:

$$\overrightarrow{k}_{10}\theta_{O}\theta_H - \overleftarrow{k}_{10}\theta_{OH}\theta_l = 0 \Rightarrow \theta_{O} = \frac{\overleftarrow{k}_{10}}{\overrightarrow{k}_{10}}\frac{\theta_{OH}}{\theta_H}\theta_l \Rightarrow \theta_{O} = \frac{K_{H_2O}P_{H_2O}}{K_{10}K_{11}K_{H_2}P_{H_2}}\theta_l$$

Now all the coverage are function of constant parameters, gaseous species partial pressures and free sites.

Active sites balance

Hernandez et al. assumed as MASI H, OH and COH. We decided to keep the same hypothesis. Therefore the site balance is:

$$\theta_H + \theta_{OH} + \theta_{COH} + \theta_l = 1$$

And substituting, we have:

$$\sqrt{K_{H_2}P_{H_2}}\theta_l + \frac{K_{H_2O}P_{H_2O}}{K_{11}\sqrt{K_{H_2}P_{H_2}}}\theta_l + K_4K_{CO}P_{CO}\sqrt{K_{H_2}P_{H_2}}\theta_l + \theta_l = 1$$

Therefore we can define the free sites as function of constants and partial pressures:

$$\theta_l = \frac{1}{\left(1 + \sqrt{K_{H_2}P_{H_2}} + \frac{K_{H_2O}P_{H_2O}}{K_{11}\sqrt{K_{H_2}P_{H_2}}} + K_4K_{CO}P_{CO}\sqrt{K_{H_2}P_{H_2}}\right)}$$

RDSs

We can finally focus on the RDSs:

- $r_3 = r_{RWGS} = \overrightarrow{k}_3\theta_{CO_2}\theta_l - \overleftarrow{k}_3\theta_{CO}\theta_O \; =$

$$= \overrightarrow{k}_3K_{CO_2}P_{CO_2}\theta_l^2 - \overleftarrow{k}_3K_{CO}P_{CO}\frac{K_{H_2O}P_{H_2O}}{K_{10}K_{11}K_{H_2}P_{H_2}}\theta_l^2 =$$

$$= \frac{\overrightarrow{k}_3K_{CO_2}P_{CO_2}\left(1 - \frac{K_{CO}K_{H_2O}}{K_3K_{10}K_{11}K_{H_2}K_{CO_2}}\frac{P_{CO}P_{H_2O}}{P_{H_2}P_{CO_2}}\right)}{\left(1 + \sqrt{K_{H_2}P_{H_2}} + \frac{K_{H_2O}P_{H_2O}}{K_{11}\sqrt{K_{H_2}P_{H_2}}} + K_4K_{CO}P_{CO}\sqrt{K_{H_2}P_{H_2}}\right)^2}$$

- $r_5 = r_{CO_{met}} = \overrightarrow{k}_5\theta_{COH}\theta_H - \overleftarrow{k}_5\theta_{CH}\theta_{OH} \; =$

$$= \overrightarrow{k}_5K_4K_{CO}P_{CO}K_{H_2}P_{H_2}\theta_l^2 - \frac{\overleftarrow{k}_5K_{CH_4}K_{H_2O}P_{CH_4}P_{H_2O}}{K_6K_7K_8K_{11}K_{H_2}^2P_{H_2}^2}\theta_l^2 \; =$$

$$= \frac{\overrightarrow{k}_5K_4K_{CO}P_{CO}K_{H_2}P_{H_2}\left(1 - \frac{K_{CH_4}K_{H_2O}}{K_4K_5K_6K_7K_8K_{11}K_{CO}K_{H_2}^3}\frac{P_{CH_4}P_{H_2O}}{P_{CO}P_{H_2}^3}\right)}{\left(1 + \sqrt{K_{H_2}P_{H_2}} + \frac{K_{H_2O}P_{H_2O}}{K_{11}\sqrt{K_{H_2}P_{H_2}}} + K_4K_{CO}P_{CO}\sqrt{K_{H_2}P_{H_2}}\right)^2}$$

D.1.3 Rate expressions

Finally, we can see that:

$$K_{H_2} = \frac{\theta_H^2}{P_{H_2}\theta_l^2}; \quad K_{CO_2} = \frac{\theta_{CO_2}}{P_{CO_2}\theta_l}; \quad K_{CH_4} = \frac{\theta_{CH_4}}{P_{CH_4}\theta_l}; \quad K_{H_2O} = \frac{\theta_{H_2O}}{P_{H_2O}\theta_l};$$
$$K_{CO} = \frac{\theta_{CO}}{P_{CO}\theta_l}; \quad K_3 = \frac{\theta_{CO}\theta_O}{\theta_{CO_2}\theta_l}; \quad K_4 = \frac{\theta_{COH}\theta_l}{\theta_{CO}\theta_H}; \quad K_5 = \frac{\theta_{CH}\theta_{OH}}{\theta_{COH}\theta_H};$$
$$K_6 = \frac{\theta_{CH_2}\theta_l}{\theta_{CH}\theta_H}; \quad K_7 = \frac{\theta_{CH_3}\theta_l}{\theta_{CH_2}\theta_H}; \quad K_8 = \frac{\theta_{CH_4}\theta_l}{\theta_{CH_3}\theta_H}; \quad K_{10} = \frac{\theta_{OH}\theta_l}{\theta_O\theta_H};$$
$$K_{11} = \frac{\theta_{H_2O}\theta_l}{\theta_{OH}\theta_H};$$

Therefore:

- $\dfrac{K_{CO}K_{H_2O}}{K_3K_{10}K_{11}K_{H_2}K_{CO_2}} = \dfrac{P_{CO_2}P_{H_2}}{P_{CO}P_{H_2O}} = \dfrac{1}{K_{RWGS}^{eq}}$
- $\dfrac{K_{CH_4}K_{H_2O}}{K_4K_5K_6K_7K_8K_{11}K_{CO}K_{H_2}^3} = \dfrac{P_{CO}P_{H_2}^3}{P_{CH_4}P_{H_2O}} = \dfrac{1}{K_{CO_{met}}^{eq}}$

We can also define:

- $k_{RWGS} = \overrightarrow{k}_3 K_{CO_2}$
- $k_{CO_{met}} = \overrightarrow{k}_5 K_4 K_{CO} K_{H_2}$
- $K_{OH} = \dfrac{K_{H_2O}}{K_{11}\sqrt{K_{H_2}}}$
- $K_{COH} = K_4 K_{CO}\sqrt{K_{H_2}}$

The final rate expressions that we derived are:

- $r_{RWGS} = \dfrac{k_{RWGS}P_{CO_2}\left(1 - \dfrac{P_{CO}P_{H_2O}}{P_{H_2}P_{CO_2}K_{RWGS}^{eq}}\right)}{\left(1 + \sqrt{K_{H_2}P_{H_2}} + K_{OH}\dfrac{P_{H_2O}}{\sqrt{P_{H_2}}} + K_{COH}\sqrt{P_{H_2}}P_{CO}\right)^2}$
- $r_{CO_{met}} = \dfrac{k_{CO_{met}}P_{CO}P_{H_2}\left(1 - \dfrac{P_{CH_4}P_{H_2O}}{P_{CO}P_{H_2}^3K_{CO_{met}}^{eq}}\right)}{\left(1 + \sqrt{K_{H_2}P_{H_2}} + K_{OH}\dfrac{P_{H_2O}}{\sqrt{P_{H_2}}} + K_{COH}\sqrt{P_{H_2}}P_{CO}\right)^2}$

D.2 Vidotto – Raco Model

D.2.1 Elementary steps

The elementary steps, that we decided to consider, are:

1. $H_2 + 2\ l \rightleftharpoons 2\ H^*$
2. $CO_2 + l \rightleftharpoons CO_2^*$
3. $CO_2^* + H^* \rightleftharpoons CO^* + OH^*$
4. $CO^* + H^* \rightleftharpoons COH^* + l$
5. $COH^* + H^* \rightleftharpoons CH^* + OH^*$
6. $CH^* + H^* \rightleftharpoons CH_2^* + l$
7. $CH_2^* + H^* \rightleftharpoons CH_3^* + l$
8. $CH_3^* + H^* \rightleftharpoons CH_4^* + l$
9. $CH_4^* \rightleftharpoons CH_4 + l$
10. $OH^* + H^* \rightleftharpoons H_2O^* + l$
11. $H_2O^* \rightleftharpoons H_2O + l$
12. $CO^* \rightleftharpoons CO + l$

In our derivation the RDSs are step 5 for the CO methanation and step 3 for the RWGS.

D.2.2 Derivation

First of all, we introduce some definitions:

$$\frac{\overrightarrow{k}_1}{\overleftarrow{k}_1} = K_{H_2}; \quad \frac{\overrightarrow{k}_2}{\overleftarrow{k}_2} = K_{CO_2}; \quad \frac{\overleftarrow{k}_{12}}{\overrightarrow{k}_{12}} = K_{CO};$$

$$\frac{\overleftarrow{k}_9}{\overrightarrow{k}_9} = K_{CH_4}; \quad \frac{\overleftarrow{k}_{11}}{\overrightarrow{k}_{11}} = K_{H_2O}; \quad \frac{\overrightarrow{k}_4}{\overleftarrow{k}_4} = K_4;$$

$$\frac{\overrightarrow{k}_6}{\overleftarrow{k}_6} = K_6; \quad \frac{\overrightarrow{k}_7}{\overleftarrow{k}_7} = K_7; \quad \frac{\overrightarrow{k}_8}{\overleftarrow{k}_8} = K_8; \quad \frac{\overrightarrow{k}_{10}}{\overleftarrow{k}_{10}} = K_{10};$$

So, from r_1:

$$\overrightarrow{k}_1 P_{H_2}\theta_l^2 - \overleftarrow{k}_1\theta_H^2 = 0 \Rightarrow \theta_H = \sqrt{\frac{\overrightarrow{k}_1 P_{H_2}}{\overleftarrow{k}_1}}\theta_l \Rightarrow \theta_H = \sqrt{K_{H_2}P_{H_2}}\theta_l$$

From r_2:

$$\overrightarrow{k}_2 P_{CO_2}\theta_l - \overleftarrow{k}_2\theta_{CO_2} = 0 \Rightarrow \theta_{CO_2} = \frac{\overrightarrow{k}_2}{\overleftarrow{k}_2}P_{CO_2}\theta_l \Rightarrow \theta_{CO_2} = K_{CO_2}P_{CO_2}\theta_l$$

From r_{12}:

$$\overrightarrow{k}_{12}\theta_{CO} - \overleftarrow{k}_{12}P_{CO}\theta_l = 0 \Rightarrow \theta_{CO} = \frac{\overleftarrow{k}_{12}}{\overrightarrow{k}_{12}}P_{CO}\theta_l \Rightarrow \theta_{CO} = K_{CO}P_{CO}\theta_l$$

From r_9:

$$\overrightarrow{k}_9\theta_{CH_4} - \overleftarrow{k}_9 P_{CH_4}\theta_l = 0 \Rightarrow \theta_{CH_4} = \frac{\overleftarrow{k}_9}{\overrightarrow{k}_9}P_{CH_4}\theta_l \Rightarrow \theta_{CH_4} = K_{CH_4}P_{CH_4}\theta_l$$

From r_{11}:

$$\overrightarrow{k}_{11}\theta_{H_2O} - \overleftarrow{k}_{11}P_{H_2O}\theta_l = 0 \Rightarrow \theta_{H_2O} = \frac{\overleftarrow{k}_{11}}{\overrightarrow{k}_{11}}P_{H_2O}\theta_l \Rightarrow \theta_{H_2O} = K_{H_2O}P_{H_2O}\theta_l$$

From r_4:

$$\overrightarrow{k}_4\theta_{CO}\theta_H - \overleftarrow{k}_4\theta_{COH}\theta_l = 0 \Rightarrow \theta_{COH} = \frac{\overrightarrow{k}_4}{\overleftarrow{k}_4}\frac{\theta_{CO}\theta_H}{\theta_l} \Rightarrow \theta_{COH} = K_4K_{CO}P_{CO}\sqrt{K_{H_2}P_{H_2}}\theta_l$$

From r_{10}:

$$\overrightarrow{k}_{10}\theta_{OH}\theta_H - \overleftarrow{k}_{10}\theta_{H_2O}\theta_l = 0 \Rightarrow \theta_{OH} = \frac{\overleftarrow{k}_{10}}{\overrightarrow{k}_{10}}\frac{\theta_{H_2O}\theta_l}{\theta_H} \Rightarrow \theta_{OH} = \frac{K_{H_2O}P_{H_2O}}{K_{10}\sqrt{K_{H_2}P_{H_2}}}\theta_l$$

From r_8:

$$\overrightarrow{k}_8\theta_{CH_3}\theta_H - \overleftarrow{k}_8\theta_{CH_4}\theta_l = 0 \Rightarrow \theta_{CH_3} = \frac{\overleftarrow{k}_8}{\overrightarrow{k}_8}\frac{\theta_{CH_4}\theta_l}{\theta_H} \Rightarrow \theta_{CH_3} = \frac{K_{CH_4}P_{CH_4}}{K_8\sqrt{K_{H_2}P_{H_2}}}\theta_l$$

From r_7:

$$\overrightarrow{k}_7\theta_{CH_2}\theta_H - \overleftarrow{k}_7\theta_{CH_3}\theta_l = 0 \Rightarrow \theta_{CH_2} = \frac{\overleftarrow{k}_7}{\overrightarrow{k}_7}\frac{\theta_{CH_3}\theta_l}{\theta_H} \Rightarrow \theta_{CH_2} = \frac{K_{CH_4}P_{CH_4}}{K_7K_8K_{H_2}P_{H_2}}\theta_l$$

From r_6:

$$\overrightarrow{k}_6\theta_{CH}\theta_H - \overleftarrow{k}_6\theta_{CH_2}\theta_l = 0 \Rightarrow \theta_{CH} = \frac{\overleftarrow{k}_6}{\overrightarrow{k}_6}\frac{\theta_{CH_2}\theta_l}{\theta_H} \Rightarrow \theta_{CH} = \frac{K_{CH_4}P_{CH_4}}{K_6K_7K_8(\sqrt{K_{H_2}P_{H_2}})^3}\theta_l$$

Active sites balance

Now we can exploit the active sites balance to find θ_l, defining as MASI the species H, OH, COH:

$$\theta_H + \theta_{OH} + \theta_{COH} + \theta_l = 1$$

$$\sqrt{K_{H_2}P_{H_2}}\theta_l + \frac{K_{H_2O}P_{H_2O}}{K_{10}\sqrt{K_{H_2}P_{H_2}}}\theta_l + K_4K_{CO}P_{CO}\sqrt{K_{H_2}P_{H_2}}\theta_l + \theta_l = 1$$

$$\theta_l = \frac{1}{\left(K_4K_{CO}P_{CO}\sqrt{K_{H_2}P_{H_2}} + \sqrt{K_{H_2}P_{H_2}} + \frac{K_{H_2O}P_{H_2O}}{K_{10}\sqrt{K_{H_2}P_{H_2}}}\right)}$$

RDSs

Now we can write the rate expressions for the RDSs. So:

$$\begin{aligned} r_5 = r_{CO_{meth}} &= \overrightarrow{k}_5\theta_{COH}\theta_H - \overleftarrow{k}_5\theta_{CH}\theta_{OH} \\ &= \left(\overrightarrow{k}_5K_4K_{CO}P_{CO}K_{H_2}P_{H_2} - \overleftarrow{k}_5\frac{K_{CH_4}P_{CH_4}}{K_6K_7K_8(\sqrt{K_{H_2}P_{H_2}})^3}\frac{K_{H_2O}P_{H_2O}}{K_{10}\sqrt{K_{H_2}P_{H_2}}}\right))\theta_l^2 \\ \overrightarrow{k}_5K_4K_{CO}P_{CO}K_{H_2}P_{H_2}&\left(1 - \frac{\overleftarrow{k}_5}{\overrightarrow{k}_5}\frac{K_{CH_4}P_{CH_4}K_{H_2O}P_{H_2O}}{K_6K_7K_8K_{10}(K_{H_2}P_{H_2})^3K_4K_{CO}P_{CO}K_{H_2}P_{H_2}}\right)\theta_l^2 \end{aligned}$$

We can notice that:

$$\begin{aligned} &\frac{\overrightarrow{k}_5}{\overleftarrow{k}_5} = K_5 = \frac{\theta_{CH}\theta_{OH}}{\theta_{COH}\theta_H}; \quad K_{CH_4} = \frac{\theta_{CH_4}}{P_{CH_4}\theta_l}; \quad K_{H_2O} = \frac{\theta_{H_2O}}{P_{H_2O}\theta_l}; \\ &K_6 = \frac{\theta_{CH_2}\theta_l}{\theta_{CH}\theta_H}; \quad K_7 = \frac{\theta_{CH_3}\theta_l}{\theta_{CH_2}\theta_H}; \quad K_8 = \frac{\theta_{CH_4}\theta_l}{\theta_{CH_3}\theta_H}; \quad K_{10} = \frac{\theta_{H_2O}\theta_l}{\theta_{OH}\theta_H}; \\ &K_{H_2} = \frac{\theta_{H_2}^2}{P_{H_2}\theta_l^2}; \quad K_4 = \frac{\theta_{COH}\theta_l}{\theta_{CO}\theta_H}; \quad K_{CO} = \frac{\theta_{CO}}{P_{CO}\theta_l}; \end{aligned}$$

And so:

$$\frac{\overleftarrow{k}_5}{\overrightarrow{k}_5}\frac{K_{CH_4}P_{CH_4}K_{H_2O}P_{H_2O}}{K_6K_7K_8K_{10}(K_{H_2}P_{H_2})^3K_4K_{CO}P_{CO}K_{H_2}P_{H_2}} = \frac{P_{CO}P_{H_2}^3}{P_{CH_4}P_{H_2O}} = \frac{1}{K_{CO_{meth}}^{eq}}$$

Then:

$$r_5 = r_{CO_{meth}} = \frac{\overrightarrow{k}_5 K_4 K_{CO} K_{H_2} P_{CO} P_{H_2}\left(1 - \frac{P_{CH_4}P_{H_2O}}{P_{CO}P_{H_2}^3 K_{CO_{meth}}^{eq}}\right)}{\left(1 + K_4K_{CO}P_{CO}\sqrt{K_{H_2}P_{H_2}} + \sqrt{K_{H_2}P_{H_2}} + \frac{K_{H_2O}P_{H_2O}}{K_{10}\sqrt{K_{H_2}P_{H_2}}}\right)^2}$$

While, for the RWGS we can write:

$$r_3 = r_{RWGS} = \overrightarrow{k}_3\theta_{CO_2}\theta_H - \overleftarrow{k}_3\theta_{CO}\theta_{OH}$$

$$= \left(\overrightarrow{k}_3 K_{CO_2}P_{CO_2}\sqrt{K_{H_2}P_{H_2}} - \overleftarrow{k}_3\frac{K_{CO}P_{CO}K_{H_2O}P_{H_2O}}{K_{10}\sqrt{K_{H_2}P_{H_2}}}\right)\theta_l^2$$

$$= \overrightarrow{k}_3 K_{CO_2}P_{CO_2}\sqrt{K_{H_2}P_{H_2}}\left(1 - \frac{\overleftarrow{k}_3}{\overrightarrow{k}_3}\frac{K_{CO}P_{CO}K_{H_2O}P_{H_2O}}{K_{10}K_{H_2}P_{H_2}K_{CO_2}P_{CO_2}}\right)\theta_l^2$$

And, again, we can notice that:

$$\frac{\overrightarrow{k}_3}{\overleftarrow{k}_3} = K_3 = \frac{\theta_{CO}\theta_{OH}}{\theta_{CO_2}\theta_H}; \quad K_{CO_2} = \frac{\theta_{CO_2}}{P_{CO_2}\theta_l};$$

So:

$$\frac{K_{CO}K_{H_2O}}{K_3K_{10}K_{H_2}K_{CO_2}} = \frac{P_{H_2}P_{CO_2}}{P_{CO}P_{H_2O}} = \frac{1}{K_{RWGS}^{eq}}$$

$$r_3 = r_{RWGS} = \frac{\overrightarrow{k}_3 K_{CO_2}P_{CO_2}\sqrt{K_{H_2}P_{H_2}}\left(1 - \frac{P_{CO}P_{H_2O}}{P_{CO_2}P_{H_2}K_{RWGS}^{eq}}\right)}{\left(1 + K_4K_{CO}P_{CO}\sqrt{K_{H_2}P_{H_2}} + \sqrt{K_{H_2}P_{H_2}} + \frac{K_{H_2O}P_{H_2O}}{K_{10}\sqrt{K_{H_2}P_{H_2}}}\right)^2}$$

D.2.3 Rate expressions

We can group some constants:

$$\overrightarrow{k}_5 K_4 K_{CO} K_{H_2} = k_{CO_{meth}}$$

$$\overrightarrow{k}_3 K_{CO_2} \sqrt{K_{H_2}} = k_{rWGS}$$

$$K_4 K_{CO} \sqrt{K_{H_2}} = K_{COH}$$

$$\frac{K_{H_2O}}{K_{10} \sqrt{K_{H_2}}} = K_{OH}$$

And write the two rate expressions:

- $$r_{CO_{meth}} = \frac{k_{CO_{meth}} P_{CO} P_{H_2} \left(1 - \frac{P_{CH_4} P_{H_2O}}{P_{CO} P_{H_2}^3 K_{CO_{meth}}^{eq}}\right)}{\left(1 + K_{COH} P_{CO} \sqrt{P_{H_2}} + \sqrt{K_{H_2} P_{H_2}} + K_{OH} \frac{P_{H_2O}}{\sqrt{P_{H_2}}}\right)^2};$$
- $$r_{RWGS} = \frac{k_{RWGS} P_{CO_2} \sqrt{P_{H_2}} \left(1 - \frac{P_{CO} P_{H_2O}}{P_{CO_2} P_{H_2} K_{RWGS}^{eq}}\right)}{\left(1 + K_{COH} P_{CO} \sqrt{P_{H_2}} + \sqrt{K_{H_2} P_{H_2}} + K_{OH} \frac{P_{H_2O}}{\sqrt{P_{H_2}}}\right)^2};$$

Bibliography

[1] Keith P Shine *et al.* "Radiative forcing of climate". *Climate change: The IPCC scientific assessment* (1990), pp. 41–68. URL: https://core.ac.uk/download/pdf/42811043.pdf.

[2] *UNFCC, The Paris Agreement*. URL: https://unfccc.int/process-and-meetings/the-paris-agreement/the-paris-agreement.

[3] *BP Energy Outlook, 2019 Edition*. URL: https://www.bp.com/content/dam/bp/businesssites/%20en/global/corporate/pdfs/energy%20-%20economics/energy%20-%20outlook/bp-%20energy%20-%20outlook-%202019.pdf.

[4] IEA. *Special report on Carbon Capture Utilisation and Storage, CCUS in clean energy transitions*. 2020. URL: https://www.iea.org/reports/ccus-in-clean-energy-transitions.

[5] *CO2 enhanced oil recovery*. URL: https://www.globalenergyinstitute.org/sites/default/files/020174_EI21_EnhancedOilRecovery_final.pdf.

[6] Frederic D Meylan, Vincent Moreau, and Suren Erkman. "CO2 utilization in the perspective of industrial ecology, an overview". *Journal of CO2 Utilization* 12 (2015), pp. 101–108. DOI: https://doi.org/10.1016/j.jcou.2015.05.003.

[7] Rosa M Cuéllar-Franca and Adisa Azapagic. "Carbon capture, storage and utilisation technologies: A critical analysis and comparison of their life cycle environmental impacts". *Journal of CO2 utilization* 9 (2015), pp. 82–102. DOI: https://doi.org/10.1016/j.jcou.2014.12.001.

[8] IEA. *Putting CO2 to Use: Creating Value from Emissions*. 2019. URL: https://webstore.iea.org/putting-co2-to-use.

[9] Paul Sabatier. "New synthesis of methane". *Comptes Rendus* 134 (1902), pp. 514–516.

[10] Manuel Götz *et al.* "Renewable Power-to-Gas: A technological and economic review". *Renewable energy* 85 (2016), pp. 1371–1390. DOI: https://doi.org/10.1016/j.renene.2015.07.066.

[11] Chalachew Mebrahtu *et al.* "CO2 methanation: principles and challenges". In: *Studies in surface science and catalysis*. Vol. 178. Elsevier, 2019, pp. 85–103. DOI: https://doi.org/10.1016/B978-0-444-64127-4.00005-7.

[12] Mohammad Songolzadeh *et al.* "Carbon dioxide separation from flue gases: a technological review emphasizing reduction in greenhouse gas emissions". *The Scientific World Journal* 2014 (2014). DOI: https://doi.org/10.1155/2014/828131.

[13] Anand B Rao and Edward S Rubin. "A technical, economic, and environmental assessment of amine-based CO2 capture technology for power plant greenhouse gas control". *Environmental science & technology* 36.20 (2002), pp. 4467–4475. DOI: https://doi.org/10.1021/es0158861.

[14] Najmus S. Sifat and Yousef Haseli. "A Critical Review of CO2 Capture Technologies and Prospects for Clean Power Generation". *Energies* 12.21 (2019). ISSN: 1996-1073. DOI: 10.3390/en12214143. URL: https://www.mdpi.com/1996-1073/12/21/4143.

[15] Ramesh Thiruvenkatachari *et al.* "Post combustion CO2 capture by carbon fibre monolithic adsorbents". *Progress in Energy and Combustion Science* 35.5 (2009), pp. 438–455. DOI: https://doi.org/10.1016/j.pecs.2009.05.003.

[16] Najmus S Sifat and Yousef Haseli. "A critical review of CO2 capture technologies and prospects for clean power generation". *Energies* 12.21 (2019), p. 4143. DOI: https://doi.org/10.3390/en12214143.

[17] MM Faruque Hasan *et al.* "A multi-scale framework for CO2 capture, utilization, and sequestration: CCUS and CCU". *Computers & Chemical Engineering* 81 (2015), pp. 2–21.

[18] MJ Tuinier, HP Hamers, and M van Sint Annaland. "Techno-economic evaluation of cryogenic CO2 capture—A comparison with absorption and membrane technology". *International Journal of Greenhouse Gas Control* 5.6 (2011), pp. 1559–1565. DOI: https://doi.org/10.1016/j.ijggc.2011.08.013.

[19] Karim Ghaib and Fatima-Zahrae Ben-Fares. "Power-to-Methane: A state-of-the-art review". *Renewable and Sustainable Energy Reviews* 81 (2018), pp. 433–446. DOI: http://dx.doi.org/10.1016/j.rser.2017.08.004.

[20] Hadi Ebrahimi and Mohammad Rahmani. "A new design for CO2 capture and usage in a syngas production unit by carbonate chemical looping". *Journal of Natural Gas Science and Engineering* 36 (2016), pp. 241–251. DOI: https://doi.org/10.1016/j.jngse.2016.10.007.

[21] Mónica Alonso *et al.* "Carbon dioxide capture from combustion flue gases with a calcium oxide chemical loop. Experimental results and process development". *International Journal of Greenhouse Gas Control* 4.2 (2010), pp. 167–173. DOI: https://doi.org/10.1016/j.ijggc.2009.10.004.

[22] Alfredo Ursua, Luis M Gandia, and Pablo Sanchis. "Hydrogen production from water electrolysis: current status and future trends". *Proceedings of the IEEE* 100.2 (2011), pp. 410–426. DOI: 10.1109/JPROC.2011.2156750.

[23] Jun Chi and Hongmei Yu. "Water electrolysis based on renewable energy for hydrogen production". *Chinese Journal of Catalysis* 39.3 (2018), pp. 390–394. DOI: 10.1016/S1872âĂŘ2067(17)62949âĂŘ8.

[24] Oliver Schmidt *et al.* "Future cost and performance of water electrolysis: An expert elicitation study". *International journal of hydrogen energy* 42.52 (2017), pp. 30470–30492. DOI: https://doi.org/10.1016/j.ijhydene.2017.10.045.

[25] Paul Sabatier and JB Senderens. "Direct hydrogenation of oxides of carbon in presence of various finely divided metals". *CR Acad Sci* 134.1 (1902), pp. 689–691.

[26] Jiajian Gao *et al.* "A thermodynamic analysis of methanation reactions of carbon oxides for the production of synthetic natural gas". *RSC advances* 2.6 (2012), pp. 2358–2368. DOI: 10.1039/c2ra00632d.

[27] Stefan Rönsch *et al.* "Review on methanation–From fundamentals to current projects". *Fuel* 166 (2016), pp. 276–296. DOI: http://dx.doi.org/10.1016/j.fuel.2015.10.111.

[28] MA Vannice. "The catalytic synthesis of hydrocarbons from carbon monoxide and hydrogen". *Catalysis Reviews—Science and Engineering* 14.1 (1976), pp. 153–191. DOI: https://doi.org/10.1080/03602457608073410.

[29] G Alex Mills and Fred W Steffgen. "Catalytic methanation". *Catalysis Reviews* 8.1 (1974), pp. 159–210. DOI: https://doi.org/10.1080/01614947408071860.

[30] Jangam Ashok *et al.* "A review of recent catalyst advances in CO2 methanation processes". *Catalysis Today* 356 (2020), pp. 471–489. DOI: https://doi.org/10.1016/j.cattod.2020.07.023.

[31] URL: https://www.mining.com/markets/commodity/rhodium.

[32] URL: https://www.mining.com/markets/commodity/nickel.

[33] URL: https://www.mining.com/markets/commodity/ruthenium.

[34] Patrizia Frontera *et al.* "Supported catalysts for CO2 methanation: a review". *Catalysts* 7.2 (2017), p. 59. DOI: 10.3390/catal7020059.

[35] Craig K Vance and Calvin H Bartholomew. "Hydrogenation of carbon dioxide on group viii metals: III, Effects of support on activity/selectivity and adsorption properties of nickel". *Applied Catalysis* 7.2 (1983), pp. 169–177.

[36] Wojciech Gac *et al.* "Effects of support composition on the performance of nickel catalysts in CO2 methanation reaction". *Catalysis Today* (2019). DOI: https://doi.org/10.1016/j.cattod.2019.07.026.

[37] MAA Aziz *et al.* "CO 2 methanation over heterogeneous catalysts: recent progress and future prospects". *Green Chemistry* 17.5 (2015), pp. 2647–2663. DOI: 10.1039/c5gc00119f.

[38] Shohei Tada *et al.* "Ni/CeO2 catalysts with high CO2 methanation activity and high CH4 selectivity at low temperatures". *International Journal of Hydrogen Energy* 37.7 (2012), pp. 5527–5531. DOI: https://doi.org/10.1016/j.ijhydene.2011.12.122.

[39] F Ocampo *et al.* "CO2 methanation over Ni-Ceria-Zirconia catalysts: effect of preparation and operating conditions". In: *IOP Conference Series: Materials Science and Engineering*. Vol. 19. 1. IOP Publishing. 2011, p. 012007. DOI: 10.1088/1757-899X/19/1/012007.

[40] Daniela CD da Silva *et al.* "The Ni/ZrO2 catalyst and the methanation of CO and CO2". *International Journal of Hydrogen Energy* 37.11 (2012), pp. 8923–8928. DOI: 10.1016/j.ijhydene.2012.03.020.

[41] Jie Liu *et al.* "Enhanced low-temperature activity of CO 2 methanation over highly-dispersed Ni/TiO 2 catalyst". *Catalysis Science & Technology* 3.10 (2013), pp. 2627–2633. DOI: 10.1039/c3cy00355h.

[42] Guoan Du *et al.* "Methanation of carbon dioxide on Ni-incorporated MCM-41 catalysts: The influence of catalyst pretreatment and study of steady-state reaction". *Journal of catalysis* 249.2 (2007), pp. 370–379. DOI: https://doi.org/10.1016/j.jcat.2007.03.029.

[43] E Jwa *et al.* "Plasma-assisted catalytic methanation of CO and CO2 over Ni–zeolite catalysts". *Fuel processing technology* 108 (2013), pp. 89–93. DOI: https://doi.org/10.1016/j.fuproc.2012.03.008.

[44] Shyam Kattel, Ping Liu, and Jingguang G Chen. "Tuning selectivity of CO2 hydrogenation reactions at the metal/oxide interface". *Journal of the American Chemical Society* 139.29 (2017), pp. 9739–9754. DOI: https://doi.org/10.1021/jacs.7b05362.

[45] Bin Miao *et al.* "Catalysis mechanisms of CO 2 and CO methanation". *Catalysis Science & Technology* 6.12 (2016), pp. 4048–4058. DOI: 10.1039/c6cy00478d.

[46] Stephan Eckle, Hans-Georg Anfang, and R Jürgen Behm. "Reaction intermediates and side products in the methanation of CO and CO2 over supported Ru catalysts in H2-rich reformate gases". *The Journal of Physical Chemistry C* 115.4 (2011), pp. 1361–1367. DOI: 10.1021/jp108106t.

[47] Qiushi Pan *et al.* "In situ FTIR spectroscopic study of the CO 2 methanation mechanism on Ni/Ce 0.5 Zr 0.5 O 2". *Catalysis Science & Technology* 4.2 (2014), pp. 502–509. DOI: 10.1039/c3cy00868a.

[48] Sang-Joon Choe *et al.* "Adsorbed carbon formation and carbon hydrogenation for CO 2 methanation on the Ni (111) surface: ASED-MO study". *Bulletin of the Korean Chemical Society* 26.11 (2005), pp. 1682–1688. DOI: https://doi.org/10.5012/bkcs.2005.26.11.1682.

[49] Shohei Tada and R Kikuchi. "Mechanistic study and catalyst development for selective carbon monoxide methanation". *Catalysis Science & Technology* 5.6 (2015), pp. 3061–3070. DOI: 10.1039/c5cy00150a.

[50] PA Ussa Aldana *et al.* "Catalytic CO2 valorization into CH4 on Ni-based ceria-zirconia. Reaction mechanism by operando IR spectroscopy". *Catalysis Today* 215 (2013), pp. 201–207. DOI: http://dx.doi.org/10.1016/j.cattod.2013.02.019.

[51] A Westermann *et al.* "Insight into CO2 methanation mechanism over NiUSY zeolites: An operando IR study". *Applied Catalysis B: Environmental* 174 (2015), pp. 120–125. DOI: http://dx.doi.org/10.1016/j.apcatb.2015.02.026.

[52] Qiushi Pan *et al.* "Insight into the reaction route of CO2 methanation: Promotion effect of medium basic sites". *Catalysis Communications* 45 (2014), pp. 74–78. DOI: http://dx.doi.org/10.1016/j.catcom.2013.10.034.

[53] Shin-ichiro Fujita *et al.* "Mechanisms of methanation of carbon dioxide and carbon monoxide over nickel/alumina catalysts". *Applied Catalysis A: General* 104.1 (1993), pp. 87–100. DOI: https://doi.org/10.1016/0926-860X(93)80212-9.

[54] Manuel Bailera *et al.* "Power to Gas projects review: Lab, pilot and demo plants for storing renewable energy and CO2". *Renewable and Sustainable Energy Reviews* 69 (2017), pp. 292–312. DOI: http://dx.doi.org/10.1016/j.rser.2016.11.130.

[55] Jan Kopyscinski, Tilman J Schildhauer, and Serge MA Biollaz. "Production of synthetic natural gas (SNG) from coal and dry biomass–A technology review from 1950 to 2009". *Fuel* 89.8 (2010), pp. 1763–1783. DOI: 10.1016/j.fuel.2010.01.027.

[56] C.Pieroni L.Maggioni. *Report on the biomethane injection into national gas grid.*

[57] Ali El Sibai, Liisa K Rihko Struckmann, and Kai Sundmacher. "Model-based Optimal Sabatier Reactor Design for Power-to-Gas Applications". *Energy Technology* 5.6 (2017), pp. 911–921. DOI: 10.1002/ente.201600600.

[58] Manuel Götz, Amy McDaniel Koch, and Frank Graf. "State of the art and perspectives of CO2 methanation process concepts for power-to-gas applications". In: *International Gas Union Research Conference*. Vol. 13. International Gas Union Fornebu, Norway. 2014.

[59] David Schlereth, Philipp J Donaubauer, and Olaf Hinrichsen. "Metallic honeycombs as catalyst supports for methanation of carbon dioxide". *Chemical Engineering & Technology* 38.10 (2015), pp. 1845–1852. DOI: 10.1002/ceat.201400717.

[60] Jonathan Lefebvre, Siegfried Bajohr, and Thomas Kolb. "Modeling of the transient behavior of a slurry bubble column reactor for CO2 methanation, and comparison with a tube bundle reactor". *Renewable energy* 151 (2020), pp. 118–136. DOI: https://doi.org/10.1016/j.renene.2019.11.008.

[61] Manuel Gruber *et al.* "Power-to-Gas through thermal integration of high-temperature steam electrolysis and carbon dioxide methanation-Experimental results". *Fuel Processing Technology* 181 (2018), pp. 61–74. DOI: doi:10.1016/j.fuproc.2018.09.003.

[62] Tadeusz Chwoła *et al.* "Pilot plant initial results for the methanation process using CO2 from amine scrubbing at the Łaziska power plant in Poland". *Fuel* 263 (2020), p. 116804. DOI: 10.1016/j.fuel.2019.116804.

[63] Haruhiko Ohya *et al.* "Methanation of carbon dioxide by using membrane reactor integrated with water vapor permselective membrane and its analysis". *Journal of Membrane Science* 131.1-2 (1997), pp. 237–247.

[64] Renaud Delmelle *et al.* "Development of improved nickel catalysts for sorption enhanced CO2 methanation". *international journal of hydrogen energy* 41.44 (2016), pp. 20185–20191. DOI: http://dx.doi.org/10.1016/j.ijhydene.2016.09.045.

[65] Stéphane Walspurger *et al.* "Sorption enhanced methanation for substitute natural gas production: Experimental results and thermodynamic considerations". *Chemical Engineering Journal* 242 (2014), pp. 379–386. DOI: http://dx.doi.org/10.1016/j.cej.2013.12.045.

[66] Dominik Schollenberger *et al.* "Scale-Up of Innovative Honeycomb Reactors for Power-to-Gas Applications–The Project Store&Go". *Chemie Ingenieur Technik* 90.5 (2018), pp. 696–702. DOI: 10.1002/cite.201700139.

[67] Kriston P Brooks *et al.* "Methanation of carbon dioxide by hydrogen reduction using the Sabatier process in microchannel reactors". *Chemical Engineering Science* 62.4 (2007), pp. 1161–1170. DOI: 10.1016/j.ces.2006.11.020.

[68] Karim Ghaib, Korbinian Nitz, and Fatima-Zahrae Ben-Fares. "Katalytische methanisierung von kohlenstoffdioxid". *Chemie Ingenieur Technik* 10.88 (2016), pp. 1435–1443. DOI: 10.1002/cite.201600066.

[69] Benjamin Collins Brodie. "II. Note on the synthesis of marsh-gas and formic acid, and on the electric decomposition of carbonic oxide". *Proceedings of the Royal Society of London* 21.139-147 (1873), pp. 245–247. DOI: https://doi.org/10.1098/rspl.1872.0052.

[70] H Scott Fogler. *Essentials of Chemical Reaction Engineering: Essenti Chemica Reactio Engi*. Pearson Education, 2010.

[71] G Garbarino, P Riani, and L Magistri. "Busca, G". *Methanation of carbon dioxide on Ru/Al* 2 (2019), pp. 21–28. DOI: 10.1016/j.ijhydene.2014.05.111.

[72] Xiang Wang *et al.* "Kinetic modeling and transient DRIFTS–MS studies of CO2 methanation over Ru/Al2O3 catalysts". *Journal of Catalysis* 343 (2016), pp. 185–195. DOI: 10.1016/j.jcat.2016.02.001.

[73] Melis S Duyar *et al.* "Kinetics of CO2 methanation over Ru/γ-Al2O3 and implications for renewable energy storage applications". *Journal of CO2 Utilization* 12 (2015), pp. 27–33. DOI: 10.1016/j.jcou.2015.10.003..

[74] Frigyes Solymosi, A.+ Erdöhelyi, and Tamás Bánsági. "Methanation of CO2 on supported rhodium catalyst". *Journal of Catalysis* 68.2 (1981), pp. 371–382. DOI: https://doi.org/10.1016/0021-9517(81)90106-8.

[75] Frigyes Solymosi, András Erdöhelyi, and Mária Kocsis. "Methanation of CO 2 on supported Ru catalysts". *Journal of the Chemical Society, Faraday Transactions 1: Physical Chemistry in Condensed Phases* 77.5 (1981), pp. 1003–1012. DOI: 10.1039/F19817701003.

[76] M Šolc. "Kinetik der hydrierung des kohlendioxyds zu methan an einem nickel-chrom (III)-oxyd-katalysator". *Collection of Czechoslovak Chemical Communications* 27.11 (1962), pp. 2621–2627.

[77] Marcin Ku? mierz. "Kinetic study on carbon dioxide hydrogenation over Ru/?-Al2O3 catalysts". *Catalysis Today* 137.2-4 (2008), pp. 429–432. DOI: 10.1016/j.cattod.2008.03.003.

[78] Jeng H Chiang and Jack R Hopper. "Kinetics of the hydrogenation of carbon dioxide over supported nickel". *Industrial & Engineering Chemistry Product Research and Development* 22.2 (1983), pp. 225–228. URL: https://pubs.acs.org/doi/pdf/10.1021/i300010a011?casa_token=pLo8uKc04_sAAAAA:vQjjfbMO85MJRMz9MfHSZmaX9Cw1DEIBgsf9N660uCGt0GP8PLagd39KIi_cy5EnR4bVDKFVyUXo.

[79] Michel Marwood *et al.* "Transient drift spectroscopy for the determination of the surface reaction kinetics of CO2 methanation". *Chemical engineering science* 49.24 (1994), pp. 4801–4809. DOI: 10.1016/S0009-2509(05)80060-0.

[80] Kaoru Takeishi and Ken-ich Aika. "Comparison of carbon dioxide and carbon monoxide with respect to hydrogenation on Raney ruthenium catalysts". *Applied Catalysis A: General* 133.1 (1995), pp. 31–45. DOI: 10.1016/0926-860X(95)00143-3.

[81] JN Dew, RR White, and CM Sliepcevich. "Hydrogenation of carbon dioxide on nickel-kieselguhr catalyst". *Industrial & Engineering Chemistry* 47.1 (1955), pp. 140–146. URL: https://pubs.acs.org/doi/pdf/10.1021/ie50541a044?casa_token=xo8d25q6jL0AAAAA:J1ieJffJrAMIkAb4tO0bjDltORwPPKEcLhIVSvwifacmx8X726TaqjKfepiz2XLWIViTcq2ZGMlq.

[82] Th Van Herwijnen, H Van Doesburg, and WA De Jong. "Kinetics of the methanation of CO and CO2 on a nickel catalyst". *Journal of Catalysis* 28.3 (1973), pp. 391–402. DOI: https://doi.org/10.1016/0021-9517(73)90132-2.

[83] Peter J Lunde and Frank L Kester. "Rates of methane formation from carbon dioxide and hydrogen over a ruthenium catalyst". *Journal of catalysis* 30.3 (1973), pp. 423–429. DOI: https://doi.org/10.1016/0021-9517(73)90159-0.

[84] R. A. Sangalli. "Produzione di Substitute Natural Gas (SNG) per idrogenazione di CO2 su catalizzatori a base di Ru: studio cinetico". Department of Energy, Politecnico di Milano, 2017.

[85] Leonardo Falbo *et al.* "Kinetics of CO2 methanation on a Ru-based catalyst at process conditions relevant for Power-to-Gas applications". *Applied Catalysis B: Environmental* 225 (2018), pp. 354–363. DOI: https://doi.org/10.1016/j.apcatb.2017.11.066.

[86] Sarvenaz Farsi *et al.* "A consecutive methanation scheme for conversion of CO2–A study on Ni3Fe catalyst in a short-contact time micro packed bed reactor". *Chemical Engineering Journal* 388 (2020), p. 124233. DOI: https://doi.org/10.1016/j.cej.2020.124233.

[87] Gordon D Weatherbee and Calvin H Bartholomew. "Hydrogenation of CO2 on group VIII metals: II. Kinetics and mechanism of CO2 hydrogenation on nickel". *Journal of Catalysis* 77.2 (1982), pp. 460–472. DOI: https://doi.org/10.1016/0021-9517(82)90186-5.

[88] HAKUAI INOUE and MASAKI FUNAKOSHI. "KINETICS OF M ETHAN ATI ON OF CARBON MONOXIDE AND CARBON DIOXIDE". *Journal of chemical engineering of Japan* 17.6 (1984), pp. 602–610. DOI: https://doi.org/10.1252/jcej.17.602.

[89] Takami Kai, Takeshige Takahashi, and Shintaro Furusaki. "Kinetics of the methanation of carbon dioxide over a supported Ni-La2O3 catalyst". *The Canadian Journal of Chemical Engineering* 66.2 (1988), pp. 343–347. DOI: https://doi.org/10.1002/cjce.5450660226.

[90] Franz Koschany, David Schlereth, and Olaf Hinrichsen. "On the kinetics of the methanation of carbon dioxide on coprecipitated NiAl (O) x". *Applied Catalysis B: Environmental* 181 (2016), pp. 504–516. DOI: https://doi.org/10.1016/j.apcatb.2015.07.026.

[91] Wenhui Li *et al.* "A short review of recent advances in CO 2 hydrogenation to hydrocarbons over heterogeneous catalysts". *RSC advances* 8.14 (2018), pp. 7651–7669. DOI: 10.1039/C7RA13546G.

[92] Jianguo Xu and Gilbert F Froment. "Methane steam reforming, methanation and water-gas shift: I. Intrinsic kinetics". *AIChE journal* 35.1 (1989), pp. 88–96. DOI: https://doi.org/10.1002/aic.690350109.

[93] Isabelle Champon *et al.* "Carbon dioxide methanation kinetic model on a commercial Ni/Al2O3 catalyst". *Journal of CO2 Utilization* 34 (2019), pp. 256–265. DOI: https://doi.org/10.1016/j.jcou.2019.05.030.

[94] Thomas Burger, Philipp Donaubauer, and Olaf Hinrichsen. "On the kinetics of the co-methanation of CO and CO2 on a co-precipitated Ni-Al catalyst". *Applied Catalysis B: Environmental* 282 (2021), p. 119408. DOI: https://doi.org/10.1016/j.apcatb.2020.119408.

[95] Jose A Hernandez Lalinde *et al.* "CO2 methanation and reverse water gas shift reaction. Kinetic study based on in situ spatially-resolved measurements". *Chemical Engineering Journal* 390 (2020), p. 124629. DOI: https://doi.org/10.1016/j.cej.2020.124629.

[96] Clara Larghi and Letizia Petulicchio. "Screening of Ni-Al Catalytic Systems for CO2 Methanation". Department of Energy, Politecnico di Milano, 2020.

[97] Sònia Abelló, César Berrueco, and Daniel Montané. "High-loaded nickel–alumina catalyst for direct CO2 hydrogenation into synthetic natural gas (SNG)". *Fuel* 113 (2013), pp. 598–609. DOI: https://doi.org/10.1016/j.fuel.2013.06.012.

[98] Joan E. Shields Seymour Lowell. *Powder Surface Area and Porosity*. Springer Science Business Media, 1991. ISBN: 9780412396908.

[99] David E Mears. "Tests for transport limitations in experimental catalytic reactors". *Industrial & Engineering Chemistry Process Design and Development* 10.4 (1971), pp. 541–547. DOI: https://doi.org/10.1021/i260040a020.

[100] Noriaki Wakao and Seiichirō Kagei. *Heat and mass transfer in packed beds*. Vol. 1. Taylor & Francis, 1982. URL: https://books.google.it/books?hl=it&lr=&id=Ya5hzOgC05wC&oi=fnd&pg=PR9&dq=Heat+and+mass+transfer+in+packed+beds.+Volume+1&ots=73wS1P-DyY&sig=YoBhFg12vD8SHDc4gYhHMOZokCc&redir_esc=y#v=onepage&q&f=false.

[101] Chiara Marcon. "Applications of Ru-based catalyst for CO2 methanation: modeling study". Department of Energy, Politecnico di Milano, 2020.

[102] Yuan Zhu *et al.* "Catalytic conversion of carbon dioxide to methane on ruthenium–cobalt bimetallic nanocatalysts and correlation between surface chemistry of catalysts under reaction conditions and catalytic performances". *Acs Catalysis* 2.11 (2012), pp. 2403–2408. DOI: https://doi.org/10.1021/cs3005242.

[103] C Wheeler *et al.* "The water–gas-shift reaction at short contact times". *Journal of catalysis* 223.1 (2004), pp. 191–199. DOI: https://doi.org/10.1016/j.jcat.2004.01.002..

[104] MS Spencer. "On the activation energies of the forward and reverse water-gas shift reaction". *Catalysis letters* 32.1 (1995), pp. 9–13. DOI: doi.org/10.1007/BF00806097.

[105] Jan Kopyscinski *et al.* "Applying spatially resolved concentration and temperature measurements in a catalytic plate reactor for the kinetic study of CO methanation". *Journal of Catalysis* 271.2 (2010), pp. 262–279. DOI: https://doi.org/10.1016/j.jcat.2010.02.008.

[106] Jie Zhang *et al.* "Kinetic investigation of carbon monoxide hydrogenation under realistic conditions of methanation of biomass derived syngas". *Fuel* 111 (2013), pp. 845–854. DOI: https://doi.org/10.1016/j.fuel.2013.04.057.

[107] Jacobus Henricus Van't Hoff and Jacobus Henricus Hoff. *Etudes de dynamique chimique*. F. Muller & Company, 1884. URL: https://books.google.it/books?hl=it&lr=&id=kOUzAAAAIAAJ&oi=fnd&pg=PA1&dq=van%5C%27t+hoff&ots=prFWvkXK07&sig=HWVTfy4rz873kZ1ZSyYmWZMkRZw&redir_esc=y#v=onepage&q=van't%5C%20hoff&f=false.

[108] Robert Perry. *Perry's chemical engineers' handbook*. New York: McGraw-Hill, 2008. ISBN: 9780071422949.

Acknowledgments

Nella nostra esperienza che ci ha visto protagonisti attivi sia nell'amato/odiato Lab3 del LCCP sia a litigare con Fortran per far convergere i modelli cinetici, ci sentiamo di dire che dei ringraziamenti sono più che doverosi, perchè senza alcun aiuto il percorso sarebbe stato molto più difficile e pieno di ostacoli.
Il primo che vogliamo assolutamente ringraziare è Ale, sempre disponibile e dotato di infinita pazienza, che ci ha seguito durante tutto il cammino, consigliandoci ad ogni bivio incontrato e lasciandoci in auto-gestione completa quando ormai eravamo in grado di camminare con le nostre gambine.
Un particolare ringraziamento va anche al Prof. Visconti, promotore di questa tesi con cui abbiamo potuto confrontarci nel percorso e "raddrizzare il tiro" quando da lui suggeritoci.
Ringraziamo dal più profondo del cuore Clara e Letizia, nostre manager di laboratorio che hanno saputo insegnarci i principi base con cui poter mandare avanti il nostro impiantino. Sono state, inoltre, sempre disponibili anche quando ormai ci avevano abbandonato perchè promosse a Dr.sse e ci hanno insegnato quanta pazienza bisogna avere in un laboratorio come il nostro, dove l'imprevisto, come quello che ci è capitato con il caro GC-baracca, è dietro l'angolo. Valorose partecipanti e co-titolari della Fortran League.
Vorremmo inoltre ringraziare Tatò e Gp, amici diventati quasi famiglia che conosciamo dai primi giorni di università e che ci hanno sempre sostenuto (a loro modo, va detto).
Un sentito grazie alle nostre famiglie al completo, ragazze e biciclette incluse, per il sostegno e per l'incalzare che ci ha portato a fine percorso.
Infine, io, Denis, rivolgo un sentito ringraziamento al mio compagno di avventura, socio, amico e fratello che ha saputo sopportarmi per un intero anno, lavorando fianco a fianco. Grazie, di cuore.

E io, Gabriele, non posso che ringraziare il miglior giocatore di Cirulla del mondo, che nonostante mi conosca da più di 5 anni, ha deciso di lanciarsi in questa avventura con me. Sei sempre stato una certezza e nell'ultimo anno sei stato un ottimo scalatore di montagne, oltre che il compagno di tesi perfetto.

Colophon

This document was created using LaTeX 2$_\varepsilon$ and edited within the TeXWorks editor, with the help of arara (by Paulo Cereda) typesetting directives. The text body is set in 11 pt Latin Modern Roman, a typeface derived from the Computer Modern fonts designed by Donald E. Knuth. Most of the graphics were generated by PUT PRORGRAM, and diagrams were typeset in PUT PROGRAM. The bibliography was typeset using BibLaTeX.

Copyright Notice